Technische Universität München
Fakultät für Physik

Dissertation

Scanning probe microscopy studies of surface confined molecules and (metal-organic) nanostructures

E20 - Molecular nanoscience and chemical physics of interfaces

Felix Bischoff

TUM – Fakultät für Physik

Scanning probe microscopy studies of surface confined molecules and (metal-organic) nanostructures

Felix M. Bischoff

Vollständiger Abdruck der von der Fakultät für Physik der Technischen Universität München zur Erlangung des akademischen Grades eines Doktors der Naturwissenschaften (Dr. rer. nat.) genehmigten Dissertation.

Vorsitzender:

Prof. Dr. Frank Pollmann

Prüfende der Dissertation:

1. Prof. Dr. Wilhelm Auwärter

2. Priv.-Doz. Dr. Markus Lackinger

3. Prof. Dr. Ingmar Swart (nur schriftliche Beurteilung)

Die Dissertation wurde am 30.11.2017 bei der Technischen Universität München eingereicht und durch die Fakultät für Physik am 06.03.2018 angenommen.

Abstract

Scanning probe microscopy permits real space structural and electronic characterizations at surfaces. For example non-contact atomic force microscopy (nc-AFM) can directly visualize the chemical structure of molecules, their conformation and changes therein caused by chemical reactions. The versatile capabilities are complemented by the possibility of controlled manipulations of matter down to the atomic scale. Based on scanning probe microscopy (SPM) studies, this dissertation presents intriguing insights into single molecule chemistry, molecular nanoscience, and functional materials.

The thesis starts by exploring metal-organic networks. Deliberately functionalized porphyrins form unprecedented two-dimensional, grid-like coordination networks. The decisive parameters for their formation are steric constraints at the coordination node in combination with intrinsic coordination characteristics of the metal. The findings advance the field of low-dimensional molecular nanostructures by emphasizing the importance of well-considered molecular design and careful metal selection. The work continues with nc-AFM studies that directly visualize the adsorption geometries of flexible, surface-anchored molecules with a pronounced 3D character. The well studied system free-base tetraphenylporphyrin (2H-TPP) on Cu(111) exhibits previously unreported extreme macrocycle distortions. This underscores the importance of characterizing adsorbates at the single-molecule level and considerably widens the scope of nc-AFM techniques beyond flat, coplanar species. Furthermore, nc-AFM investigations characterize surface-assisted chemical reactions of porphyrins. Atomic-level structural analyses unambiguously identify the bonding motifs in porphyrin oligomers and the molecular structure of planarized porphyrin derivatives uncovering a hitherto unreported tripyrrolic fragment. The observations highlight the capabilities of heterogeneous catalysis and suggest a novel route for destabilization and deconstruction of chemically and structurally robust macrocylces. Finally, manipulation experiments demonstrate nanoscale phase engineering of the transition metal dichalcogenide niobium diselenide ($NbSe_2$). The scanning tunneling microscope (STM) tip is used to create atomically sharp structural and electronic phase boundaries. The different phases express distinct charge density pattern that are characterized by STM. The results contribute to the understanding of charge order phenomena in $NbSe_2$ and highlight the capabilities for atomic-level nanopatterning techniques.

Zusammenfassung

Rastersondenmikroskopie ermöglicht strukturelle und elektronische Charakterisierungen an Oberflächen im realen Raum. Zum Beispiel kann nicht-Kontakt Rasterkraftmikroskopie (engl. nc-AFM) die chemische Struktur von Molekülen, deren Konformation und Änderungen darin, die durch chemische Reaktionen verursacht werden, direkt visualisieren. Die vielseitigen Fähigkeiten werden durch die Möglichkeit der kontrollierten Manipulation von Materie bis in den atomaren Maßstab ergänzt. Auf der Grundlage von SPM-Studien liefert diese Dissertation faszinierende Erkenntnisse für die molekulare Nanowissenschaft, die Einzelmolekülchemie und funktionelle Materialien.

Die Arbeit beginnt mit der Erforschung metallorganischer Netzwerke. Gezielt funktionalisierte Porphyrine bilden neuartige zweidimensionale, gitterartige Koordinationsnetzwerke. Die entscheidenden Parameter für ihre Entstehung sind sterische Einschränkungen am Koordinationsknoten in Kombination mit intrinsischen Koordinationseigenschaften des Metalls. Die Erkenntnisse erweitern das Gebiet der niederdimensionalen molekularen Nanostrukturen, indem sie die Wichtigkeit einer wohlüberlegten Molekülkonzeption und einer gezielten Metallauswahl hervorheben. Die Arbeit fährt mit nc-AFM Studien fort, die die Adsorptionsgeometrien von flexiblen, oberflächenverankerten Molekülen mit ausgeprägtem 3D-Charakter direkt visualisieren. Das gut untersuchte System Tetraphenylporphyrin (2H-TPP) auf Cu(111) zeigt bisher nicht beschriebene extreme Makrozyklusdeformationen. Dies unterstreicht, wie wichtig es ist, Adsorbate auf Einzelmolekülebene zu charakterisieren und erweitert den Anwendungsbereich von nc-AFM Techniken über flache, koplanare Spezies hinaus. Darüber hinaus charakterisieren nc-AFM Untersuchungen oberflächengestützte chemische Reaktionen von Porphyrinen. Strukturanalysen auf atomarer Ebene identifizieren eindeutig die Bindungsmotive in Porphyrin-Oligomeren und die Molekülstruktur von planarisierten Porphyrin-Derivaten, die ein bislang nicht berichtetes tripyrrolisches Fragment aufdecken. Die Beobachtungen unterstreichen die Möglichkeiten der heterogenen Katalyse und schlagen einen neuen Weg zur Destabilisierung und Dekonstruktion von chemisch und strukturell robusten Makrocyclen vor. Schließlich zeigen Manipulationsexperimente die nanoskalige Gestaltung verschiedener Phasen im Übergangsmetall-Dichalcogenids Niobdiselenid ($NbSe_2$). Mit der Spitze eines Rastertunnelmikroskops (engl. STM) werden atomar scharfe strukturelle und elektronische Phasengrenzen erzeugt. Die verschiedenen Phasen drücken unterschiedliche Ladungsdichtemuster aus, die mittels STM charakterisiert werden. Die Ergebnisse tragen zum Verständnis von Ladungsordnungsphänomenen in $NbSe_2$ bei und verdeutlichen die Fähigkeiten für Nanostrukturierungstechniken auf atomarer Ebene.

Acknowledgments

Many have contributed directly or indirectly to this work, despite only one author name at the beginning. I'd like to thank

- Prof. Johannes Barth and Prof. Willi Auwärter for the possibility to conduct research at E20 and for providing a perfect environment to do so. Thank you for your support—especially for my own ideas—for your ideas and guidance, discussions, and everything I learned.

- Knud Seufert and Yuanqin He for setting up the LT-AFM lab together. It was a great experience and it finally worked ;).

- the rest of the LT-AFM lab, especially Manuela Garnica, Jacob Ducke, and Alexander Riss.

- Viktoria Blaschek, Karl Eberle, Max Glanz, Karl Kölbl, and Reinhold Schneider for administrative and technical support.

- David Écija, and Carlos Palma for fruitful discussions.

- all other members of E20 for discussions, help, procrastination and distraction from work as well as the good times after work.

- everyone at the Physik-Department (work shop, electronics, post office, administration, cryo supplies, etc.) who supported my work through their work.

I was lucky to be involved in several collaborations and research visits. I'd like to thank

- Prof. Jascha Repp for giving me the opportunity to spent several weeks at Universität Regensburg. Without your support, this work probably would not have been so successful. Here, I'd like to specially thank Florian Albrecht for introducing me to nc-AFM and the great time working together. Also, I'd like to thank Petra Wild and everyone else at UR in the groups of Prof. Repp and Prof. Giessibl for making my stays in Regensburg such pleasant ones.

- Prof. Agustin Schiffrin and Prof. Michael Fuhrer for hosting me for three months at Monash University. Financial support by DAAD was greatly acknowledged. Special thanks goes to Bent Weber for great experimental ideas, the work together, and the discussions. I'd also like to thank Jean Pettigrew and Robert Seefeld for administrative support. Moreover, I'd like to thank Cornelius Krull, Jimmy Kotsakidis, Jack Hellerstedt, Mark Edmonds, and everyone else in Melbourne for including me warmhearted, the great working atmosphere, beers and barbecue and for showing me around to make my Australian experience unforgettable. Thank you, Gustl and Claire for the shelter and the most amazing food!

Acknowledgments

- Olesia Snezhkova, and Joachim Schnadt for the joint work on FePc and including me in the project.

- Daphné Stassen, and Davide Bonifazi for synthesizing and supplying novel porphyrin linkers.

I'll miss the lunch crew Lorenz, Martin, Sandrine, and Tobi. Thank you for good times over average food. Furthermore, I'd like to thank everyone else—especially my friends—with whom I had a smile, laugh, or beer along the way.

Special thanks got to my parents Gisela und Klaus, my brother Peter and his family, Oma Anni as well as the rest of the Bischoff and Hens pack. And of course I would never forget to thank Lena for her support and being with me. I'm looking forward to experience all other things to come together with you and Janne.

Contents

Contents

List of figures

List of tables

List of abbreviations

1D	one-dimensional
1D-CDW	one-dimensional charge density wave
1T	TMD polymorph with one layer per repeat unit and trigonal lattice structure
1T-CDW	charge density wave of a TMD in the 1T phase
1T-NbSe$_2$	niobium diselenide in the 1T phase
2D	two-dimensional
2H	TMD polymorph with two layers per repeat unit and hexagonal lattice structure
2H-NbSe$_2$	niobium diselenide in the 2H phase
2H-P	free-base porphine
2H-TPCN	tetra[(4-cyanophenyl)phen-4-ylporphyrin
2H-TPP	free-base tetraphenylporphyrin
2H-TPyPP	tetra[(4-pyridyl)phen-4-ylporphyrin
2L	two layer
3D	three-dimensional
(3 x 3)-CDW	charge density wave with 3 x 3 periodicity
AFM	atomic force microscopy
AM-AFM	amplitude modulation atomic force microscopy
CDW	charge density wave
CO	carbon monoxide
Co-TPP	cobalt-tetraphenylporphyrin
Cu-TPP	copper-tetraphenylporphyrin
DOS	density of states
fcc	face centered cubic

List of abbreviations

FFT	fast Fourier transform
FM-AFM	frequency modulation atomic force microscopy
HOMO	highest occupied molecular orbital
hcp	hexagonally close packed
LDOS	local density of states
lHe	liquid helium
LJ	Lennard-Jones
lN	liquid nitrogen
LT	low temperature
LT-SPM	low temperature scanning probe microscopy
LT-STM	low temperature scanning tunneling microscopy
LUMO	lowest unoccupied molecular orbital
ML	monolayer
NaCl	sodium chloride
NbSe$_2$	niobium diselenide
nc-AFM	non-contact atomic force microscopy
nn	next neighbor
OMBE	organic molecular beam epitaxy
PLL	phase locked loop
PPD	planarized porphyrin derivative
PTP-TriPyr	planarized tetraphenyl tripyrrin
SP	set point
SPM	scanning probe microscopy
STM	scanning tunneling microscopy
STS	scanning tunneling spectroscopy
TMD	transition metal dichalcogenide
TPP	tetraphenylporphyrin
UHV	ultra high vacuum
vdW	van der Waals

1. Introduction

Nanoscience bares great promise for the discovery and development of novel materials with potentially great impact for information technology[1,2], the energy sector[3,4], catalysis[5], and other key technologies. Within the large field of nanoscience, molecular nanoscience addresses functional organic molecules and their potential for nanotechnology from three-dimensional materials down to the single molecule. The interdisciplinary research combines biology, chemistry and physics. Its significance is emphasized by several Nobel Prizes in related fields in the past decade. The prestigious prize was awarded for research in molecular surface science[6], graphene[7] and molecular machines[8].

Naturally, a prerequisite for both, optimized applications as well as fundamental understanding, is the characterization of molecular properties and of all relevant physical and chemical phenomena at the molecular and even atomic scale. For investigating nanostructures at surfaces, scanning probe microscopy (SPM) has been established as advanced research tool. SPM techniques facilitate real space structural and electronic characterizations of low-dimensional architectures, single molecules and individual atoms. One of the most fascinating capabilities of SPM is the direct visualization of the molecular structure of surface-confined organic adsorbates. It was first achieved by means of small-amplitude non-contact atomic force microscopy (nc-AFM) with functionalized tips[9] and paved the way for related experimental techniques with ultimate resolution[10]. By implementing a qPlus sensor as probe, simultaneous scanning tunneling microscopy (STM) measurements are feasible. This also enables characterizations of the sample's electronic structure by high resolution scanning tunneling spectroscopy (STS). Additionally, well-established STM procedures allow nanoscale manipulations like the controlled movement of individual atoms. Such combined STM/AFM investigations are of utmost interest for the atomic-scale control and understanding of two-dimensional materials, interfaces, (organic) adsorbates and their on-surface chemical reactions.

Promising building blocks for molecular nanoscience are macrocyclic tetrapyrrole compounds like porphyrins[11,12]—often referred to as "pigments of life". Their nickname refers to their intense color and relevance for vital biological processes[13]. Porphyrin properties can be tailored by choice of the metal ion within the macrocycle and by modifying the molecular periphery. The biological applications in combination with a great chemical versatility inspires the implementation of tetrapyrroles in functional materials. Examples are single molecule magnets[14,15], catalysts[16,17], light harvesting applications[18,19], and the bottom-up fabrication of functional, extended, two-dimensional nanostructures and metal-organic networks[20].

Furthermore, porphyrins can be employed for the engineering of hybrid materials with tunable functionalities. Various approaches have been reported, including combinations of porphyrins with organic compounds such as fullerenes[21,22] or graphene[23,24] as well as hybrid systems with inorganic materials[25] like transition metal dichalcogenides (TMDs)[26,27]. Herein, it is important to note that the mentioned hybrid components themselves are of

great interest for nanotechnology and warrant appropriate, comprehensive studies. Especially, (atomically thin) two-dimensional materials like graphene and TMDs have attracted widespread attention owed to many promising applications[28–30].

This work aims to advance the fundamental understanding of porphyrin-based molecular nanoscience and low-dimensional materials by combined STM/AFM investigations. The thesis starts by giving theoretical background for SPM techniques in Part I as well as experimental details (Part II). Since the scanning probe setup was installed as part of this doctorate, descriptions of its parts and newly established experimental routines are detailed. The thesis continues with Part III presenting the following experimental topics:

Metal-organic porphyrin networks. Deliberately functionalized porphyrins form two-dimensional, grid-like coordination networks with single copper adatoms. The influence of the functional tectons and the metal on the formation pathways are elaborated.

Adsorption geometry determination of individual porphyrins. A flexible porphyrin derivative adapts different adsorption geometries on different metal substrates. nc-AFM investigations identify the molecular conformations and reveal extreme macrocycle distortions.

Investigation of on-surface chemical reactions. Heating surface-confined porphyrins triggers intermolecular C–C coupling reactions and cyclodehydrogenation. Nc-AFM structurally characterizes the reaction products and uncovers a hitherto unreported porphyrin fragment.

Phase engineering of a TMD. STM-assisted manipulation experiments demonstrate nanoscale structural and electronic phase engineering of a transition metal dichalcogenide. All phases express distinct charge density patterns that are characterized by STM.

The experiments address some of today's issues in molecular nanoscience. In order to engineer surface-confined, porphyrin-based materials, it is essential to understand molecular properties and how they influence the final nanostructures and their formation. However, a detailed understanding of all parameters is often lacking. Section 6 provides a detailed discussion of many influencing parameters for metal-organic network formation and therefore opens routes for the deliberate design of nanostructures. Despite many STM studies of porphyrins, their investigation by nc-AFM is scarce[24,31–34]. This is owed to the structural flexibility and 3D character of many derivatives. In contrast to planar species, strong distortions prevent direct access to all molecular moieties. Nevertheless, nc-AFM investigations of strongly deformed and 3D molecules might also provide insights into molecular properties by comparing intramolecular heights and by investigating surface-parallel parts only[34–37]. This will be demonstrated in Section 7. Additionally, nc-AFM has not been applied for studying porphyrin nanochemistry. Therefore, the structure of reaction products could only be inferred from STM images and simulations and was often subject to discussion. This issue will be broached in Section 7.2. The real-space characterization of all reaction products will verify suggested structures and moreover, it will

identify an unreported deconstructed macrocycle. The results Part ends with Section 11 providing insights into the formation of charge density waves in niobium diselenide—an unconcluded topic in TMD research. Furthermore, the engineering of atomically sharp phase boundaries between substantially different electronic phases suggests the TMD for future atomically small electronic devices.

Finally, the thesis concludes with a summary and outlook (Section 12).

Part I.

Fundamentals of scanning probe microscopy

Introduction to SPM

Scanning probe microscopy (SPM) employs a physical probe—usually referred to as tip—to scan a surface pixel–by–pixel at very close distances. At each pixel the tip locally interacts with the sample. The interaction is measured and converted into an intensity map that is often referred to as scanning probe image. Since SPM does not rely on optical methods for imaging, unprecedented resolution down to the sub–Ångstrom regime ($<$ 10^{-10} m) can be achieved and true atomic resolution is feasible. Basically, SPM visualizes tip–sample interactions in real space with ultimate resolution in a non-destructive manner. Therefore, it is well-established in surface science and nano science. The most prevalent SPM techniques are scanning tunneling microscopy (STM) and atomic force microscopy (AFM), which are as well the research methods of this work. Historically, the development of both is closely related[38]. First, STM was invented by Binnig and Rohrer in the early 1980s at IBM Zürich[39,40], the first image of the 7×7 reconstruction of Si(111) impressively demonstrated its capabilities for atomic resolution in 1983[41] and led to the Nobel Price for its inventors in 1986. However, STM is limited to conducting surfaces. This drawback led to the development of the AFM by Binnig, Quate and Gerber in 1986[42] and the extension of SPM to insulating surfaces and biological systems such as DNA and polymers[43,44]. Judging from the citation count of the pioneering publications on STM and AFM ($\approx$ 5000 vs. $\approx$ 16 000), today AFM is the most widely applied SPM technique. It is also interesting to note that the experimental realization has basically remained unchanged for STM while AFM has undergone substantial development, especially concerning signal detection techniques, experimental operation modes and force sensors (i.e. the probe itself). Only recently the latest generations of AFM sensors were developed, namely the quartz tuning fork sensor (qPlus sensor)[45–47] and needle sensors[48,49]. It should be noted that STM and AFM are completely independent techniques, which can offer complementary data. Therefore it can be desirable to operate a microscope that combines both techniques in one probe. Although multiple concepts for such combined STM/AFM probes were developed, it was the qPlus–sensors that led to a breakthrough and it has been established as state-of-the-art tool for combined STM/AFM measurements[47,50]. This work presents qPlus based STM/AFM experiments. Thus, the following chapter discusses the fundamentals of STM and AFM in Section 2 and 3. STM is introduced from the basic concept of tunneling via a theoretical description of the tunneling current to its experimental implementation. The AFM–section follows the same structure (from basics to experiment) and additionally presents the qPlus sensor in detail.

2. Scanning tunneling microscopy – STM
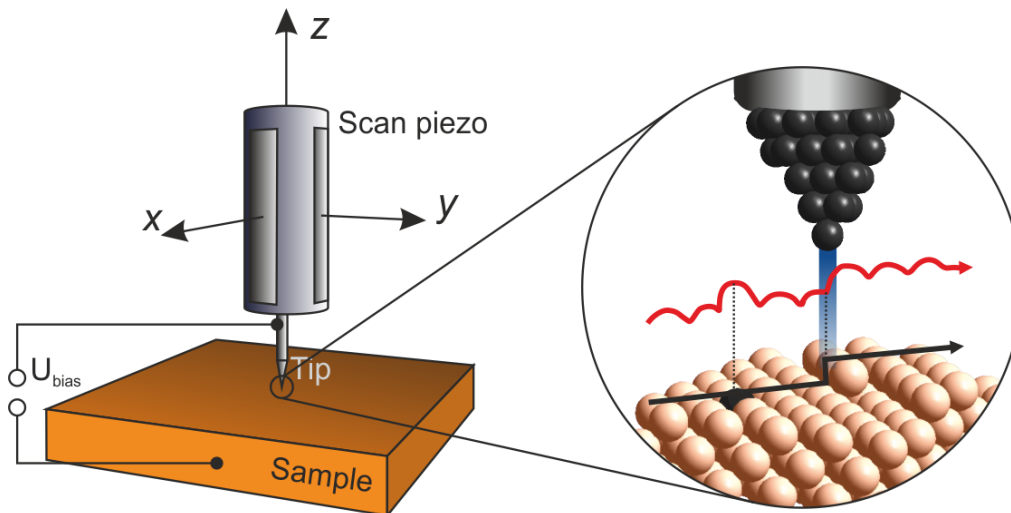
Figure 2.1. Principle of scanning tunneling microscopy. An atomically sharp tip is brought in close proximity of a conducting sample. A bias voltage U is applied between the tip and the sample, which results in a tunneling current. A feedback system keeps the tunneling current constant by adjusting the tip height z while scanning the tip across the surface. In this so called constant current mode the tip follows the contour of electronic and topographic structures on the structures. The x–, y– and z–positions of a metallic tip are controlled via a piezo tube.

STM bases on the quantum mechanical tunneling effect. In classical mechanics a particle cannot overcome a potential barrier higher than its total energy. Therefore the barricade itself and the space beyond are classically forbidden regions. In quantum mechanics however, a particle is described by a wave function that decays exponentially into the potential barrier. As a result there exists a finite probability for the particle to be at the opposing side. This effect is called tunneling. Tunneling is a general quantum phenomena characteristic to all particles, but the tunneling probability decreases exponentially with increasing mass (vide infra equation (2.1)). Therefore it is more likely for light particles such as electrons. The collective effect of many tunneling electrons can be measured as current and will be referred to as tunneling current I. The principle of STM relies on the detection and visualization of I between an atomically sharp tip and a sample while scanning the tip with sub-Ångstrom precision. For this purpose, a metal tip is positioned with piezoelectric actuators (piezos) within a few Ångstroms to a conducting substrate to realize a spatial overlap between the wave functions of both. The gap in between represents the tunneling barrier. A potential difference between sample and tip—the bias

voltage $U^\ddagger$—gives rise to a tunneling current in the order of pico- to nano-ampere that exponentially depends on the tip–sample distance (see equation (2.2)). As a consequence, small changes in the gap e.g. induced by nano-structures result in considerable current changes. The variations in the tunneling current can be recorded and displayed directly during scanning with fixed tip height as two-dimensional intensity plots $I(x, y)$. This scan mode is called "constant height mode". However surface features higher than the tip–sample spacing would result in crashes. Therefore I is usually not displayed directly, but acts as control variable in a feedback loop that regulates the tip height z. If the current increases (decreases), the feedback retracts (approaches) the tip in order to re-establish the original current set point. The tip height is then displayed as $z(x, y)$ plot. This mode is called "constant current mode" and represents the most common STM operation. In a simplified picture these plots represent high-resolution images of the surface topography. In reality, the tunneling current also depends on the local density of states (LDOS) of the surface and STM images represent a convolution of the sample's topography and electronic structure (compare equation (2.6)). The basic working principle of STM is schematically illustrated in Figure 2.1, STM operation modes are summarized in Section 2.3. For details on the setup used in this work, please see Chapter II.

The following section will discuss the theoretical derivation of the tunneling current as well as the experimental implementation. Since this work only focuses on a few important aspects, the reader is referred to available textbooks on the matter for a more detailed description[52–55].

2.1. Theoretical discussion of the tunneling current

Since the early 1900s—decades before the invention of STM—a multitude of theoretical approaches to tunneling have been reported and have contributed to the understanding of tunneling phenomena such as the α–decay. Since they offer general solutions, they can of course also be applied to STM. Mathematically, the Schroedinger equation (SE) describes the evolution of a particle's wave function ψ. The tunneling effect can be understood from a simple one dimensional, time independent model where an incident wave ψ_0 encounters a constant rectangular potential barrier of height V_0 and width d as illustrated in Figure 2.2. The explicit approach to the problem will not be discussed here, but can be found in corresponding literature.[52,54,55] Basically, by parameterizing the wave function to the three areas before, within and behind the barrier and by applying the continuity conditions on the wave function and its derivative, one obtains the solutions of the SE in all areas. Most interestingly, this leads to a non-vanishing amplitude t behind the barrier even if the incoming particle does not carry enough energy to overcome the barrier ($E < V_0$). The transmissivity $T = |t|^2$ can be derived by calculating the ratio of the transmitted flux to the incoming flux. In the weak tunneling limit, i.e. a simplification assuming a wide

---

$^\ddagger U$ as symbol for the (bias) voltage is used according to German and European accepted usage, while V for voltage is common in North America and recommended in IEEE-standards[51]. When referring to the differential conductance dI/dV, V is used for historical reasons, since the prefix dI/dV as for example in "dI/dV spectra" has been established in the nomenclature of experimental techniques. In general, both, U and V are accepted.
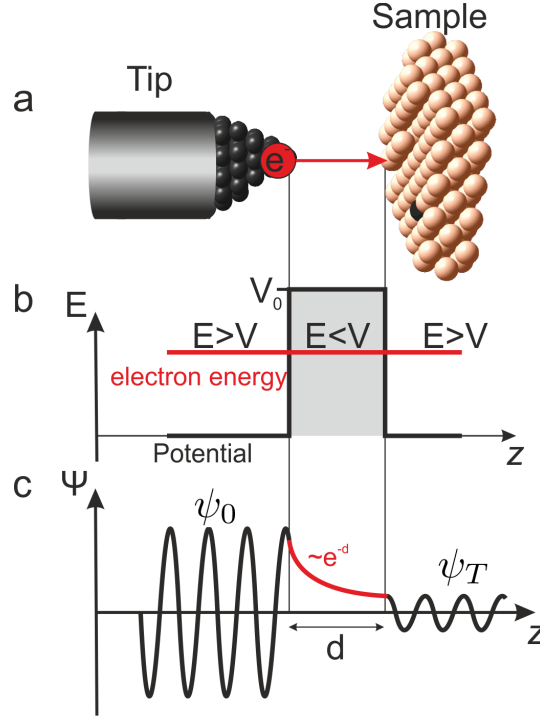
Figure 2.2. Schematic of the tunneling process. a) Real space situation. A vacuum gap d separates the tip and the sample. In a classical view the current circuit is not closed and no electrons can flow. b) Energy diagram. The metal–vacuum–metal arrangement imposes a rectangular potential barrier for the electrons (thick black line, assuming the same work function for both sides). The red line indicates the electron's energy. Inside the metal its total energy is higher, in the gap it is lower than the potential. c) Wave function picture. An incident wave ψ_0 encounters the one dimensional, rectangular potential barrier of width d, decays exponentially within the barrier and is finally partially transmitted as ψ_T to the opposing side. This process is called tunneling.

and high barrier, this yields:

$$T \propto \mathrm{e}^{-2d\sqrt{2m(V_0-E)/\hbar^2}}, \tag{2.1}$$

where d is the barrier width, V_0 its height, $\hbar$ is the reduced Planck constant, m is the electron mass, and E its total energy. For STM a metal tip is positioned in the range of a few Ångstrom above a conducting surface. In a vaccum at a metal surface, thus a metal–vacuum–metal tunneling junction is formed. The height of the potential barrier is given by the energy needed to remove an electron from the tip into vacuum, i.e. by the work function Φ; the width of the barrier is defined by the tip–sample distance d. A bias voltage U defines the electron energy $E = eU$. Assuming that tip and sample exhibit the same work function Φ and for small bias voltages (i.e. $eU \ll \Phi$), the tunneling current I is proportional to T and can take the form

$$I \cong I_0 \mathrm{e}^{-2d\sqrt{2m\Phi/\hbar^2}} = I_0 \mathrm{e}^{-2\kappa d}. \tag{2.2}$$

This simple form of *I* features important consequences for STM. The current can give an indication about the work functions of the employed materials as shown in initial tunneling experiments[56]. Assuming a typical work function of $4-5\,\mathrm{eV}$, the decay constant κ is in the order of $1\,\text{Å}^{-1}$. As a result the tunneling current approximately changes by one order of magnitude per $1\,\text{Å}$ derivation in the tip–sample distance. This distinctive distance dependence involves important implications for STM applications: i) high vertical resolution and ii) the foremost atom at the tip–apex strongly dominates the tunneling current while contributions from the rest of the tip at larger separations can be neglected. Therefore the probe is highly localized, which leads to high lateral resolution (in combination with other considerations for the tunneling current discussed below, as well as high precision actuators for moving the tip in a highly stable, low-noise environment). A more
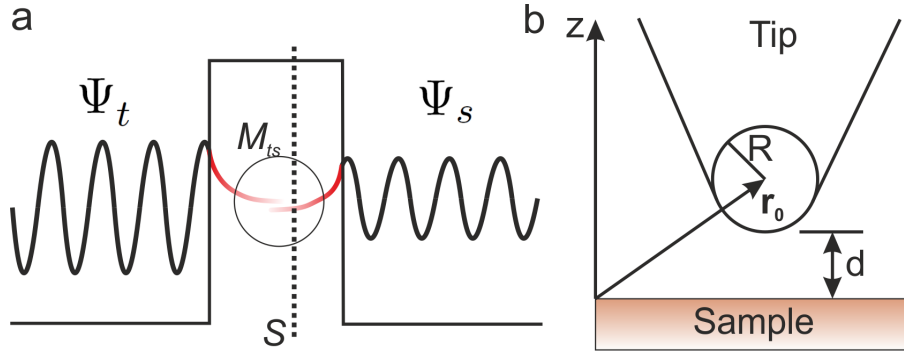
Figure 2.3. Bardeen tunneling formalism and Tersoff-Hamann approximation. a) The Bardeen formalism treats tunneling as a many particle, perturbation problem. The tip wave function Ψ_t and the sample wave function Ψ_s both decay exponentially inside the vacuum and overlap. The matrix element M_{ts} describes their interaction that leads to tunneling through an arbitrary area S between tip and sample. b) Assumptions of the Tersoff-Hamann solution for the tunneling current. The tip is positioned at $\vec{r_0}$ with distance d to the sample and features a spherical tip apex of radius R.

sophisticated treatment of the tunneling junction is offered by the Bardeen formalism.[57] This approach provides a general solution (not limited to one dimension) for the tunneling probability in a time-dependent, many-particle treatment. Tip and sample are considered as independent wave functions, i.e. electronic states, and tunneling is then treated as a transitions from one state to the other. In the following, the basic ideas for the theoretical treatment of the tunneling current are summarized according to the work of Tersoff and Hamann[58]. To describe the tunneling process in STM with Bardeen's approach, the initial and final states will here be denoted by the tip wave function Ψ_t and the sample wave function Ψ_s. The two are connected by the matrix element M_{ts}

$$M_{ts} = -\frac{\hbar^2}{2m}\int_S (\Psi_t^*\vec{\nabla}\Psi_s - \Psi_s\vec{\nabla}\Psi_t^*)\mathrm{d}\vec{S}, \qquad (2.3)$$

whereby the integration is carried out over an arbitrary surface S between tip and sample through which the tunneling occurs. The transition probability is then given by $|M_{ts}|^2$.

The general expression for the tunneling current

$$I = \frac{2\pi e}{\hbar} \sum_{t,s} f(E_t)[1 - f(E_s + eU)]|M_{ts}|^2 \delta[E_t - (E_s + eU)] \tag{2.4}$$

strongly resembles Fermi's Golden Rule, i.e. a first order perturbation. The Fermi function $f(E_t)$ describes the distribution of occupied states at the tip and $1 - f(E_s + eU)$ gives the distribution of unoccupied states at the sample with applied bias U. The product therefore imposes a selection rule that favors transition from occupied to unoccupied states only. The sum over $\delta[E_t - (E_s + eU)]$ only adds states from both sides with the same energy, i.e. it imposes energy conservation (elastic tunneling). Please note that tunneling is here described in one direction only and back-tunneling from sample to tip is neglected. In the limit of small voltages and low temperature (i.e. no self-excitation above the barrier and the Fermi functions become step-like) the tunneling current can be written as[59]

$$I_t \propto U \sum_{t,s} |M_{ts}|^2 \delta(E_s - E_F) \delta(E_t - E_F) \,. \tag{2.5}$$

Here the δ–functions within the sum indicate that tunneling is limited to the corresponding available states just around Fermi (small voltage limit). The matrix element can be evaluated by proper choice of the wave functions and under the following assumptions: i) the tip is assumed to be spherical at the apex with radius R, ii) the tip and surface work functions Φ are equal and iii) the angular dependence of Ψ_t is neglected, i.e. the tip wave function is assumed to be of s-wave character. This leads to

$$I_t \propto U \cdot \Phi^2 R^2 e^{2\kappa R} \cdot \rho_t(E_F) \cdot \sum_s |\Psi_s(\vec{r_0})|^2 \delta(E_s - E_F) \,, \tag{2.6}$$

where $\vec{r_0}$ is the position of the center of the spherical tip. The exponential dependence on the tip-sample spacing d discussed before enters here via

$$|\Psi_s(\vec{r_0})|^2 \propto e^{-2d\sqrt{2m(\Phi)/\hbar^2}} \,. \tag{2.7}$$

The sum-term in equation (2.6) represents the density of states of the sample ρ_s at Fermi at the position of the tip $\vec{r_0}$, and is therefore referred to as local density of states (LDOS);

$$\rho_s(\vec{r_0}, E_F) = \sum_s |\Psi_s(\vec{r_0})|^2 \delta(E_s - E_F) \,. \tag{2.8}$$

By assuming that the tip parameters are constant and by assuming metal-typical values for Φ, R and $\rho_t(E_F)$, one obtains

$$I_t \propto U \cdot \rho_s(\vec{r_0}, E_F) \,. \tag{2.9}$$

This means that the tip follows an equipotential contour of the surface DOS for a constant current while maintaining the exponential distance dependence. From this expression the convolution of topography and electronic structure is obvious: the STM will adjust the tip height until the tip "sees" the same density of states. For a heterogeneous sample, as for example in the case of impurities in a crystal surface, the LDOS will differ substantially between individual atoms. Therefore a change in tip height can occur at an atomically

smooth surface as illustrated in the inset of Figure 2.1. Another example are organic adsorbates on a metal surface. An increase in topography by an adsorbate will not result in the same retraction of the tip due to the fundamentally different electronic structures of metal and molecule.

The convolution of topography and electronic structure is generally not trivial to disentangle, if not to say impossible to separate and therefore aggravates true topographic imaging with STM. Based on the theoretical considerations, the initial tunneling sketch
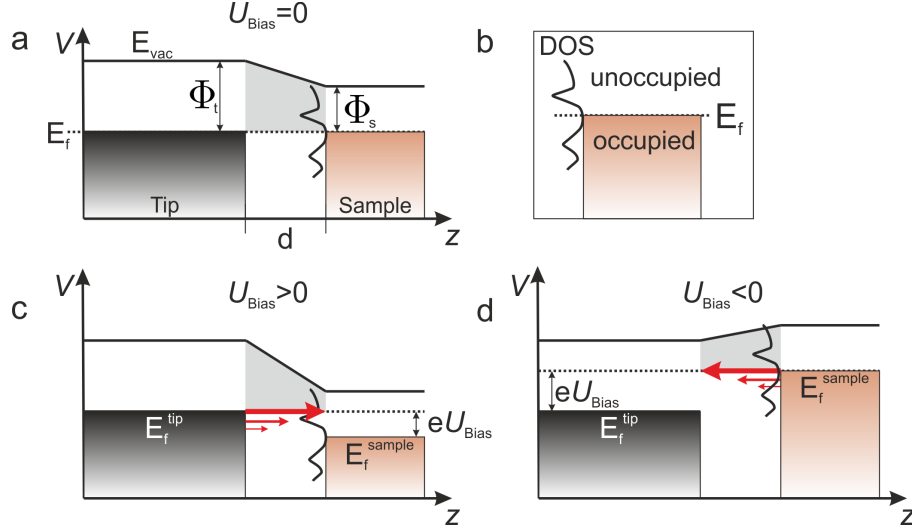
Figure 2.4. Energy level diagrams for sample and tip. a) When tip and sample are in close contact and at thermal equilibrium, their Fermi levels E_f align. The vacuum level E_{vac} is defined at each side of the barrier by the work function of the tip Φ_t and of the sample Φ_s, respectively. Because their values are usually different, a trapezoidal potential barrier forms. b) While the tip is assumed to have a flat density of states, the sample can exhibit a rich electronic structure represented here by the black curve. Unoccupied states are located above Fermi, occupied states below. The DOS is assumed to have a fixed relation to the Fermi level of the sample. c) When applying a positive bias at the sample, the tip Fermi level is shifted upward with respect to the sample. Therefore electrons from occupied states at the tip can tunnel into unoccupied states of the sample and give rise to a tunneling current. The energy of the probed unoccupied states is defined by the bias voltage eU. d) Vice versa, if a negative bias is applied at the sample, its Fermi level is shifted up and electrons from occupied states of the sample tunnel to the tip. Therefore the sign of the current inverses.

in Figure 2.2 can be extended to a more realistic situation to illustrate the dependence of the tunneling current on the bias and the electronic structure. Please note that the following paragraph only descriptively explains STM and the underlying real experimental and physical processes involve more complex considerations. Figure 2.4 shows an energy diagram representing the tip (left) and the sample (right). Their Fermi levels are located below the vacuum level by the amount of the corresponding work function (Φ_s or Φ_t). In thermodynamic equilibrium and close proximity the Fermi levels align to form a trapezoidal tunneling barrier (2.4a). This situation represents an STM setup with zero bias voltage. If a bias voltage U (which will simply be referred to as bias) is applied to the sample while the tip is at ground, its energy levels are shifted against the tip's by $|eU|$—

down if the bias is positive (Figure 2.4c) and up if it is negative (Figure 2.4d). Note that electrons always tunnel from the negatively biased electrode to the positive one. Consequently, the tunneling direction can be controlled and is not limited to the direction from the tip to the sample—in contrast to what the aforementioned theoretical description might have suggested. At negative bias, electrons tunnel from sample to tip.

The wave function of an electron decays exponentially from a solid into the vacuum. Electrons in high energy states, i.e. states near the Fermi level, have the highest probability for tunneling and contribute dominating (cf. red solid arrows in Figure 2.4). Please note, that this is in agreement with equation (2.5) for the tunneling current. Considering the selection rules from Bardeen's formalism, these electrons can only tunnel into unoccupied states and will choose the energetically lowest ones. This has important implications for the interpretation of STM data. For positive bias (tip–to–sample tunneling) the STM probes unoccupied states of the sample and for negative bias (sample–to–tip tunneling), the STM visualizes occupied sample states. In the case of (surface-confined) molecules these electronic states are usually referred to as lowest unoccupied molecular orbitals (LUMO) and highest occupied molecular orbitals (HOMO). Additionally, the magnitude of the bias selects the energy of the involved states, i.e. electronic structures can be probed which gives rise to scanning tunneling spectroscopy (STS).

2.2. Scanning tunneling spectroscopy – STS
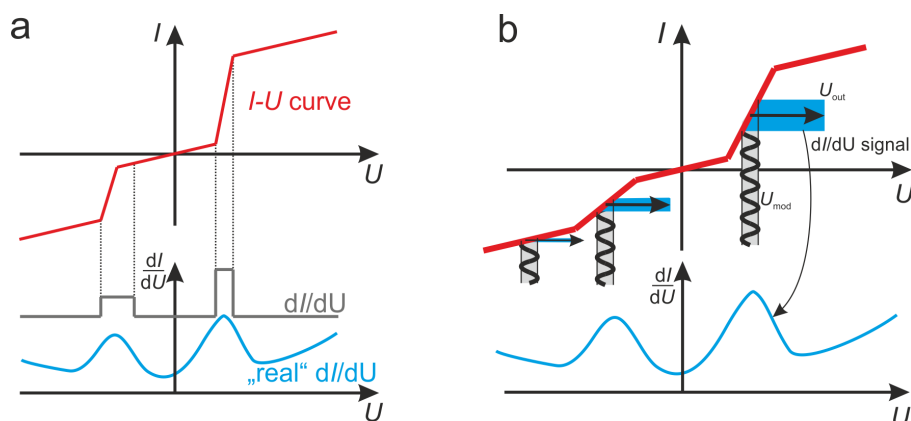
Figure 2.5. Principle of STS. a) Sweeping the bias voltage while recording the tunneling current yields I–U curves (red). By definition or by the way of biasing the setup, the tunneling current exhibits negative values for negative bias. A steeper slope in I–U curves corresponds to a higher density of states at the sample. If a state is energetically localized, a slope transition occurs across the bias sweep that manifest as distinct step in the current derivative dI/dU (gray). In a more realistic situation (e.g. limited energy resolution, thermal broadening, hybridization of states) these steps manifest as peaks. b) Working principle of recording the dI/dV signal with a lock-in amplifier. A fixed voltage modulation U_{mod} is superimposed onto the DC bias that causes a modulation of the resulting tunneling current. The steeper the slope of the I–U curve, the larger is the response (cf. blue beams). Therefore it is possible to measure the slope of I–U curves and get information on the DOS of the sample.

As argued in the previous section, the tunneling current depends on the surface density of states and the bias voltage defines the energy of the tunneling electrons, i.e. it selects the participating states. Furthermore, it becomes obvious that tunneling is suppressed when no states are available and it is strongly enhanced when the bias is in resonance with a high density of states—often referred to as resonant tunneling. Resonant tunneling can be detected as increase in the conductance $\sigma = I/U$ that is experimentally accessible as the slope of *I–U* curves. *I–U* curves are recorded by measuring the tunneling current while sweeping the voltage at a fixed tip position. A change in the slope causes distinct steps in its derivative $\mathrm{d}I/\mathrm{d}U$—the differential conductance. For sharp spectral features the enhancement of the tunneling current is confined to a narrow energy/bias range resulting in $\mathrm{d}I/\mathrm{d}U$ steps (gray curve in 2.5). However, due to experimental aspects such as thermal broadening and limited energy resolution, the differential conductance exhibits peaks instead of steps (blue curve in 2.5). The emergence of peaks in the differential conductance is exploited by STS to study the local electronic properties of the sample. The following considerations are based on the work of Hamers[60].

Equation (2.4) sums over all available states and therefore suggest the use of an energy integral in a continuous picture. Assuming low temperature and an average transmission probability $\langle |M_{ts}|^2 \rangle = T(\vec{r}, E, U)$, the tunneling current can be written as

$$I \propto \int_0^{\mathrm{e}U} \rho_s(\vec{r}, E) \rho_t(\vec{r}, E - \mathrm{e}U) T(\vec{r}, E, \mathrm{e}U) dE \,, \tag{2.10}$$

where ρ_s (ρ_t) is the DOS of the sample (tip) at location $\vec{r}$. The differentiation of (2.10) with respect to the voltage results in

$$\frac{\mathrm{d}I}{\mathrm{d}U} \propto \rho_s(\vec{r}, \mathrm{e}U) \rho_t(\vec{r}, 0) T(\vec{r}, \mathrm{e}U) + \int_0^{\mathrm{e}U} \rho_s(\vec{r}, E) \rho_t(\vec{r}, E - \mathrm{e}U) \frac{\mathrm{d}T(\vec{r}, E, \mathrm{e}U)}{\mathrm{d}U} dE \,. \tag{2.11}$$

The remaining integral term describes the voltage dependence of the transmission probability that vanishes if T is assumed constant. If furthermore the tip DOS is assumed to be constant, then

$$\frac{\mathrm{d}I}{\mathrm{d}U} \propto \rho_s(\vec{r}, \mathrm{e}U) \,. \tag{2.12}$$

The differential conductance is therefore directly dependent on the LDOS of the sample ρ_S and changes in of $\mathrm{d}I/\mathrm{d}U$ can by associated with changes in the density of states of the sample. This allows spectroscopic characterizations of the local electronic structure of the sample, so called $\mathrm{d}I/\mathrm{d}V$ [‡] measurements or STS. Depending on further experimental settings the most common STS techniques either spectroscopically probe the local electronic structure ($\frac{\mathrm{d}I}{\mathrm{d}V}(V)$: ST-spectra) or the spatial extent of distinct electronic contributions can be mapped across the surface ($\frac{\mathrm{d}I}{\mathrm{d}V}(x,y)$: $\mathrm{d}I/\mathrm{d}V$-maps).

It is worthwhile to comment on the simplifications that led to equation 2.12, namely constant T and ρ_t. In a real situation, the transmission probability T increases monotonically with the voltage and contributes a smoothly varying background in ST-spectra. This

---

[‡]As already mentioned in the introduction of this chapter, this work uses U as symbol for the (bias) voltage according to German accepted usage, while V is common in North America and recommended in IEEE-standards[51]. When referring to the differential conductance $\mathrm{d}I/\mathrm{d}V$, V is used for historical reasons: the prefix $\mathrm{d}I/\mathrm{d}V$ as for example in "$\mathrm{d}I/\mathrm{d}V$ spectra" has been established in the nomenclature of experimental techniques. In general, both, U and V are accepted.

effect can potentially conceal contributions from electronic states, but can be corrected by proper background subtraction[61], respectively by normalizing the differential conductance to I/U or by more complex treatments[62]. Furthermore, the tip density of states can vary considerably and hamper spectroscopic studies. To exclude tip contributions for meaningful experiments, first the well-defined electronic structure of a clean (single crystal) metal substrate is probed. An ideal metal reference ST-spectrum of Ag(111) or Cu(111) is flat and only exhibits a step-like feature at the energy of its two dimensional surface state. If this it not true, the tip is repeatedly modified and checked until the condition is satisfactorily fulfilled. In this case, the assumption of a non-contributing tip is sufficiently good. Nevertheless, some effort has been put forward to deconvolute tip and sample DOS in ST-spectra evaluation[63,64].

Lock-in technique

dI/dV experiments can be realized by numerical differentiation of I–U curves, but are most commonly implemented via a lock-in technique. For this purpose a small, high frequency, sinusoidal voltage modulation $U_{mod} = u_{mod} \sin(\omega_{mod}t + \phi_{mod})$ is superimposed onto the constant bias while a lock-in amplifier detects the change in the tunneling current as a function of the bias voltage. By expanding the tunneling current $I(U + U_{mod})$ in a Taylor series it reads

$$I(U + U_{mod}) \cong I(U) + \frac{\mathrm{d}I}{\mathrm{d}U}u_{mod}\sin(\omega_{mod}t + \phi_{mod}) + \frac{\mathrm{d}^2I}{\mathrm{d}U^2}u_{mod}^2\sin^2(\omega_{mod}t + \phi_{mod}) + \cdots.$$
(2.13)

This current is converted by a preamplifier into a voltage signal U_{out} that exhibits the same form and then a lock-in amplifier multiplies a reference signal $U_{ref} = u_{ref}\sin(\omega_{ref}t + \phi_{ref})$ of the same frequency as the voltage modulation. Integration over time $\tau \gg \omega_{mod}^{-1}$ of the combined signal produces the mean of every component $\overline{U_{out}^i}$. Basically the integration evaluates

$$\overline{U_{out}^i} = \frac{1}{\tau}\int_0^\tau u_i\sin(\omega_i t + \phi_i)u_{ref}\sin(\omega_{ref}t + \phi_{ref})\mathrm{d}t =$$
(2.14)

$$= \begin{cases} \frac{1}{2}u_iu_{ref}\cos(\phi_i - \phi_{ref}) & \text{for } \omega_i = \omega_{ref} \\ 0 & \text{otherwise} \end{cases}.$$
(2.15)

The lock-in integration therefore filters out every component that does not match the reference frequency (band pass filter) and only the spectral components close or equal to the modulation frequency survive. Herein, a longer integration time means a lower pass bandwidth and consequently a better signal-to-noise ratio. With regard to equation (2.13), the time integration means that only the signal corresponding to the second component proportional to dI/dU is passed on. In other words, the lock-in measures the slope of I–U curves. A handwaving explanation of the working principle is shown in Figure 2.5b. The band-pass characteristic of the lock-in can furthermore be exploited to detect higher derivatives d$^n I$/dU^n by choosing the corresponding higher harmonics ω_n as reference signal. A prominent example is inelastic electron tunneling spectroscopy (IETS)[65–67]. Please note, that the output signal of the lock-in amplifier in equation (2.15) still depends on the relative phase of the reference signal. Experimentally, the signal is optimized to its

maximum value at $\cos(\phi_i - \phi_{ref}) = 1$ by varying the reference phase and monitoring the signal amplitude.

In a real setup the current signal also carries noise of various frequencies that can be transmitted through the filter if they match the band pass. Therefore the lock-in should be operated at frequencies that do not match internal resonances of the experimental setup and it is therefore usually operated in the range of $0.5 - 2.5\,\text{kHz}$. Additionally the noise spectrum of the current signal can be analyzed prior to an experiment and accordingly the lock-in is set to a frequency that exhibits little noise in the current signal.

2.3. STM operation modes

Soon after the impressive demonstrations of the topographic imaging capabilities of STM, techniques for spectroscopic characterizations[68–70] and atomically precise manipulations of adsorbates[71,72] were developed. Furthermore, reports of standing wave patterns in the two-dimensional electron gas at metal surfaces showed that STM is capable of mapping the local density of states in real space and that it can visualize quantum mechanical scattering and interference effects[73–75]. In combination with targeted manipulation of adatoms the tip of an STM was used to build nanostructures that confine the 2D electron gas and impressively demonstrate the possibilities of STM manipulation procedures for nanotechnology[76]. Additionally, tip-assisted atomic scale modifications of materials by the application of voltage pulses was developed and recognized as powerful tool for nanochemistry[77].

Based on the introduction of the fundamentals of STM in the preceding sections, here the experimental implementations are described. The following section gives a short overview on different STM techniques from imaging over spectroscopic characterizations to manipulations, which are all routinely employed in STM studies.

In general, STM operation relies on at least three actuating variables:

- Lateral tip position (x, y), and

- bias voltage U.

Additionally, one of the following signals is defined as observable for data visualization

- Vertical tip position z,

- tunneling current I, or in the case of STS,

- differential conductance $\mathrm{d}I/\mathrm{d}V$ (or higher harmonics $\mathrm{d}^n I/\mathrm{d}V^n$).

If z is recorded, I takes the role of the constant control parameter for the feedback loop. Furthermore, a multitude of other parameters can be set, e.g. feedback constants, lock-in parameters, scan speed, scan size, and scan direction to name just a few. These settings are relevant for real operation, but are irrelevant for the introduction of the basic operation schemes and will therefore be omitted. Here, the feedback always refers to the regulation of the tip height z in order to keep the control value constant. Consequently, a disabled feedback always refers to a constant tip–sample spacing, defined by the set point (SP) right before the feedback is switched off. In STM, the control parameter is given by

a current value. In contrast, for AFM the feedback can also be regulated to a frequency shift Δf. Although the feedback is only controlled via I in STM, the set point is defined in combination with the bias voltage, because both parameters define the tip-sample spacing. According to equation (2.2), a higher current and a lower voltage reduce the tip-sample spacing. The SP acts as reference in experiments that require a disabled STM feedback, such as STS and constant height measurements. Typical SPs—also for imaging modes— are in the range of $U = 50 - 2000\,\mathrm{mV}$ and $I = 50 - 200\,\mathrm{pA}$. Furthermore, it should be noted that the acquisition of two-dimensional STM data, or SPM data in general, proceeds pixel–by–pixel along one direction (usually x) and only then jumps to the pixel in the next line along the other direction (usually y). As a result, each image features a fast-scan direction along x and a slow-scan direction along y. Figure 2.6 schematically shows STM modes that are briefly introduced below.

STM: Constant current mode

The constant current mode is the most common imaging technique. The tunneling current I is fed into a feedback loop that adjusts the tip height z in order to keep the tunneling current constant. STM data exhibit the tip height for each pixel $z(x, y)$ as heat map for a predefined SP (I, U). This scan mode reduces the risk of tip crashes due to rough or non-planar surfaces, high features and vertical drift caused by a temperature gradient or piezo creep. It is the most stable and reliable operation mode.

STM: Constant height mode

The constant height mode acquires images with disabled z-feedback. STM data depict the magnitude of the tunneling current at each pixel as $I(x, y)$ intensity map for constant tip height z. The initial tip–sample distance is determined by the I, U set point. Usually the set point is chosen above the bare metal substrate to generate a reproducible tip–sample spacing. This mode can only be applied at very smooth surfaces, e.g. bare metal surfaces, for small scan frames and in very stable conditions (no piezo drift/creep). Otherwise, the tip could crash into asperities higher than the preset tip–sample separation. Constant height measurements are commonly employed in $\mathrm{d}I/\mathrm{d}V$ mapping and in AFM, but find almost no application for standard STM imaging.

STS: Differential conductance spectroscopy

STS allows characterizations of the local electronic structure with high resolution of both, the occupied and unoccupied states. To record an ST-spectrum, the differential conductance $\mathrm{d}I/\mathrm{d}V$ is recorded as a function of the bias voltage U, respectively electron energy eU. STS is usually carried out by detecting the response of the current signal to a sinusoidal voltage modulation with a lock-in amplifier as described in Section 2.2). The tip is stabilized by the initial set point values, the feedback is disabled and the voltage is ramped between preset values. After the voltage sweep, the feedback is enabled again. Ideally, the SP voltage matches the start value of the sweep in order to avoid artifacts due to sudden voltage changes at the beginning of the spectra. Especially bias sign changes should be avoided. Furthermore, the SP should not coincide with a high density of states that would result in an apparently larger tip–sample separation and could attenuate other
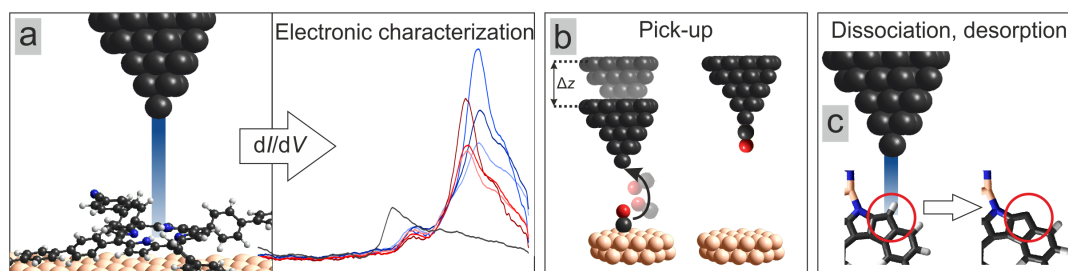
Figure 2.6. Experimental STM techniques. a) STS affords studies of the electronic structure of the surface and adsorbates. b) Vertical manipulation can transfer adsorbates from the sample to the tip (pick-up), e.g. to functionalize the tip. c) Highly localized tip–sample interactions can be employed to built nanostructures or carry out "nano-surgery" to desorb and dissociate atoms and molecules.

contributions. The signal-to-noise ratio can be enhanced by directly stabilizing at closer SPs or by approaching the tip toward the surface after opening the feedback. A series of ST-spectra can be recorded along a line or on a grid for comparative studies of the electronic structure at different sites. When comparing spectra from different locations, the set point is ideally chosen in a way that it always yields the same tip–sample distance. This is however impossible to achieve at highly inhomogeneous samples as in the case of surface-confined molecules. Therefore usually the starting voltage of the sweep is chosen as SP voltage.

STS: Differential conductance mapping

The spatial distribution of electronic features can be visualized with $\mathrm{d}I/\mathrm{d}V$ maps. For this purpose, the bias voltage is set to the resonance energy of an electronic feature while scanning the surface with activated lock-in, but disabled feedback. The resulting signal is then displayed as heat map $\frac{\mathrm{d}I}{\mathrm{d}V}(x,y)$. To gather information on the spatial distribution at different energies, a series of maps with successive change in the bias can be carried out. It should be mentioned that the $\mathrm{d}I/\mathrm{d}V$ signal requires a longer integration time at each pixel for a sufficient signal-to-noise ratio compared to standard STM images. Therefore acquisition times for $\mathrm{d}I/\mathrm{d}V$ maps are considerably longer ($\approx \times 10$) and will be effected by thermal drift in the z direction. Furthermore, for nanostructures with pronounced 3-D character such as porphyrin molecules, the height differences can cause tip crashes or prohibit imaging due to signal-loss at considerably lower parts in the case of constant height mode. To overcome these limitations, differential conductance maps are carried out in constant current mode. The interpretation of these constant current $\mathrm{d}I/\mathrm{d}V$ maps however has to be taken with care, because sudden changes in topography can induce unwanted features[78] and the adaption of the tip height can enhance or attenuate electronic contributions. On the other hand, an STM topograph can be recorded simultaneously.

STM: Local manipulation

The goal of local manipulation techniques is to induce atomically precise modifications of the sample via localized tip–sample interactions. This is often also referred to as vertical manipulations (VM). Local manipulations can be carried out by approaching the tip, by applying a voltage pulse or by a combination of both. Such tip-induced manipulations can be employed to modify the surface through desorption or dissociation, they can change the conformation of molecules or the tip can deliberately pick-up adsorbates. Often, the tunneling current is recorded during manipulation to directly detect signatures of the induced changes. The underlying interaction mechanisms of the manipulations are not relevant for this work. However, they rely on interactions due to the electric field (e.g. field evaporation), electrostatic interactions, excitations from inelastic tunneling electrons (e.g. bond dissociation), local heating, and short range (chemical) interactions[79,80]. Local manipulation allows the control of the position of single atoms, the engineering of structures and modifications of molecules at the nanoscale and is therefore a powerful tool for nanochemistry, nanotechnology and nanoscience. In this work, local manipulation techniques are exploited to functionalize the STM tip by pick-up of CO molecules from the surface and for the deprotonation of hydrocarbons.

STM: Lateral manipulation

During a lateral manipulation (LM) the tip approaches the sample at one site, follows a lateral path across the surface at a constant height and withdraws from the sample at the end of the path. Due to the close tip–sample distance during the manipulation, the tip can interact with adsorbates attractively or repulsively and pull or push them along the path. With the help of this technique, the famous quantum resonators were realized[76].

3. Frequency modulation atomic force microscopy – FM-AFM

Atomic force microscopy (AFM) generates topographic images of surfaces and can also be applied to electrically insulating substrates. The imaging mechanism bases on the forces between a sharp tip and a sample. Experimentally, the tip is mounted at the end of a cantilever. The basic idea was already implemented by contact-type stylus profilers: Similar to a needle that glides over a vinyl record on a turntable, a stylus is brought in contact with a surface and then moved across the surface at constant velocity. The deflections of the cantilever are recorded to obtain surface height variations[81]. Initially, the AFM was operated by the very same principle, but employed very soft cantilevers with nanometer scaled probes that were regulated by a feedback[82]. Therefore the probe–sample contact could be maintained at very low forces in the range of nanonewtons (nN) and AFM could even achieve atomic resolution[83]. This AFM operation scheme is called static mode. Since its invention, AFM technology has massively progressed—especially by dynamic operation that uses oscillating cantilevers[84]—and modern AFM techniques are diversified with regard to operation modes (e.g. contact, tapping, non-contact), detection techniques (e.g. beam deflection, piezoelectric sensing, interferometry)[85], imaging signal (deflection, amplitude modulation[86], frequency modulation[84]) as well as the probe itself (silicon cantilever, needle sensor[48], tuning fork sensor[45]). However the working principle remains the same: a tip is raster-scanned across a surface and for each pixel tip–sample forces are detected via a derived quantity to image surface features with high resolution. For single organic molecule investigations, combined STM/AFM setups housing a tuning fork force sensors (qPlus) have been established as state-of-the-art. Its superb resolution allows visualizing the chemical structure of surface confined molecules[9] while maintaining STM functionality and therefore such setups can deliver comprehensive data for chemical, structural and electronic characterizations.

This work focuses on dynamic, non-contact AFM (nc-AFM) in the form of frequency modulation atomic force microscopy (FM-AFM) based on qPlus sensors. Please note that in literature, nc-AFM and FM-AFM are often used synonymously, although nc-AFM also includes non-contact amplitude modulation AFM (AM-AFM). The following sections outline the fundamentals of FM-AFM and present a simple derivation of the frequency shift as a function of the tip–sample interactions. Furthermore relevant forces will be briefly introduced. Additionally, experimental details are given, such as the implementation of an AFM feedback system, the operating mode of the qPlus sensor, the contrast mechanism in tip-functionalized FM-AFM, and AFM operation modes.
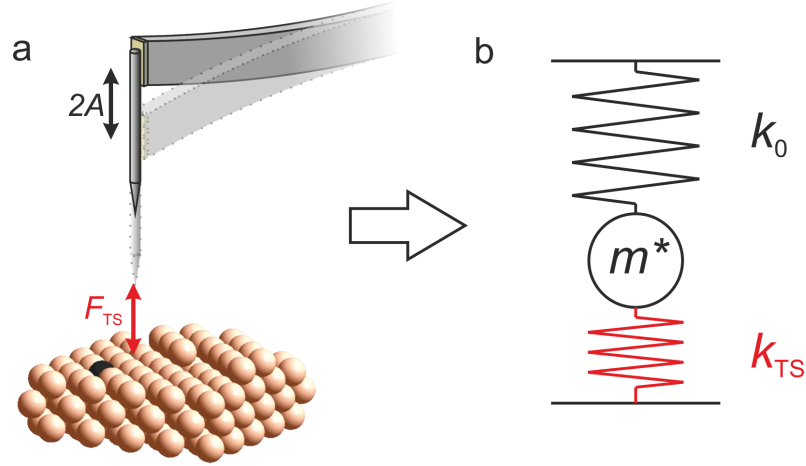
Figure 3.1. Simplified model for tip–sample interactions in FM-AFM. a) Oscillating cantilever with tip above a sample surface (not to scale). The cantilever's characteristics are given by its spring constant k_0 and eigenfrequency f_0. The oscillation amplitude is given by half the difference of the deflection maxima. The red arrow symbolizes the total tip–sample forces. b) Corresponding mass and spring model. The cantilever with tip can be modeled as spring with spring constant k_0 with effective mass m^*. The tip–sample force is modeled by an additional spring with spring constant k_{TS}.

3.1. Theoretical discussion of the frequency shift

As illustrated in Figure 3.1a, in FM-AFM a cantilever oscillates close to its eigenfrequency f_0 of several tens kilohertz above a sample. At the end of the cantilever is an atomically sharp probe whose mean distance to the surface is only in the nanometer range or below, but does not touch. Hence the attribute "non-contact". The tip interacts with the surface through various forces that result in the net force F_{TS} that alters the cantilever's resonance frequency. This frequency change can be detected as frequency shift Δf. The resulting frequency shift depends on the sign (repulsive or attractive) and magnitude of the total force that depends on the tip–sample distance in a non-trivial manner. In order to relate the observable Δf to physically relevant forces, it is necessary to derive an analytical expression for the frequency shift. Furthermore it is instructive to discuss relevant tip–sample forces.

The freely oscillating cantilever can be modelled as spring with spring constant k_0 and the eigenfrequency of a harmonic oscillator $f_0 = \frac{1}{2\pi}\sqrt{\frac{k_0}{m^*}}$, where the mass m^* represents the effective mass at the end of the cantilever. When the cantilever is close to a surface, the tip–sample force can be modeled as the result of a second spring between sample and tip with spring constant k_{TS}. This simplification assumes a linear distance dependence of the tip–sample force, i.e. the spring constant k_{TS} is constant over one oscillation cycle. In the limit of small oscillation amplitudes ($A < 1\,\text{Å}$) this is a good approximation. The effective spring constant then is $k^* = k_0 + k_{TS}$. The resonance frequency f_{res} of the two-spring

system is given by

$$f_{res} = \frac{1}{2\pi}\sqrt{\frac{k^*}{m^*}} = \frac{1}{2\pi}\sqrt{\frac{k_0 + k_{\text{TS}}}{m^*}} = \frac{1}{2\pi}\sqrt{\frac{k_0}{m^*}}\sqrt{1 + \frac{k_{\text{TS}}}{k_0}} \,. \tag{3.1}$$

The tip–sample spring constant is given by atomic interactions and an upper limit can be imposed by the interatomic spring constant of atoms in a solid $k_{\text{TS},max} \leq 10\,\text{N/m}$[82]. Here, the quartz tuning fork employed as cantilever has a stiffness of $k_0 = 1800\,\text{N/m}$ and therefore $k_{\text{TS}} \ll k_0$. The last square-root in equation 3.1 can therefore be approximated by the first two terms of the Taylor series $\sqrt{1 + x} = 1 + \frac{1}{2}x + \ldots$ and the frequency shift of the cantilever at the surface with respect to the freely oscillating cantilever is

$$\Delta f = f_{res} - f_0 = \frac{f_0}{2k_0}k_{\text{TS}} \,. \tag{3.2}$$

The stiffness of a spring is given by the second derivative of its potential V or the derivative of the resulting force F along its deformation (here along z):

$$k_{\text{TS}} = \frac{\partial^2 V_{\text{TS}}}{\partial z^2} = -\frac{\partial F_{\text{TS}}}{\partial z} \,. \tag{3.3}$$

The experimentally observable frequency shift Δf can be expressed as a measure of the tip–sample force gradient

$$\Delta f(z) = -\frac{f_0}{2k_0}\frac{\partial F_{\text{TS}}}{\partial z} \,, \tag{3.4}$$

and can yield information on physically relevant forces[87–89]. More elaborate calculations describing the cantilever motion with a first-order perturbation approach lead to the same result in the limit of small amplitudes[90]. Please see Reference [91] and citations therein for generic derivations of $\Delta f(z, A)$.

In the vast majority of experimental setups the cantilever oscillates parallel to the surface normal that is usually defined along the z-axis, while the surface is defined to lie in the x-y-plane. The AFM is therefore sensitive to tip–sample interactions perpendicular to the surface. For completeness, it should be mentioned that efforts have also been made to measure lateral, in-plane forces from $\Delta f(z)$-data[92,93] and with force sensors oscillating parallel to the surface ("pendulum geometry")[94,95] or by exciting torsional modes[96]. Pendulum geometry measurements are particularly interesting to investigate friction down to the atomic scale[94]. Please note that most examples given here base on LT/UHV experimental setups with qPlus sensors investigating single molecules as they are closely related to this work. However, many more AFM applications exist as for example medical- and biology-inspired studies of polyproteins[97] or AFM in liquids[98] to just name a few.

Relevant tip–sample forces

An appropriate AFM data analysis can relate the experimental observable Δf to the underlying force F_{TS} and moreover give great insight into physically and chemically interesting issues such as mechanical properties of surfaces or the adsorption forces of molecules.

Since the frequency shift is proportional to the tip–sample force gradient ($\Delta f \propto \partial F_{\mathrm{TS}}/\partial z$), the relevant tip–sample forces need to be considered in order to successfully transform the frequency shift to forces. In UHV conditions, the following forces can act between two microscopic bodies.

- Magnetic forces

- Electrostatic forces

- Van-der-Waals-forces (vdW)

- Chemical forces

Magnetic forces are not relevant in the context of this thesis and the interested reader is referred to literature on magnetic (exchange) force microscopy (M(Ex)FM) for more details[99–102]. Since tip and sample form a capacitor, electrostatic forces are active in the experimental setup and contribute as attractive forces to the imaging contrast. However, their contributions to Δf in the zero-bias measurements carried out here are assumed to be small and will not be further discussed. Nevertheless, it should be mentioned that detecting forces due to electrostatic interactions between tip and sample opens intriguing experimental possibilities in the form of kelvin probe force microscopy (KPFM), also called local contact potential difference (LCPD) mapping, with atomic resolution[89,103].

Van-der-Waals forces

When two neutral atoms or molecules are at close distance (nanometer regime), they experience attractive interactions mediated by van der Waals forces. Generally, these forces stem from dipole interactions of any sort including interactions between two permanent dipoles (Keesom force), between a permanent and an induced dipole (Debye force) and between two (instantaneously) induced dipoles (London dispersion force). Random, temporary fluctuations in a particle's electron density result in the opposite polarization of adjacent particles. The result is an attractive (dipole) potential. The vdW potential V_{vdW} of two particles at distance d can be modeled as

$$V_{vdW} \propto -\frac{1}{d^6} \, . \tag{3.5}$$

Naturally, due to the joint contributions of all constituent atoms, two macroscopic objects experience similar attractive forces when brought in close distance as it is the case for tip and sample in AFM. The total force between two macroscopic objects can be calculated by integration over their volumes with constant density of atoms. Assuming a spherical tip with radius R in close distance d to a flat (infinite) surface, the vdW force can be calculated by the Hamaker approach[104] and for $d \ll R$, it is given by[105,106]

$$F_{vdW} = -\frac{A_H R}{6d^2} \, , \tag{3.6}$$

where A_H represents the material dependent Hamaker constant in vacuum that considers the materials's polarizability and density.[‡] A_H for coinage metals like Au, Ag or Cu lies

---

[‡]The vdW force also depends on the tip geometry. When manufacturing an AFM tip from metal wire by etching, a spherical or parabolic tip can be assumed. Here however, the tip wire was cut at an

around $33 \cdot 10^{-20}$ J ≈ 2 eV[105]. Assuming a typical (STM) tip with a radius of ≈ 150 nm[107] and a tip–sample distance of $d \approx 5$ Å, the vdW force can be estimated to be $F_{vdW} \approx -33$ nN. To put this value in perspective, a typical silicon cantilever with spring constant $k_0 \approx 33$ N/m[91] would have to be driven at amplitudes larger than 1 nm in order to avoid the tip from being pulled into the sample ("jump-to-contact"). Although it is possible to achieve atomic contrast on crystal surfaces, such "large" amplitudes do not allow sub-molecular resolution on organic adsorbates as will be discussed below. Furthermore, the vdW force acts between the whole microscopic tip and a large area of the sample—in contrast to the tunneling current that is only dominated by the front-most atoms of tip and sample. vdW interactions are therefore not highly localized, which hinders high lateral resolution. Additionally, the relatively slow decay (d^{-2} dependence), characterizes vdW forces as long range. Consequently, attractive vdW interactions always contribute to the AFM signal—even for atomically sharp tips—and often conceal other forces that are of primary experimental interest. Therefore it is desirable to minimize vdW contributions. As can be derived from equation 3.6, decreasing the tip radius will decrease the vdW force and the requirements for manufacturing AFM tips are more demanding than for STM tips.

Chemical forces

When two particles are in the distance regime of interatomic distances in chemical compounds, their wave functions start to overlap. An orbital overlap is a requirement for tunneling as described in Section 2 and therefore this situation represents the experimental conditions in combined STM/AFM setups. At such close proximity chemical forces become relevant and dominate over the continuum vdW forces described above. Chemical forces are mediated by the tip front-atom and the closest adjacent atom at the surface. However, no general potential function exists that describes the close–range distance dependence universally, but several empirical potentials have been suggested. As will be discussed below, their common characteristic is a strong repulsion at very small distances[106,108].

Hard Sphere Potential In a simple picture, atoms and molecules can be considered as hard, incompressible spheres with radius $\sigma/2$, where σ is the equilibrium separation of two particles. This radius is often referred to as vdW radius and lies in the range of 1 Å[106]. As a result, a sudden, infinite repulsive force sets in when the two particles are brought closer than their equilibrium distance. The hard sphere potential V_{hs} can be described by[106]

$$V_{\mathrm{hs}} = + \left(\frac{\sigma}{d} \right)^n \quad , \text{where } n \to \infty \,, \tag{3.7}$$

and d is the distance of the particles. For $d > \sigma$, the value is zero, while for $d < \sigma$, it becomes infinite.

---

angle by a focused ion beam. Therefore the tip apex is more likely to be of wedge-type. Nevertheless, the distance dependence is the same ($F_{vdW} \propto 1/d^2$) and for simplicity a spherical tip is assumed. Contrary, for pyramidal and conical tips, a $1/d$ dependence holds. For more details on tip shape dependencies, please see Reference [90]

Power-Law Potential: Soft Repulsion   The infinitely steep rising repulsion of the hard sphere potential can be softened by replacing the limit $(n \to \infty)$ by a finite exponent in order to more accurately represent a real atomic potential. One example is the repulsive term of the Lennard-Jones potential, where $n = 12$.

$$V_{\text{LN, repulsion}} = + \left(\frac{\sigma}{d}\right)^{12} , \tag{3.8}$$

Lennard-Jones Potential   For AFM, the empirical Lennard-Jones (LJ) potential is well suited to describe the experimental situation[90]. It combines the attractive vdW potential (equation 3.5) of two atoms with the soft repulsion at very small distances.

$$V_{\text{LJ}} = -E_{min} \left[\left(\frac{\sigma}{d}\right)^{12} - 2 \left(\frac{\sigma}{d}\right)^{6} \right] , \tag{3.9}$$

where E_{min} is the minimum energy of the interaction, sometimes also referred to as binding energy. Due to the two competing contributions, the LJ potential exhibits a global minimum. The depth of the minimum is defined by E_{min}, the position by σ (see red curve and thin dotted lines in Figure 3.2a). The tip–sample force of the tip front-atom with the surface is then given by

$$F_{\text{LJ}} = -12 \frac{E_{min}}{\sigma} \left[\left(\frac{\sigma}{d}\right)^{13} - \left(\frac{\sigma}{d}\right)^{7} \right] . \tag{3.10}$$

Total tip–sample interaction
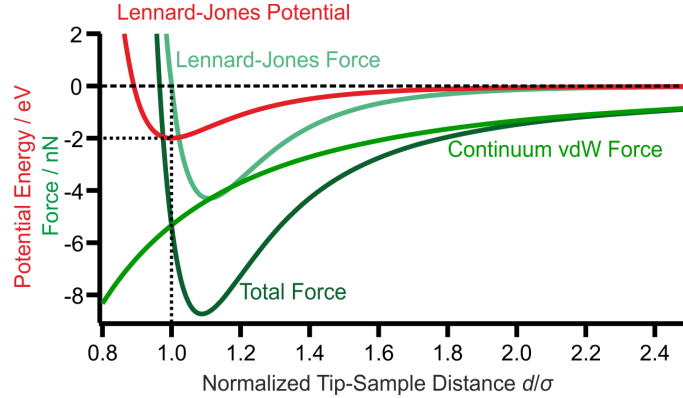
Figure 3.2. Distance dependence of tip–sample interactions. Plot of a Lennard-Jones potential (red), the resulting Lennard-Jones force (light green) along with the continuum vdW force (green) and the total force (dark green). All curves are plotted as function of the normalized tip–sample distance $x = d/\sigma$. Parameters: $E_{min} = -2\,\text{eV}$, $\sigma = 2\,\text{Å}$, $A_H = 2\,\text{eV}$, $R = 4\,\text{nm}$.

The LJ potential only describes the tip–sample interaction as pair potential of two atoms at close proximity where the interatomic forces dominate over the continuum vdW force. Nevertheless the long range vdW interaction of the bulk tip behind the front-atom

has to be taken into account to correctly describe the tip–sample potential. The two contributions are assumed to be additive and result in the total tip–sample potential

$$V_{\text{TS}} = -E_{min}\left[\left(\frac{\sigma}{d}\right)^{12} - 2\left(\frac{\sigma}{d}\right)^{6}\right] - \frac{A_H R}{6d}, \tag{3.11}$$

which results in the total tip–sample force

$$F_{\text{TS}} = -12\frac{E_{min}}{\sigma}\left[\left(\frac{\sigma}{d}\right)^{13} - \left(\frac{\sigma}{d}\right)^{7}\right] - \frac{A_H R}{6d^2}. \tag{3.12}$$

Alternatively, the "standard" Lennard-Jones potential can be adapted to LJ-type potentials of the form $V = (a/d)^b - (u/d)^v$ with free fit parameters a, b, u, v in order to fit experimental or theoretical data[9]. Beyond LJ-type potentials, also other potentials with similar characteristics (long range attraction + short range repulsion) can be employed, as e.g. the Morse potential[93,106,109].
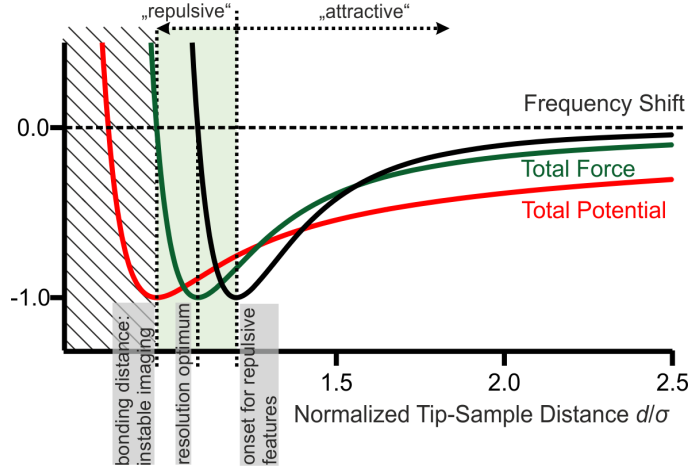
Figure 3.3. Distance dependence of total tip–sample potential (red), force (green) and resulting frequency shift (black); all normalized to the corresponding minimum value. The tip–sample distance can roughly be divided in three sections: attractive interaction, repulsive interaction with resolution optimum, and bonding distance. All curves are plotted as function of the normalized tip–sample distance $x = d/\sigma$. Parameters: $E_{min} = -2\,\text{eV}$, $\sigma = 2\,\text{Å}$, $A_H = 2\,\text{eV}$, $R = 4\,\text{nm}$.

Figure 3.2 and Figure 3.3 depict plots of the discussed quantities. The following parameters were choosen: $E_{min} = -2\,\text{eV}$, $\sigma = 2\,\text{Å}$, $A_H = 2\,\text{eV}$, and $R = 4\,\text{nm}$. Positive forces correspond to repulsion, negative values to attraction. When following the total force F_{TS} in Figure 3.2 from large to small separations, i.e. when approaching the tip to the surface, first attractive bulk vdW contributions dominate, while the LJ interatomic forces a nearly zero. Then attractive forces from both vdW terms add to cause strong attraction. Finally, at very small distances, the repulsive LJ term takes over, causes a steep rise and net repulsive forces. The resulting experimental implications for small amplitude FM-AFM are visualized in Figure 3.3. The dark green graph represents the total tip–sample force

F_{TS} that result from the total tip–sample potential (red) and lead to the experimentally observable frequency shift (black). At large tip–sample separations the frequency shift is caused by attractive interactions until it reaches its minimum. Experimentally it turns out that at a distance close to the Δf minimum repulsive tip–sample interactions start showing in AFM images, despite the force still being negative. This effect can be attributed to the tip oscillation. The zero-crossing of Δf, the force minimum respectively, was found to lead to a resolution optimum (for constant height Δf images)[9]. When the tip–sample distance reaches the energy minimum, tip and sample are in the distance regime of chemical bonding, which causes very strong interactions and instable imaging conditions.

Due to the terms with different sign, F_{TS} exhibits a global minimum and so does the frequency shift Δf, however shifted to larger distances (cf. green and black curves in Figure 3.3). This has important implications for AFM: $\Delta f(z)$ is a non-monotonic function—in contrast to the tunneling current—and for a given experimental Δf-value, it remains undetermined at which side of the minimum the value is measured and which slope Δf follows for changes in z. Therefore, regulating $z(\Delta f)$ for constant Δf imaging is more demanding. Generally, a stable feedback can only be realized in regions of a monotonic feedback signal, i.e. at either side of the minimum and without crossing it.

3.2. AFM feedback system
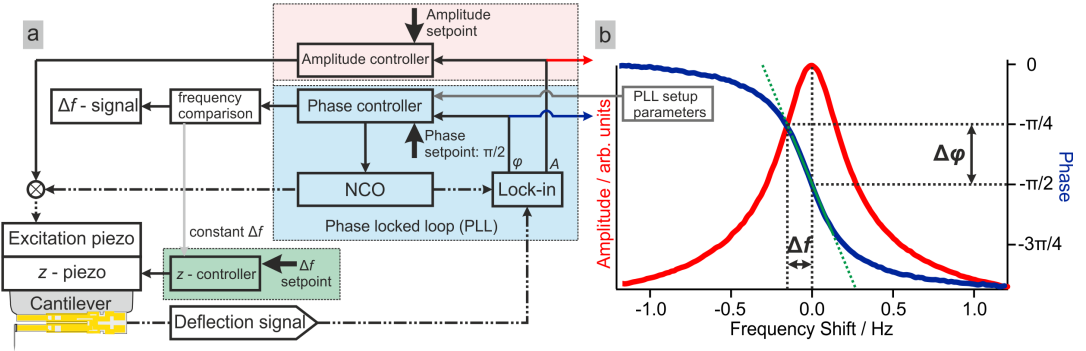
Figure 3.4. a) Schematic of the AFM feedback system. It consists of three independent feedback loops: z-feedback (green) regulated by Δf for constant frequency shift experiments (or by the tunneling current in STM mode), amplitude feedback (red), and a phase locked loop (PLL, blue). The PLL consists of a lock-in, a phase controller and a numerically controlled oscillator (NCO). It ensures resonant excitation by setting a fixed phase relation of $\pi/2$ to the driving signal with respect to the deflection signal of the cantilever. For more details see the text. Solid lines represent DC signals, dashed lines AC signals. b) Frequency sweep of the excitation signal around the resonance frequency of the cantilever. The curves depict the response of the cantilever amplitude (red) and phase (blue). The green line is a linear fit of the phase around $\pi/2$. The frequency sweep determines parameters for correct PLL operation (see text).

For AFM operation, the cantilever is driven by an external excitation, implemented here by a piezoelectric actuator. This means, the cantilever oscillates at the driving frequency f_{exc}. In order to keep the oscillator in resonance ($f_{exc} = f_{res}$), the phase between

the excitation and the cantilever has to be kept at $\varphi = \pi/2$ (cf. Figure 3.4b). However, the phase of an oscillating cantilever varies during scanning, due to changes in the tip–sample interaction. For FM-AFM, also the amplitude needs to be kept constant to avoid frequency shifts caused by amplitude changes that naturally cause changes in tip–sample distance. Consequently, FM-AFM requires at least two feedback loops: a phase feedback (also: phase locked loop, PLL) and an amplitude feedback. If the microscope is operated in constant frequency shift mode, an additional feedback adapts the tip–sample separation (z-feedback) according to a predefined Δf setpoint. Such "true" AFM operation is necessary to investigate insulating samples as well as for setups without STM capabilities. For more information on AFM operation modes, please see Section 3.4.

The AFM feedback system is schematically illustrated in Figure 3.4a. It contains three independent feedback loops: one for the z-piezo (tip–sample distance, green), two for the cantilever (amplitude, red and phase, blue). Within this work, the z-feedback was exclusively regulated by the tunneling current, i.e. operated in STM mode. Therefore issues arising from the non-monotonic Δf behavior were circumvented. Independent of the control variable, the z-feedback works with DC signals which makes experimental implementation relatively easy. In contrast, controlling the cantilever requires the processing of AC signals in order to derive the frequency (shift) and amplitude. Here, the deflection signal from the cantilever connects to a lock-in amplifier. The lock-in generates two signals: amplitude and phase. The amplitude is passed to a controller that adapts the excitation amplitude in order to keep the cantilever oscillation at a predefined amplitude setpoint (amplitude feedback, masked in red in Figure 3.4a). The phase is given with respect to a reference signal supplied by a numerically controlled oscillator (NCO). Since the same NCO signal also drives the excitation piezo, the phase corresponds to the phase between the excitation signal and the cantilever deflection signal that needs to be $\pi/2$. In order to keep the phase locked, a controller adapts the NCO frequency f_{exc} accordingly (vide infra). Finally, the signals from the amplitude controller is multiplied with the NCO signal to form the updated excitation signal with correct amplitude and frequency $f_{exc} = f_{res}$ to drive the excitation piezo.

Additionally, the PLL derives the frequency shift

$$\Delta f = f_{res} - f_0 \,, \tag{3.13}$$

where $f_{res} = f_{exc}$ is the resonance frequency of the cantilever in interaction with the surface and f_0 is the resonance frequency of the freely oscillating cantilever. Depending on the AFM mode, Δf is either the imaging signal (constant height) or the tip-height feedback signal (constant Δf).

The above described PLL tasks require proper calibration for correct execution.

- A_{res}/U_{exc}: The physical cantilever amplitude A_{res} ($[A_{res}] = $ m) has to be related to the electronic excitation amplitude U_{exc} ($[U_{exc}] = $ V)—also called gain $g = A_{res}/U_{exc}$.

- f_0: The resonance frequency f_0 of the free cantilever has to be determined.

- $\varphi(\Delta f)$: The response of the relative phase between excitation and deflection signal to a change in resonance frequency has to be established as $\varphi(\Delta f)$.

First however, the physical amplitude of the cantilever has to be calibrated. Here, this can be carried out relatively easy by exploiting the calibration of the STM piezo in z-direction. As depicted in Figure 3.1, the cantilever amplitude is half the peak-to-peak deflection. When the amplitude is large ($A > 1\,\mathrm{nm}$), the tunneling current is determined by the lower turn-around of the cantilever. Therefore, when changing the amplitude with activated STM-feedback, the z-setpoint should change accordingly and the electronic deflection signal can be assigned a calibration constant $c_{deflection}$ ($[c_{deflection}] = \mathrm{m/V}$). For the calibration of all other PLL parameters, a frequency sweep is carried out. A frequency sweep records phase and amplitude while varying the excitation frequency around f_0 for a fixed excitation amplitude U_{exc}, i.e. excitation voltage. Self-evidently, the AFM feedbacks are disabled during the sweep and it is carried out for the freely oscillating cantilever, i.e. the sensor is retracted from the surface. A phase and amplitude plot as functions of Δf is depicted in Figure 3.4b. The phase curve (blue) follows an arctan, the amplitude (red) is a Lorentz distribution as it represents the solution for the motion of an (under) damped, forced resonator. The phase is analyzed for the curvature change of the arctan—where $\varphi(f_{exc}) = \pi/2$ for an idealized resonator—to determine f_0. In a real experimental setup however, the phase for resonant excitation can take an arbitrary value φ_0 due to additional (capacitively) induced phase shifts. f_0 is then used to extract the amplitude maximum A_{res} in order to set an amplitude-to-excitation ratio A_{res}/U_{exc} for the amplitude controller. Furthermore, the phase can be fitted linearly around $f_{exc} = f_0$ as indicated by the green line. The slope of the fit $m_\varphi = \Delta\varphi/\Delta f$ is related to the frequency response bandwidth f_c of the cantilever[110]

$$f_c := - \left(\frac{\partial \varphi}{\partial f_{exc}} \right)^{-1}_{f_{exc}=f_0} = \frac{f_0}{2Q} \approx -\frac{1}{m_\varphi} \,, \tag{3.14}$$

where Q is the quality factor of the cantilever. Q is a measure for the internal damping of any oscillating system. It can also be expressed as ratio (stored energy)/(energy dissipated per oscillation cycle). Therefore, a high Q means little energy loss. Following equation 3.14, the Q-factor can be deduced from the frequency sweep as

$$Q \approx -\frac{f_0}{2}m_\varphi \,. \tag{3.15}$$

Q, f_0, and φ_0 are passed to the phase controller. This enables the controller to calculate the frequency shift Δf from the experimentally determined phase φ. A visualization of the measuring scheme is given by the dotted lines in Figure 3.4b. The freqency shift is[111].

$$\Delta f \approx -f_0 \frac{\varphi - \varphi_0}{2Q} \,. \tag{3.16}$$

Δf measurements therefore depend on the characteristics of the cantilever. However f_0 and Q are subject to changes. For example f_0 can change due to changes at the tip during in-situ tip preparations, and Q is temperature dependent. Therefore it is strictly necessary to thoroughly calibrate the PLL prior to every FM-AFM experiment.

The phase controller is realized with a proportional-integral controller (PIC). The response of the controller to a change in the signal is determined by the integral constant

I, the proportional constant P and the time constant T. The PIC has a characteristic frequency[110]

$$f_{PI} = \frac{I}{2\pi P} = \frac{1}{2\pi T}$$

(3.17)

The frequency sweep also helps to choose the feedback constants by setting $f_{PI} = f_c$.[110]

3.3. High resolution FM-AFM with the qPlus sensor
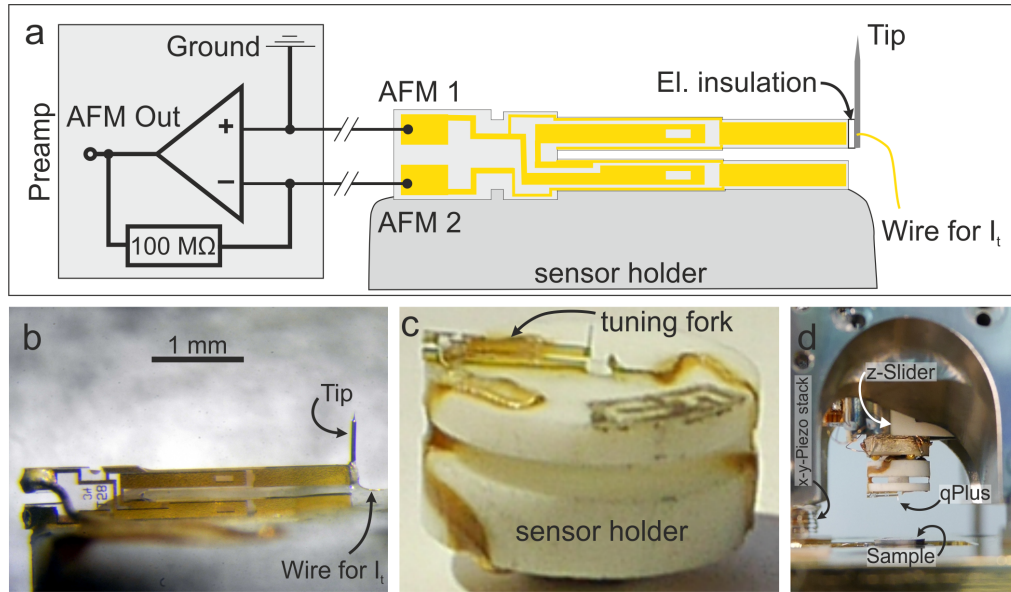
Figure 3.5. qPlus sensor. a) Schematic drawing of the tuning fork glued with one prong to a sensor holder. At the free tine, a tip is glued with electrically insulating epoxy and contacted via an external wire. The electrodes that read out the AFM signal are shown in yellow. At the base of the tuning fork the signal is tapped and connected to a preamplifier circuit. The preamplifier is located at the LN radiation shield. b) Photo of a real qPlus sensor taken through a microscope. c) Photo of the full sensor assembly. The notch at the sensor holder allows in-situ tip exchange via a gripper tool and the manipulator. d) Side view of the sensor at the bottom of the scan piezo above a sample. The sensor is held magnetically.

The motivation for microscopy tools has always been ultimate resolution. For AFM however true atomic resolution of arbitrary surfaces was (and still is) a challenging task. An experimental issue in dynamic AFM are oscillation instabilities caused by "jump-to-contact" (j-t-c), i.e. the tip being pulled into the surface by attractive forces exceeding the restoring force of the cantilever. For stable operation empiric stability criteria were formulated, one stating that "the product between spring constant and amplitude kA has to be larger than $\approx 100\,\text{nN}$ to provide a sufficiently strong withdrawing force"[91]. Therefore, A and k should be large. On the other hand however, large amplitudes result in large tip–sample separations over almost the whole oscillation cycle. As discussed above (compare Figure 3.2) at large distances the unwanted bulk vdW interactions dominate and prohibit high lateral resolution. Furthermore, when examining Figure 3.2, it is intuitive to see that

oscillating a cantilever at close distances with small amplitudes (e.g. at $d/\sigma = 1$ with $A \approx \sigma/4 = 0.5\,\text{Å}$), the tip only covers a distance regime in which short range chemical forces dominate. The tip never reaches larger distances where the continuum vdW forces conceal other contributions. Therefore, the oscillation amplitude allows to tune the AFM sensitivity to different force contributions: small amplitudes are sensitive to short range chemical forces, large amplitudes select long range continuum forces. A more detailed (mathematical) treatment can be found in Reference [91]. For atomic contrast on organic adsorbates it is crucial to select short range chemical forces only and usually the cantilever is driven with oscillation amplitudes below $100\,\text{pm}$. Considering the stability criterion, small amplitudes therefore require stiff cantilevers with high k.

Piezoelectric quartz tuning forks exhibit a high $k = 1800\,\text{N/m}$, are commonly employed for reliable time reference in quartz watches, i.e. they exhibit high frequency stability, and are mass produced with high quality at a cheap price. When fixing one prong, the other is free to oscillate and can serve as cantilever. Such a setup was introduced by Giessibl as "qPlus-sensor"[45,112] who also demonstrated its superb imaging capabilities by atomically resolving the highly reactive $Si(7 \times 7)$ surface[113]. $Si(7 \times 7)$ had previously imposed stability issues on traditional micro-machined cantilevers. The piezoelectric material of the qPlus furthermore facilitates oscillation read-out. The deformation causes surfaces charges that can be discharged by contacting the prongs via vacuum deposited metal electrodes. An operational amplifier wired as current-to-voltage converter then transforms the periodic discharge current into a voltage signal that can be processed as described above. Therefore, sensitive beam deflection setups, as often employed in AFM, are redundant. Additionally, the quartz has little internal damping which results in a high Q factor. A high Q value is advantageous because it lowers the frequency response bandwidth (cf. equation 3.14) enhancing the sensor sensitivity and reducing noise[114]. Furthermore, it reduces the dissipated power. Less power dissipation in the form of heat is wanted for low temperature experiments as described herein. Furthermore, the cantilever is large compared to Si devices and allows easy assembly of a wide variety of probes[91]. Therefore qPlus sensors have been established as state-of-the-art force sensors for high-resolution FM-AFM imaging in UHV, especially by equipping the qPlus with STM capabilities for combined STM/AFM experiments[47,50]. All AFM results presented in this thesis were obtained with a qPlus sensor.

Figure 3.5 shows a schematic and photographs of the herein employed qPlus sensor for combined STM/AFM experiments. The unmodified tuning fork (type E158) is made from piezoelectric quartz and is composed of a base and two prongs. It has a resonance frequency of $f_0 = 32\,768\,\text{Hz}$ and stiffness of $k = 1800\,\text{N/m}$ to $2000\,\text{N/m}$[115]. The total length is $\approx 3.5\,\text{mm}$. The tine length is $\approx 2.4\,\text{mm}$, with a height of $\approx 210\,\mu\text{m}$ and a width of $\approx 120\,\mu\text{m}$[50,115]. Gold electrodes cover all sides of the prongs in order to drain charges from the surface when the piezoelectric material deforms. Note, that a deflection also causes a contraction/thickening of the prong perpendicular to the deflection. Therefore the signal can be enhanced by tapping all sides and processing two signals (labeled AFM1 and AFM2 in Figure 3.5a). The electrodes can be contacted at the base of the device. When exploited as force sensor, the device is glued onto a base plate (here: sensor holder) with one prong, while the other remains free to oscillate normal to the sample surface. The electrodes connect to a preamplifier circuit that converts the current evoked by the surfaces charges into a voltage signal with 10^8 amplification (left part in Figure 3.5a). A tip at the

end of the free prong serves as probe. In the case of a combined STM/AFM sensor, the tip is a metal wire (here tungsten) that is electrically insulated from the sensor electrodes to avoid signal cross-talk. Therefore the tip requires external contacting via a separate wire for the tunneling current. The additional wire however negatively influences the cantilevers quality factor. The described qPlus configuration is the most widely used, as the sensors can easily be home-built without sophisticated manufacturing equipment. Only the latest version of the qPlus sensor is not based on watch oscillators, but is specifically manufactured for the use as force sensor featuring an optimized geometry and advanced electrode configuration with an additional electrode for the tunneling current[116,117].
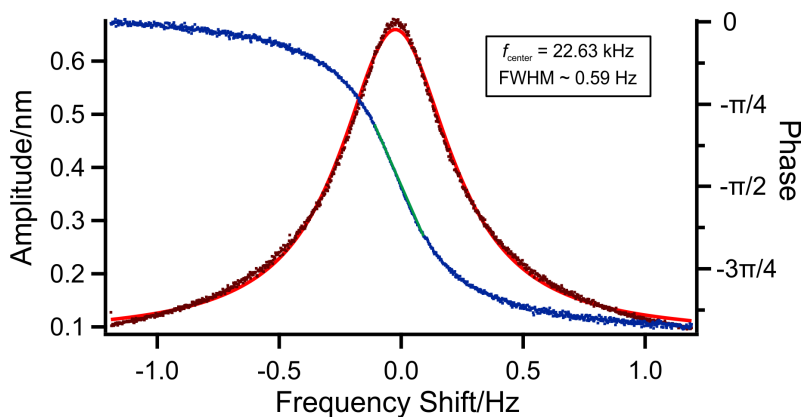
Figure 3.6. Characterization of the qPlus sensor. Resonance curve (black dots), Lorentz fit (red) and phase response (blue dots) with linear fit (green) of the employed qPlus sensor as a function of frequency shift. Measurements were taken at 4.9 K. From the sweep the following values were determined: $f_0 = 22.63$ kHz, $Q = 59891$.

To characterize the herein employed qPlus sensor, a frequency sweep as described above was carried out and is depicted in Figure 3.6. The resonance frequency was determined to be at 22.63 kHz with a FWHM of ≈ 0.59 Hz. The difference to the non-modified tuning fork ($f_0 = 32.77$ kHz) stems from the additional mass of tip and glue. At 4.9 K the observed frequency response corresponds to a Q factor of 59891.

Sub-molecular resolution

Although atomic resolution is possible at crystal surfaces with small amplitude FM-AFM, sub-molecular resolution at organic adsorbates, as routinely achieved by STM, is more challenging. As already mentioned, high resolution FM-AFM passes high demands on the probe tip. The (bulk) tip radius should be as small as possible to reduce vdW interactions (cf. equation 3.6). Additionally, the tip apex should avoid bonding to the sample at very close distance to prevent instable imaging conditions (cf. Figure 3.3), i.e. the tip apex should be chemically inert. Another precondition is an atomically well defined tip termination that favors pair-interaction between only the two foremost atoms of tip and sample in order to maximize lateral resolution. Additionally, it should be possible to easily recover the tip after an accidental tip crash. Summarizing, exceptional control over the tip apex is required. Such control is difficult to achieve by random tip preparation

processes such as sputtering or tip indentation into the surface—although possible via front atom identification techniques [118, 119]. Fortunately, all demands are met by functionalized tips and well-established STM tip-functionalization protocols can be employed for enhancing AFM contrast. Combined STM/AFM setups reliably achieve sub-molecular resolution on organic adsorbates as first demonstrated by Gross et al.[9]. The most widely applied tip termination is a single CO molecule, although other functionalizations work as well (please see Section 5.3 and reference [120]). All AFM data presented in this thesis was recorded with a CO-functionalized tip.

Contrast mechanism
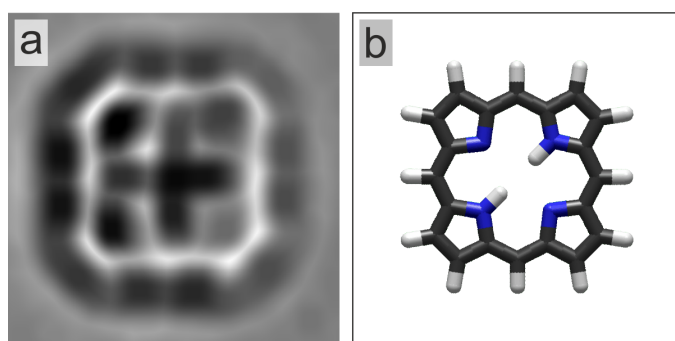
Figure 3.7. Atomic contrast on organic adsorbates in FM-AFM. a) Constant height Δf map of a porphine molecule. Atoms and bonds appear bright, i.e. as less negative Δf values. The data was post-processed to enhance atomic contrast. b) Corresponding model.

Atomic resolution on molecules is hardly feasible with metal tips, but easily realized by CO terminated probes. Hence, interactions between the CO and the adsorbate are responsible for the contrast formation. To fully understand the underlying contrast mechanism, it is necessary to disentangle all contributions to the imaging contrast, i.e. to the Δf signal. Attractive forces result in a negative frequency shift (cf. Figure 3.3). Sub-molecular features only become apparent at very small tip–sample distances and appear as bright, "less-negative" frequency shift (i.e. less attractive interaction) within a dark, "more-negative" Δf background (see Figure 3.7). Therefore, high molecular resolution bases on repulsive interactions solely between the CO molecule and the adsorbate. This was shown by a detailed analysis of the forces acting between a CO terminated tip and a pentacene molecule[121]. The metal tip only contributes one third to the overall repulsive force and does not show atomic corrugations. The CO molecule on the other hand accounts for two-thirds and features sub-molecular features. The same study furthermore elucidates Pauli repulsion as the origin of the repulsive forces. In a simplified picture, the electron wavefunctions of the CO and the molecule overlap, however, the Pauli exclusion principle forbids the electrons to occupy the same state, which results in repulsion[120,121]. Furthermore, this effect is strongest at areas of high electron density. Hence, the repulsive contrast is highly localization at chemical bonds and atoms and represents the adsorbates' chemical structure in the case of flat, organic molecules adsorbed coplanar to the surface.

Generally, the contrast mechanism is also active for metal tips as well as other tip func-

tionalizations. However, the repulsive interactions responsible for atomic contrast only set in at very close tip–sample distances. The tip needs to be approached closer than the distance of the maximum attractive force. For reactive tips, such as metal tips, imaging instabilities—e.g. lateral displacements of the adsorbates due to bond formation—occur before distances necessary for atomic contrast can be reached. Nevertheless, it should be noted that high resolution AFM is indeed possible with pure metal tips. For example, the honeycomb structure of graphene can clearly be resolved[122], as well as the constituent rings of C_{60} molecules within bucky ball arrays[123] and the chemical structure of organic adsorbates via a second pass technique[35]. However, such reports are scarce, the resolution is inferior, and single molecule investigations, especially on insulating layers, are not feasible. CO on the other hand is chemically inert and allows a close approach without bond formation. Additionally, the chemical and electronic structure of the CO further facilitate atomic resolution.

CO is a linear molecule with a bond length of $\approx 1.13\,\text{Å}$ that binds with the carbon to the tip and ideally points perpendicular to the surface. Considering a metal–carbonyl bond of length $\approx 1.5\,\text{Å}$ and an oxygen covalent radius of $\approx 0.7\,\text{Å}$, the CO separates the bulk tip by more than $3\,\text{Å}$ and can significantly reduce attractive continuum vdW forces at close distances (cf. Figure 3.2). Furthermore, the wavefunctions of the CO are laterally strongly confined and therefore represent an "electronically sharp tip" pointing towards the surface, which is favorable for high lateral resolution[121].

Imaging artifacts

Repulsive features above molecular bonds as shown in Figure 3.7 are sharpened by relaxations of the CO at the tip. Because the CO is flexibly attached, it bends laterally at close tip–sample distances. The deflection depends on the landscape of the repulsive potential of the sample. For example, the CO deflects above a chemical bond, which increases the (lateral) forces and enhances the Δf signal: the bonds appear sharpened[124]. However two neighboring atoms without chemical bond impose a very similar potential landscape. Consequently the CO is likewise deflected and Δf exhibits a repulsive ridge connecting the atoms[124,125]. Especially when imaging molecular arrays, this can lead to intermolecular contrast without intermolecular bonds. The assignment of bright features to chemical bonds has to be made with caution.

The deflection of the CO is also responsible for image distortions. The oxygen atom at the end of the tip defines the interaction. However, when the CO does not point straight down, the tip apex (the oxygen) is offset from the tip. But the contrast values are assigned according to the tip position and not the tip apex. Therefore the recorded tip position can deviate from the position where the interaction takes place. When imaging organic molecules, the CO always points towards the center of the molecule at its outer edge due to anisotropy of the attractive interactions[124]. This means that the oxygen is above the edge, the tip however is located slightly next to the molecule. The result is an apparent expansion. For more details on image artifacts and image correction please see Reference [124] and references therein. Although the flexibility of the CO causes image distortions, it does not prohibit the determination of chemical structures. To avoid tip-flexibility effects, different functionalizations can be employed, as e.g. xenon atoms.

3.4. AFM operation modes

Similarly to STM operation modes described in Section 2.3, different AFM operation modes were developed. AFM operation is diversified and ranges from topographic imaging over vertical force measurements, manipulation techniques, and lateral force measurements (friction) to contact potential difference mapping, magnetic imaging and dissipation measurements[10,126,127].

The following section gives a short overview on different FM-AFM techniques that are relevant for single molecule investigations within the scope of this work. Many remarks to SPM operation in general were already made when discussing STM operation modes in Section 2.3 and will not be repeated.

As any scanning microscopy technique, AFM offers at least two actuating parameters, namely the lateral tip position (x, y). In the scope of this work, one of the following signals was defined as observable for data visualization.

- Vertical tip position z

- Frequency shift Δf

- Tunneling current I (in combined STM/AFM setups)

However there exist many more options, such as the excitation signal U_{exc} or the cantilever amplitude A amongst others. The latter two are usually recorded simultaneously in order to check correct AFM operation. The amplitude signal is supposed to stay constant as well as the excitation. If the excitation signal shows considerable variations, energy is dissipated, e.g. in inelastic deformations of the substrate. This is unwanted and should be avoided. A general remark should be made to AFM imaging. As often for electronic signal detection when employing lock-ins, filters, and amplifiers, a consideration has to be made between fast measurement and a good signal-to-noise ratio. The AFM signal however is intrinsically small and subject to many noise sources, which requires favoring the signal quality over data acquisition time. Therefore AFM measurements are usually slow, compared to STM for example. A typical AFM image requires approximately half an hour to one hour. AFM noise will not be discussed here, but is comprehensively addressed in literature[91].

Constant frequency shift mode

The operation in constant Δf mode is the analog to the constant current mode in STM. Δf is fed into a feedback loop that adjusts the tip height z in order to keep a constant frequency shift. AFM data exhibit the tip height for each pixel $z(x, y)$ as heat map for a predefined Δf setpoint. It is probably the most widely applied AFM technique.

Constant height mode

The constant height mode acquires images with disabled z-feedback. AFM data depict the magnitude of the frequency shift at each pixel as $\Delta f(x, y)$ intensity map for constant tip height z. The initial tip–sample distance is determined by an STM set point I, U. The

set point is chosen above the bare metal substrate to generate a reproducible initial tip–sample spacing. This mode can only be applied at very smooth surfaces, e.g. bare metal surfaces, or for small scan frames and in very stable conditions (no piezo creep/thermal drift). Constant height imaging furthermore requires proper tilt correction to accurately define the scan plane parallel to the surface prior to the experiments. Otherwise, the tip could crash into asperities higher than the preset tip–sample separation. Usually many successive constant height images are recorded, decreasing the tip–sample distance after every scan. This results in a contrast evolution from a dark attractive background to bright repulsive features. During such a sequence, repulsive interactions are detected first above the highest molecular parts.

$\Delta f(z)$-**spectroscopy**

Constant height AFM can detect height differences qualitatively via the relative onset of repulsive features, either between molecules or between different moieties within the same molecule. However quantitative statements cannot be made. $\Delta f(z)$ spectroscopy allows to quantitatively determine (adsorption) height differences. To do so, $\Delta f(z)$ is recorded while approaching the surface. Assuming an isotropic tip–sample interaction, the z position of the Δf minima can be directly compared[128].

Furthermore, $\Delta f(z)$ spectroscopy allows a quantitative analysis of the local tip–sample interaction—then often referred to as force spectroscopy. Forces can be derived from the frequency shift by mathematical treatment as e.g. described by Sader and Jarvis[87]. It is also possible to record three dimensional datasets and visualize the full force field above the sample[88].

Part II.

Experimental setup, materials and methods

4. Experimental setup

Before any experiments could be carried out, the experimental setup was installed in Munich as part of this work. The following chapter describes all components in detail starting with the UHV- and cryogenic system as well as the heart of the experiment—the scanning probe microscope itself—including the operation principles of key parts such as the nano-positioning system. Furthermore, dedicated sections introduce all employed materials (samples and specimen) and explain crucial experimental routines for sample and tip preparation.

All experiments were carried out with low-temperature scanning probe microscopes (LT-SPMs) housed in ultra high vacuum (UHV) chambers operating at $\approx 10^{-10}$ mbar and ≈ 5 K. Owing to several collaborations during the conferral of the doctorate, experiments were carried out at different laboratories located in Munich, at the University of Regensburg[†] and at the Monash University Melbourne[‡]. The experimental setup in Munich is depicted in Figure 4.1a and a photograph of the Monash lab is shown in Figure 4.1b. Since most results base on data from the STM/AFM lab in Munich, the following chapter focuses on said setup and crucial experimental procedures at it. For a detailed description of the Regensburg lab, see references [129–131].

4.1. Ultra high vacuum system

UHV is required for the here presented surface studies to guarantee well-defined, clean samples and to prevent deterioration of the sample over the timescale of the experiment. The UHV system is made of a stainless steel vessel manufactured by VAb GmbH[134] (blue and yellow parts in Figure 4.1a) that features multiple ports of different sizes for additional mountings (cf. e.g. green, red and purple dyed parts in Figure 4.1a). All additions are connected via CF flanges with copper gaskets to ensure extremely leak-tight seals compatible with UHV conditions. The system is divided into two chambers: a preparation chamber (blue in Figure 4.1a) and an SPM analysis chamber (yellow in Figure 4.1a) that are separated by an integrated gate valve. Each chamber comprises several elements described below. A base pressure in the low 10^{-10} mbar regime is maintained throughout the whole system by a combination of different pumping techniques (vide infra). The pressure inside the cooling shields is supposedly orders of magnitudes lower due to effective pumping of the cryostat (red in Figure 4.1a). The whole setup rests on four pneumatic dampers[135] to decouple the experiment from low frequency vibrational noise of the building.

[†]Prof. Jascha Repp, Institute of Experimental and Applied Physics, University of Regensburg, 93053 Regensburg, Germany

[‡]Dr. Bent Weber, Prof. Agustin Schiffrin, Prof. Michael Fuhrer, School of Physics and Astronomy and Monash Centre for Atomically Thin Materials, Monash University, Victoria 3800, Australia
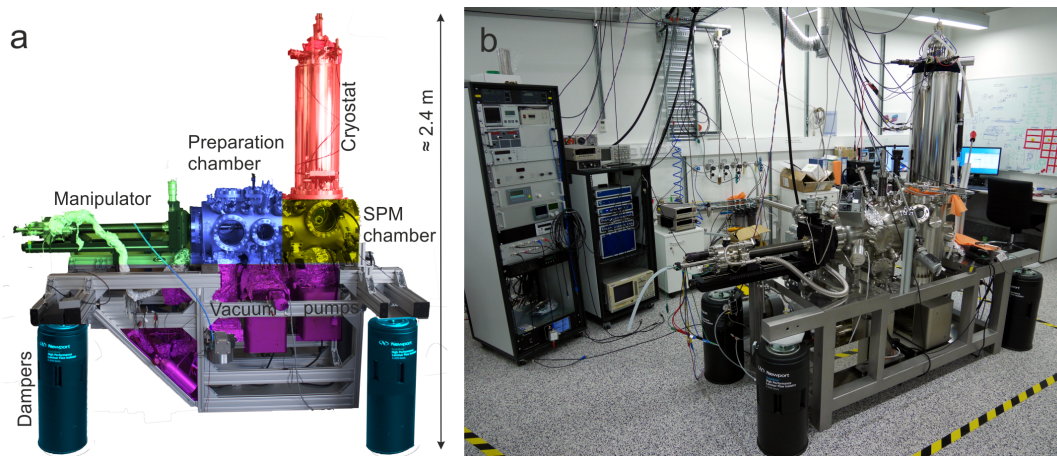
Figure 4.1. LT-STM/AFM experimental setups. a) Custom designed vacuum chamber that was set up in the course of this work. The different parts of the setup are dyed as guide to the eye. Light blue: pneumatic damper; purple: vacuum pumps; green: manipulator; blue: preparation chamber; yellow: SPM chamber; red: cryostat. The image was adapted from Yuanqin He[132]. b) Photo of a laboratory at the Monash University in Melbourne hosting a commercial setup by CreaTec[133]. On the left of the image are two racks with equipment necessary for sample preparations such as sputter gun electronics and power supplies, as well as the hardware for signal processing and control of the microscope. For details on the control electronics please see Section 4.2.

Maintaining UHV

Initially, the system is evacuated through pumps installed at the preparation chamber and baked at $120\,°C$ for three days. When the gate valve that separates the chambers is closed, both sections can maintain UHV conditions independently. The preparation chamber requires more pumping due to vacuum deteriorative processes such as outgassing of molecular powders, sputtering and sample preparations. A closed gate valve therefore also protects the SPM chamber against contamination. Additionally, the preparation chamber can be vented and baked independently while the SPM remains under vacuum and at cold temperature. At the preparation chamber an ion (getter) pump and a series of two turbomolecular pumps (TMP) with a diaphragm pump (DP) constantly maintain a UHV in the low 10^{-10} mbar range. Additionally, a combination of a cold trap (CT) with a titanium sublimation pump (TSP) can be run to (temporarily) improve the vacuum conditions. At the SPM analysis chamber an ion pump is installed. Furthermore, the cryostat functions as a permanent cold trap. The different pumping techniques mentioned above are shortly laid out in the following. For further information on UHV and pumping techniques see the corresponding technical literature (e.g. [55, 136]).

TMPs and DP A TMP consists of multiple rotor/stator stages similar to a turbine. In operation the rotors rotate at $\approx 1000\,Hz$ and hit residual gas molecules and atoms with angled blades. The collision transfers momentum to the gas particles. Due to the orientation of the blades the direction of the momentum transfer faces away from the vacuum

volume, i.e. particles are transported through the stages to the outside. Additionally this leads to a compression of the gas and consequently a pressure increase along the pump. For effective operation, the gas particles should keep their momentum in the direction of the pumping line and not get deflected by collision with other particles. In other words, the mean free path has to be larger than the separation of rotor/stator stages even for the last stage. Therefore the outlet of a TMP is always backed up by another pump. At the preparation chamber, a sequence of two TMPs[137] with a diaphragm pump[138] is installed. The first TMP transports gas from the preparation chamber to the second TMP that leads to a rough vacuum of ≈ 2 mbar supplied by a DP. The TMPs can evacuate the UHV system down to the low 10^{-10} mbar regime and are especially effective for larger gas loads occurring during sample preparation procedures as well as for noble gas loads. The pumping speed of the first TMP is ≈ 300 l/s. However the mechanical motion of the pumps can transmit as noise to the SPM. Therefore the pumping line can be separated by a pneumatic gate valve to turn off all mechanical pumps. The UHV is then maintained by motionless and vibration free ion getter pumps only.

Ion Getter Pump An ion getter pump or short just ion pump is built of an array of parallel steel tubes in between two titanium plates that are close to the steel tube's open ends. Therein the cylinders act as anode and the titanium plates as cathode between which a high voltage of up to 8000 V is applied. Furthermore, the cathode-anode-cathode sandwich is in between the poles of strong permanent magnets that apply a magnetic field parallel to the tubes' axes. The working principle relies on ionization of residual particles and their acceleration toward and crashing into the titanium cathodes. Electrons are emitted from the Ti plates and are accelerated helically in the anodic tubes. On their trajectory they ionize gas particles by impact. These ionized particles are then accelerated towards the cathode and eventually hit it. Due to the impact, titanium atoms are expelled from the surface and the ions are embedded. This process is called sputtering and also has a great relevance for preparing a clean sample surface (see Section 5.2). The sputtered Ti covers the inner walls of the ion pump and reacts chemically with the ions, thus binding them to the walls and extracting them from the vacuum volume. The sputtering with ions can be detected as current whose magnitude is directly related to the pressure. If calibrated, the ion pumps can therefore also act as pressure sensor. The pumping speed of the ion pumps is ≈ 200 l/s $- 300$ l/s. One ion pump is installed at the analysis chamber and one at the preparation chamber. The manufacturer of both is Gamma Vacuum[139].

TSP with Cold Trap A titanium sublimation pump (TSP) consists of resistively heated Ti filaments. When heating the filaments, Ti sublimates and covers the surrounding walls. Due to the high chemical reactivity of Ti, residual gas is chemically bound and therefore removed from the UHV volume. The effectivity of the TSP can be supported by a cold trap (CT). The CT simply is a reservoir for liquid nitrogen that cools down the TSP to 77 K and therefore traps free particles by freezing them to the walls and exposing them to the Ti.

4.1.1. SPM analysis chamber

The SPM analysis chamber consists of the central vessel (yellow in Figure 4.1a) and the cryogenic system (red in Figure 4.1a and Figure 4.2). At the end of the cryostat, the SPM is mounted inside radiation shields. Additionally, a gas inlet line is installed for dosing gases onto the cold sample and a gate valve can be equipped with an evaporator for in situ preparations while the sample is kept cold inside the scanner.
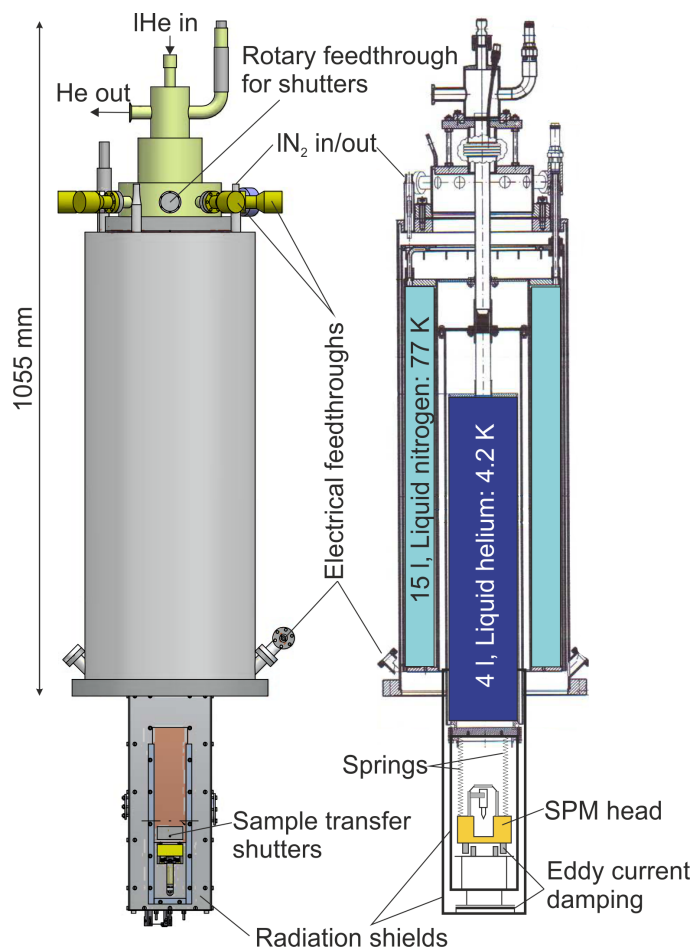
Figure 4.2. Cryogenic system with cryostats and radiation shields. The left part shows a technical drawing, the right one a cross section. It consists of two dewars that a radially arranged: one for liquid nitrogen and one for liquid helium. The figures are adapted from [140, 141].

Cryogenic system   Low sample temperatures are desired for high resolution single molecule investigations as carried out in this work in order to deprive adsorbates from thermal energy for diffusion and to establish stable investigation conditions. Furthermore LT provides many more advantages, such as improved energy resolution for STS and noise reduction in AFM. Usually, LT is achieved by placing the sample within a cryogenic system

that provides a heat sink in the form of a cryostat. Here, a bath cryostat cools the sample to $\approx 5\,\mathrm{K}$ simply by cryogenic liquids in storage tanks. Figure 4.2 shows a technical drawing of the cryogenic system with cryostat and radiation shields and its cross section. The assembly is constructed of two coolant tanks and two radiation shields. While the outer tank is rigidly mounted to the outside wall, the inner cryostat hangs free. To counteract movements an eddy current damping is installed at the bottom of the inner radiation shield. The shields are completely closed, but can be opened with the help of shutters to allow in situ preparations and most importantly sample transfers. Furthermore windows assure optical access to the sample. Usually, the cryostat is filled with liquid nitrogen in the outer tank (lN, $V = 15\,\mathrm{l}$, $T = 77\,\mathrm{K}$, heat load $\approx 8\,\mathrm{W}$) and with liquid helium in the inner one (lHe, $V = 4\,\mathrm{l}$, $T = 4.2\,\mathrm{K}$, heat load $\approx 35\,\mathrm{mW}$). Alternatively, both reservoirs can be filled with lN and not at all. In combination with a heating diode at the SPM scanner, this allows operation in the range of $4.8\,\mathrm{K}$–$20\,\mathrm{K}$, at $77\,\mathrm{K}$ and at room temperature. The SPM is mounted at the bottom of the cryostat and thermally connected to the inner tank, which therefore defines the SPM temperature. The standard operating temperature of the SPM is below $5\,\mathrm{K}$. The outer tank thermally shields the inner one from ambient temperature in order to extend its holding time. Additionally, the lN tank is isolated against the outer cryostat walls by a radiation shield that is cooled by the exhaust nitrogen gas. Due to the cooled radiation shield, the stand time of the outer tank is extended by approximately one day compared to a cryostat without the shield. The consumptions of coolants amounts to $\approx 4.5\,\mathrm{l/d}$ for lN and $\approx 1.2\,\mathrm{l/d}$ for lHe. Therefore the volumes of the reservoirs allow a holding time of more than three days. The cryostat was manufactured by CryoVac[142] and customized by CreaTec[133].

4.1.2. Preparation chamber

The preparation chamber consists of the central vessel (blue in Figure 4.1a), the manipulator (green in Figure 4.1a) and many additions to the central chamber that are crucial for sample preparation such as evaporators, leak valves with gas lines, a sputter gun, a parking deck to store samples and a mass spectrometer. Some are described below. Most additions are connected via a gate valve to allow their exchange without braking the vacuum of the chamber.

Load-lock   A magnetic, rotatable linear transfer with separate TMP is installed as vacuum lock. The head of the transfer can carry samples as well as STM tips and AFM sensors. It allows to introduce new parts or exchange and repair broken items without venting the chamber.

Sputter-gun   The sputter-gun is an ion source by Specs[143] used for preparing atomically clean sample surfaces. The main parts are a gas inlet, a cathode as electron source and an accelerating cathode. Argon is lead through the gas inlet into the sputter gun, where it is ionized by electron collision. The positively charged Ar-ions (Ar^+) are accelerated by the accelerating cathode, focused and directed onto the sample to sputter it. For the process of sputtering see Section 5.2.

Mass Spectrometer   A quadrupole mass spectrometer SRS 300[144] can be used for residual gas analysis, leak detection, analysis of the composition of preparation substances to check their purity and for determining desorption parameters.

Atom and molecule sources   The deposition of atoms and molecules onto a sample surface is realized via atomic and molecular beam epitaxy from thermal sources. In this work a home-built three-cell organic molecular beam epitaxy (OMBE) system was developed and employed for the evaporation of organic molecules. For this purpose, quartz crucibles filled with molecular powders are resistively heated. The temperature in all OMBE cells can be monitored via thermocouples.

Manipulator   A rotatable linear manipulator is used for moving objects inside the vacuum system. It allows in situ tip exchanges, transferring the sample between the preparation and analysis chamber and placing the sample in different positions for preparation steps. The manipulator consists of the manipulator arm with the manipulator head at its end. It is mounted in the center-line of the UHV system, can be moved in all three spatial directions and rotated around its central axis. It should be noted that the rotation is realized mechanically via a rotary feedthrough that is viton sealed. It therefore requires differentially pumped stages to be UHV compatible. The differential pumping is connected to the TMP pumping line. The sample can be grabbed with the manipulator head by mechanical clamping (see Figure 4.3b). Furthermore the sample can be contacted electrically for heating and for temperature read-out or it can be cooled indirectly by flowing liquid nitrogen or helium through a flow cryostat within the manipulator head. Usually, lHe cooling was employed prior to sample transfer into the SPM cryostat. Cooling the sample from room temperature to $\approx 90\,\mathrm{K}$ takes about 15 minutes. The temperature of the manipulator head can be monitored via a silicon diode. More information can be found in [145]. The manipulator was supplied by VAb GmbH[134].
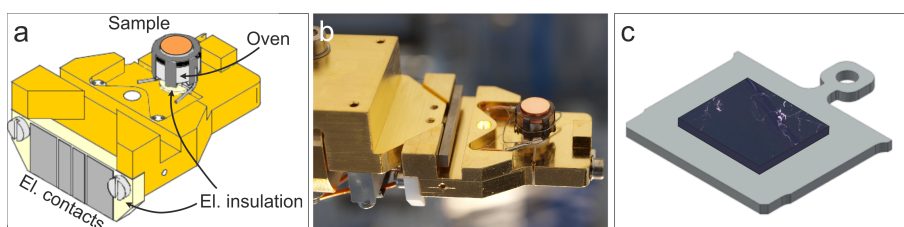
Figure 4.3. Sample holders. a) Technical drawing of the CreaTec sample holders. Adapted from [146]. b) Photo of a sample holder with copper crystal grabbed by the manipulator. c) Sketch of an Omicron[147] sample plate with TMD sample as used at Monash University.

Sample holders   For most experiments single crystal metal samples were used that are described in more detail in Section 5. These samples need to be thoroughly cleaned by repeated cycles of sputtering and annealing (Section 5), which requires heating and temperature control. In this experimental setup, the heating is implemented by direct current button heaters[148] onto which the samples are clamped. Temperature read-out is realized

by spot welded k-type thermocouple wires at the samples. The sample/heater assemblies are mounted onto sample holders as shown in Figure 4.3a[145,146]. The sample holders feature electrical contacts for the thermocouples as well as for the heaters. These metallic pads can be contacted via the manipulator head and at the same time allow the application of a bias voltage inside the SPM scanner. The main base plate of the holders however is electrically insulated against the samples/heaters. For experiments on transition metal dichalcogenides (TMDs) at the Monash University, TMD samples were glued with conductive epoxy onto sample plates[147] as illustrated in Figure 4.3c. For these sample plates electron heating and temperature read out is integrated at the manipulator head and a different sample transfer system is used (not shown).

4.2. Scanning probe microscope
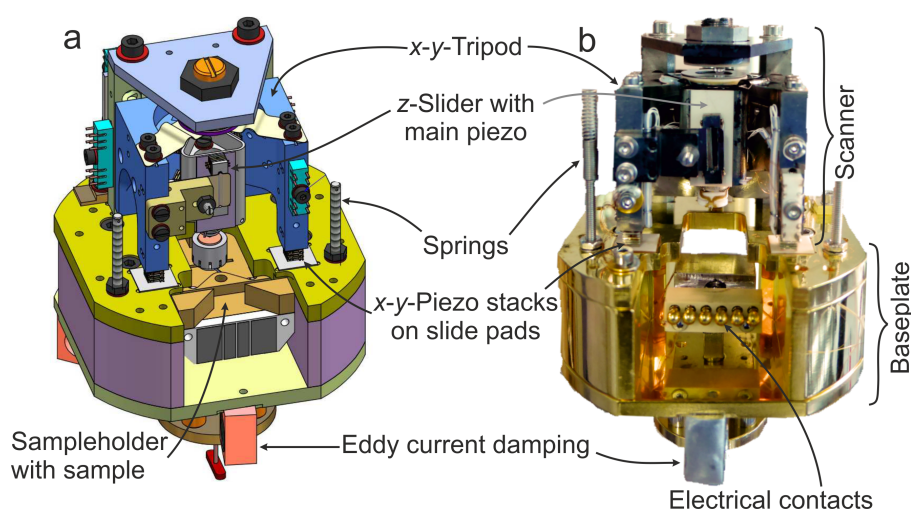
Figure 4.4. Scanning probe microscope head consisting of a base plate (yellow/purple in a, gold in b) and the tip positioning system (scanner) on top of the base. a) Technical drawing adapted from [141]. b) Photograph.

The SPM itself, also referred to as scan head, is made of two main parts: a baseplate with sample retainer including sample contacts on which the tip positioning system or scanner rests. The setups in Munich and Melbourne house a CreaTec slider-type SPM, however employing different sample transfer systems based on Omicron plates (Figure 4.3). In Regensburg the same sample transfer as in Munich was used, but the scanner was a Besocke-type[131,145,149]. Figure 4.4 depicts the scan head as technical drawing next to a photo. The baseplate is colored in yellow/purple in the drawing and shows as gold coated, horse shoe shaped component in the photograph. The photo also reveals six pins for electrically contacting the sample. The drawing on the other hands demonstrates how the sample sits inside the retainer. The tip positioning system is constructed with a tripod frame that rests on top of the base plate on piezo stacks. The tripod is stabilized by a superstructure that pushes it onto the baseplate (cf. topmost light blue part with a central screw in Figure 4.4a). At the center of the frame is a triangular prism—the Pan-type *z*-

slider[150]—inside which the main scan piezo is located. The SPM sensor is magnetically mounted at the bottom of the main piezo and can be exchanged in situ. The *z*-slider is held by friction through pairs of vertically aligned piezo stacks at each side of the triangular prism (cf. Figure 4.6). During SPM measurements, the whole STM head hangs with three springs from the bottom of the cryostat inside the radiation shields (see Figure 4.2). An eddy current damping hinders swinging and damps oscillations of the springs. For sample and tip transfers the scanner can be pulled down and fixated. Additionally, the fixated position allows faster cooling due to direct thermal contact to the lHe shield. The SPM head is commercially available from CreaTec GmbH[133].

4.2.1. Piezoelectric actuators

The tip positioning system relies on piezoelectric actuators, also called piezoelectric motors or just short piezos. A set of piezos drives the coarse motion up to millimeter movements while a separate piezo is responsible for scanning and fine positioning from the sub-nanometer regime up to a maximum of approximately one micrometer. Piezo actuators base on the converse piezoelectric effect of certain ceramic materials: an appropriately applied electric field results in strain. This strain expresses as deformation of the material. The deformation then directly moves an object like the tip at the end of the main piezo or it is transformed into motion by adding many deformation steps. The electric field induced strain depends on the magnitude of the applied field. In the case of the herein employed actuators, this requires voltages of up to 200 V. In the following the working principle of the employed actuators is shortly described.
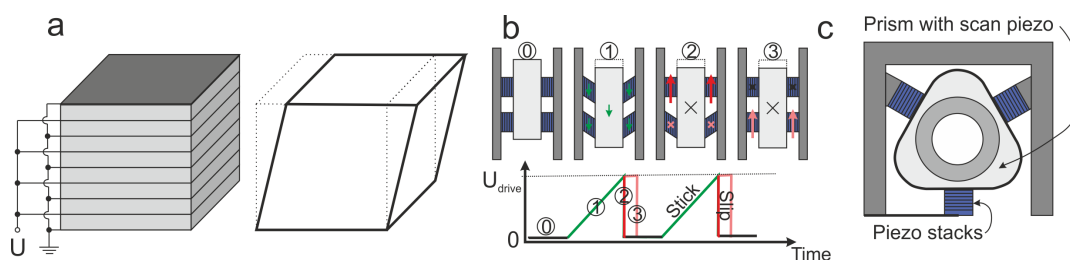
Figure 4.5. Coarse piezos and *z*-slider. a) Schematic drawing of a piezo stack. When a voltage is applied to such a stack, it shears sideways. b) Working principle of the *z*-slider. Two AC sawtooth signals are applied: one at the top piezos, one at the bottom stacks. One step corresponds to one sawtooth. Step 1) The voltage slowly increases simultaneously at the top and bottom piezos causing them to shear in a stick-motion that moves the central prism. Step 2) A sudden decrease in voltage causes the top piezos to slip back, while the second signal stays constant. Step 3) The second signal slips the bottom piezos in the original configuration as well. The signal chart shows two stick-slip cycles. c) Schematic top view of the slider. Vertically aligned piezo pairs clamp a triangular prism at three sides.

Coarse piezos Coarse movements in all directions are realized by stacks of shear piezos. When a voltage is applied to these stacks, they shear in one direction. For movement, the mechanical inertia of the moveable parts is exploited in a stick-slip motion. When shearing fast, the stacks slip across the supporting contact surfaces, a subsequent slow

relaxation in the opposite direction however will cause a displacement of the stacks and the attached parts (or vice versa). One such step only causes a movement of a few Å to micrometer. However, a signal of a few hundred Hz will result in considerable displacement over acceptable time spans. By applying an appropriate (sawtooth) AC signal[151] simultaneously to the three piezo stacks mounted under the legs of the tripod, the scanner can be moved laterally. To realize two dimensional motion in the x- and y-direction, the actuators combine two sets of piezo stacks rotated by 90°. In principle the same stick-slip operating scheme is applied for vertical movements of the Pan-type z-slider[150]. However, to prevent the slider from falling during a slip cycle due to gravity, additional, vertically aligned piezos are driven with a second signal. That way the top (bottom) piezos always clamp the slider while the bottom (top) piezos slip as described in Figure 4.5.

Compared to the older CreaTec Besocke-type scanner, the CreaTec Pan-type can travel considerably larger distances in z-direction ($\approx 20\,\text{mm}$ vs. $2\,\text{mm}$) which gives two advantages: i) no great attention has to be given to the tip length/sensor height and sample height, and ii) the scanner design achieves a larger angle for in situ access to the sample. The first greatly simplifies sensor and sample assembly and affords more variability, the latter allows convenient optical access, e.g. for the coupling of (laser) light and more effective in situ dosing of adsorbates. Furthermore, the slider allows a macroscopic retraction of the tip and re-approaching the very same spot on the sample within a few hundred Å.
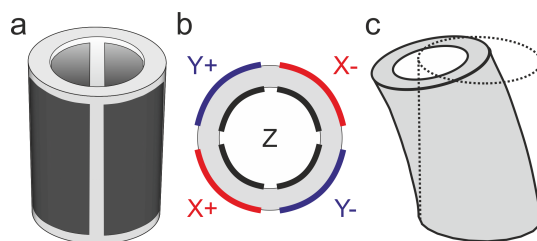
Figure 4.6. Main scan piezo. a) Drawing of a piezo tube. b) The tube has two outer electrode pairs for x- and y-deflection and inner electrodes for $z-$motion. c) One side of the tube is fixated. When a voltage is applied to an outer electrode pair, the tube bends in one direction causing a lateral deflection of its end where the SPM sensor is mounted.

Scanning piezo The main scanning piezo is a thin walled, hollow piezo cylinder, often referred to as tube piezo fixated at one end (Figure 4.6a). It features two pairs of electrodes on the outside walls for deflections in x- and y-direction (Figure 4.6b). When a voltage is applied to one of the outer electrode pairs, the wall expands (contracts) which causes a vertical contraction (elongation) and a large lateral deflection of the tube's end. The tube deflects towards the electrode with the positive voltage. The SPM sensor is mounted at the end of the tube. The illustration in Figure 4.6c greatly exaggerates the tube deformation and therefore suggests a bending of the tube. In real SPM operation, the bending can be neglected for small scan frames, i.e. small tube deflections or it can be compensated by proper background subtraction. Adaptations of the tip height, i.e. an elongation or contraction of the whole tube can be achieved by simultaneously applying a voltage to all outer electrodes or to inner electrodes. The lateral translation is approximately given

by[152]

$$\Delta s = U \frac{2\sqrt{2} d_{31} L^2}{\pi D h} = U c_{piezo} \,, \tag{4.1}$$

where U is the applied voltage in x- or y-direction, d_{31} is the piezoelectric constant of the material along the relevant direction, L is the length of the tube, D the outside diameter, h the wall thickness and c_{piezo} represents the piezo constant that has to be calibrated for every actuator. Assuming typical values for the tube of $d_{31} = -200 \cdot 10^{-12}\,\mathrm{m/V}$, $L = 10\,\mathrm{mm}$, $D = 5\,\mathrm{mm}$ and $h = 0.7\,\mathrm{mm}$ and a voltage of $U = 10\,\mathrm{V}$, the deflection is

$$\Delta s = 10\,\mathrm{V} \frac{-2\sqrt{2} \cdot 200 \cdot 10^{-12}\,\mathrm{m/V} \cdot 100\,\mathrm{mm}^2}{\pi \cdot 5\,\mathrm{mm} \cdot 0.7\,\mathrm{mm}} = 10\,\mathrm{V} \cdot -5.14\,\mathrm{nm/V} \approx -50\,\mathrm{nm} \,. \tag{4.2}$$

The real deflection of the tube has to be calibrated by using a well defined grid. Here, the atomic corrugations of the Ag(111) surface were used to set the voltage–to–deflection piezo constant to $c_{x,y} \approx 3.70\,\mathrm{nm/V}$ (see Section 5). Furthermore, monoatomic steps at the Ag(111) surface were investigated for the calibration of $c_z \approx 0.87\,\mathrm{nm/V}$.

4.2.2. Control electronics
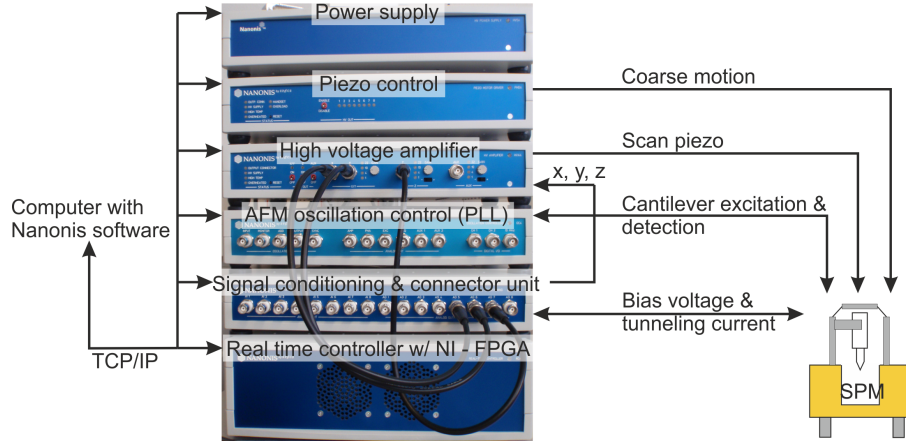
Figure 4.7. System architecture of SPM control electronics. For details please see the main text.

Figure 4.7 shows a scheme of the system architecture of the Nanonis[153] control electronics. The communication to the user (Nanonis software) is realized via TCP/IP network protocol to the real time controller (RC) that includes a field programmable gate array (FPGA) from National Instruments (NI)[154]. The RC controls all other modules, namely the signal conditioning and connector unit (SC), the oscillation controller (OC), the high voltage amplifier (HVA) and the piezo motor driver (PMD). The SC features eight analog inputs and eight analog outputs that are used to apply the bias voltage, receive the voltage signal of the tunneling current from the STM preamplifier, record the SPM temperature and pass the piezo control signals to the HVA. The HVA is an ultra low noise high voltage amplifier specifically designed for nano-positioning applications and sets the

high voltage at the main scan piezo. The output channels can be manually adjusted to four gains (1, 4, 15, 40) to define the maximum piezo range and to adapt to different operating temperatures. The PMD drives the coarse piezos. It generates a sawtooth output signal. The amplitude of the output waveform can be varied continuously between $0\,\text{V}$ and $\pm 400\,\text{V}$, and its frequency continuously between $1\,\text{Hz}$ and $20\,\text{kHz}$. Additionally, the OC is needed for AFM operation. It comprises an input for the cantilever signal as well as outputs for the AFM signals, such as frequency shift, excitation signal and phase. Its operation bases on a phase-locked loop (PLL) with a lock-in amplifier and a numerically controlled oscillator (NCO) as depicted in Figure 4.8.
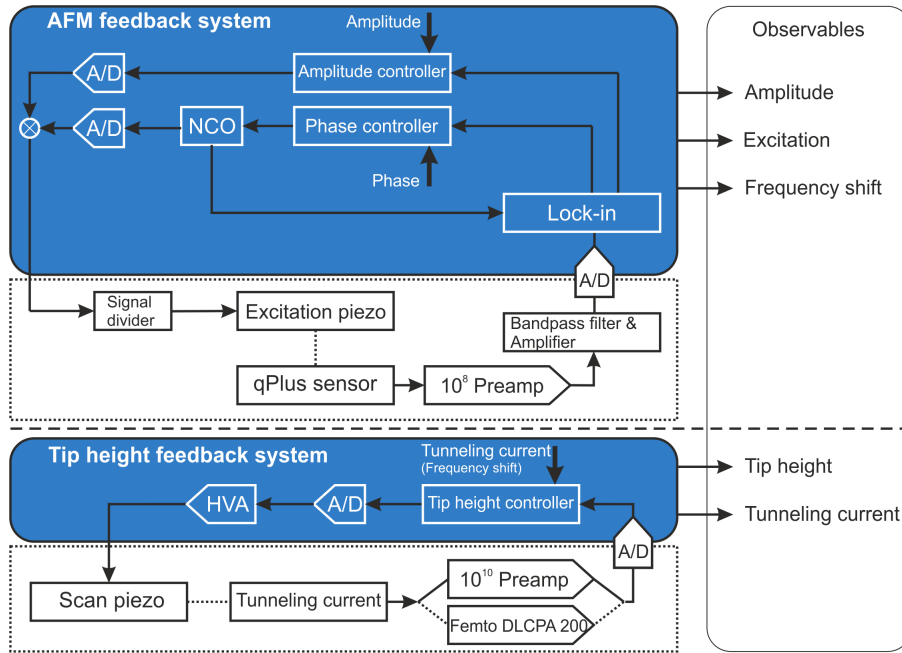
Figure 4.8. Feedback loops implemented for AFM and STM operation. The blue colored blocks indicate elements implemented by the Nanonis hard- and software. Elements within the dashed framed boxes are situated at the experimental setup. The blocks above the horizontal dashed line correspond to the AFM system, the block below to the STM or tip height feedback.

The SPM feedback system is schematically illustrated in Figure 4.8. The upper part corresponds to the AFM feedback, the lower part to the STM feedback. Parts in blues represent features implemented by the Nanonis electronics and software, the white blocks with a dashed frame depict elements installed at the experimental setup. The feedback system generates five observables that can be recorded during AFM operation (amplitude, excitation, frequency shift, tip height, and tunneling current) and two signals for pure STM operation (tip height and tunneling current). Not shown is the connection from the AFM loop to the tip height controller that allows constant frequency shift measurements. A detailed description of the AFM feedback is given in Section 3.2.

5. Materials and methods

The following section gives an overview of all employed materials and basic experimental routines. The substrates are described with focus on experimentally relevant parameters such as its symmetry and crucial dimensions. Furthermore, this section describes methods for sample preparation from in-situ cleaning procedures (sputtering and annealing), via growth of sodium chloride adlayers to molecular and atomic deposition. Additionally, tip-preparation protocols, including tip-functionalization, are laid out in detail as they are extremely relevant for high-resolution SPM investigations.

5.1. Samples: coinage metals, NaCl, TMDs

For the investigation of organic adsorbates, well defined, atomically smooth surfaces with low reactivity are required that are easy to clean and prepare. The low-index surfaces of coinage metals are well characterized and understood and serve as substrates in many surface science studies. Therefore, most studies were carried out on single crystal metal surfaces, namely Cu(111) and Ag(111). For experiments in the last part of the thesis, the surface of the transition metal dichalcogenide (TMD) niobium diselenide (NbSe$_2$) was investigated. All relevant lattice parameters for all employed samples are summarized in Table 5.1.

Table 5.1. Lattice parameters and surface directions of all substrates as defined in Figure 5.1 and Figure 5.3 and Figure 5.2. Lattice directions for the hexagonal TMD are given in three index notation $\langle uvw \rangle$ of the lattice vectors a_1, a_2, c in real space. The lattice parameters are given for the most common 2H polytype. For NaCl, the step height refers to the experimentally determined height from Cu(111) to a double layer (2L) NaCl. All distances are in Å.

	Bulk struc.	a	c	Surf. plane / Sym.	nn-direction	d_{nn}	$d_\perp$-direction	$d_\perp$	step height
Ag	fcc	4.09	–	(111) / hex.	$\langle \bar{1}10 \rangle$	2.89	$\langle \bar{1}\bar{1}2 \rangle$	2.50	2.36
Cu	fcc	3.61	–	(111) / hex.	$\langle \bar{1}10 \rangle$	2.55	$\langle \bar{1}\bar{1}2 \rangle$	2.21	2.08
NaCl	fcc	5.64	–	(100) / square	$\langle 110 \rangle$	3.99	$\langle 110 \rangle$	3.99	3.60
NbSe$_2$	hex.	3.44	12.48	(0001) / hex.	$\langle 100 \rangle$	3.44	$\langle 210 \rangle$	2.98	6.24

Metal samples

Silver and copper both occur as crystals with a face centered cubic (fcc) structure with lattice constant a. Depending on the cut and polishing, samples with different surface orientations can be manufactured, i.e. different lattices are exposed that can express different symmetries. Herein, the hexagonal (111) facets of the metal crystals were employed
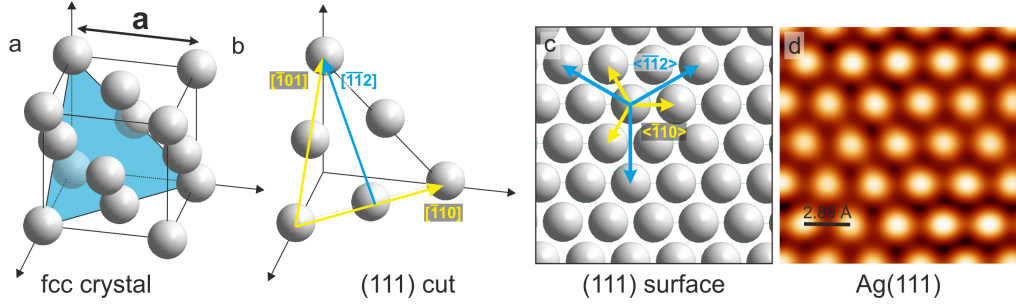
Figure 5.1. (111) surface of fcc crystals. a) Model of the bulk fcc crystal. The blue triangle indicates the (111)-plane. b) Same model as in a) omitting all atoms that do not coincide with the (111) plane. The next neighbor directions are indicated in yellow. The perpendicular direction in blue. c) The top view of the (111) plane illustrates the hexagonal surface symmetry. d) Typical atomically resolved STM data of Ag(111). One protrusion corresponds to one silver atom.

as sample surfaces. Figure 5.1a depicts a three-dimensional model of a fcc crystal with the (111) plane highlighted in blue. In Figure 5.1b, all atoms that are not included in the (111) plane are omitted. Figure 5.1c depicts a two dimensional model of the (111) cut from Figure 5.1b. The colored arrows mark the high symmetry $\langle \bar{1}10 \rangle$ lattice directions along the dense packed atomic rows (yellow) as well as the perpendicular $\langle \bar{1}\bar{1}2 \rangle$ directions (blue). The distance along the perpendicular direction between neighboring atomic rows will be denoted by $d_\perp = a\sqrt{3}/2$. The lattice constants along the dense packed directions, i.e. the next neighbor (nn) distance $d_{nn} = a\sqrt{2}/2$, for silver and copper are $d_{nn}^{Ag} = 2.89\,\text{Å}$, $d_{nn}^{Cu} = 2.55\,\text{Å}$. The distance between adjacent (111) planes defines the monoatomic step height $z_{step} = a/\sqrt{3}$ Please note that the lattice directions are always represented by the lattice vectors of the three-dimensional crystal. Figure 5.1d shows STM data of the Ag(111) surface used for calibration of the voltage–to–deflection constant of the scan piezo.

Adding seasoning to copper: Halite double layers on Cu(111)

For single molecule investigations, often NaCl (sodium chloride, also known as table salt or halite) islands are grown on (transition) metal surfaces. The insulating layers electronically decouple adsorbates from the substrate, enable the characterization of their (nearly) unperturbed electronic structure[103,155–157] and offer a platform to study the charge states of adsorbates by artificial charging through electrons from the STM tip[158,159]. Yet, the surface wave function extends through the insulating layers and allow tunneling without crashing the STM tip. The tunneling junction with adsorbates on top of the insulating film then corresponds to a double barrier (metal–insulator–adsorbate–insulator–metal) that requires a more sophisticated treatment of tunneling phenomena. However, this thesis does not deal with the peculiarities for STM and STS and refers to corresponding literature for a detailed description[160–163]. A convenient side-discovery of the studies of adsorbate/NaCl/metal systems was the greatly simplified and well-reproducible transfer of CO molecules from the salt to the tip—known as tip functionalization. Figure 5.2 shows
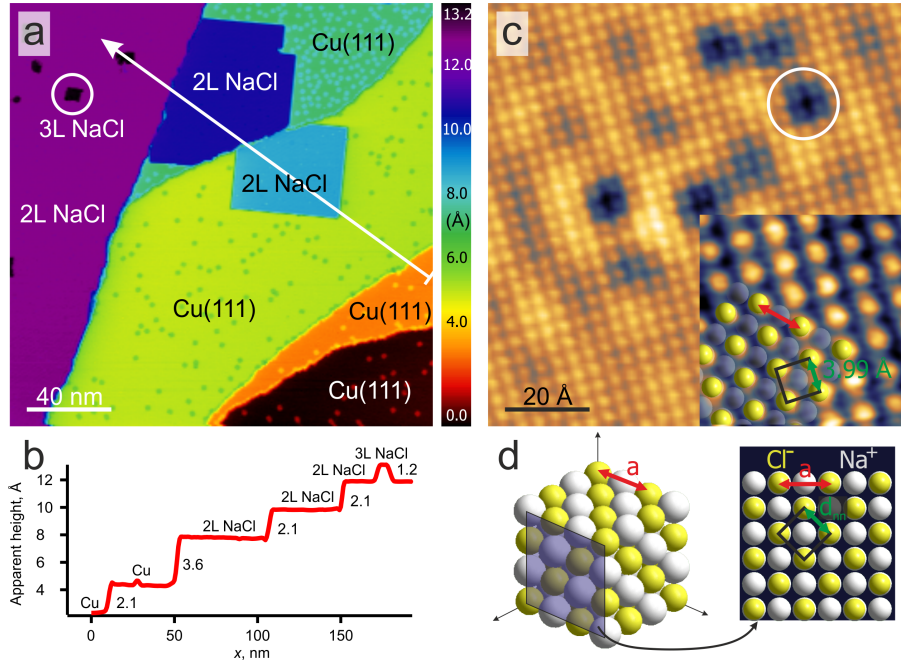
Figure 5.2. Sodium chloride on Cu(111). a) Typical overview image of salt islands. The NaCl patches are easily distinguishable from copper terraces due to their straight edges and perpendicular corners (cf. blue islands). The inset shows different molecular densities at the same sample. The salt islands displace and compress adsorbates on the metal terraces. b) Line profile along the white arrow in a). The numbers next to the steps give the step heights in Å. c) High resolution STM data of NaCl. STM only images the chlorine ions. The inset depicts a zoom-in with a model overlay. d) NaCl bulk model with highlighted (100) plane and model of the (100) surface. NaCl islands on Cu(111) are (100) terminated which leads to a square lattice with next neighbor distance $a_{nn} = 3.99\,\text{Å}$. The bulk lattice constant $a = 5.64\,\text{Å}$ is indicated in red, a_{nn} in green. Scan parameters: a, c) $U = 100\,\text{mV}$, $I = 11\,\text{pA}$; inset $U = 100\,\text{mV}$, $I = 30\,\text{pA}$.

NaCl islands grown on Cu(111) by beam epitaxy. Very similar to the deposition of organic molecules described in Section 5.2, thoroughly degassed NaCl powder (purity $\geq 99.999\,\%$, Sigma-Aldrich[164]) was resistively heated in a quartz crucible to $900\,\text{K}$ and deposited for $2\,\text{min}$ onto a sample held roughly at room temperature. The preparation parameters lead to a coverage considerably below one monolayer (ML). NaCl was grown on the sample as last preparation step before transfer to the SPM chamber. On the surface, Na^+ and Cl^- ions self-assemble into extended islands. The islands are easily discernible from metal terraces by their strikingly straight edges and perpendicular corners as shown in Figure 5.2a in light blue and blue color. NaCl grows as double layers (2L) on Cu(111)[165,166] with a nearly bias independent step height of $\approx 3.6\,\text{Å}$. Figure 5.2b shows a line profile across Figure 5.2a spanning across a copper step edge, the transition to NaCl, NaCl to NaCl on different Cu-terraces and at the end across a three layer (3L) NaCl patch. The corresponding step heights are given at the steps in Å. The islands are (100)-terminated exposing alternating Na^+ and Cl^- ions to vacuum that consequently result in non-polar step edges. The lattice constant of bulk NaCl is $a = 5.64\,\text{Å}$[165]. However STM is only sensi-

tive to the chlorine and therefore images a square lattice with a next neighbor distance of $d_{nn} = 3.99$ Å (see inset in Figure 5.2c and Figure 5.2d). 3L NaCl starts growing before the surface is fully covered with two layers corresponding to a Volmer–Weber island growth. Furthermore, sodium chloride islands smoothly overgrow surface features like defects and step edges following a carpet-like growth mode[166]. Apart from the atomic protrusions of the chlorine ions, NaCl is mostly transparent in STM owing to its insulating properties. Contrast variations at salt islands can be related to the copper surface underneath. As an example, Figure 5.2c depicts STM data that features the NaCl/Cu(111) interface state[166] scattered at Cu-impurities and defects, all overlaid by the bright protrusions of the chlorine ions (cf. white circle in Figure 5.2c). Adsorbates on the other hand are displaced and compressed on the Cu terraces where NaCl islands formed. Apparently the sample temperature during salt deposition did not supply enough thermal energy for the adsorbates to diffuse across step edges. This leads to the interesting possibility to prepare samples with varying adsorbate densities to study coverage dependent effects on the very same surface. Coverage dependent ordering phenomena e.g. are reported for organic adsorbates[167,168].

Transition metal dichalcogenides

The last part of the thesis presents investigations of the TMD $NbSe_2$. Contrary to the coinage metal samples, the TMD does not act as support substrate, but it is the system of interest itself. Therefore TMDs are briefly introduced here. More introductory notes, especially concerning $NbSe_2$, can be found at the beginning of Section 11. As the name transition metal dichalcogenide already states, TMDs exhibit a stoichiometric ratio of one transition metal M to two chalcogens X that results in compounds of formula MX_2. Relevant TMDs of current (surface science) research are quasi two-dimensional materials that consist of three-atom thick, van-der-Waals stacked layers. Within each layer, two hexagonal chalcogen sheets are covalently bound to one metal sheet in between as depicted by the side view in Figure 5.3a, d. The coordination geometry of the central metal ion can adopt trigonal prismatic or octahedral coordination (cf. middle column in Figure 5.3). Furthermore, the layer stacking sequence results in different crystalline polymorphs of which the 2H and 1T type are presented in Figure 5.3 as they are relevant in later Sections. In general, the digits within the type denomination represents the number of layers per repeat unit, i.e. the number of X-M-X layer per unit cell. The letter stands for the lattice structure trigonal and hexagonal. Figure 5.3c ,f shows the crystal structure for 2H and 1T polymorphs. Interestingly, the coordination geometry of the metal sheet defines the interlayer stacking. 2H crystals consist of trigonal prismatic coordinated layers, 1T crystals exhibit octahedral coordination. The great structural diversity of TMDs featuring different polymorphs and coordination as well as their constituent variety expressed by many metal-chalcogen combinations, leads to extremely versatile chemical and physical properties. For example the electronic characteristics range from insulating via semiconducting to metallic. This offers opportunities for technological research and applications in the fields of (opto-) electronics, sensing, energy storage and catalysis[30,169–171]. Furthermore many TMDs feature exotic properties such as superconductivity (SC)[170], charge density waves (CDWs)[172], and Mott transitions[173], which has made them very popular for fundamental research for many decades. Additionally, the research interest was boosted by the discovery
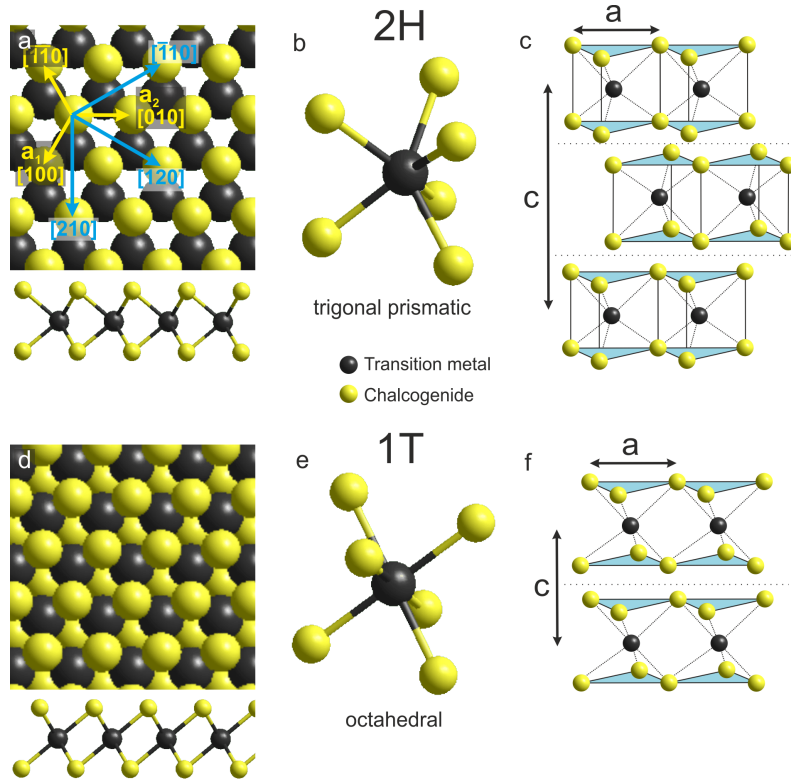
Figure 5.3. Transition metal dichalcogenides. The top row depicts the 2H polytype, the bottom one 1T. a) Top and side view of one layer with trigonal prismatic coordination. The 2H surface is hexagonal with every top chalcogen situated right above the lower one. Therefore the hollow sites either show a "void" (here: white space) or a metal atom (black). b) The metal ion exhibits trigonal prismatic coordination. c) The 2H structure is characterized by two layers per repeat unit. Every second layer is aligned. For values of the lattice constants please refer to Table 5.1. d) Top and side view of one layer with octahedral coordination. The surface is also hexagonal, but compared to the trigonal prismatic coordination, the top layer is shifted by $d_\perp/2$ along the $\langle 210 \rangle$ direction. The top chalcogens are now situated at the "void". e) The metal is coordinated octahedrally in 1T crystals. f) Layer sequence. $c_{1T} = c_{2H}/2$.

of graphene and its rich physics arising in single layers. For TMDs alike, the layered structure leads to strong anisotropy of the in-plane properties compared to out-of-plane. Similar to graphene, the interactions within a layer are of covalent nature while the interlayer interactions are of van-der-Waals character. This allows for an easy preparation of single layers through (chemical) exfoliation. Note however, that in the case of TMDs a single layer is always three atomic sheets thick. Interestingly, some technologically relevant characteristics only manifest within such quasi two-dimensional single layers[170,174]. For example the semiconducting MoS_2 features a transition from an indirect band gap in the bulk to a direct band gap in the single layer making it ideal for (opto-) electronic devices such as photodetectors[170]. TMDs are therefore a very interesting class of materials featuring rich physics and a large playground for research. Furthermore SPM techniques have been successfully employed in many TMD studies. Since SPM is mostly sensitive

to the topmost layer, it images the upper chalcogen sheet that features a hexagonal symmetry very similar to the (111) surfaces of fcc metals. The lattice directions are often described by the four-indices Weber symbols $\langle UVTW \rangle$, but will here be given in three-index notation $\langle uvw \rangle$ in terms of the real space hexagonal lattice vectors a_1, a_2, c as depicted in Figure 5.3a. Therefore the same directions of the two-dimensional hexagonal lattices of TMDs and fcc-(111) surfaces are denoted by different sets of indices. The lattice parameters of the herein investigated 2H-NbSe$_2$ are $a = a_1 = a_2 = d_{nn} = 3.44\,\text{Å}$ along the close packed directions, $c = 12.48\,\text{Å}$, that results in a monolayer step height of $z_{step} = c/2 = 6.24\,\text{Å}$, and $d_\perp = a\sqrt{3}/2 = 2.98\,\text{Å}$ for the interrow distance.

5.2. Sample preparation

An essential prerequisite for successful surface science investigations are well defined samples. Different preparation techniques have been established for various materials. In the case of layered materials such as TMDs cleaving leads to an atomically defined surface. The simplest form of cleaving is mechanical exfoliation with adhesive tape in ambient conditions. In the case of NbSe$_2$ however this led to a contaminated surface. Consequently in vacuo sample preparation was introduced. A clean, few mm long aluminum cylinder was glued to the TMD sample with UHV compatible epoxy prior to introduction to the UHV system. Inside the chamber, the pole was then driven against an obstruction which caused it to tip and remove several layers of material from the sample. The aluminum pole falls and remains inside the chamber. Subsequently, the sample was transferred into the SPM within a few minutes.

Sputtering and annealing

Sputtering is the process of fast ions hitting a surface and expelling particles from the top layers. In sample preparation sputtering is used in combination with annealing to produce an atomically clean and flat surface. Here, the preparation chamber is flooded with Argon to a pressure of $P = 2.5 \cdot 10^{-5}\,\text{mbar}$ through a direct gas inlet flange at the sputter gun. It should be noted that the chamber can either be disconnected from all pumping and kept at Ar atmosphere or it can be sputtered in an Ar flow while pumping. Inside the sputter gun, the sputter gas is ionized by electron collision and accelerated to an energy E_s of $0.5\,\text{keV}$ to $1.5\,\text{keV}$. The ions are focused in a beam and directed onto the sample where they sputter the surface. The Ar$^+$ ions expel particles from the samples' surface, e.g. molecules and atoms from previous preparations as well as atoms from the samples' top layers. For metals, the sputter yield Y is defined as the number of atoms removed from the surface per incident ion. It is a well-studied quantity for many combinations of sputter gases, energies and samples[175] and can be used to estimate the amount of material removed during the sputtering process. For perpendicular ion incidence, the removed material along the surface normal per unit time is given as sputter rate $\Delta z/t$ by[176]

$$\frac{\Delta z}{t} = \frac{M}{\rho \text{N}_\text{A} \text{e}} Y \frac{I_s}{A}\,, \tag{5.1}$$

where M is the molar mass of the metal sample, ρ is its density, $\text{N}_\text{A} = 6.022 \cdot 10^{23}\,\text{mol}^{-1}$ is Avogadro's constant, $\text{e} = 1.602 \cdot 10^{-19}\,\text{C}$ is the electron charge, I_s is the sputter current

flowing from the sample, and A is the sample surface area. For sputtering Ag(111) with Ar at an ion energy of $E_s = 0.8\,\mathrm{keV}$, $Y = 3.292$[175,177], furthermore $M = 0.108\,\mathrm{kg/mol}$, $\rho = 10.490 \cdot 10^3\,\mathrm{kg/m^3}$ and in this experimental setup $I_s = 7\,\mathrm{\mu A}$ and $A = 5.027 \cdot 10^{-5}\,\mathrm{m^2}$. The sputter rate can then be estimated to be

$$\frac{\Delta z}{t} = 4.892 \cdot 10^{-11}\,\mathrm{m/s} = 29.352\,\mathrm{\mathring{A}/min} \approx 12\,\mathrm{ML/\,min}\,, \tag{5.2}$$

where the monoatomic step height was used to convert to monolayer (ML).

During sputtering ions can be embedded in or adsorbed to the surface. Furthermore the material is not stripped layer-wise, but the surface is roughened due to randomly hitting ions. To prepare atomically well defined surfaces, the samples have to be heated after sputtering to remove Ar and to restore the surfaces' crystallographic order. This process is called annealing. Typical annealing temperatures for an Ag and Cu sample are (670 to 870) K. Annealing can be done in a fast way ("flash-annealing") by applying the maximum current to the heater necessary to reach the desired temperature and switching off as soon as the temperature is reached. Or the sample can be kept at the annealing temperature for a longer time, usually 10 min. Regardless of the procedure, the cooling rate should not exceed (1 to 2) K/s to avoid sample strain and guarantee an ideal surface morphology. In the case of (111) surfaces large, flat terraces with only few steps are desired. Prior to all experiments presented in this thesis repeated cycles of Ar$^+$ sputtering with an energy of (0.8 to 1) keV followed by annealing to $\geq 720\,\mathrm{K}$ were carried out.

Atomic and molecular deposition

Deposition of solid materials like metals and molecules or gases is a key preparation step for molecular surface science, e.g. to create surface confined nano-structures. Gas deposition is realized by partially flooding the (preparation) chamber with the desired gas through a high precision leak valve. Gaseous substances can act as precursor for surface assisted chemical reactions as in the case of growing graphene from ethylene[178] or boron nitride from borazine[178]. Or the gases themselves are of interest as molecular ligands[179] or adsorbates. In the latter, preparations are carried out in situ due to the low desorption temperature of the gases, i.e. the cold sample inside the scanner is exposed to a gas background pressure. Solid materials such as larger organic molecules and metals are deposited onto the sample by beam epitaxy. In the case of organic molecules the technique is referred to as organic molecular beam epitaxy (OMBE). An atomic or molecular beam is generated by evaporating* solid substances. The evaporation requires thermal sources that can base on different heating principles such as direct current heating (also: resistive heating) or electron collision heating (also: e-beam heating). Herein, only resistively heated sources were used, commonly called evaporators. Metals can be evaporated by resistively heating support wires with a high melting point and high electrical conductivity like tungsten. For example a high purity copper wire was wound around a tungsten filament to deposit copper adatoms for experiments in Section 6. Molecular powders were evaporated from quartz crucibles with the same button heaters as employed for sample heating. All evaporators create a particle beam that is directed via pinholes onto the sample. The

---

*The physically correct process is mostly sublimation. However, the notation of the preparation method as evaporation and of the employed mounting parts as evaporators is common.

deposition time is usually controlled by a shutter in front of the pinhole. The flux j ($[j] = 1/\mathrm{s}$) of particles hitting a surface area A at distance L away from the evaporator is given by[55]

$$j = \frac{p(T)A}{\pi L^2 \sqrt{2\pi m k_\mathrm{B} T}}, \tag{5.3}$$

where $p(T)$ is the equilibrium vapor pressure of the deposited substance that depends on the substance's temperature T, m is the particles' mass, and k_B is the Boltzmann constant. The inverse-squared distance dependence should be highlighted. To increase the flux, the evaporators are brought as close as possible to the sample via linear transfers with bellows. The coverages are controlled during preparations by adjusting temperature and deposition time. Initial evaporation parameters are chosen from experience and the initial coverages are determined experimentally by STM. The correlation between the deposition time and the coverage can be assumed to be linear.

Porphyrins
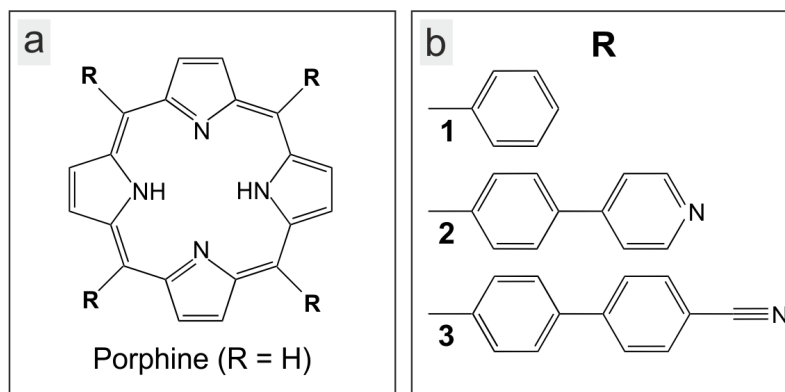
Figure 5.4. Chemical structure of porphyrins. a) The porphyrin macrocycle consists of four pyrrole units interconnected by methine bridges. Peripheral hydrogens were omitted for clarity. The most simple porphyrin unit is often referred to as porphine. The macrocycle allows manifold structural modifications, e.g. by substituting the hydrogens at one, two, three or all four meso positions as indicated by **R**. b) Possible substituents as employed in this work were 1: phenyl, 2: phenylpyridine, and 3: biphenyl-carbonitrile.

Porphyrins and their derivatives are well know molecules in biological processes, especially for their function in the metabolism of mammals. For example, they take a key role in the respiratory cycle, where a porphyrin within heme binds oxygen and carbon dioxide in the blood. Furthermore vitamin B12 contains a porphyrin as functional catalytic center, which is indispensable for the correct functioning of biological processes in the human organism. Also, the porphyrin containing chlorophyll absorbs light to supply energy for photosynthesis in plants. Inspired by their outstanding performances in nature, porphyrins—also known as the pigments of life—have become promising building blocks for molecular nano-science. Beyond applications mimicking natural processes such as gas sensors[180] or photovoltaics[18], they have e.g. also been utilized in cancer treatment[181] or catalysis[17].

Common to all porphyrins is a central cyclic unit, the so called porphine. It consists of four pyrrole rings interconnected via methine bridges. As free base derivative, the macrocyclic ring system features two hydrogen atoms bound to nitrogens in the inner cavity (see Figure 5.4). However, it represents a chemically active "pocket" and the central hydrogens can be replaced by a metal ion. Furthermore, the periphery allows manifold structural modifications, e.g. by substituting the hydrogens at one, two, three or all four meso positions as indicated by **R** in Figure 5.4a. Exemplary, three possible substitutions are shown in Figure 5.4b, all of which were employed in this work. Here, all four meso positions were replaced by the same functional tectons. In the case of phenyl (**1**) this leads to tetraphenylporphyrin (TPP), in the case of phenylpyridine (**2**) to tetra[(4-pyridyl)-phen-4-yl]porphyrin (2H-TPyPP), and in the case of biphenyl-carbonitrile (**3**) to tetra[-(4-cyanophenyl)phen-4-yl]porphyrin (2H-TPCN).

Other modifications include simple (meso-) substituents at the macrocycle as well as more complex fused systems[182], the synthesis of larger conjugated porphyrin arrays[183,184] and the combination with functional materials such as graphene[24]. The porphyrins' functional versatility is further broadened by their comprehensive metal coordination chemistry and structural robustness. Hence they serve as extremely versatile building blocks for 2D architectures[11,12,185].

5.3. Tip preparation

The STM tip used for Section 6 was an electrochemically etched tungsten wire[107]. For manufacturing STM tips, a W wire of 0.25 mm diameter is introduced in an etching lamella produced by dipping a gold ring into a 2 mol/l caustic soda solution [NaOH(aq)]. A direct current potential of 3 V is then applied between the gold ring and the tip to trigger an etching reaction. This procedure yields two tips: the lower part falls down and is caught standing upright, the upper part remains at the lamella. As tip, usually the lower part is used. Other techniques carry out etching in a beaker with an automated etch-stop circuit[107,186]. Here, this is not necessary, because the etching stops at the lower end when it falls. Tip etching produces microscopically sharp tips that can be directly used as probes. However, during the etching process, or afterwards when exposed to air, electrically insulating tungsten (tri-)oxide layers form[187]. These layers can cause instabilities in the tunneling junction or even suppress tunneling completely and cause tip crashes while approaching. Therefore further treatment of the tips is required. Herein, sputtering was applied to remove oxide layers. Further treatments—however not executed here—include annealing and field emission amongst other methods. For details on tip preparation and optimization please see references [186, 188]. The STM/AFM tungsten tip at the qPlus sensor was initially prepared by cutting the attached wire with focussed ion beam (FIB) milling in a 45° angle and did not require further treatment.

To reshape and optimize the tip apex during experiments, in situ tip forming (TF) and bias pulsing were carried out. A TF is a controlled tip crash into the sample. The tip contacts a clean metal part of the sample, is coated with substrate atoms by locally melting it through a high current flow (nano ampere) and is withdrawn afterwards. A bias pulse is realized by a fast voltage change in the range of a few volts with disabled z-feedback. The sudden change and increase in electric field is supposed to desorb in-stable adsorbates

at the tip or to reshape the apex by field emission or rearrangement of metal atoms at the apex. Both tip shaping techniques are random processes and can likewise result in improvement or deterioration. After each modification, the quality of the tip has to be checked. Depending on experimental needs, the prerequisites for the tip vary. For STM imaging, a sharp tip with high resolution is wanted. A suitable tip images surface features without blurriness and "ghost images". This can for example be checked by scanning across step edges. The step should only show as single feature of $\approx 2\,\text{Å}$ width. For STS on the other hand, high image quality is not the top priority. As mentioned in the last paragraph of Section 2.2, the tip density of states can vary considerably and influence spectroscopic studies. To exclude detrimental tip contributions, the ST-spectrum of a clean metal area is checked. It should be flat with only a step-like feature at the energy of its two dimensional surface state. For AFM, on the other hand, the tip is optimized for minimum interaction with the sample. Compared to the freely oscillating cantilever away form the surface, the frequency shift should be less than $5\,\text{Hz}$ in tunneling contact above bare metal. This guarantees minimal long range contributions and indicates a sharp tip. Please note that an ideal STM tip with high resolution can have a very large frequency shift. Usually many tip changes are necessary to reach a stable, well-defined tip configuration that meets the experimental demands.

Tip functionalization

A special form of tip preparations are tip functionalizations. Here, tip functionalization refers to the in situ process of deliberately transferring an adsorbate from the surface to the tip apex by STM manipulation techniques in order to enhance the chemical, electronic or spatial contrast. For STM imaging, already two decades ago, the functionalization with carbon monoxide (CO) molecules was reported to provide chemical contrast[189]. Additionally, organic molecules exposing functional groups sensitive to metal centers were employed to distinguish coordination nodes[190]. Since a key objective for STM has always been high resolution, functionalizations for improved imaging were explored and led to scanning tunneling hydrogen microscopy (STHM)[191,192] and functionalizations with Xenon (Xe), carbon monoxide (CO), and methane (CH_4)[193]. Furthermore, pentacene tips enhance the lobe structure of organic molecular orbitals[155] and CO tips afford high resolution imaging of the molecular electronic structure[156]. The underlying mechanisms for enhanced resolution however vary and are explained in detail in the corresponding references and elsewhere[194]. The introduction of reliable combined STM/AFM setups with qPlus sensors enabled AFM measurements with modified tips based on the well-established STM functionalization routines. Consequently, also considerable effort was put into improving the imaging capabilities of AFM through tip modifications—especially for developing sub-molecular contrast at organic adsorbates. This finally led to the imaging of the chemical structure of organic molecules with CO tips[9]. For more details about high resolution AFM imaging please see Section 3.3. Soon, other tip modifications were explored, including large molecules like C_{60}[195], PTCDA[196] and pentacene[9] as well as single atoms like Xe[197] or oxygen (in the form of copper oxide)[198] and many more[197,199]. However due to its easy pick-up routines and superb resolution—especially for organic molecules—CO is the most widely used molecule for tip modifications.

In the following, the in situ preparation and pick-up routines for CO are described. A
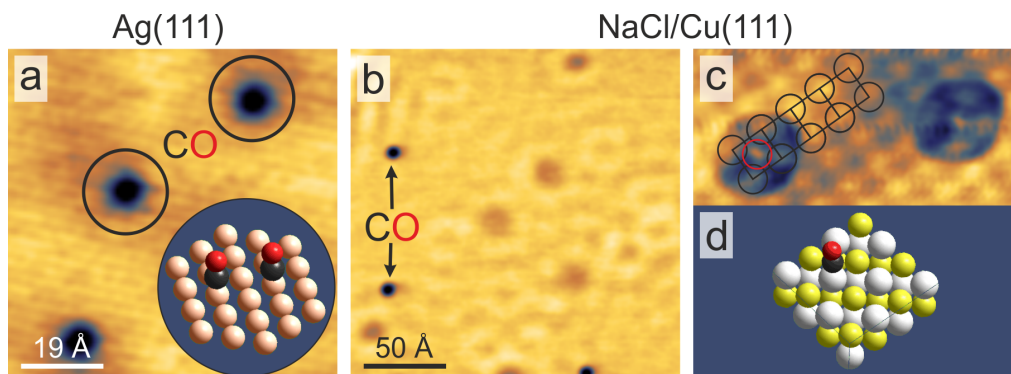
Figure 5.5. Carbon monoxide adsorption. a) Co appears as circular depression on Ag(111). As the model in the inset illustrates, it adsorbs at top sites standing upright. b) On NaCl/Cu(111) carbon monoxide exhibits a similar appearance as on metals. It is clearly distinguishable from defects. c) Adsorption site on halite. The carbon monoxide binds standing upright with the partially negative carbon to the positive Na^+ ion. A black square on c) connects four chlorine ions that are circled in black as guide to the eye to visualize the CO adsorption site. d) Model of CO adsorbed at the Na^+ ion. Scan parameters: a) $U = -30\,mV$, $I = 100\,pA$; b) $U = 100\,mV$, $I = 8\,pA$; b) $U = 100\,mV$, $I = 6\,pA$.

mini-can (1 l, 12 bar) of carbon monoxide (purity: 3.7) is mounted at the SPM chamber via a high precision leak valve. To apply a minute amount of gas molecules onto the cold sample inside the scanner, the SPM chamber is flooded to $\approx 3 \cdot 10^{-8}\,mbar$ and the sample transfer shutters are opened for $\approx 3\,s$ or a pin-hole at the side of the radiation shields for $\approx 15\,s$. Figure 5.5 shows typical STM images of Ag(111) and NaCl/Cu(111) after in situ dosing of CO. On both, metal and salt, CO appears as circular depression of $\approx 9\,Å$ diameter and $\approx 1\,Å$ depth (Figure 5.5). It is clearly distinguishable from (sub-) surface defects by its darker, i.e. apparently deeper, appearance. CO adsorbs with the carbon atom down and the oxygen pointing up on metal surfaces[189,200]. On many transition metals like Ag(111) and Cu(111), it primarily adsorbs at top sites[201], which can be exploited to determine molecular adsorption sites without atomically resolving the metal substrate[202]. For this work, all samples that were exposed to CO, were beforehand also decorated with low coverages of molecules ($< 0.1\,molecules/nm^2$). CO arriving at these samples was usually not found as individual units on bare metal, but mostly co-adsorbed at the sides of organic molecules as indicated in Figure 5.6c resulting in dark areas at the periphery. During scanning, the dark spots showed "fuzzy" features indicating instabilities or hopping[179] between preferred sites. To provide individual CO at such samples, NaCl islands can be grown prior to gas dosage. On NaCl carbon monoxide also appears a depression (Figure 5.5c). As illustrated by Figure 5.5d, CO adsorbs at Na^+ ions and therefore also adsorbs with the carbon atom that carries a negative partial charge.

During the transfer of a CO from the sample to the tip, the CO flips $180°$[189,200,203]. The energy for desorption and flipping is raised by tunneling electrons via an inelastic tunneling channel[200]. On Cu(111) a pick-up routine employing voltage- and z-ramps was reported[189] that turned out to be difficult to reproduce reliably for many groups. Therefore, the most common approach for tip modifications on Cu(111) is picking up CO from NaCl/Cu(111)

layers where CO is only weakly physisorbed[33,36]. To transfer a carbon monoxide from NaCl, only a tip approach of $\Delta z = 1\,\text{Å}$ to $5\,\text{Å}$ is necessary from a typical setpoint of $I = 6\,\text{pA}\,/\,U = 100\,\text{mV}$ above CO. The success rate is nearly $100\,\%$ with an appropriately preconditioned tip (metal tip, sharp surface features, $\Delta f < 5\,\text{Hz}$). The exact same pick-up routine works reliably on Ag(111) as well. Contrary, an earlier report required a voltage- and current-ramp[203].
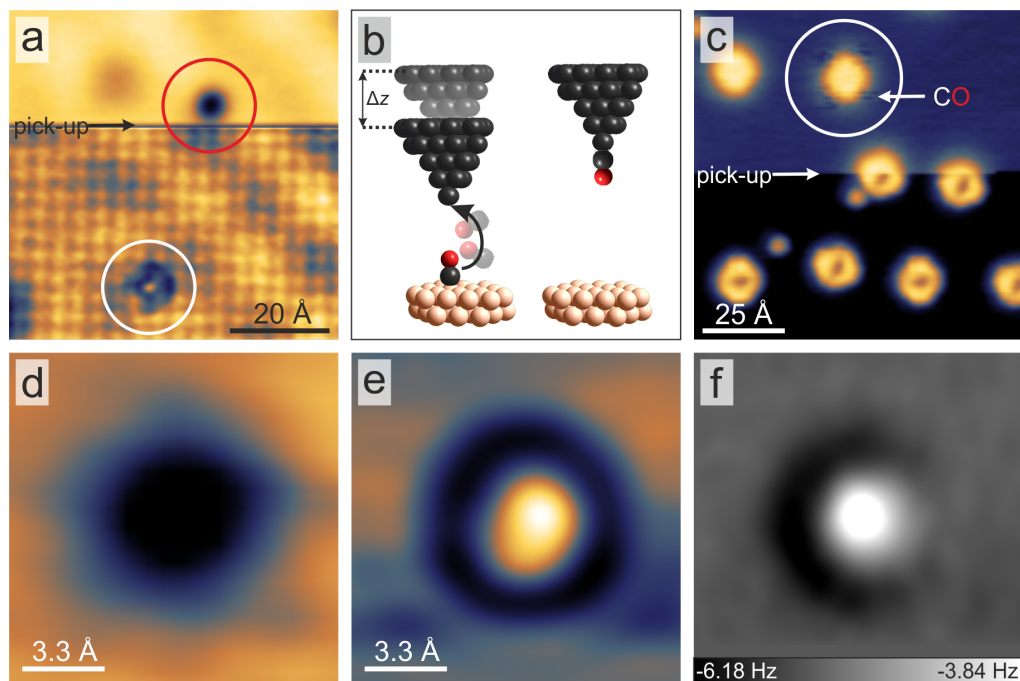
Figure 5.6. CO tip functionalization. a) Pick-up on NaCl by approaching the tip at the upper molecule (red circle) during scanning. The line in which the functionalization was carried out is indicated by the black arrow and is obvious because of the contrast change. A second CO is circled in white. The appearance has changed from a dark depression to a bright spot. b) Illustration of the transfer routine. c) Deliberate pick-up from the side of a porphine (white circle). The CO is visible as "fuzzy" dark contrast at the side of a molecule (white arrow). After pick-up the STM resolution is considerably improved. d) CO/Cu(111) imaged with a metal tip and e) a CO tip. f) Δf channel recorded simultaneously with e). Scan parameters: a) $U = 100\,\text{mV}$, $I = 6\,\text{pA}$; c) $U = 500\,\text{mV}$, $I = 80\,\text{pA}$; d), e), f) $U = 5\,\text{mV}$, $I = 15\,\text{pA}$;

Figure 5.6a shows a tip functionalization "on-the-fly" at NaCl. After scanning across a CO, the scan is paused in the middle of a line, the tip is moved above the molecule (cf. red dot in Figure 5.6a) and then approached. Subsequently, the scan is continued. The distinct contrast change to atomic resolution is a clear sign for a successful CO transfer on NaCl. Furthermore, an enhanced lateral resolution is also visible at molecules as depicted in Figure 5.6c. Here, a coincident CO pick-up from the side of a molecule happened. If no CO is available on bare metal, a CO can also be taken from the periphery of a molecule with the same approach-procedure. It should be noted that for all tip modifications, the AFM was in operation, i.e. the sensor was oscillating with activated AFM feedback. The attachment of a CO to the tip corresponds to a change of the oscillator mass and also

changes the tip–sample interactions. Therefore, the frequency shift also changes by $\approx 1\,\mathrm{Hz}$. During CO manipulation, the frequency shift was observed in real-time to immediately confirm a successful transfer.

Another indication for successful manipulation is the changed appearance of second CO at the bottom of Figure 5.6a. Indeed, a contrast inversion of CO from dark to bright is a characteristic signature of a CO modified tip[9,189,200]. Figure 5.6d, e show a CO on Ag(111) imaged with a metallic tip (d) and a CO-tip (e). The appearance of the surface-confined molecule changes from a dark disc to a bright, central protrusion surrounded by a dark ring. This signature furthermore helps to test the symmetry of the tip. Depending on the tip apex, the CO can sit off-center, i.e. not at the front atom of the tip. If so, the bright feature of the control molecule is asymmetric with respect to the dark ring, or even lies outside. Such a tip will also cause asymmetries and artifacts in AFM data and should therefore not be used. Figure 5.6f exhibits the Δf channel recorded simultaneously with Figure 5.6e. A CO molecule features repulsive (bright) contrast, perfectly symmetrical within a circular attractive background. Only if a tip satisfied these tests, it was used for acquiring FM-AFM data.

Part III.

Results

During the conferral of the doctorate I was involved in several projects resulting in the following publications. For a full list of publications please see Appendix 12.

1. Snezhkova, O., Lüder, J., Wiengarten, A., Burema, S. R., Bischoff, F., He, Y., Rusz, J., Knudsen, J., Bocquet, M.-L., Seufert, K., Barth, J. V., Auwärter, W., Brena, B., and Schnadt, J. Nature of the Bias-Dependent Symmetry Reduction of Iron Phthalocyanine on Cu(111). *Phys. Rev. B* **92**.7, 075428 (2015). DOI: 10.1103/PhysRevB.92.075428.

2. Snezhkova, O., Bischoff, F., He, Y., Wiengarten, A., Chaudhary, S., Johansson, N., Schulte, K., Knudsen, J., Barth, J. V., Seufert, K., Auwärter, W., and Schnadt, J. Iron Phthalocyanine on Cu(111): Coverage-Dependent Assembly and Symmetry Breaking, Temperature-Induced Homocoupling, and Modification of the Adsorbate-Surface Interaction by Annealing. *J. Chem. Phys* **144**.9, 094702 (2016). DOI: 10.1063/1.4942121.

3. Garnica, M., Schwarz, M., Ducke, J., He, Y., Bischoff, F., Barth, J. V., Auwärter, W., and Stradi, D. Comparative Study of the Interfaces of Graphene and Hexagonal Boron Nitride with Silver. *Phys. Rev. B* **94**.15, 155431 (2016). DOI: 10.1103/PhysRevB.94.155431.

4. Bischoff, F., He, Y., Seufert, K., Stassen, D., Bonifazi, D., Barth, J. V., and Auwärter, W. Tailoring Large Pores of Porphyrin Networks on Ag(111) by Metal-Organic Coordination. *Chem. Eur. J.* **22**.43, 15298–15306 (2016). DOI: 10.1002/chem.201602154.

5. He, Y., Garnica, M., Bischoff, F., Ducke, J., Bocquet, M.-L., Batzill, M., Auwärter, W., and Barth, J. V. Fusing Tetrapyrroles to Graphene Edges by Surface-Assisted Covalent Coupling. *Nat. Chem.* **9**.1, 33–38 (2017). DOI: 10.1038/nchem.2600.

6. Albrecht, F., Bischoff, F., Auwärter, W., Barth, J. V., and Repp, J. Direct Identification and Determination of Conformational Response in Adsorbed Individual Nonplanar Molecular Species Using Noncontact Atomic Force Microscopy. *Nano Lett.* **16**.12, 7703–7709 (2016). DOI: 10.1021/acs.nanolett.6b03769.

7. Bischoff, F., Auwärter, W., Barth, J. V., Schiffrin, A., Fuhrer, M., and Weber, B. Nanoscale Phase Engineering of Niobium Diselenide. *Chem. Mater.* (2017). DOI: 10.1021/acs.chemmater.7b03061.

8. Bischoff, F., Michelitsch, G., Riss, A., Reuter, K., Barth, J. V., and Auwärter, W. Surface-catalyzed ring-opening reaction and porphyrin deconstruction via conformational design. In preparation.

The following chapter presents results from 4–8. Section 6 adapts and reproduces text and figures from publication 4 with permission from Wiley-VCH Verlag GmbH & Co. KGaA. Experiments in Section 6.3 were performed at the University of Regensburg[†]

[†]Group of Prof. Jascha Repp, Institute of Experimental and Applied Physics, University of Regensburg, 93053 Regensburg, Germany

in collaboration with Florian Albrecht. Figure 8.4 in Section 8 shows STM/AFM data published in 5 (Copyright ©, 2016 Nature Publishing Group). Section 7 reproduces text and adapts Figure 7.2 from 6 (Copyright ©, 2016 American Chemical Society). Figure 7.2e was recorded by Florian Albrecht in Regensburg. Section 11 reproduces text and figures from 7 (Copyright ©, 2017 American Chemical Society). The experiments were carried out at Monash University Melbourne[‡] in collaboration with Bent Weber[§]. For experimental details see Appendix 12.

6. Metal-organic porphyrin networks on Ag(111)

The engineering of nanoarchitectures to achieve tailored properties relevant for macroscopic devices is a key motivation of organometallic surface science. To this end, understanding the role of molecular functionalities in structure formation and adatom coordination is of great importance. In this study, the differences in formation of Cu-mediated metal-organic coordination networks based on two pyridyl- and cyano-bearing free-base porphyrins on Ag(111) are elucidated by use of LT-STM. Distinct coordination networks evolve via different pathways upon codeposition of Cu adatoms. The cyano-terminated module directly forms 2D porous networks featuring fourfold-coordinated Cu nodes. By contrast, the pyridyl species engage in twofold coordination with Cu and a fully reticulated 2D network featuring a pore size exceeding $3\,\mathrm{nm}^2$ only evolves via an intermediate structure based on 1D coordination chains. The STM data and complementary Monte Carlo simulations reveal that these distinct network architectures originate from spatial constraints at the coordination centers. Cu adatoms are also shown to form two- and fourfold monoatomic coordination nodes with monotopic nitrogen-terminated linkers on the very same metal substrate—a versatility that is not achieved by other 3d transition metal centers but consistent with 3D coordination chemistry. This study discloses how specific molecular functionalities can be applied to tailor coordination architectures and highlights the potential of Cu as coordination center in such low-dimensional structures on surfaces.

The section is thematically divided into two parts. The first part presents an STM study on the formation of metal-organic porphyrin networks on Ag(111) and differences arising from varying functional groups that engage in the coordination. The second part focuses on the FM-AFM characterization of the cyano–nitrogen coordination node observed in the first part to elucidate the structure of the node.

Introduction

Supramolecular coordination chemistry is a vivid field of research as the combination of organic or metal-organic ligands and metal centers yields structures and properties that are not achievable by the individual building blocks. Recent examples highlighting the potential of metal-organic compounds include reports alluding to information storage[207]and processing[208], energy storage[209,210], catalysis[211], and molecular electronics[212]. Considerable efforts have been dedicated to adapting design principles from such three-dimensional (3D) supramolecular structures to a two-dimensional (2D) environment represented by surfaces in a controlled UHV setting[20,213,214]. Also in this 2D scenario, the functionality of metal-organic coordination networks is represented by the combination of metal nodes, offering, for example, active sites for energy conversion chemistry[215,216], and the ligands,

73

dictating the pore sizes, the confinement of adsorbates[217–221], and the (magnetic) coupling between the metals[222]. Specifically, the coordination number and symmetry at the nodes are decisive for the topology of the resulting metal-directed architectures[223]. Despite the many reports on surface-anchored metal-organic architectures[20,213–223], strategies to engineer and deliberately tailor assemblies still need to be further developed and refined. For example, extended 2D networks featuring a grid-like structure with square pores and mononuclear nodes are rarely reported[224–226]. In this respect, molecules offering fourfold symmetry might yield advantages compared to the frequently applied ditopic linear linkers. Hereby, tetrapyrroles as porphyrins are ideal candidates, which proved to be stable and versatile building blocks for self-assembled molecular structures on surfaces[11,12,227–231]. The central macrocycles, which host two hydrogens or a metal center, add functionality to the system, as they can be used as molecular switches[232], can undergo metalation reactions directly on a surface[233–235], and have potential for heterogeneous catalysis[236] and spintronics[237]. Most importantly, the tetrapyrrole macrocycle can be substituted by a wide variety of terminal moieties, offering vast possibilities to steer intermolecular and metal-organic interactions[11,12,224,227,238]. The following section presents an LT-STM study comparing the Cu-directed assemblies on Ag(111) of two de novo-synthesized porphyrins, functionalized with biphenylene-cyano (2H-TPCN) and phenylene-pyridyl substituents (2H-TPyPP), respectively. Although both molecules feature nitrogen terminated ligands and assemble into similar organic arrays, they respond markedly differently to the copper atoms. TPCN directly forms 2D metal-organic networks with small pores and fourfold coordination nodes, whereas TPyPP follows a hierarchic pathway from 1D metal coordination chains to an open porous 2D metal-organic network with linear twofold-coordinated metal centers. Monte Carlo simulation and comparison of Co- and Cu-directed networks, indicate that the origin of the two- and fourfold coordination motif results from an interplay between the steric hindrance at the coordination center and the inherent coordination properties of Cu.

6.1. 2H-TPCN and 2H-TPyPP on Ag(111)

The porphyrins investigated in this section are tetrapyrrolic macrocycles substituted at all four meso positions either with biphenylene-cyano or with phenylene-pyridyl moieties. Structural models of these two porphyrin derivatives, namely tetra[(4-cyanophenyl)phen-4-yl]porphyrin (2H-TPCN) and tetra[(4-pyridylphenyl)phen-4-yl]porphyrin (2H-TPyPP) are depicted in Figure 6.1a, h. We recently reported on the successful deposition and characterization of 2H-TPCN on Ag(111) and BN/Cu(111)[226,234], whereas 2H-TPyPP is addressed in this study for the very first time. Compared to commercially available tetraphenyl- (TPP) or tetrapyridylporphyrins (TPyP) featuring only one phenyl or pyridyl unit in each meso substituent, these novel modules introduce an additional degree of conformational freedom as the terminal ring R2 can rotate around the C-C single bond connecting it to R1 (cf. Figure 6.1a and e). Upon surface confinement, this enhanced molecular flexibility strongly influences the molecular self-assembly and coordination characteristics (see below). The adsorption of TPP and TPyP species on Ag(111) induces a saddle-shaped macrocycle deformation where the terminal rings are rotated typically $(50-60)°$ out of the surface plane[232,239]. Saddle-shape deformations-induced by

steric hindrance between the macrocycle and rotated moieties R1—are also expected for both 2H-TPCN and 2H-TPyPP. However, as R1 acts as a spacer, geometrically decoupling the terminal rings R2 from the macrocycle, a rather parallel alignment of R2 with the Ag(111) surface is anticipated as both, individual benzene and pyridyl rings adsorb on Ag(111) in a planar fashion[240]. Figure 6.1b, c, f and g show high-resolution STM
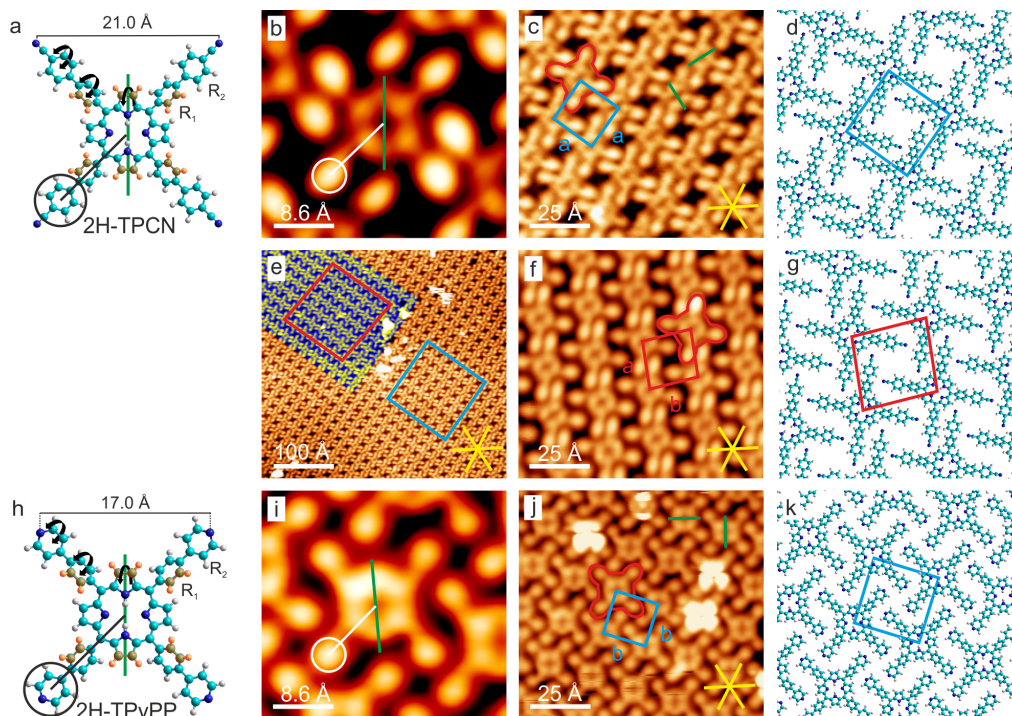
Figure 6.1. Organic assemblies of 2H-TPCN and 2H-TPyPP on Ag(111). a, h) Structural models of the porphyrin derivatives. The higher parts of rotated molecular moieties are highlighted in orange for better comparison to the magnification on single molecules (b, i) within self-assembled, dense-packed islands on Ag(111) (c, j). The green lines highlight the molecular axis through the upward rotated pyrroles. A single molecule is outlined in red in (c, f j) as a guide to the eye and the blue squares indicate the unit cells that include one molecule for both compounds. When cooling the sample immediately after preparation, organic islands with a rhomboid unit cell evolve for 2H-TPCN (e–g). Such ordering is highlighted in blue/yellow contrast in e). The unit cell is indicated by a red rhomboid in (f, g). The rhomboid structure relaxes into islands with a square unit cell after >15 h at room temperature. The substrate dense-packed directions are represented by yellow lines. d, g, k) Sketch of the assembly structure. The models were created with HyperChem and the molecular dimensions in (a, h) were extracted after geometry optimization of the free molecule within the semi-empirical AM1 framework. Scan parameters: b) $U = -1\,\text{V}$, $I = 30\,\text{pA}$; c) $U = -1\,\text{V}$, $I = 70\,\text{pA}$; e, f) $U = -1\,\text{V}$, $I = 70\,\text{pA}$; i, j) $U = -1\,\text{V}$, $I = 100\,\text{pA}$.

images of 2H-TPCN and 2H-TPyPP/Ag(111) representing occupied states. Both species present four peripheral lobes associated to the meso substituents and a donut shape that is assigned to the macrocycle. The latter shows twofold symmetry and appears with a depression in the center, as observed previously for free-base TPP on Ag substrates[232].

The elongated meso substituents of 2H-TPCN are reflected in the larger apparent size of the molecule and an increased intermolecular distance compared to 2H-TPyPP (see below). Nevertheless, the overall appearance of both species is rather similar, as the cyano group does not contribute considerably to the STM contrast[241–243]. Based on a comparison of sub-molecular features, presented in Figure 6.1b and f with structural models, a tentative conformation of the meso substituents' orientation can be inferred. Whereas R2 looks disk-like, indicating a planar adsorption, R1 appears as a narrow bridge connecting the macrocycle and R2. The asymmetric appearance of R1 with respect to the axis through the meso position of the macrocycle (white lines in Figure 6.1b and f) provides an indication for the rotation of R1. The upper part of the phenyl group dominates the image contrast, in full agreement with previously reported high-resolution STM data (see the Supporting Information of ref. [232]). Steric hindrance between the rotated R1 and the pyrroles of the macrocycle leads to its saddle-shape deformation. R2 appears as a broad protrusion symmetric with respect to the axis connecting opposing legs, in line with the contrast reported for terminal pyridyl groups adsorbed parallel to the Ag(111) surface[244–247]. We thus conclude that the R2 rings are aligned approximately parallel to the surface. As discussed below, the adsorption geometry of the terminal pyridyl rings in TPyPP is decisive for the distinct coordination behavior from TPyP, in which the pyridyl group is rotated considerably out of the surface plane. The adsorption geometry inferred from STM data is supported by FM-AFM investigations presented in Section 6.3.

Note that the larger apparent height of the legs compared to the macrocycle prevails only at small bias voltages and thus is assigned to an electronic effect (cf. Figure 6.2). Indeed, 2H-TPCN arrays on Ag(111) exhibit a voltage dependent contrast. When probing the HOMO region ($U < 0\,\mathrm{V}$) and for bias voltages $U < 0.4\,\mathrm{V}$ the molecules present four peripheral lobes associated to the four meso-substituents and a donut shape in the center that is assigned to the macrocycle (Figure 6.2a). For bias voltages $0.4\,\mathrm{V} < U < 1\,\mathrm{V}$ the molecules show an adsorption site dependent contrast: some appear brighter than others (Figure 6.2b). All molecules finally appear alike with a fourfold, window-like structure for $U > 1\,\mathrm{V}$ (Figure 6.2c). Qualitatively however all molecules show the same appearance and trend. This is also reflected in dI/dV spectra of differently appearing molecules. The spectra have the same shape, but are shifted towards lower energies for molecules appearing bright first. This indicates that the arrays consist of the same molecular species and the bias-dependent contrast arises from an alternated interaction with the substrate caused by different adsorption sites.

After room-temperature deposition on Ag(111), both modules self-assemble into highly ordered, extended two-dimensional islands (Figure 6.1c and g; corresponding structural models are shown in Figure 6.1d and h). Both assemblies feature a square unit cell with internal angles of $(90 \pm 1)°$ (marked in blue in Figure 6.1c and g) with side lengths $a = (20.4 \pm 0.5)\,\text{Å}$ for 2H-TPCN and $b = (18.2 \pm 0.5)\,\text{Å}$ for 2H-TPyPP. In addition, a distinct metastable structure characterized by a rhombic unit cell can be achieved when depositing 2H-TPCN at high flux (see Figure 6.1e–g).

For both porphyrin modules, the molecular axis through the two upward-bent pyrroles of the macrocycle (green lines in Figure 6.1a and e) is either aligned with the $\langle \bar{1}\bar{1}2 \rangle$ or the $\langle \bar{1}10 \rangle$ high-symmetry directions of the Ag(111) lattice (green lines in Figure 6.1 and f). Whereas 2H-TPCN mostly aligns along $\langle \bar{1}\bar{1}2 \rangle$, as reported for Co-TPP/Ag(111)[248], no preference is discernible for 2H-TPyPP. Despite these distinct azimuthal orientations
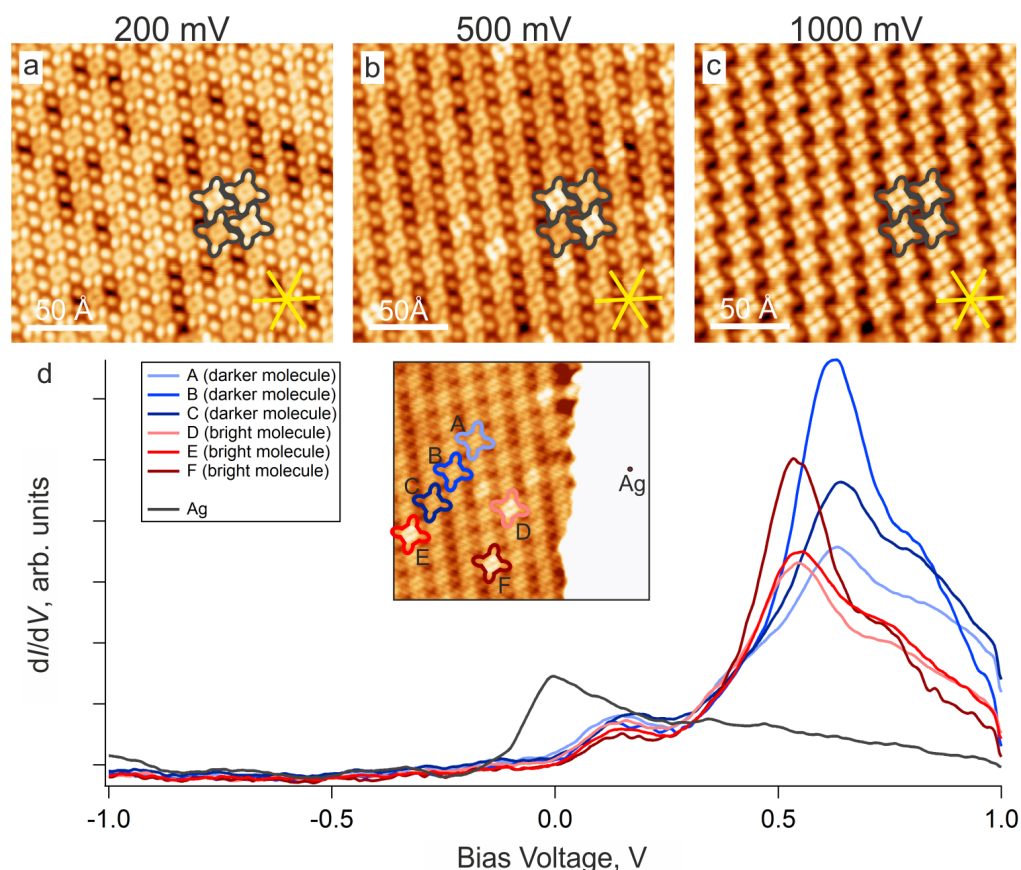
Figure 6.2. Electronic structure of 2H-TPCN within self-assembled organic islands. a–c) STM images at selected voltages indicated above the image for comparison. d) ST spectroscopy of brighter and darker species. The yellow stars represent the substrate's dense packed directions. Scan parameters: Bias voltage indicated above the image, $I = 100 \, \text{pA}$.

induced by the Ag(111) surface, site-specific interactions do not prevail over lateral intermolecular interactions and the 2H-TPCN and 2H-TPyPP arrays are not commensurate with the underlying Ag(111) lattice, as revealed by bias-dependent imaging and $\mathrm{d}I/\mathrm{d}V$ spectroscopy (Figure 6.2). Both assemblies are stabilized by lateral non-covalent interactions between neighboring nitrogen-phenylene groups.

6.2. Formation of metal-organic coordination networks

To investigate the response of the porphyrin species to metal adatoms, Cu was deposited with sub-monolayer, monomolecular coverages at room temperature. Figure 6.3 shows the fully reticulated metal-organic coordination networks and the corresponding structural models. For TPCN, a highly regular porous network with a rectangular unit cell of size $c = (21.9 \pm 0.5) \, \text{Å}$ and $d = (24.0 \pm 0.5) \, \text{Å}$ evolves, featuring domains that extend over hundreds of square nanometers with a low defect density (Figure 6.3a). The long-range order and the symmetry of the network are reflected in the autocorrelation plot and a sharp

fast Fourier transform (FFT) pattern (Figure 6.3b). High-resolution images (Figure 6.3c) reveal details of the network structure, with a pore size of approximately $86\,\text{Å}^2$ exposing bare Ag. Clearly, every node—assigned to a Cu adatom—links four TPCN units through their carbonitrile termini, resulting in a 1:1 stoichiometric ratio between TPCN and Cu. The projected N–Cu distance is $(1.6 \pm 0.5)\,\text{Å}$, in agreement with previously reported interfacial cyano–Cu coordination[249]. Within the network, the molecules appear slightly compressed compared to the organic phase; their aspect ratio deviates from unity, resulting in an "X"-like shape. This is also reflected in the rectangular unit cell, which differs from the
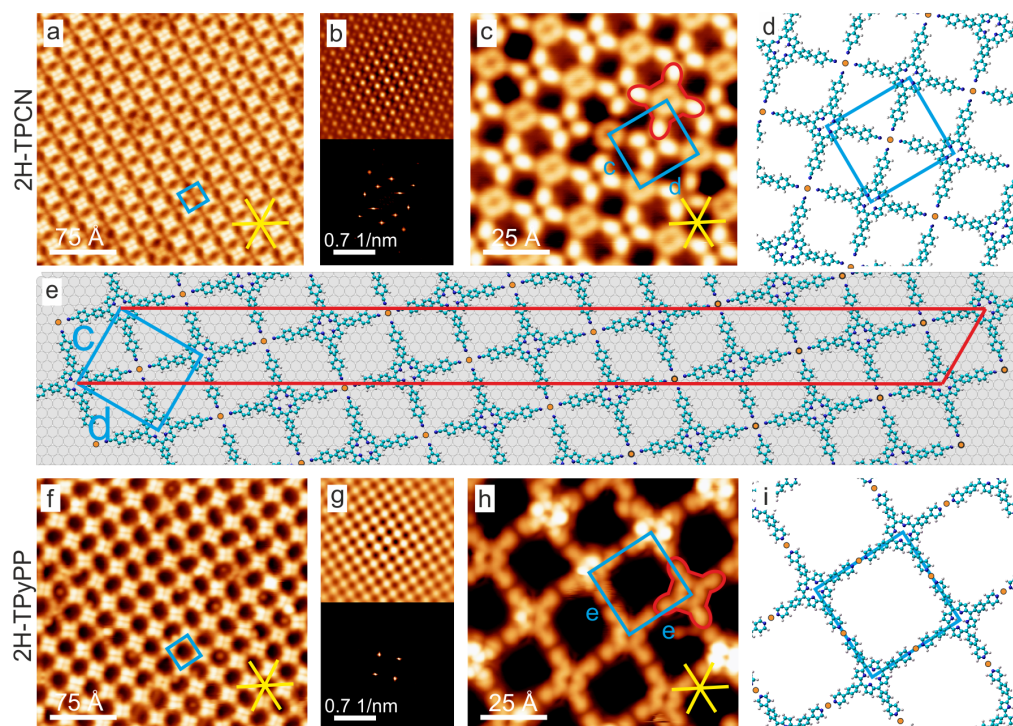
Figure 6.3. Formation of metal-organic networks upon deposition of Cu atoms. The blue squares indicate the unit cells and one molecular unit is outlined in red as a guide to the eye in (c) and (h). For TPCN (a–d) every coordination node is surrounded by four molecules and the unit cell consists of one molecule and one Cu atom. In contrast, the unit cell of TPyPP/Cu (f–i) consists of one molecule and two Cu atoms. Differences in the molecular appearance are assigned to the interaction of the macrocycle with Cu adatoms. The regularity of the metal-organic networks is reflected in autocorrelation plots (upper images in b and g) and sharp spots in FFT images (lower images in b and g). d, i) Model sketches of the networks. e) Sketch of the TPCN/Cu network with accordingly scaled and idealized Ag(111) surface. The molecules were compressed from a square outline to a rectangular outline with the same side length ratio as the unit cell to account for the flexibility of the biphenyl-cyano legs. All metal centers show the same adsorption site. The Ag(111) surface was laterally displaced so that all metal atoms sit at hollow sites. The unit cell of the structure derived from STM data is depicted in blue, and in red the (8×80) superstructure unit cell. The yellow stars represent the substrate's dense-packed directions. Scan parameters: a) $U = 0.7\,\text{V}$, $I = 50\,\text{pA}$; c) $U = 0.2\,\text{V}$, $I = 200\,\text{pA}$; f) $U = 0.9\,\text{V}$, $I = 80\,\text{pA}$; h) $U = -0.2\,\text{V}$, $I = 80\,\text{pA}$.

square unit cell reported for Gd-coordinated TPCN networks[234]. The reduced symmetry might be induced by the flexibility of the meso substituents combined with the favorable hollow site absorption of Cu adatoms on Ag(111)[250,251]. Indeed, a simple model overlay of the coordination network onto a lattice representing the Ag(111) substrate demonstrates that a highly regular, commensurate (8×80) structure can evolve with Cu adatoms exclusively at hollow sites (cf. Figure 6.3e). Apparently, the energy gained by formation of the commensurate network—enabled by the specific dimensions of 2H-TPCN—exceeds the energy costs for deforming the molecule. As usual for 3d transition metals, the coordination center is not visualized in STM[252,253]. However, an indirect fingerprint of the metal coordination is observed, as the coordinated terminal groups of TPCN appear higher than those that are non-coordinated (see Figure 6.4). For TPCN, fully reticulated metal-organic coordination networks were obtained, coexisting with dense-packed organic islands and large Cu clusters on the Ag(111) support under all employed preparation conditions. Thus, the yield for the metal-organic network formation is not optimal at the given preparation temperature and copper flux. However, additional architectures based on a simultaneous expression of metal-organic and organic bonding motifs were never observed for TPCN and Cu[254]. This was confirmed by the Monte Carlo simulations (see below). For TPyPP,
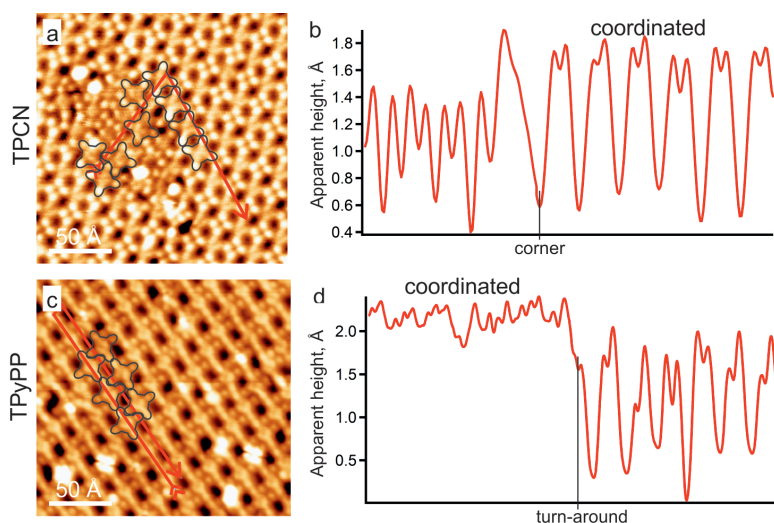
Figure 6.4. Different appearance of coordinated vs. uncoordinated legs evidenced by line profiles across the porphyrin linkers' substituents within the same image. a, b) TPCN; c, d) TPyPP. At the given scan parameters the coordinated substituents appear brighter, i.e. exhibit a higher apparent height. Scan parameters: a) $U = -1.2\,\mathrm{V}$, $I = 50\,\mathrm{pA}$; c) $U = -0.7\,\mathrm{V}$, $I = 100\,\mathrm{pA}$.

an extended metal-organic coordination network also evolves upon exposure to Cu, characterized by a molecule/Cu adatom ratio of 1:2 (Figure 6.3e and g). All four pyridyl termini of 2H-TPyPP are connected with the adjacent molecules by pyridyl–Cu–pyridyl coordination motifs, forming a square unit cell with a side length of $e = (28.2 \pm 0.5)\,\text{Å}$. The projected N–Cu distance amounts to $(1.9 \pm 0.5)\,\text{Å}$, in agreement with the previous reports[244,252]. Similar head-on, twofold Cu-mediated coupling motifs of pyridyl moieties are well-known in surface-confined coordination chemistry[224,244,249,252,255]. Compared to

the dense-packed organic arrays, TPyPP modules within the metal-organic network are rotated by 45°. Apparently, the energy arising from metal coordination exceeds the energy penalty from deviation from the original adsorption orientation, underlining the weak site-specific molecule-substrate interaction. The network domains extend over hundreds of square nanometers and exhibit long-range regularity (see autocorrelation plot and FFT pattern in Figure 6.3f). However, high-resolution STM data reveal that the pores vary in size and shape (Figure 6.3g). This local disorder is attributed to the flexibility of both the pyridyl–Cu–pyridyl motif, which features bond angles deviating from 180°, and the meso substituents[244,249]. Thus, a variety of pore shapes that deviate from a perfect square can coexist, which classifies this architecture as a 2D short-range disordered crystalline network[256,257]. The average pore size amounts to $340\,\text{\AA}^2$. To our knowledge, such a large area is unprecedented for homomolecular surface-supported porphyrin-based architectures. Consequently, the Cu-directed TPyPP network might serve as a template to trap and order large adsorbates or even molecular aggregates[258]. To this end, the intrinsic flexibility opens perspectives for hosting and sorting specific molecular guest species, enabling an adaptive behavior of the pores, thus representing a two-dimensional analogue of a "soft porous crystal"[259,260]. In contrast to the fully reticulated TPCN coordination architecture that evolves directly from the organic islands, the TPyPP coordination follows a hierarchic pathway upon increasing the (local) density of Cu adatoms. After depositing small amounts of Cu adatoms onto a sub-monolayer of 2H-TPyPP/Ag(111), a porous array appears that is characterized by chain-like sub-structures (Figure 6.5a). A close inspection reveals that it expresses simultaneously metal-organic and organic bonding motifs like those described in ref. [254]. As visualized in the corresponding structural model (Figure 6.5c), TPyPP tectons are dense-packed in one direction (organic bonding, marked with "f") and form a head-on configuration along the other direction (marked with "e"), which is assigned to a pyridyl–Cu–pyridyl coordination bond, in analogy to the fully reticulated network (cf. Figure 6.3e). The network is thus formed by 1D metal-organic chains that mutually interact through lateral non-covalent interactions between neighboring nitrogen–phenylene groups and follow the dense-packed substrate directions. The structure features a rhomboid unit cell of size $e = (28.0 \pm 0.5)\,\text{\AA}$ and $f = (18.2 \pm 0.5)\,\text{\AA}$ including an angle of $(60 \pm 1)°$ and a TPyPP/Cu adatom ratio of 1:3. When the Cu dosage is increased and (locally) exceeds a 1:1 ratio of Cu adatoms to molecules, the organic bonds are transformed into pyridyl–Cu–pyridyl coordination bonds and the structure evolves into a fully reticulated 2D metal-organic network. Figure 6.5b and the corresponding structural model in Figure 6.5d show the transition from 1D coordination chains to a 2D coordination network. Both architectures coexist locally and TPyPP can form coordination bonds from Cu to two, three, or four adjacent molecules. Clearly, the meso substituents engaged in coordination bonds appear brighter than their non-coordinated counterparts (cf. Figure 6.5a and Figure 6.4), in line with the results discussed for TPCN.

Monte Carlo modeling

To rationalize the experimental findings, Monte Carlo (MC) modeling was performed, as structure formation is known to be correctly reproduced in such simple simulations for a variety of functional tectons, including porphyrins[238,261,262] and phthalocyanines[263]. However the results will only be briefly summarized here. For details of the modeling
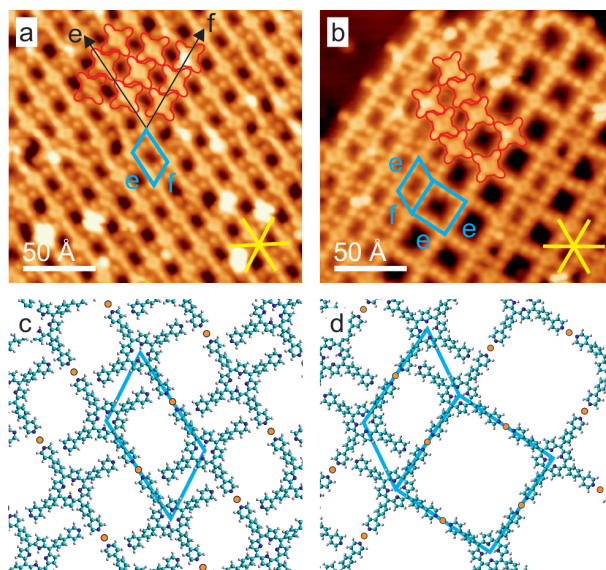
Figure 6.5. Network formation hierarchy for TPyPP. For TPyPP, depending on the (local) Cu density, metal coordination evolves in one or two directions. a) 1D coordination along one specific direction, indicated here by the black arrow labeled with "e", coexists with organic interactions along "f". Coordination will firstly be completed along one direction before starting in another direction (as shown in b). c, d) Models. As a guide to the eye, some molecules are outline in red. The yellow stars represent the substrate dense packed directions. Scan parameters: a, b) $U = -0.7\,\text{V}$, $I = 100\,\text{pA}$.

and the full results please see the original publication and the corresponding supporting information[204]. The most important finding of the simulations are that they reflect all assemblies observed experimentally and correctly reproduce a key difference between TPyPP and TPCN, namely the fact that 1D metal–organic chains emerge exclusively from TPyPP, even though they would be allowed for TPCN. Furthermore the agreement with experiments is simply achieved by restricting TPyPP to form one- and twofold coordination nodes only, as observed in the experiment, and TPCN is allowed to engage in one-, two-, three-, or fourfold coordination. These preconditions are designed to account for the naturally occurring spatial constraints around the coordination centers.

Discussion

Based on the above findings, the following conclusions can be drawn. Without steric hindrance, Cu adatoms favor a fourfold coordination to the nitrogen termini of porphyrins on Ag(111). In the experiments, this situation is realized for the slender cyano moieties of TPCN. Restricting the nodal symmetry to twofold by introducing spatial constraints due to planar or near-planar pyridyl groups in TPyPP, assemblies featuring 1D coordination chains can be achieved for molecule to adatom ratios below 1:1. Increasing the adatom concentration induces formation of additional pyridyl links, thus yielding a fully reticulated porous coordination network. Regarding ligands, the observed linear pyridyl–Cu–pyridyl

motif was tentatively assigned to steric hindrance by several studies[224,244,249,252]. Only when relaxing these constraints by rotating terminal pyridyl rings out of the surface plane, for example, by using the TPyP modules, a fourfold coordination to mononuclear centers can be achieved[264–266] (Figure 6.6). Such square-planar motifs are well known for pyridyl
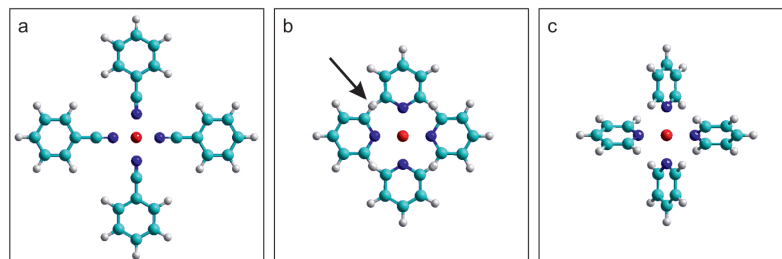
Figure 6.6. Model cartoons of coordination nodes including a central metal atom and four ligands. The experimentally observed (projected) metal–nitrogen distances of (1.6 ± 0.5) Å (cyano–N) and (1.9 ± 0.5) Å (pyridyl–N) were chosen to construct the models. a) Fourfold coordination employing four cyano moieties does not exhibit steric hindrance. b) As indicated by the arrow, four flat pyridyl moieties in the same coordination plane overlap. c) When rotated by 60° as commonly reported for pyridyl legs within TPyP, steric restrictions do not prohibit fourfold coordination.

complexes in 3D coordination chemistry[267–269], but uncommon in a 2D environment[270]. Their rare occurrence on metallic supports might be attributed to several aspects: A large adatom–nitrogen distance with respect to the surface induced by the rotation of the pyridyl ring out of the surface plane, weakening the pyridyl–adatom interaction, the nature of the coordinating metal center (see below) or simply the limited number of studies addressing molecular modules featuring rotated terminal pyridyl moieties. To achieve fourfold coordination with coplanar adsorbing moieties, a terminal group inducing minor steric constraints (e.g. cyano) is required. In this sense, the pyridyl-phenylene substitution of the de novo-synthesized 2H-TPyPP providing rotational flexibility to the termini is crucial for the formation of linear pyridyl–Cu–pyridyl binding motifs and for the construction of large-pore Cu-mediated coordination networks. Spatial constraints at the coordination center, which can be tuned by the geometric footprint of the terminal moieties, can be deliberately exploited to control the coordination number and thus the topology of the network architectures. Additionally, the Monte Carlo simulations show that the spatial constraints of the pyridyl groups not only influence the final architectures, but also induce an energetic preference for the formation of 1D coordination chains and therefore are the origin of the hierarchic assembly protocol in the case of TPyPP.

Regarding the role of the metal center, our experiments reveal that single Cu adatoms—somewhat neglected in on-surface coordination chemistry to date—can link four ligands in a quasi square-planar arrangement. Fourfold mononuclear 3d-metal nodes on metal substrates reminiscent of the square-planar coordination motif have been observed for Mn[271,272], Fe[264,270],Co[243,265,270] and Ni[272]. Recently, on-surface fourfold coordination was achieved in porphyrin-based metal-organic networks by either applying lanthanide centers[234] that support high coordination numbers[273] or by introducing a boron nitride spacer layer[226]. To our knowledge, a coordination number of four on surfaces was only

reported for Cu dimers[274] in metal-organic networks and for distorted Cu–carboxylate complexes[275]. This study introduces the first coordination network based on a square-planar motif based on monoatomic Cu centers. Accordingly, on Ag(111), Cu adatoms can form coordination bonds to two[244,249,252,276], three[277], or four nitrogen atoms. This diversity in on-surface coordination numbers discriminates Cu from other 3d metals such as Co, for which threefold coordination reminiscent of the trigonal planar motif known from 3D coordination chemistry prevails. Even for cross-like TPCN molecules on Ag(111), Co-coordination results in a random metal-organic network in which three- and fourfold nodes coexist[234], thus ruling out a dominating role of the molecular symmetry on the resulting metal-organic architecture. Indeed, a quantitative analysis of coordination geometries of d-block metals in 3D supramolecular complexes and solid-state structures shows a frequent occurrence of square planar and square pyramidal motifs for Cu, which only play a negligible role for Co[278]. Of course, one should be well aware that the metallic surface can drastically influence the coordination behavior, allowing for non-integer oxidation states, coordination spheres unachievable in solution, and coordinatively unsaturated centers exposing apical sites to vacuum. This is exemplified by the coordination of cyano to Co with dicarbonitrile-polyphenyl linkers[217] or to Cu with 9,10-anthracenedicarbonitrile molecules[279]. Furthermore, the metallic surface might mimic an additional ligand[280] and thus reduce the coordination number in the 2D adsorbate systems[217]. From this point of view, the twofold pyridyl–Cu–pyridyl link translates to a T-shaped coordination sphere of Cu with three ligands (two pyridyl groups and Ag). Indeed such T-shaped motifs are observed for Cu centers in 3D complexes, in contrast to Co preferring tetrahedral or pyramidal geometries[278,281]. Additionally, TPyP molecules form a fourfold coordination motif with Fe[264] but a twofold coordination with Cu[224] on Au(111), which fits observations from 3D chemistry where Fe, similar to Co, strongly prefers coordination to four or more partners. Thus, in addition to the important steric constraints induced by the pyridyl rings adsorbed approximately parallel to the surface, as discussed above, the naturally preferred coordination geometries of Cu itself might contribute to the stabilization of the linear pyridyl-Cu-pyridyl motif prevalent on coinage metal surfaces and at the same time support fourfold coordination in the case of TPCN.

Summary

In summary, by exploiting the preferred coordination geometries of copper in combination with a deliberate porphyrin functionalization, it was possible to design extended, 2D, grid-like metal-organic coordination networks on Ag(111). Both TPCN and TPyPP thus offer a basis for the fabrication of bimetallic[234] and mixed-valence[224] open porous networks through orthogonal insertion of metals[234]. Additionally, for TPyPP, the large pore size and the flexibility of the pyridyl-Cu-pyridyl links result in a 2D structure reminiscent of a soft porous crystal, providing opportunities to act as a template for the selective adsorption of molecular guests or nanostructures[231]. To rationalize the formation of distinct Cu-mediated structures from TPCN and TPyPP, Monte Carlo simulations were performed —presented here shortly—and related the experimental findings to reports on Co-mediated coordination networks and metal-organic complexes in solution chemistry. This comparison reveals that the choice of coordinating metal is decisive for

the emerging coordination motif; for example, replacing Co by Cu in TPCN coordination assemblies results in a highly regular network rather than a random structure. Here, coordination geometries in 3D metal-organic complexes can provide some clues for an appropriate selection of suitable metal for a targeted motif. Co preferentially binds in a tetrahedral fashion and therefore is not a promising candidate for the formation of linear, twofold coordination motifs on surfaces. In contrast, Cu was identified by this study as a versatile center supporting different coordination numbers and geometries. TPCN forms the first surface-based coordination network relying on a fourfold motif and a mononuclear Cu center. Additionally, the results indicate that the ligand properties (e.g., rotated pyridyl vs. planar pyridyl vs. cyano moieties) must fit the targeted nodal geometry and thus can be used to tailor the resulting network structure and their formation pathway through spatial constraints. Furthermore, this section briefly mentioned the benefits of basic Monte Carlo simulations in selecting suitable molecular modules for metal-organic architectures prior to the actual experiment. Consequently, the findings introduce prospects for the programmed design and selection of molecular and monoatomic building blocks for surface-confined supramolecular networks and thus contributes to controlled engineering of metal-organic/organic architectures.

6.3. FM-AFM investigation of cyano–copper coordination nodes

The following section presents the FM-AFM investigation of the fourfold cyano–copper nodes expressed in TPCN–Cu networks introduced in the preceding section.

Introduction

The limitations of STM for true topographic imaging becomes especially evident in studies of surface confined molecules and metal-organic networks. The convolution of topography with electronic structure often renders the determination of the adsorption geometry of molecules difficult and can even lead to misinterpretation of STM data[33]. Furthermore, for 3d transition metals, the coordination center often cannot be visualized in STM[252,253] as described above. Although, an indirect fingerprint of the metal coordination can sometimes be observed, as e.g. the coordinated terminal groups of TPCN appear higher than those that are non-coordinated (see Figure 6.4), the fingerprint only indicates the formation of a coordination complex, but does not reveal insights about the center such as the number of involved metal atoms. The number of metal adatoms at the coordination node is usually tentatively determined by measuring the projected length of the metal-organic bond in combination with spatial considerations[282,283]. However, the functional properties of coordination complexes is strongly determined by the characteristics of the coordination center, i.e. the number of metal atoms, the resulting coordination geometry and oxidation number (valence) of the metal. The metal-organic node determines the electronic structure of the complex that in turn defines e.g. opto-electronic and magnetic properties as well as chemical reactivity[264,266,284,285]. For example peculiar opto-electronic and magnetic properties are suggested by DFT calculations for tri-iron terpyridine complexes, but not for similar complexes involving only one or two iron atoms. Experimentally, the coordination center is however non-trivial to characterize by STM[284]. Furthermore, the number of metal atoms within a cluster can determine its catalytic functionality[286].

It is therefore of fundamental interest to thoroughly characterize surface confined metal clusters and the coordination nodes of two-dimensional metal-organic networks for which AFM bares potential. FM-AFM with CO functionalized tips has been established as state-of-the-art imaging tool for structure determination in organic molecules[9,33,36,37,128,287], for on-surface nano chemistry[24,287–291], for imaging of metal clusters[292,293], and for investigations of organometallic complexes[287,288,294].

2H-TPCN adsorption geometry and 4CN–Cu coordination node
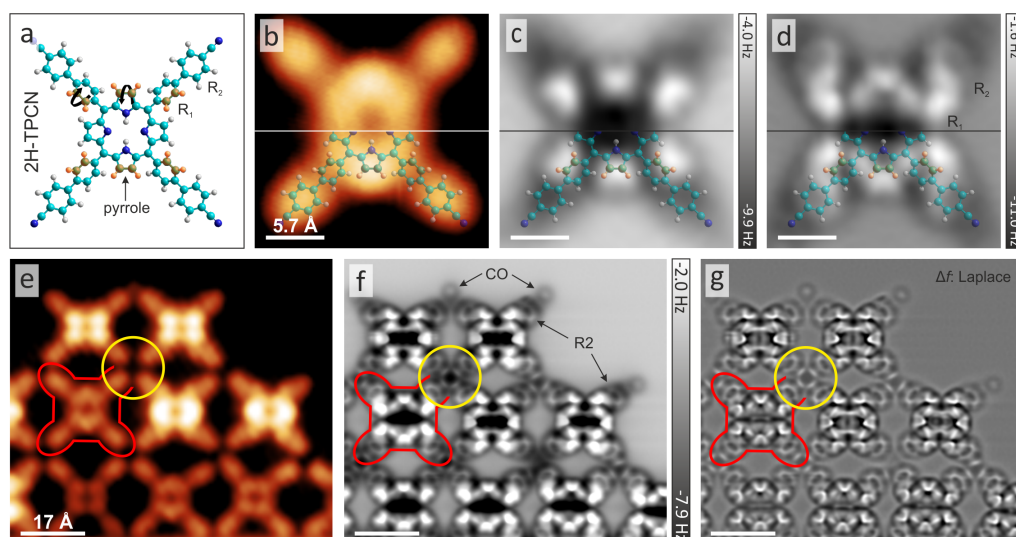
Figure 6.7. FM-AFM data of single TPCN and its Cu induced network. a) 2H-TPCN model. Higher molecular parts are dyed orange. b) STM image of a single 2H-TPCN. The lower part features a model overlay. c) Constant height Δf map. Higher molecular parts show as bright features. The observed deformation corresponds to the saddle shape of the suggested model. d) Δf data at closer tip–sample distance reveal nearly surface parallel outer phenyl rings R_2. e) STM image of the TPCN network. f) AFM image and g) Laplace filter of f). One molecule is outlined in red. A coordination node is highlighted by a yellow circle. Scan parameters: b) $U = 150\,\text{mV}$, $I = 3\,\text{pA}$; c)$\Delta z = -0.6\,\text{Å}$; d) $\Delta z = -1.4\,\text{Å}$; e) $U = 20\,\text{mV}$, $I = 30\,\text{pA}$; f) $\Delta z = -1.6\,\text{Å}$.

As describe above in Section 6.1, 2H-TPCN exhibits various degrees of conformational freedom. The model of the molecule and STM data are presented in Figure 6.7a, b. The macrocycle adopts a saddle shape that results in rotated phenyl rings R_1. As a consequence some molecular parts are relatively higher and are highlighted in orange in Figure 6.7a. However, as R_1 acts as a spacer, geometrically decoupling the second rings R_2 from the macrocycle, the R_2 rings are assumed to aligned approximately parallel to the surface and relatively closer. In constant height Δf mapping, molecular moieties protruding higher above the surface interact repulsively with the tip at larger distances[128,288,295]. Therefore these parts contribute as bright features in FM-AFM data at larger tip–sample distances while the rest of the molecule only appears as dark, attractive background. Figure 6.7c shows FM-AFM data with a model overlay that features repulsive interactions at the

R$_1$ rings as well as at two opposing pyrroles of the macrocycle. Only at considerable closer approach, the rest of the molecule shows repulsive interactions (cf. Figure 6.7d). Finally, rings R$_2$ evolve into ring-like features well-known for (nearly) surface-parallel hydrocarbons[9,36] (Figure 6.7d and Figure 6.8c). We thus conclude that the R$_2$ rings are aligned approximately parallel to the surface. The terminal cyano groups however cannot be imaged with the closest tip–sample spacings achievable for imaging the entire molecule. To resolve the terminal groups, the imaging plane has to be zoomed onto the terminal groups only to avoid crashing the tip into considerably higher moieties at the molecular center during further approach. Only then scanning with smaller tip–sample spacing is feasible and can establish a T-shaped contrast at the C–N. Although the strong deformation of the molecules prohibits direct imaging of the entire molecular structure, the evolution of repulsively interacting molecular parts fits very well the macrocycle's saddle shape, correctly reproduces the dependence of the phenyl rotation and the tilt of pyrrole units qualitatively and furthermore gives direct experimental proof for nearly surface parallel rings R$_2$. Therefore, the suggested molecular conformation in Section 6.1 can be confirmed.
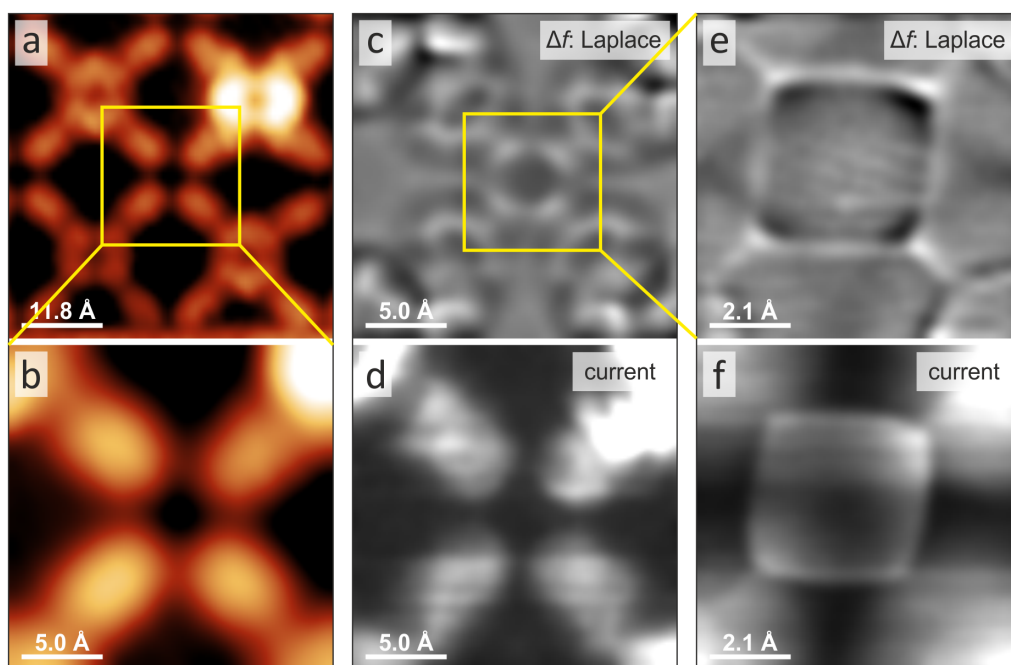
Figure 6.8. Detailed investigation of the cyano–Cu coordination node. a) STM image showing one coordination node with the four involved TPCN molecules. b) Zoom onto the node as highlighted in yellow. c) Laplace filtered AFM data of the node presented on b). d) The simultaneously recorded current channel. e) Closer zoom and z approach onto the node. f) Current channel recorded with e). FM-AFM cannot visualize the copper within the coordination node and no signature can be found in the current channel. Scan parameters: a), b) $U = 150\,\text{mV}$, $I = 3\,\text{pA}$; c) $\Delta z = -1.65\,\text{Å}$; e) $\Delta z = -2.45\,\text{Å}$.

Figure 6.7e–g shows the rectangular metal-coordination network formed after the deposition of Cu adatoms onto 2H-TPCN/Ag(111) described in detail in Section 6.2. The

STM data in Figure 6.7e serves as references for the AFM data next to it. The different contrast of the same molecular species in STM indicates an altered electronic structure. This modification could arise from different adsorption sites as previously described in Section 6.1 or it could stem from interactions of the macrocycle with adatoms. FM-AFM data not shown here additionally relate the brighter contrast in STM to a conformational difference, i.e. a stronger macrocycle deformation. However the origin remains elusive and is not relevant here. Figure 6.7f, g show a constant height Δf map and its Laplace filtered image. As guide to the eye a single molecule is outlined in red and a coordination node is circled in yellow. Again, due to its strong 3D character, the molecular structure of the porphyrin backbone cannot be imaged, the fourfold coordination node however only comprises flat moieties and is therefore accessible by FM-AFM. Within the yellow circle four rings can be discriminated that are assigned to the four phenyls R_2 just behind the cyano group engaging in the coordination. Figure 6.8c shows a zoom onto the coordination node (STM reference in Figures 6.8a, b). The cyanos appear T-shaped with the top bar facing toward the center. The coordinated metal however does not contribute to the image contrast and the node shows as dark area in between the T-shaped terminal groups. At even closer approach, the C–N groups appear Y-shaped, and the coordination center remains structureless. As assumed from constant current STM data, the simultaneously recorded current channel during constant height AFM measurements does not reveal details about the coordination center either (Figures 6.8d, f).

Discussion

First a comment on the AFM contrast of the terminal groups. Both, the T- and Y- shape are most likely artifacts arising from the deflections of the flexible CO tip caused by the potential landscape of the terminal groups and do not represent atomic bonds[125,194,195,296,297]. A similar contrast with perpendicular bright features was reported for single carbon links in graphene–porphine structures[24], for carbon triple bonds and for triply bonded terminal carbon atoms[298,299]. The T-shape seems to be the characteristic Δf contrast for the cyano moiety. Here, it is the same for coordination nodes at the edge featuring two or three bonds and even for single individual legs at island edges in coordinated networks and purely organic arrays as well as for cyanos within organic islands (last two not shown). However, when engaging in interactions with metal adatoms or with neighboring molecules in organic islands, the legs seem to be "straightened", i.e. the T-shaped contrast evolves around the same tip–sample distance as the atomic contrast at the phenyl rings R_2. Without interaction, the tip has to be approached further to establish the distinct contrast. Due to interactions with the substrate, the linear moieties probably bend toward the surface similar to unsaturated carbon atoms at hydrocarbon systems[289,300,301].

Unfortunately, the coordination node cannot be resolved. A characterization via constant current or constant height STM, nor by AFM was successful. Apparently the coordinated metal does not interact electronically or topographically with the CO terminated probe. In contrast, individual metal adatoms can be imaged by both, STM and AFM due to their electronic and topographic features[288,293]. Furthermore, a coordinated metal adatom at the center of a tetrapyrrole macrocycle does exhibit distinct features in STM and AFM as described later in Section 9. On the other hand, the distinct central signature of a coordinated tin ion inside a phthalocyanine molecule (SnPc) can be manipulated

through the STM tip. The Sn atom can be pushed and pulled through the macrocycle to be located slightly above or below the macrocyclic plane. When being below, the Sn signature cannot be distinguished in STM. Similarly here, the copper adatom is most likely located at a hollow site of the Ag(111) surface (cf. Figure 6.3 in Section 6.2) below the plane of the C–N moieties. Therefore the terminal organic groups are assumed to obscure the metal.

Summary

Summarizing, the 2H-TPCN adsorption geometry and the fourfold coordination node of four terminal cyano moieties of TPCN molecules with a single copper adatom was investigated by means of FM-AFM. The pronounced 3D character of the porphyrin derivatives prohibits true structure determination, nevertheless, the evolution of repulsive features in frequency shift maps approaching the surface reproduces the saddle shape qualitatively. The conformation derived from high resolution STM data could be confirmed, especially concerning the second phenyl rings. The spatial decoupling from the macrocycle allows an alignment almost coplanar to the surface. Unfortunately, the metal center within the coordination node could not be imaged. The metal atom is assumed to be concealed by higher lying cyano groups. Routes to imaging the coordination center include employing metals with a larger covalent radius such as lanthanides[234,302–304], employing different substrates as e.g. sodium chloride[288] or different tip functionalizations. The CO tip is ideal for high lateral resolution, but is chemically inert. Coordinated metals could be visualized through chemically sensitive tips as demonstrated by enhanced contrast above the metal ion of metalo-porphyrins with modified STM tips[190,305]. More work has to be done to establish experimental routines for imaging the coordination center in metal-organic networks.

7. Adsorption geometry of 2H-TPP on coinage metal surfaces

In recent years AFM at highest resolution was widely applied to mostly planar molecules, while its application toward exploring species with structural flexibility and a distinct 3D character remains a challenge. Herein, the scope of noncontact AFM is widened by investigating conformational differences occurring in the well-studied reference systems 2H-TPP on Ag(111) and Cu(111). Different adsorption conformations can be recognized in conventional constant-height AFM images. On Ag(111), constant-height imaging allows a qualitative characterization of the substrate-induced saddle-shape conformation apparent in the orientation of different molecular subunits[31–34]. On Cu(111) on the other hand, the macrocycle of 2H-TPP adapts a strongly deformed configuration. The observed large structural variability of the molecular geometries underscores the importance of characterizing molecular conformations at the single-molecule level in real space, going beyond space-averaging techniques.

Introduction

Porphyrins with meso-substituents such as tetraphenylporphyrin (TPP) typically exhibit a saddle-shape conformation of their macrocycle upon adsorption onto coinage metal surfaces[248,306–312]. This saddle-shape adaptation leads to distinct molecular properties such as unusual ligation schemes of adducts[179] or molecular self-assembly[306]. Hence, a prerequisite for the development of a (technological) application is the understanding and control of properties of individual molecules at the molecular and even the atomic scale. This implies that conformational characterization is essential. The experimental techniques for molecular nanoscience at interfaces employed so far are mainly STM, STS, X-ray photoelectron spectroscopy (XPS), and near-edge-X-ray absorption fine structure (NEXAFS)[11,12,313]. While XPS can yield averaged information about the chemical state of the macrocycle for example, with STM, topographic and structural investigations of porphyrin arrays as well as single molecules can be carried out in real space. The high lateral resolution of low-temperature STM allows gathering local information at the single-molecule level. The convolution of topography and electronic structure in STM data, however, generally prohibits a direct interpretation in terms of the sample's geometric shape. Information on molecular conformation could so far only be obtained by synchrotron-based NEXAFS measurements[312], with the drawback of averaging over countless molecules and—most importantly—all molecular moieties, or for specific cases by comparison of STM data with calculated images[239,307,314]. Over the last years, small-amplitude nc-AFM in the form of FM-AFM with CO or other functionalized tips has been established as an extremely powerful and versatile tool for the structure analysis of surface-confined organic molecules in real space[9,36,37,128,288,290,291,299,300,315,316]. Its

capability to resolve individual molecular bonds allows a direct identification of molecular structures[9,36,37,288,315], conformation[316], and even changes thereof upon chemical reactions[37,291,299,300]. So far, FM-AFM investigations have mainly addressed flat species adsorbing (nearly) coplanar to the surface, and merely a few nonplanar molecules were investigated[33,35,37,128,287,316]. However, heavily deformed, flexible molecules like Porphyrins have not been addressed so far.

The geometry of 2H-TPP on Ag(111) (Figure 7.1) and Cu(111) (Figure 7.2) are well-understood in surface science, and their molecular structures have been investigated with a multitude of experimental approaches[11,12]. In a simplified view, the conformation of TPP on a surface is determined by the balance of surface interactions and steric interference of different molecular moieties. The rotation of the phenyl legs is linked to the tilting of the pyrrole units of the macrocycle[317]. Flatter phenyl legs, i.e., small dihedral angles between the legs and the surface plane, cause a stronger deformation of the macrocycle. Vice versa, a planar macrocycle will lead to more upright legs. Upon adsorption onto metal substrates, many porphyrin derivatives adapt a saddle-shape conformation[248,306–312]. The saddle shape describes a tilting of the pyrrole moieties out of the macrocyclic plane. On Ag(111), the aminic pyrroles point toward the surface. Contrary, on Cu(111), the two iminic nitrogens point toward the surface, while the pyrrolic/aminic nitrogens point away from it (compare Figure 7.1 and Figure 7.2). For 2H-TPP on Cu(111) space-averaging NEXAFS measurements of a monolayer coverage indicate out-of-plane rotation angles of $\theta_{phenyl} \approx 50°$ and $\rho_{pyrrole} \approx 20°$ for the macrocycle moieties and the phenyl legs, respectively. Upon self-metalation the macrocycle of Cu-TPP flattens, and the tilt angles of macrocycle and phenyl legs roughly interchange[235,312] and represent a configuration very similar to 2H-TPP on Ag(111) ($\theta_{phenyl} = 53°$, $\rho_{pyrrole} = 25°$[232]). Accordingly, TPP molecules do not comprise any hydrocarbon ring systems parallel or nearly parallel to the surface in contrast to most molecular systems assessed so far in FM-AFM studies. For molecules with a pronounced 3D conformation with many internal degrees of freedom—as in the case of TPPs—a detailed structural characterization is not possible from constant-height FM-AFM images[35]. Nevertheless, constant-height imaging can yield useful information about the molecular conformation. Molecular moieties protruding higher above the surface interact repulsively with the tip at larger distances[37,128,295]. Therefore, conclusions about relative height differences within a single molecule and for neighboring molecules can be drawn from constant-height FM-AFM imaging as also demonstrated recently for porphyrins[31,32,34].

7.1. 2H-TPP on Ag(111): saddle shape

In high resolution STM images, the saddle shape of 2H-TPP on Ag(111) can already be discriminated (Figure 7.1a). The molecule is imaged as an ellipse with central depression (macrocycle) and four protrusions at its periphery (phenyls). Furthermore the macrocycle ellipse features two prominent bulges at the antipodal points of its major axis while the minor axis appears lower. As for porphine, the bulges can be associated with an electronic feature of the macrocyclic hydrogens[232], however they are amplified by the topographic contributions of the higher outer parts of the rotated pyrroles (compare orange parts in the model in Figure 7.1d). Mapping Δf at constant height across individual 2H-TPP on
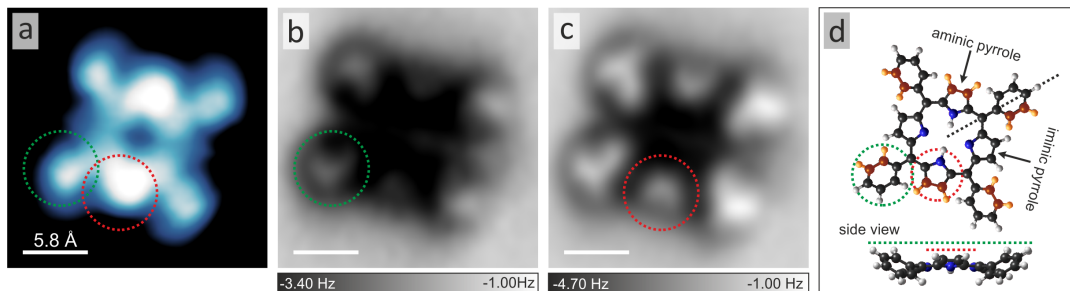
Figure 7.1. Conformation of 2H-TPP on Ag(111). a) High resolution STM image of an individual 2H-TPP. The four legs at the periphery are associated with the phenyl legs, highlighted in green. The red circle indicates a pyrrole. b, c) Constant-height FM-AFM images approaching the surface from $\Delta z = \mathrm{SP} + 1\,\text{Å}$ to $\Delta z = \mathrm{SP} + 0.6\,\text{Å}$. The contrast evolution indicates a saddle shape that is characterized by two pyrroles bending down and two up. The aminic pyrrole points toward the surface and can be associated to the two protrusions above the macrocycle in a). The macrocycle deformation is interlinked with a rotation of the phenyl legs. d) Molecular model sketch in top and side view. Higher molecular parts are dyed orange. The black line in the top view serves as guide to the eye to show the alignment of the substituents with the macrocycle. The colored dotted lines in the side view symbolize the height difference between phenyls (green) and pyrroles (red). Scan parameters: a) $U = 100\,\text{mV}$, $I = 20\,\text{pA}$.

Ag(111) results in the evolution of the contrast from dark areas above the molecule (attractive background) for large tip heights (not shown)[9] to sub-molecular resolution of the molecular structure at close distances, owing to laterally confined repulsive interactions at the molecular bonds that result in a bright contrast[121]. Molecules with pronounced 3D character have been shown to exhibit bright Δf contrast at highest molecular parts first[37,128,295]. In the Δf image recorded with the largest tip–sample spacing, the dark attractive background indicates the outline of each molecule (not shown). Then, the phenyls interact repulsively (see green markers in Figure 7.1b), and at closer distances two opposing pyrroles at the macrocycle follow (red rings in Figure 7.1c). None of the ring systems comprised in the molecular species can be directly imaged with single bond resolution due to four possible constraints: (i) the tilt is too large[37,316], (ii) other moieties might interfere, as for example the pyrroles lie above/below the phenyls (see model in Figure 7.1d), (iii) the necessary tip approach cannot be achieved due to other considerably higher moieties that would cause a tip crash, and (iv) the flexible CO-tip can be influenced laterally by neighboring molecular parts[36]. Although the strong 3D character of the molecules prohibits direct imaging of the entire molecular structure, the evolution of repulsively interacting molecular parts fits very well the saddle-shape conformation and correctly reproduces the dependence of the phenyl rotation and the tilt of pyrrole units qualitatively. Additionally, we showed that the AFM contrast evolution correctly reproduces the phenyl–pyrrole dependencies: A molecule, whose phenyl legs appear bright at a greater distance, has to be approached closer in order to detect the pyrroles. Equivalently, in the picture of the saddle shape, more upright phenyls correspond to a flatter macrocycle[33]. This also means that the relative onset of the corresponding repulsive features is a measure for the macrocycle flatness: the larger the difference, the more upright the phenyls and the flatter the

macrocycle. For 2H-TPP/Ag(111), the order agrees well with a (moderate) saddle shape and the onset of repulsive contrast at each moiety is separated by $\approx 0.2\,\text{Å}$ (cf. dotted lines in model side view in Figure 7.1). For comparison, in the case of Cu-TPP/Cu(111) the relative height difference is larger ($\approx 0.5\,\text{Å}$)[33]. These findings suggest a flatter macrocycle for Cu-TPP/Cu than for 2H-TPP/Ag, which is in good agreement with NEXAFS data[11]. Interestingly, the aminic pyrroles point towards the surface on Ag(111). This was first suggested by the electronic signature of the hydrogens inside the macrocycle[232], and is fully supported by AFM data.

7.2. 2H-TPP on Cu(111): extreme distortion

In STM, 2H-TPP on Cu(111) exhibit a central, elongated protrusion that appears higher than the remaining parts (Figure 7.2a and Figure 9.1). In constant-height FM-AFM data approaching the surface, the sequence for the repulsive features is reversed compared to the silver substrate. Moieties interact repulsively first at the macrocycle where one would expect strongly tilted iminic pyrroles of a heavily deformed macrocycle. Four repulsive spots at the center of the molecule indicate the hydrogen atoms of the iminic pyrroles sticking out furthest from the sample surface (see Figure 7.2c). The remainder of the molecule merely appears as an attractive background. Imaging at closer tip–sample spacing to also resolve the phenyl legs is not possible due to the very upright orientation of the iminic pyrroles. To evade this limitation of constant-height imaging, an activated STM z-feedback can be used to prevent a tip crash while following the surface contour at very close distances (low bias, high current set point). So far, this method was used to determine adsorption sites of molecules on insulating films[316,318]. In the Δf channel (Figure 7.2b) the phenyls can be clearly distinguished as rings in the periphery; however, the structure in the center as described before is lost. Furthermore, the Δf signal may be heavily affected by tip-height variations along the constant-current contour. Nevertheless, this technique can supply very fast (preliminary) structure determination of strongly deformed molecules. The structure of the lower lying parts can be confirmed when omitting the molecular center and inspecting only the periphery in constant height. The phenyl legs feature the ring-shaped contrast (Figure 7.2d) well-known from related, extensively studied flat-lying hydrocarbon cyclic systems[9,37,291,299]. Interestingly, at the long edges of the molecule a three-segment bridge in between two phenyls can be identified. Such a contrast matches expectations for nearly planar pyrroles of the macrocycle. This allows the suggestion that the macrocycle is strongly deformed with the iminic pyrroles strongly tilted upright and the aminic pyrroles nearly flat while the phenyl legs are rotated almost coplanar to the surface. Furthermore, to avoid the repulsive regime of the nearly flat aminic pyrroles' periphery, the legs rearrange parallel to the surface as evidenced by the rectangular outline of the molecules. The in-plane rotation of the phenyls is visualized by the dotted lines in Figure 7.2f. The suggested structure is supported by mapping the minima of $\Delta f(z)$ curves on a dense grid across the entire molecule[128]—see Figure 7.2e. The pertaining map shows two features: In the center, the $\Delta f(z)$ minima appear at a height of $\approx 0.5\,\text{Å}$ consistent with the iminic pyrroles sticking out. At the positions of the phenyl legs, the minimum values are $\approx 2\,\text{Å}$ closer to the sample, and the contrast is very homogeneous. The reduced contrast within this area is in line with the phenyl rings being
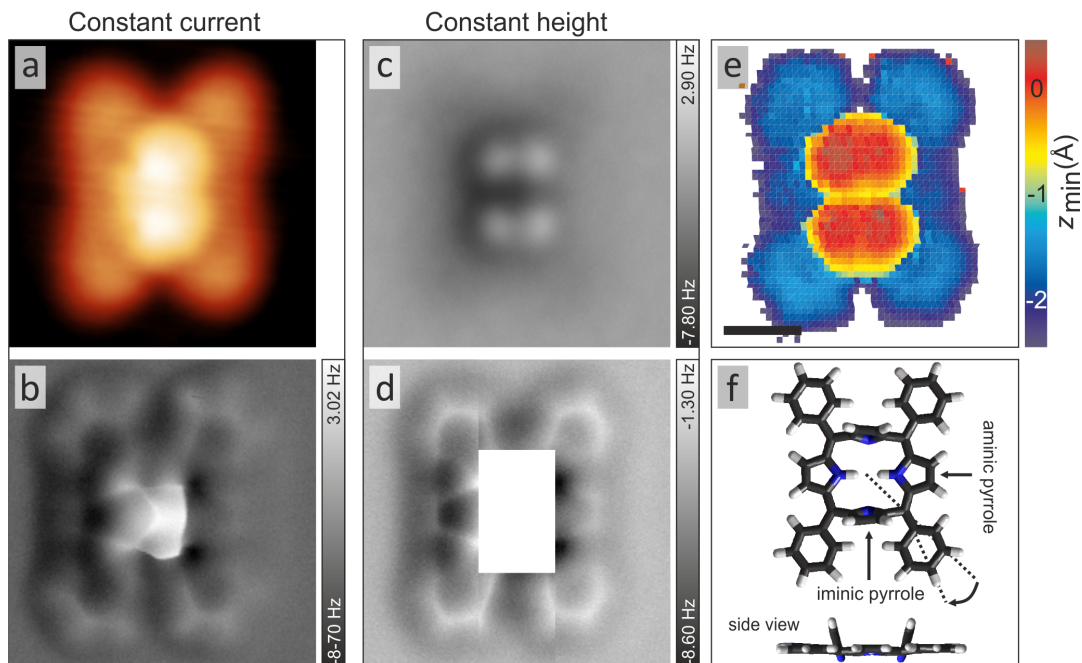
Figure 7.2. Conformation of 2H-TPP on Cu(111). (a) Constant-current STM data . (b) Δf channel recorded simultaneously to the topography depicted in (a): four phenyl rings can be identified in the periphery, while the structure in the center cannot be resolved. (c) Constant-height Δf image: Only four point-like spots at the center of the molecule interact repulsively with the tip in agreement with the four hydrogen atoms of the two iminic pyrrole rings sticking out furthest from the sample. (d) Composed constant-height Δf image from four scans omitting the central area of a molecule deposited onto a sample held at room temperature. All molecular moieties shown in this image appear flat and parallel to the sample surface. (e) Map of vertical positions of minima in $\Delta f(z)$ curves. The phenyl rings appear to be (almost) parallel to the sample surface. The z_{min} values at the positions of the upright pyrrole rings appear at ≈ 2 Å larger tip heights as compared to the rest of the molecule. At white pixels the minimum was not reached. A z_{min} value of zero corresponds to an STM SP of $U = 100$ mV, $I = 2$ pA on copper. Scale bars are 5 Å . (f) Molecular model of 2H-TPP as derived from experimental insights: The molecule is (almost) flat except for the two iminic pyrroles. The exact tilt angle of the upright iminic pyrroles could not be deduced from our experiments, which is therefore depicted with blurriness. Scan parameters: a) $U = 5$ mV, $I = 23$ pA; c) SP: $U = 100$ mV, $I = 2$ pA; 0.8 Å retracted from SP $U = 5$ mV, $I = 50$ pA.

coplanar to the surface. In addition, the contrast at positions of the aminic pyrroles is flat and shows very similar values as for the phenyl legs. We note that a quantitative comparison of minima positions in $\Delta f(z)$ curves between phenyl legs and iminic pyrroles is not possible due to the different chemical species at different positions of the molecule interacting with the tip. The findings of very upright iminic pyrroles and planar legs are consistent with NEXAFS data on 2H-TPP/Cu(111)[312]; however, the nearly flat orientation of the aminic pyrroles is revealed in this study for the first time. The resulting conformation represents an extreme case for distortions of surface-confined tetrapyrrole species[11,319] though further studies are required to completely disentangle its intricate

nature and potential role or appearance in 2D assemblies.

A chemical reaction can be ruled out as cause of the (nearly) flat phenyls for 2H-TPP/Cu(111) as planarized TPP species that underwent cyclodehydrogenation appear distinctly different (see Section 9). The adsorption geometries described above for TPP on Ag(111) and Cu(111) correspond to two different states. It has been shown before that the related tetrapyrrole species can adapt two different conformations upon adsorption onto metal substrates[31,32,34,320,321]. However, the structural assignment was based on STM data that convolutes topography and electronic structure and require model calculations for data interpretation. Theoretical support is also essential for space-averaging NEXAFS measurements to disentangle the contributions from different molecular moieties if the individual resonances overlap[312]. In contrast, high-resolution FM-AFM can provide direct access to the adsorption conformation and to the orientation of molecular moieties in real space and is therefore an ideal tool for the investigation of strongly deformed molecules with multiple degrees of freedom.

Summary and outlook

Summarizing, this section presented different adsorption geometry of individual 2H-TPP on Ag(111) and Cu(111). On Ag(111) the expected (moderate) saddle shape was identified. On Cu(111) however, the molecules adopt a conformation with an extremely deformed macrocycle along with nearly flat phenyl legs. The experimental findings refine the understanding of the molecular systems and provide information neither accessible by STM imaging nor space-averaging experiments. A more detailed study of the adsorption geometry of Cu-TPP and 2H-TPP in cold preparations ($\approx 10\,\mathrm{K}$) can be found in reference [33]. Therein, constant height imaging is complemented by comprehensive $\Delta f(z)$ spectroscopy in the form of vertical images. Vertical imaging allows the deduction of structural information along the surface normal and can give high resolution, quantitative vertical information. For example, the elevation of the central copper ion by $\Delta h_{Cu} = 0.5\,\text{Å}$ could be detected as result of a conformational adaptation of Cu-TPP[33]. FM-AFM can therefore be employed as a powerful tool for the structural analysis of strongly deformed molecules with a pronounced 3D character—in many cases without requiring sophisticated simulations for data analysis. By employing $\Delta f(z)$ spectroscopic techniques the tilt angle of molecules can be determined[37,128]. It is thinkable that similar techniques can give information about the tilt of molecular moieties only, which would help to directly determine the rotation of the phenyl legs for example.

Synthesis of covalent nanostructures and single molecule chemistry

Interfacial molecular nanoscience aims to develop synthesis protocols for the bottom-up engineering of functional, low-dimensional architectures[20,322]. An example was already given in Section 6 that characterized the formation of extended organo-metalic networks from individual porphyrins linked by metal adatoms. Other approaches rely on different intermolecular interactions and assembly protocols as for example weaker organic interactions mentioned in Section 6.1 or stronger covalent coupling[322,323]. Covalent coupling is recognized as promising approach for the preparation of stable, surface-confined structures by linking precursor molecules into extended nanoarchitectures. This approach is especially useful for carbon-based materials. Synthesis of carbon-based structures by (cyclo-) dehydrogenative reactions of precursor molecules is a readily employed approach in on-surface chemistry. Often, the synthesis is based on thermal activation of C–H bonds that lead to ring-closing and -fusing reactions as well as linear C–C links[24,184,324–327]. The recipe can be applied to form a large variety of structures from complete monolayer sheets[328] down to single molecules[324].

Promising building blocks are tetrapyrroles such as porphyrins as they serve as extremely versatile building blocks for 2D architectures[11,12,185]. It is possible to synthesize conjugated porphyrin arrays[184] and to combine them with functional materials such as graphene[24]. Usually porphyrins are processed in wet-chemical techniques. On the other hand, in-vacuo heterogeneous nanochemistry bares the potential for creating compounds not achievable in homogeneous approaches due to the catalytic properties of the surface[233,235] or because the reactivity of intermediate or final products prohibits their handling[289,290,329]. Therefore it is reasonable to employ surface science approaches for the investigation and/or the synthesis of novel porphyrin-related molecules and surface-confined structures.

The following sections present combined LT-STM and FM-AFM studies of surface-assisted, porphyrin-based synthesis of covalent nanostructures and single molecule nanochemistry.

8. Dehydrogenative homocoupling of porphine molecules

The templated synthesis of porphyrin dimers, oligomers, and tapes has recently attracted considerable interest due to their tunable electronic gap and promise for photovoltaic devices. A clean, temperature-induced covalent dehydrogenative coupling mechanism between unsubstituted free-base porphine units yielding dimers, trimers, and larger oligomers directly on a Ag(111) support under ultrahigh-vacuum conditions was introduced by Wiengarten et al.[184] This sections presents a detailed FM-AFM structure analysis of covalently fused porphine dimers synthesized by in-vacuo on-surface synthesis and complements the work of Wiengarten et al.[184]. Here for the first time, the porphine coupling motifs are determined in real space (Figure 8.2), moreover an unreported reaction intermediate is identified, and an outlook toward the synthesis of porphine functionalized graphene is given.

Introduction

Free-base porphine (2H-P) is the simplest porphyrin unit and consists only of the tetrapyrrole macrocycle containing two hydrogens. A model is depicted in Figure 8.1c. Due to its comparably low number of atoms, it is often implemented as model system for theoretical studies of porphyrin properties as e.g. metalation[330]. Likewise, it constitutes an ideal prototypic macrocyclic compound for experimental studies of fundamental characteristics of surface-anchored porphyrins and to clarify the influence of (meso-)substituents[167,331–333]. Additionally, 2H-P itself is a very interesting module for two- and three-dimensional nanoarchitectures[184,334]. Conjugated one-dimensional arrays of porphine macrocycles— so called porphine tapes—have been recognized as light harvesting material exhibiting a steadily decreasing band gap as a function of tape length[335,336] and furthermore featuring interesting non-linear properties[337,338]. Here again, it can be instructive to reduce the system of interest to a simplified unit: a dimer formed by covalently linking two porphines[339–341]. Porphyrin oligomers are usually synthesized and characterized in solution-based approaches[340,342]. However, especially for (opto-)electronic applications it is desirable to directly contact the molecular entities with conducting (metal) electrodes for their integration in electrical circuits. The molecule–electrode interface can however influence molecular properties through charge transfer[167], conformational adaptations (vide infra Section 7) and other effects. Therefore a surface-confined characterization in a well-defined UHV environment is desirable for understanding molecular systems with promise as building block in molecular electronic devices.

8.1. Adsorption of 2H-P and interfacial homo-coupling on Ag(111)

Unlike many other porphyrin derivatives (as e.g. described in Section 6), porphines do not self-assemble into regular organic islands, but adsorb as individual units on Ag(111) even in room temperature preparations as depicted in Figure 8.1e. Considerable substrate–adsorbate interactions cause a charge transfer from the substrate to the molecule and lead to repulsive molecule–molecule interactions[167]. In STM the macrocycle appears square-like with two protrusions with and a central depression (Figure 8.1). The protrusions can be associated with the electronic fingerprints of the inner hydrogens[167], but do not represent a topographic effect as for example for 2H-TPP (see Section 7). Instead, 2H-P adsorbs flat, i.e. with the macrocycle plane coplanar to the surface. A flat adsorption and a flat molecular conformation manifests as equally evolving atomic bonds across the whole molecule in constant height AFM data approaching the surface (Figure 8.1e, f). The porphine structure can nicely be identified in these Δf maps. The pyrroles show as five-member rings interconnected by a kink that corresponds to the methine bridge. Bright lines sticking out perpendicularly from the molecular edge can be associated to the peripheral hydrogens. Interestingly, the inner hydrogens cannot be identified: 2H-P appears fourfold symmetric in AFM. In contrast, the electronic effect of the hydrogens break the symmetry in STM. On a side note, please take a detailed look at the center of both porphine units in Figure 8.2g. While the right porphine exhibits a dark center, the left one is bright. The same contrast difference can be seen in the porphine units in Figure 8.2j, k in comparison to the individual molecule. The difference is tentatively assigned to the adsorption site. 2H-P adopts a preferred adsorption with the center of the molecule above a bridge site[167] which then shows as dark molecular center in Δf maps. Therefore a bright AFM contrast might allow the assumption that the adsorption site differs. For more details on the adsorption and characterization of 2H-P please see reference [167]. After heating the sample to 570 K for 20 min, a high yield of triply fused dimers and oligomers is achieved as shown in Figure 8.1f and Figure 8.2. The only reaction byproduct of the coupling is hydrogen, which desorbs from the surface at the given preparation conditions. Therefore the tape synthesis does not involve surface contamination through byproducts, in contrast to many reactions involving halogen leaving groups[343].

8.2. Structure analysis of dimeric units

In STM, repeating dimeric units can be identified. However, the intermolecular bond formation remains elusive. For the first time, the porphine coupling motifs are directly determined in real space (Figure 8.2) and moreover an unreported reaction intermediate is identified (Figure 8.2m–p). The coupling leads to three distinct coupling motifs between neighboring 2H-P units exemplified by the dimers in Figure 8.2. Motif 1 is formed by the dehydrogenation of three neighboring carbon atoms per molecule and the formation of three covalent C–C bonds between *β-β*, *meso-meso*, *β-β* atomic positions. The atomic positions are labeled in Figure 8.1. Motif 1 results in collinear porphine units and straight oligomers. Motif 2 (*meso-β*, *β-meso* bonding) is assigned to the dehydrogenation of two carbon atoms per molecule forming two covalent C–C bonds. It can be obtained from
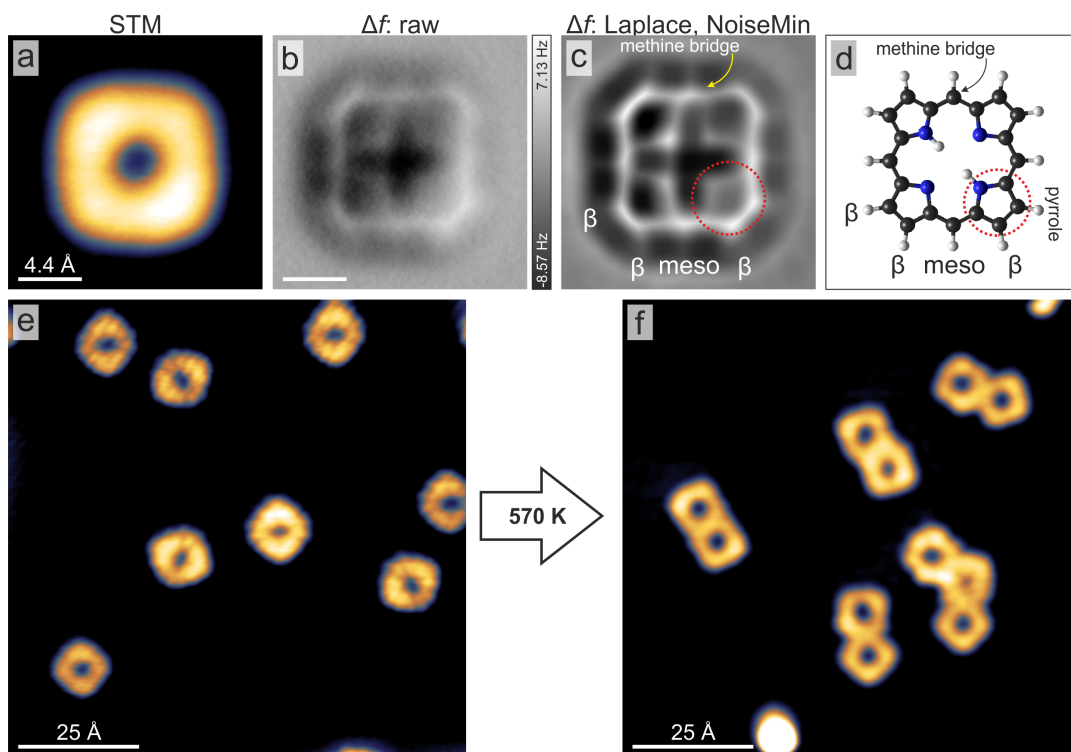
Figure 8.1. Dehydrogenative homocoupling of porphine molecules. a) STM image of an individual 2H-P with square-like appearance. Protrusions are located in the upper left and lower right corner. b) Δf image and c) its processed version. A pyrrole ring is highlighted by a red circle. d) Model of 2H-P. The peripheral carbon positions are denoted by "β" at the pyrroles and "*meso*" at the methine bridges in between. e) Overview image of a low coverage of porphine molecules on Ag(111). The molecules interact repulsively and adsorb as individual units. f) When heated to 570 K, porphines form covalently coupled oligomers. Scan parameters: a) $U = 200\,\mathrm{mV}$, $I = 70\,\mathrm{pA}$; b) SP from a), $\Delta z = -0.2\,\text{Å}$; e) $U = 100\,\mathrm{mV}$, $I = 80\,\mathrm{pA}$; f) $U = 150\,\mathrm{mV}$, $I = 10\,\mathrm{pA}$.

motif 1 by laterally shifting one molecule by one bond. For motifs 1 and 2 the constituent units are oriented along the same direction with respect to the underlying substrate[184]. Binding motif 3 (β-β, *meso*-β) is associated with two covalent C–C bonds between rotated porphines. Furthermore, motif 3* —mentioned by Wiengarten et al., but not observed— could clearly be identified. It features a single β-β bond between two porphines in the same adsorption orientation. The units are therefore strongly laterally shifted against each other. Contrary, solution-based approaches describe the porphyrin polymerization as a multistep process that proceeds via *meso*–*meso* linked oligomer intermediates[340,344] owing to relatively better stability of the β-C–H bond compared to the *meso*-C–H bond[342]. Therefore, the occurrence of motif 3* is surprising and the relative bond stability for porphines is apparently not fully sustained on the surface. C–H bond cleavage can occur at the *meso*- and β-positions, and not exclusively at the *meso*-C. For surface-assisted porphine oligomerization, the reaction pathway was suggested to be a multistep process[184]. An initial dehydrogenation produces monomeric radicals that diffuse across the surface
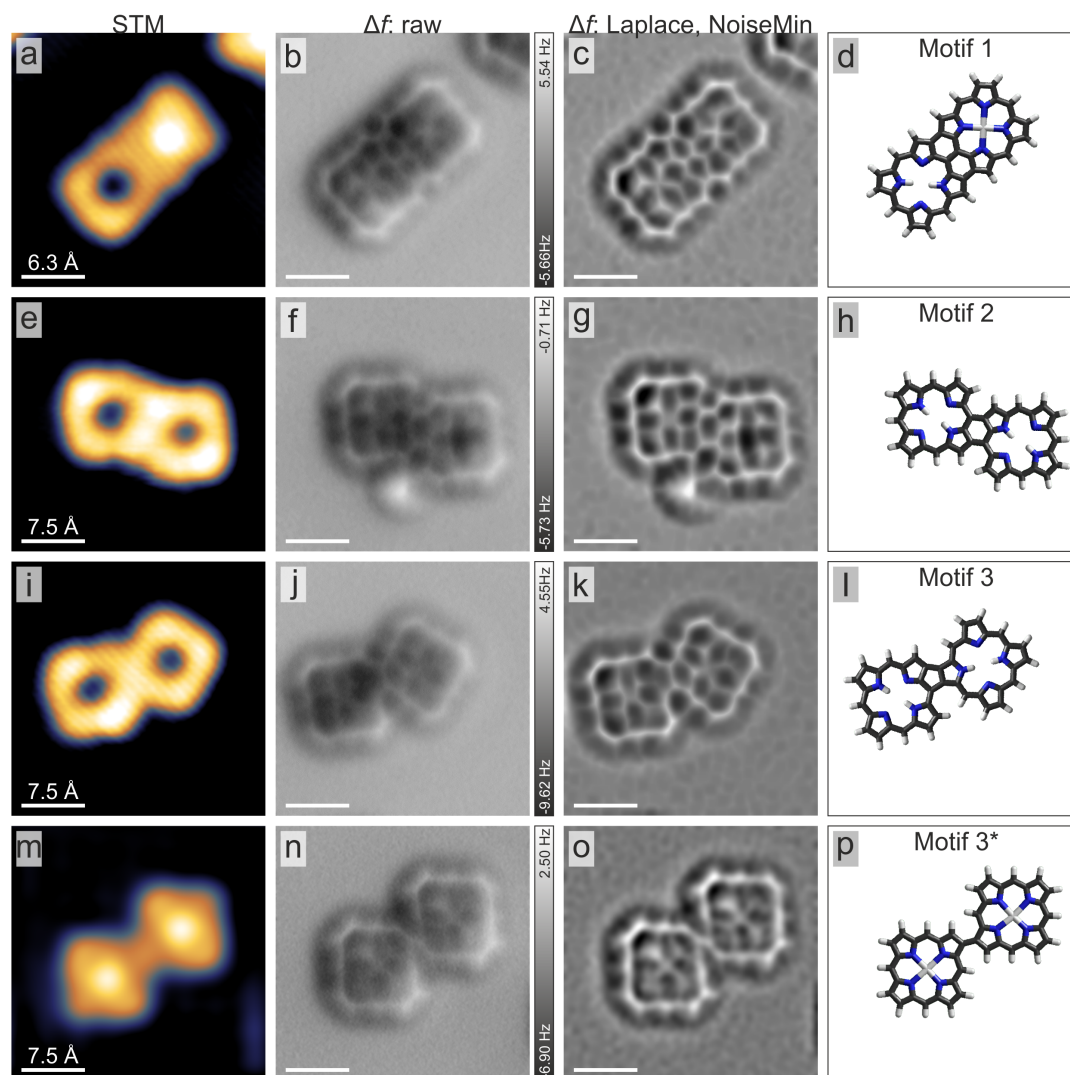
Figure 8.2. Structure analysis of porphine dimers. a–d) Porphine tape fused with β-β, *meso-meso*, β-β binding motif 1. e–h) Dimer motif 2 exhibiting *meso*-β, β-*meso* bonding resulting in a laterally offset between the two units. i–l) Motif 3 features β-β, *meso*-β bonding with one rotated species. m–p) Dimer stabilized by a β-β single bond, referred to as motif 3*. The data type presented is indicated above each column. The Δz approach is always given with respect to the STM SP in the first column. Scan parameters: a) $U = 200\,\text{mV}$, $I = 70\,\text{pA}$; e, i, m) $U = 200\,\text{mV}$, $I = 50\,\text{pA}$; b, f, j) $\Delta z = -0.6\,\text{Å}$; n) $\Delta z = -0.8\,\text{Å}$.

and subsequently couple with each other. The observation of the singly coupled dimer strongly supports this picture. Motif 3* can be considered as reaction intermediate. For a dimer stabilized by motif 3*, one of the constituting units can rotate around the newly formed C–C bond, i.e. "folding" toward a planar configuration, bringing the four adjacent unreacted C–H bonds to close proximity and yielding a straight dimer (motif 1) via a cyclodehydrogenation process[345]. As an alternative pathway, motif 3* might also be transformed to motif 3 by an in-plane rotation. Both mechanisms imply a liftoff of the

porphine units from the surface either during the *meso-meso,* bond formation or the folding process. This assumption is realistic, as the 2H-P desorption readily happens at the applied substrate temperature[184]. Other bonding motifs expressing single C–C bonds were not observed. Most likely, the full dimerization is energetically strongly favored for all other intermediate configurations. For more details on the reaction pathway, please see reference [184]. However it should be noted that the observation of motif 3* has to be taken with care for the following two reasons. Neither STM nor AFM data can clarify whether the *meso*-position underwent deprotonation as well, but did not engage in covalent coupling. Furthermore, all motif 3* units seem to involve metalized porphines. The metal center might change the reaction energetics and bond stabilities.

8.3. Adsorption height changes induced by chemical modifications of the macrocycle
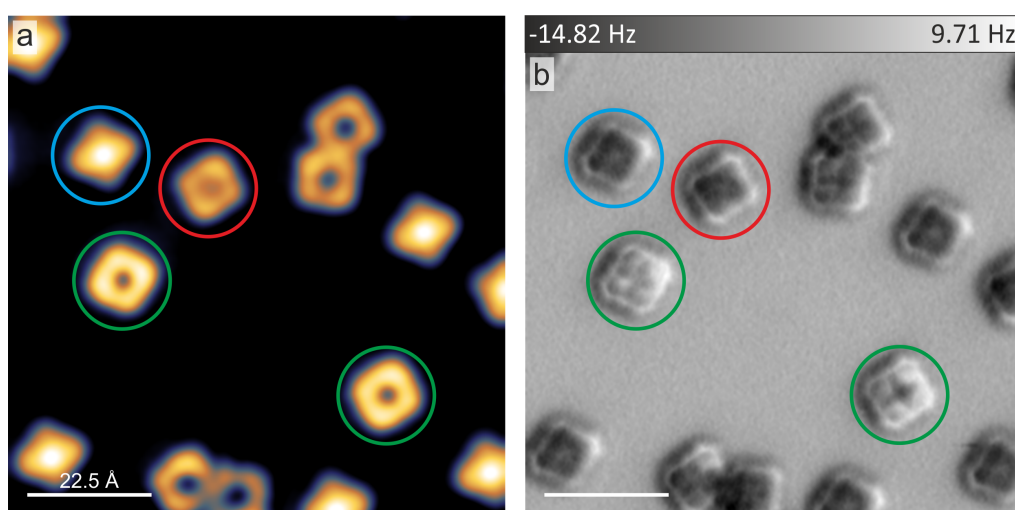
Figure 8.3. Adsorption height of porphine species. a) Overview image comprising individual 2H-Ps (green, red), dimers, and metalated porphines (blue). b) In constant height AFM data approaching the surface, the non-reacted species (green) develop bright repulsive feature at the center of the pyrroles at larger tip–sample distances. This suggests a larger adsorption height. Scan parameters: a) $U = 200\,\mathrm{mV}$, $I = 50\,\mathrm{pA}$; b) SP from a), $\Delta z = -0.9\,\text{Å}$.

The intermediates of a stepwise surface-confined oligomerization should be observable if their lifetimes result in a considerable probability to remain on the surface over the timespan from formation until cool-down and transfer to the SPM analysis chamber. As argued above this is probably not the case for other singly coupled dimers. However, deprotonated monomers should be found on the surface for the given preparation conditions as individual units remain on the surface and dimer formation has occurred. It seems unlikely that every deprotonated monomer had reacted or that always an even number of radicals were formed. However unreacted, deprotonated porphines do not show a clear difference in STM data[184]. AFM on the other hand can be sensitive to unsaturated carbons, because molecules often bent downward due to the formation of a covalent bonds to the surface

as described in detail in Section 10. Figure 8.3 shows an overview Δf scan. The image is extracted from a series of constant height images approaching the surface. In such series, molecules with larger adsorption height interact repulsively first and likewise, bright Δf artifacts inside carbon-based ring systems like pyrroles appear first for the higher adsorbates. Such features within rings are caused by very small tip–sample separations that result in image artifacts due to relaxations of the CO at the tip[36]. Therefore the overview scan allows conclusions about relative adsorption heights. Figure 8.3 includes individual porphines (green, red), self-metalated Ag-P[184] (blue), and dimers. Repulsive features are only discernible at 2H-P by their obviously brighter appearance (green). A further approach of $\approx 0.3\,\text{Å}$ is required to establish similar repulsive features at all other species. This allows the conclusion that the adsorption height changed upon chemical modifications of the macrocycles: the molecules are pulled toward the surface after metalation and dimerization. Consequently, this would also indicate a changed molecule–substrate interaction. Interestingly, individual units exhibiting smaller adsorption heights can be distinguished (red). In STM however they appear very similar to 2H-P with two protrusions and a central depression, excluding a deprotonation inside the macrocycle. This leaves two possibilities: either 2H-P can be driven into a closer adsorption by annealing or these species could be radicals whose enhanced substrate interactions pull the whole molecule toward the surface. Further investigations as for example tip-induced deprotonation experiments as described in Section 10 in combination with Δf spectroscopy[33,37,128,287] as presented in Section 7 are needed to draw definite conclusions with quantitative results. Regardless of the interpretation for porphine, the presented FM-AFM data clearly exhibits differences in adsorption heights caused by chemical modifications and therefore allows conclusions about changes in the substrate–adsorbate interactions. Such insight is usually non-trivial to obtain for one given species on a multi-species sample and requires massive theoretical modeling including the metallic support, and/or considerable effort with multi-technique approaches. To my knowledge this is the first report showcasing FM-AFM as powerful technique for the direct detection of relative adsorption height changes on the single molecule level.

Summary

The FM-AFM investigations presented above proved the structural models suggested by Wiengarten et al.[184] right by directly imaging covalent bonds. Furthermore the observation of the reaction intermediate motif 3* strongly supports a stepwise reaction mechanism for the oligomerization of porphines on Ag(111). The results therefore represent important supplementary information to previously published data. Additionally this section impressively demonstrates the capabilities of FM-AFM with functionalized tips. While Wiengarten et al. put much effort in a multi-technique approach to determine the flat adsorption geometry and to suggest dimer structures, the AFM data presented here gives direct experimental proof with little effort and can even yield deeper insights, as for example changes in adsorption height. Furthermore, the AFM capabilities for direct imaging of chemical bonds can be applied to nanostructures that do not allow a simple interpretation from STM images. As an example and outlook to covalent porphine nanostructures, Figure 8.4 depicts the functionalization of graphene edges by addition of a porphine[24].

Such covalent coupling of functional molecular units enables new routes to create hybrid systems in which individual components perform specific functions. In the case of graphene/porphine, graphene represents a charge transport material that contacts functional porphyrin units and would therefore guarantee electrical contact even after transfer to insulating substrates. Furthermore, the functionality of the porphines is not suppressed. For example, their ability for metalation and gas ligation is preserved. For the full publication please see reference [24].
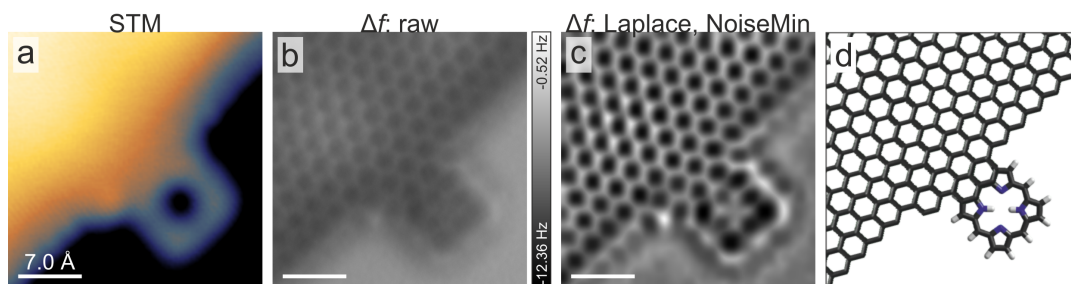
Figure 8.4. Covalent coupling of porphine to graphene edges. Scan parameters: a) $U = 180\,\text{mV}$, $I = 70\,\text{pA}$; SP from a), b) $\Delta z = -0.2\,\text{Å}$.

9. Cyclodehydrogenative flattening of porphyrins

On coinage metal surfaces, a cyclodehydrogenation reaction can be thermally activated in 2H-TPP. The reaction fuses the phenyl legs to the macrocycle accompanied by flattening of all molecular moieties producing planarized porphyrin derivatives (PPDs). Herein, FM-AFM investigations with CO-functionalized tips characterize all PPDs structurally on Cu(111) and Ag(111) by visualizing the intramolecular bonds. The results will clarify the outcome of ring-closing reactions in single porphyrins that have recently been addressed in several studies and led to contradicting conclusions[324,346–351]. Furthermore, the reaction pathways of simultaneous flattening and self-metalation reactions on Cu(111) are elaborated.

Introduction

As already mentioned, porphyrins bare great potential for functional nano-architectures regarding their intriguing properties in nature and technical applications. Additionally they serve as model systems to investigate on-surface chemical reactions. For example a study on surface-assisted cyclodehydrogenation of tetraphenylporphyrins (TPP) on Ag(111) demonstrated how the symmetry of the educts influences the relative yields of the products[324]: The TPPs adopt a saddle-shape adsorption geometry on silver with four upright phenyl rings. Upon heating a ring-closing reaction occurs between the phenyls and the macrocycle resulting in completely planarized species. The fusing of the phenyls can occur at different positions leading to four possible products (Figure 9.1 a). While the twofold symmetric free-base TPP (2H-TPP) exhibits a strong preference for one final species, the fourfold, metalated derivative does not. Therefore the selectivity of the reaction can be greatly enhanced by reducing the symmetry[324].

Chemically, reaction selectivity is of great importance for the efficiency of a given process and can reduce unwanted byproducts significantly. It therefore has important implications for the development of future catalysts and for (industrial) applications. In on-surface, heterogenous catalysis important factors for selectivity include surface reactivity[352] and structure[353], as well as the molecular geometry[345,354–356]. In the case of TPP/Ag(111), the surface however was ruled out to have a significant influence on the outcome[324]. Contrary, this section will demonstrate a distinct influence of the underlying substrate for the outcome of the cyclodehydrogenative flattening of 2H-TPP on Cu(111) that overrides the effects of molecular symmetry observed on silver.
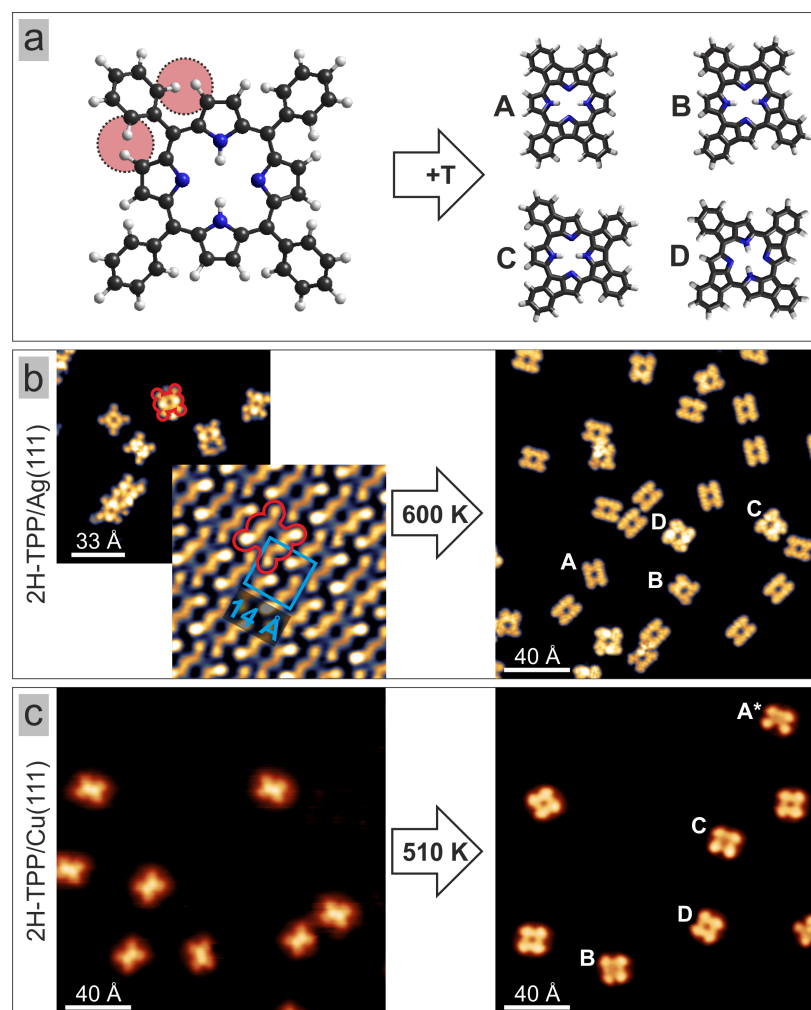
Figure 9.1. Overview of thermally activated formation of PPDs by fusion of the phenyl substituents to the macrocycle. a) Model of 2H-TPP (left) and planarized porphyrin derivatives (PPDs) denoted by **A**–**D** (right). PPDs are synthesized by the formation of a second C–C bond between the phenyl legs and the macrocycle. Each leg has two possible sites for bond formation as indicated in red. b) Overview STM images before (left) and after (right) annealing 2H-TPP on Ag(111). When deposited on a cold surface (≈ 80 K), individual molecules can be investigated (left, image in the back). Warmer preparations lead to the formation of organic arrays (left, image in front) with square unit cell of side length 14 Å (cf. blue square). One molecule is outlined in red. After annealing to 600 K PPDs form on Ag(111) (right hand side). c) Overview STM images before (left) and after (right) annealing 2H-TPP on Cu(111). The strong surface–adsorbate interaction inhibits aggregation into organic islands for low coverages of 2H-TPP on Cu(111) and individual molecules can be observed (left). The right hand side depicts planarized species after heating the sample to 510 K. Species **A** was not observed on Cu(111), but only a related fragment **A*** that is discussed in detail in Section 10. Scan parameters: c, top) $U = -0.66$ V, $I = 0.3$ nA; c, bottom) $U = 100$ mV, $I = 20$ pA; d) $U = -100$ mV, $I = 50$ pA; e) $U = 20$ mV, $I = 0.2$ nA; f) $U = -1000$ V, $I = 30\,000$ pA.

9.1. Overview of cyclodehydrogenation reactions

Figure 9.1 shows overview images before and after flattening reactions of free-base TPP on Ag(111) and Cu(111) alongside models of the species before and after. TPP has four phenyl legs attached via single C–C bonds at the meso positions of the macrocycle (Figure 9.1a). As indicated in red at the model, each phenyl leg can react with the macrocycle at two positions to form a second C–C bond, which is equivalent to a ring-closing reaction under release of H_2—known as cyclodehydrogenation. The cyclodehydrogenation results in an alignment of the phenyl leg in the macrocycle plane, accompanied by a flattening of the corresponding pyrrole. This finally produces completely planarized species. The various combinations for all substituents lead to four possible PPDs **A**–**D**. The denomination follows the work of Wiengarten et al.[324].

Figure 9.1b shows 2H-TPP on Ag(111) after deposition onto a sample held at $\approx 80\,\mathrm{K}$ (left, image in the back) and after room temperature deposition (left, top image). Only when the molecules are deprived of thermal energy for diffusion they can be found as individual units on silver. Otherwise TPPs assemble into extended, close-packed organic islands with a square unit cell of side length $a = 14\,\text{Å}$[248] as highlighted in blue in Figure 9.1b. The arrays are stabilized by attractive T-type intermolecular interactions between neighboring phenyls[248,357,358]. The image at cold preparations helps to identify individual molecules and allows a comparison of the molecular conformation to 2H-TPP/Cu(111) (Figure 9.1c left). One single molecule is encircled in red. Heating to $600\,\mathrm{K}$ for $10\,\mathrm{min}$ triggers a cyclodehydrogenation as described above and all four PPDs can be observed (right hand side of Figure 9.1b). However, the formation of **A** is clearly favored (86 %), followed by **B** (12 %) and almost negligible portions of **C** and **D** (Figure 9.4). The statistics for the silver case are taken from Wiengarten et al.[324]. Due to the flat phenyls, T-type interactions can no longer stabilize molecular arrays and the islands disintegrate into individual units. Although the situation in overview images resembles 2H-P/Ag(111) as described in Section 8, PPDs do not interact repulsively[324].

The deposition of 2H-TPP on Cu(111) yields individual species even at room temperature due to pinning of the molecules by strong substrate–adsorbate interactions (left hand side of Figure 9.1c). As described in detail in Section 7 the surface interactions also leads to nearly flat phenyls accompanied by an extreme macrocycle deformation. Annealing to $510\,\mathrm{K}$ for $5\,\mathrm{min}$ results in PPDs (right hand side of Figure 9.1c). Surprisingly however, **A** was not found on Cu(111). Instead, pincer-like species **A*** with a missing pyrrole could be identified (see Figure 10.1) and will be discussed in detail in Section 10. For high coverages on Cu(111) ($> 0.56\,\mathrm{molecules/nm^2}$), a hierarchic reaction sequence was reported in which a metalation occurs before dehydrogenation and primarily leads to the formation of **D**[348]. In the very low coverage regime investigated here ($0.02\,\mathrm{molecules/nm^2} - 0.05\,\mathrm{molecules/nm^2}$), the reaction exhibits a preference for the same outcome (**D**: 59.5 %), but no strongly pronounced selectivity. Moreover, in STM data the PPDs can express a bright or a dim center (Figure 9.3) indicating simultaneous and competing metalation and flattening reactions for the low-coverage investigated here (vide infra).

9.2. Structure determination of PPDs

The herein presented high-resolution FM-AFM data directly image the molecular structure of the PPDs for the first time. They confirm the models based on STM images originally suggested by Wiengarten et al.[324] and clarify the outcome of flattening reactions reported recently[324,346–351]. All species were imaged multiple times with different tips and did not differ. Therefore the structures presented in Figure 9.2 are assumed to underlie the STM data presented in the first row. Similar to the contrast formation at the center of the macrocycle of porphines (cf. Section 8), the aminic pyrroles cannot be distinguished from the pyrrolic ones and a central cross structure is visible. However these bright lines in Δf—usually associated with a chemical bond—are most likely scan artifacts. Such "ghost-bonds" are caused by relaxations of the flexible CO induced by the potential landscape of surface features[125,194,195,296,297]. Assuming that all PPDs are completely planar, their horizontal molecular plane represents a mirror plane. Depending on the configuration of the fused phenyls different symmetries can be deduced: **A** belongs to the D_{2h} symmetry group; **B** only exhibits said mirror plane and its symmetry is reduced to C_s; **C** has C_{2v} symmetry; and **D** C_{2h} with protonated macrocycle and C_{4h} when metalated. According to the number of additional mirror planes, **A** is referred to as twofold symmetric, **C** as symmetric, and **B** and **D** as asymmetric. The positions of the hydrogens at the models in the last column of Figure 9.2 follow the energetic preferences observed in DFT ground state calculations in reference [324]. In the model top view in Figure 9.1, the two possible reaction sites for one phenyl can be assigned a rotational direction—clockwise or counterclockwise. Accordingly, the asymmetric derivatives express chirality and both enantiomers can be observed (cf. Figure 9.2b, e and Figure 9.2g).

Metalated and free-base PPD on Cu(111) and Ag(111) can be discriminated by the STM contrast at the molecular center. Non-metalated species exhibit a central depression, metalated ones a protrusion[184,332,351]. This is obvious by eye and is supported by minima/maxima in line profiles. The white curves that are overlaid onto the STM data in Figure 9.3 exemplary depict the apparent height across the molecular centers of the corresponding molecules. Profiles across free-base species exhibit a central minimum, metalated species on the other hand express a maximum at the center. Interestingly, in constant height Δf images the chemical state of the macrocycle can hardly be discriminated, but both metalated and free-base PPDs appear very similar at the center [compare Figure 9.3c (Figure 9.3d) vs. Figure 9.3f (Figure 9.3g)]. Line profiles in Δf data nevertheless do exhibit a similar trend as in STM images. The metalated species features a (local) maximum at the center (Figure 9.3f). However the central Δf maximum is lower than the C–C bond of the pyrroles to the left and right and therefore clearly does not dominate the image contrast as in STM. The central protrusion in STM therefore is primarily of electronic nature and does not reflect the topography.

9.3. Statistical analysis of flattening reactions

Figure 9.4 presents a histogram of the flattening reactions of 2H-TPP and Co-TPP on Cu(111) and Ag(111). The data for 2H-TPP on Ag(111) are taken from Wiengarten et al.[324], the data for Co-TPP/Ag(111) from Wiengarten[359]. The flattening reaction of 2H-
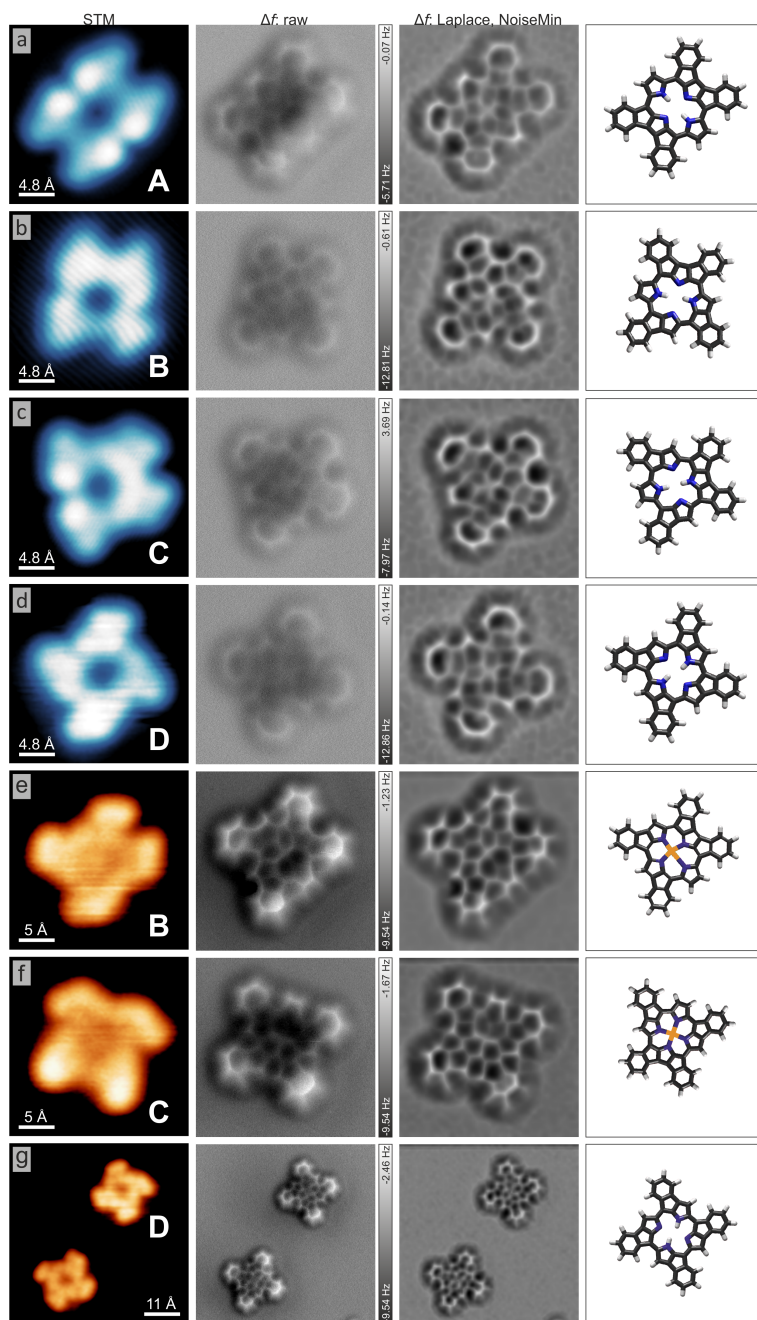
Figure 9.2. Structure determination of planarized porphyrin derivatives of 2H-TPP on Ag(111) (blue color scale) and Cu(111) (orange color scale). The data type presented is indicated at the top of each column. Row a) Twofold symmetric **A** which represents the majority species on silver. Row b) and row e) Asymmetric species **B**. Row c and row f) Symmetrically fused derivative **C**. Row d) and row g) Type **D** that is the preferred PPD on copper. SPM data on Cu(111) depict both enantiomers of **D**. Scan parameters of STM data and setpoint for constant height mode: a, e, m) $U = 500\,\mathrm{mV}$, $I = 50\,\mathrm{pA}$; i) $U = -500\,\mathrm{mV}$, $I = 50\,\mathrm{pA}$; approach Δz for constant height imaging: b) $-2.4\,\mathrm{\AA}$; f, n) $-2.1\,\mathrm{\AA}$; j) $-0.9\,\mathrm{\AA}$.
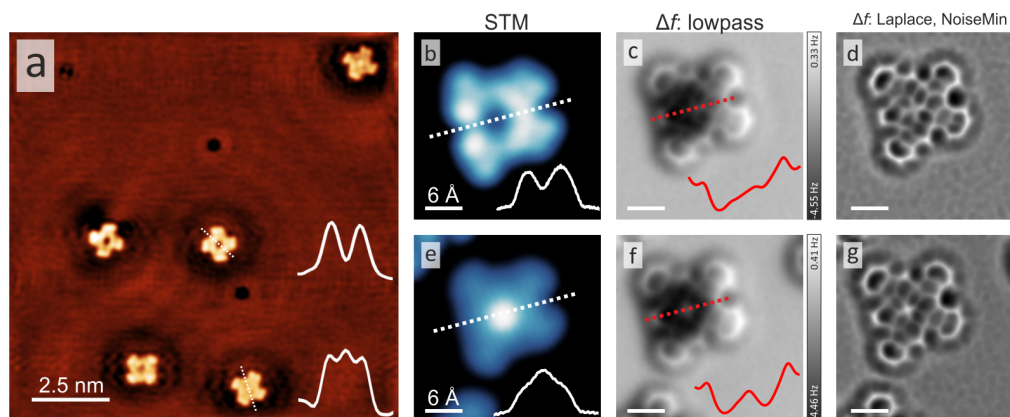
Figure 9.3. SPM appearance of metalated and free-base PPDs on (a) Cu(111) and (b–g) Ag(111). The two chemical states can be differentiated in the STM data at the molecular center. A central metal ion is reflected by a protrusion, the free-base macrocycle by a central depression. The white (red) dotted lines indicate the position of the line profiles that are presented as overlays onto the STM (AFM) images next to the molecules. a) On Cu(111) only **D** was found to occur non-metalated and therefore allows for a direct comparison. In this image **D** occurs exclusively. b–g) Comparison of both states on Ag(111) in STM (b, g) and AFM (c, d, f, g). Scan parameters of STM data and setpoint for constant height mode: a) $U = 100\,\mathrm{mV}$, $I = 6\,\mathrm{pA}$; b, e) $U = -500\,\mathrm{mV}$, $I = 50\,\mathrm{pA}$; Approach Δz for constant height imaging: c, f) $-0.7\,\mathrm{\AA}$.

TPP on Cu(111) is weakly selective for **D** (59.5 %) (light orange bars in Figure 9.4a). For Co-TPP on the other hand, a highly selective outcome for **D** is observed (93.3 %) (framed orange bars in Figure 9.4a). Surprisingly, this finding is different from the same reactions on silver. For 2H-TPP/Ag(111), the flattening expresses a strong selectivity for **A** (86 %)[324] (light grey in Figure 9.4a) while the metalated counterparts Co-TPP[359] (framed grey bars in Figure 9.4a) and Ru-TPP[324] (not shown here) do not express a preferred product. The varying outcome of the same reactions on different substrates therefore has to be related to the surfaces themselves and/or their influences on the adsorbates. Here, especially the distinctly different molecular conformations of 2H-TPP on Ag(111) and Cu(111) (cf. Section 7) could explain the observations as molecular geometry is a key parameter for selectivity in heterogeneous chemistry[345,354–356]. On Ag(111), the reaction selectivity follows gas phase DFT ground state calculations resulting in **A** and suggesting little influence of the substrate on the molecules.[324] In contrast, on Cu(111) the substrate is reported to strongly interact with 2H-TPP adsorbates and cause extreme molecular distortions (Section 7). This substrate influence likely steers the planarization reaction towards **D**. Interestingly, also for Co-TPP the product occurrences diverge for the two substrates, despite a similar saddle-shape adsorption geometry. The choice of the substrate therefore turns out to be decisive for the reaction outcome additionally to molecular symmetry.

Furthermore, the comparison of 2H-TPP on Ag(111) and Cu(111) has to be taken with care. 2H-TPP can form Cu-TPP before or during flattening (vide infra). In general, free-base tetrapyrroles can undergo self-metalation when annealed on a metal surface, i.e. they
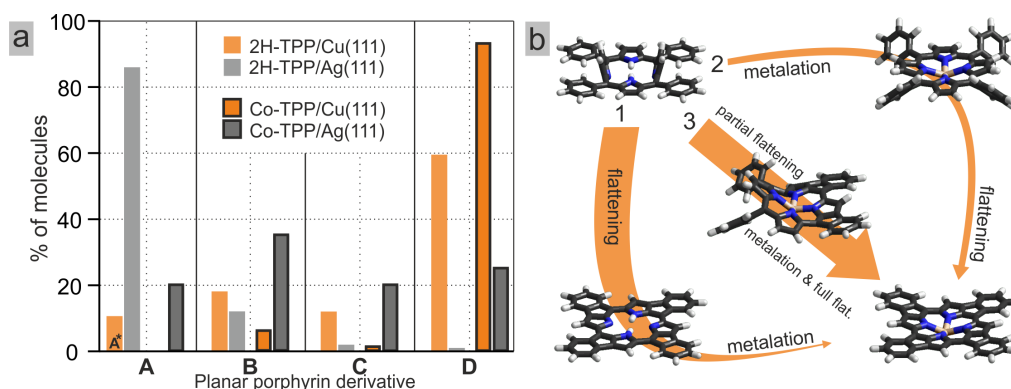
Figure 9.4. Analysis of flattening reactions. a) Statistical analysis of the cyclodehydrogenative planarization of TPP on Ag(111) and Cu(111). Histogram representing the relative occurrences of different PPD from 2H-TPP on Cu(111) (light orange) and 2H-TPP on Ag(111) (light grey, taken from Wiengarten et al.[324]) as well as PPD formed from Co-TPP on Cu(111) (framed orange) and from Co-TPP on Ag(111) (framed grey, adapted from Wiengarten[359]). Several hundred molecules were sampled for all histograms. b) Schematic reaction routes for the formation of PPD on Cu(111). Route **1**: 2H-TPP flattens directly and can metalate thereafter. Route **2**: 2H-TPP self-metalates first only after which Cu-TPP undergoes cyclodehydrogenation. Route **3**: Flattening and metalation occur simultaneously. Some phenyl rings fuse to the macrocycle first to form a partially flattened species that metalates before completing cyclodehydrogenation. The arrow thickness represents the likeliness for each route as observed here. For details see text.

metalate with adatoms supplied by the substrate. On Cu(111) self-metalation of 2H-TPP is well documented[235] with an onset temperature of $\approx 390\,\text{K}$[235]. Self-metalation is likely to occur during flattening experiments as they exceed annealing temperatures of $390\,\text{K}$. This is supported by annealing 2H-TPP/Cu(111) at considerably lower temperatures for longer periods of time ($395\,\text{K}$ for $20\,\text{min}$), which resulted in metalated species, (partially) flattened derivatives (cf. Figure 10.3) and pristine molecules. These findings corroborate an earlier report that describes a simultaneous onset for metalation and flattening for low molecular coverages ($< 0.37\,\text{molecules/nm}^2$).[348] Please note that for high coverages ($> 0.56\,\text{molecules/nm}^2$) a hierarchic reaction sequence is reported in which full metalation occurs before dehydrogenation leading to the formation of mostly **D**[348].

Discussion

While metalated PPDs can clearly be identified, it remains ambiguous when the metalation happened: after (route **1** in Figure 9.4), before (route **2**) or during flattening (route **3**), which complicates the interpretation of the statistical analysis. The three possible reactions routes **1**, **2**, and **3** are illustrated in Figure 9.4b. Please note that this problem does not arise on Ag(111). For silver substrates, self-metalation is only reported for flat tetrapyrroles adsorbing coplanar to the surface like free-base porphine[24,184] or phthalocyanine derivatives[360], but not for macrocycles elevated from the surface by their substituents as in the case of 2H-TPP. Therefore it seems plausible that PPDs on Ag

only metalate after planarization, i.e. all molecules follow reaction route **1** and mostly do not even metalate[324]. The flattening of Co-TPP/Ag(111) trivially only follows the second branch of route **2**. Therefore the flattening reactions of the two species on silver are strictly separated. Contrary for 2H-TPP/Cu(111), metalation before planarization (route **2**) results in mixed free-base/metal-TPPs as precursor molecules and the PPD statistics always represent free-base and metal-TPP planarization. As it turns out (see below), metalation can additionally proceed during cyclodehydrogenative planarization illustrated as route **3** in Figure 9.4b. In route **3**, the free-base molecule first partially flattens and then metalates before completing planarization. The differences in the reaction outcomes for Co-TPP on Ag(111) and Cu(111) underline the substrate influence on the reaction. Therefore it would be desirable to get insights into the role of the substrate for 2H-TPP only, i.e. excluding self-metalated molecules. In an attempt to disentangle the two reaction paths (2H-TPP → M-TPP → PPD, cf. right hand side of Figure 9.4a and 2H-TPP → PPD, left hand side of Figure 9.4a), Co-TPP was deposited onto Cu(111) and annealed to get insights into route **2** only. It is assumed that the Cu-TPP/Cu(111) planarization follows the same distribution as Co-TPP/Cu(111). This assumption is reasonable since Cu-TPP/Cu(111) was reported to form primarily species **D**[348] as does Co-TPP: the reaction yields 0 % **A**/**A***, 6.0 % **B**, 0.7 % **C** and 93.3 % **D**.

Table 9.1. Statistics of PPDs on Cu(111). The first row shows the statistical analysis of PPD from the Co-TPP/Cu(111) precursor also depicted by the framed orange boxes in Figure 9.4. Data in the second row correspond to the occurrences of PPDs from 2H-TPP/Cu(111). The lower values show the statistics for metalated PPDs only, i.e. all of **A***, **B**, and **C** and 5 % of **D**.

Precursor	**A***	**B**	**C**	**D**
Co-TPP/Cu(111)	0 %	6.0 %	0.7 %	93.3 %
2H-TPP/Cu(111)	10.6 %	18.0 %	12.0 %	59.5 %
only M-PPD counted	24.2 %	41.4 %	27.4 %	7.3 %

Surprisingly, when heating 2H-TPP/Cu(111), only 5 % of **D** appear metalated while the rest remains free-base; yet **D** is the dominating species (59.5 %). In contrast, all of **A***, **B** and **C** are metalated. The very low occurrence of metalated species **D** suggests that metalation largely does not take place after planarization. The reaction barrier for metalation is assumed to be very similar for all PPD considering that all exhibit the same molecular core and theoretical studies always only take into account the porphine macrocycle for the calculation of reaction barriers. Additionally, it is obvious that the M-PPD distribution from 2H-TPP does not match the occurrences of PPD from Co-TPP/Cu(111) (compare row one and three of Table 9.1). This allows the conclusion that they were not formed via route **2**, i.e. only a small fraction of 2H-TPP metalates before flattening. Therefore almost all Cu-PPD are formed via route **3**. Consequently, it is not possible to disentangle route **1** and **2**. The dominating reactions routes for cyclodehydrogenative planarization of 2H-TPP on Cu(111) under the given preparation conditions are route **1** and **3** as indicated by the arrow thickness in Figure 9.4b. Interestingly route **1** produces almost

exclusively species **D**, while route 3 mainly leads to **A***, **B** and **C**. Please note, that for **A***, the macrocycle most likely disintegrates before metalation, as the metal center would greatly stabilize the molecular structure and prevent a pyrrole loss. Therefore, metalated half-planar species mostly result in **B** and **C**.

Summary

Summarizing, this section presented a comparative study of the cyclodehydrogenation reactions of TPP on Ag(111) and Cu(111) by means of high resolution scanning probe techniques. For the first time, all PPDs were structurally unambiguously characterized by FM-AFM with CO-functionalized tips. Furthermore, the reaction pathways were thoroughly discussed. While 2H-TPP/Ag(111) follows the energetically preferable pathways derived from gas-phase calculations[324] that primarily leads tp **A**, the reaction of 2H-TPP/Cu(111) turns out to be more complex. The copper surface influences the cyclodehydrogenative flattening reaction distinctly in two ways: firstly, the strong substrate—adsorbate interaction steers the reaction towards **D** for 2H-TPP and secondly, all relevant reactions exhibit a very similar onset temperature around 390 K. Therefore, self-metalation produces mixed 2H-TPP/Cu-TPP precursor molecules. The following conclusions for the reaction pathways can be drawn for the very low coverage investigated here ($0.02\,\text{molecules/nm}^2 - 0.05\,\text{molecules/nm}^2$). i) Flattening and metalation do not only proceed strictly separated as on Ag(111), but simultaneously (route **1** and **2**) and moreover also in an entangled way (route **3**); and ii) metalated, partially planarized TPP will primarily produce **B** or **C** while metalated precursors (i.e. Cu-TPP) as well as non metalated molecules will result in **D**. The choice of the substrate therefore turns out to be decisive for the reaction pathway and outcome additionally to molecular symmetry.

An issue however remains unresolved. Why could species **A** not be observed on Cu(111) and what is **A***? The next section will proceed by characterizing **A*** in more detail.

10. Surface-catalyzed porphyrin deconstruction

The deconstruction of macrocyclic compounds is of utmost importance in manifold biological and chemical processes, usually proceeding via oxygenation induced ring-opening reactions. This section introduces a surface chemical route to selectively break a prototypical porphyrin by cleaving one pyrrole unit and forming a tripyrrin. This process— operational in a ultra-high vacuum environment at moderate temperatures usually guaranteeing tetrapyrrole integrity— is enabled by a distinct molecular conformation induced by the copper support. LT-STM and FM-AFM investigation provide an atomic-level characterization of the surface-anchored tripyrrin, its reaction intermediates, and byproducts. The findings rationalize the ring-opening by a rupture of the macrocycle's aromaticity, destabilizing the system and open a route to steer ring-opening reactions by conformational design and to stabilize intriguing metal-organic complexes on surfaces.

Introduction

Current porphyrin research does not just settle for tetrapyrroles in the search for new materials, but develops artificial porphyrinoids with expanded, contracted or otherwise modified macrocycles[361,362]. Common synthesis pathways combine precursors with one- two or three pyrrolic units to form porphyrin related compounds[361]. The initial building blocks however do not just develop useful properties as fully assembled cyclopyrroles. Oligopyrroles such as dipyrrin and tripyrrin e.g. can be employed as metal-complexing agents in functional organo-metalic compounds[363–365] or as fluorescent sensors[366,367]. Furthermore tripyrrins are biologically relevant molecules—usually referred to as biotripyrrins—that naturally occur as oxidative metabolites of bilirubin[368], which in turn is a metabolite of the porphyrin related heme. Oligopyrroles and porphyrin fragments are therefore intrinsically interesting for nanoscience and important for understanding biological processes. A majority of porphyrin research relies on solution-based approaches and consequently it is not of surprise that studies of synthetic porphyrinoids and porphyrin fragments have drawn some attention in the field of organic chemistry. Despite considerable research interest in functional oligopyrroles in physical and chemical surface science[11,12], reports of e.g. expanded porphyrins, di- or tripyrrins and related species are scarce and these classes of molecules remain nearly unstudied[315,369,370]. A limitation arises from their thermal instability rendering them inapplicable for standard UHV preparation techniques. On the other hand, in-vacuo heterogeneous nanochemistry bares the potential for creating compounds not achievable in homogeneous approaches due to the catalytic properties of the surface[233,235] or because the reactivity of intermediate or final products[289,290,329] prohibits their handling. Therefore it is reasonable to employ surface science approaches for the investigation and/or the synthesis of novel porphyrin-related molecules. As demonstrated here,

a surface chemical route leads to pyrrole cleaving from 2H-TPP on Cu(111) during cyclodehygenative flattening. The novel copper metalated tripyrrin derivative is structurally characterized by visualizing its chemical bonds via FM-AFM with CO-functionalized tips and via tip manipulations. Furthermore a possible reaction pathway will be suggested by identifying a distinct reaction intermediate.

10.1. Structure determination of a porphyrin fragment
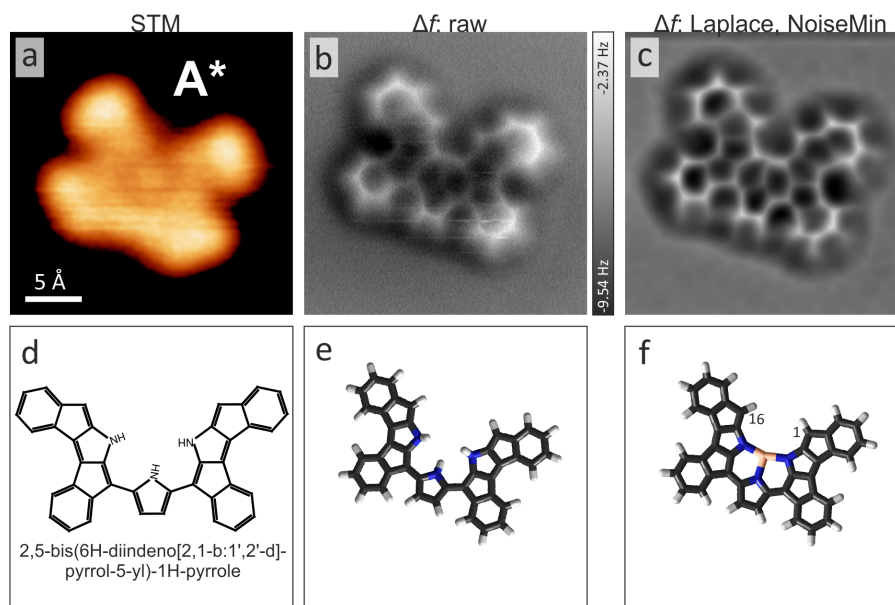
Figure 10.1. Novel pincer-like tripyrrolic porphyrin fragment. a) STM data ($U = 30\,\mathrm{mV}$, $I = 10\,\mathrm{pA}$). b) Constant height Δf map (setpoint as for a), approach $\Delta z = -1.4\,\text{Å}$) and c) the same AFM data as in c) post-processed to emphasize the chemical structure. d) Chemical structure of the free-base derivative 2,5-bis(6H-diindeno[2,1-b:1′,2′-d]pyrrol-5-yl)-1H-pyrrole. The nomenclature follows IUPAC naming. To emphasize the species' relation to tetrapyrroles, it will be referred to as PTP-TriPyr (see text). e) Model of free-base PTP-TriPyr . f) Suggested model of the observed tripyrrin that exhibits a central copper ion.

When annealing a low coverage ($(0.02 - 0.05)\,\mathrm{molecules/nm^2}$) of 2H-TPP on coinage metal surfaces, planarized porphyrin derivatives—denoted by **A** through **D**—are synthesized as described in Section 9. For 2H-TPP/Cu(111), the most striking observation however is the absence of **A** after annealing and instead the occurrence of **A***. Figure 10.1a depicts STM data of the unexpected species with a rectangular outline. Along one of its longer sides (here, the lower one), the molecule appears like **A**, however at the opposing side, a triangular void is discernible. The void reduces the symmetry of the molecule from $D_{2\mathrm{h}}$ to $C_{2\mathrm{v}}$. The molecular structure however remains elusive. Constant height Δf maps give structural insights (Figure 10.1c, d): **A*** features four flat phenyls that are pairwise fused to two opposing pyrroles, the third pyrrole did not engage in ring-closing and the fourth one is completely missing from the macrocycle, causing the

triangular void in STM and resulting in a pincer-like chemical structure. Obviously, the aromatic, macrocyclic backbone of the TPP was destroyed during the annealing procedure on copper. Consequently, **A*** is not a porphyrin derivative like the PPDs, but a porphyrin metabolite. Following IUPAC nomenclature, the novel free-base species is 2,5-bis(6H-diindeno[2,1-b:1′,2′-d]pyrrol-5-yl)-1H-pyrrole (Figure 10.1d). However, to emphasize the species' relation to tetrapyrroles, it will be referred to as tripyrrin derivative[371]; namely planarized tetraphenyl tripyrrin (PTP-TriPyr). A comparison of the gas-phase geometry optimized structures of a metalated and a free-base PTP-TriPyr with the AFM data however suggest metalation and the formation of copper-2,5-bis(6H-diindeno[2,1-b:1′,2′-d]pyrrol-5-yl)-1H-pyrrole, or Cu-PTP-TriPyr. The pincer of the non-metalated tripyrrin model opens further (Figure 10.1e) and does not correspond to the experimental data. Furthermore, **A*** exhibits a bright molecular center in STM (Figure 10.1a) that indicates metalation (cf. Figure 9.3). Therefore Figure 10.1f depicts the suggested molecular structure of the novel pincer-like tripyrrin featuring a central copper ion. Furthermore, deprotonation experiments will show that the tripyrrin is protonated at positions 1 and 16 indicated in Figure 10.1f.

A surface radical? Tip-induced deprotonation experiments

The removal of a pyrrole from the macrocycle leaves two unsaturated carbons at the (formerly) meso positions, here indicated by the carbon count 1 (C1) and 16 (C16) of the tripyrrin in Figure 10.1f. To clarify whether the on-surface synthesis yields pincer-radicals or saturated species, manipulation experiments were performed . By applying voltage pulses of $\approx 3.4\,\text{V} - 4\,\text{V}$ with the STM tip, a targeted deprotonation can be triggered at tetrapyrroles[372] and carbon structures[300,301,373–375]. To carry out the manipulation, the CO was removed from the tip by pulsing ($\approx 2\,\text{V} - 3\,\text{V}$) at adequate distances from the area of investigation, followed by the manipulation procedure and subsequent re-functionalization with CO. Figure 10.2 depicts the sequential deprotonation within the pincer. First a pulse at C1 resulted in a depression in the STM image as indicated in Figure 10.2e by the black circle and in an increased apparent height for one phenyl (white arrow in Figure 10.2e). The changes can also be tracked in AFM data. At the position of the pulse, the atomic contrast is lost, but can be restored by approaching the tip towards the sample (Figure 10.2j, k). This proves that the carbon frame is still intact after the pulse, but the molecule bents downwards caused by the formation of a covalent bond to the surface[289,300,301,374]. Following a seesaw mechanism, a phenyl is lifted as indicated by the strong repulsive interaction at the center of the ring (cf. white arrow in Figure 10.2f). Such features within carbon rings are caused by very small tip-sample separations that result in image artifacts due to relaxations of the CO at the tip[36]. A second pulse at C16 produces similar changes (cf. white arrow and black circle in Figure 10.2m) and restores the molecular symmetry. As marked by white arrows in Figure 10.2n, o the manipulated atoms appear darker than other peripheral carbons, indicating tip-induced deprotonation followed by carbon–surface bond formation. Likewise, all other peripheral carbons can be manipulated and show similar effects, which supports the suggested deprotonation within the pincer. Obviously, the pincer takes up hydrogen from the surface or the residual gas after separation of the pyrrole and does not exist in an unsaturated form.
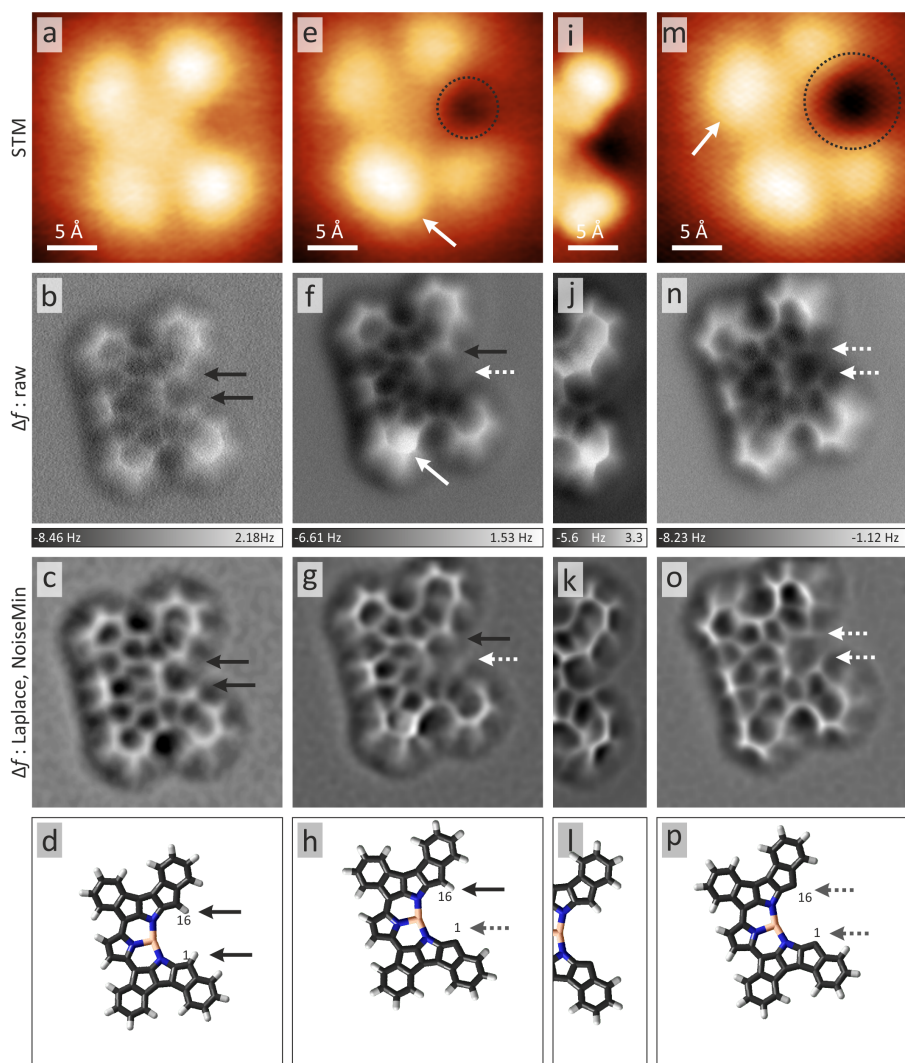
Figure 10.2. Tip-induced deprotonation inside the tripyrrin. The presented datatype is indicated to the left of each row. a–d) Tripyrrin before voltage pulses applied at the carbons 1 and 16. e–h) After a voltage pulse at carbon 1. i–l): A detailed investigation of the deprotonated area confirms an intact carbon backbone. m–p) After a voltage pulse at carbon 16. The deprotonation manifests in the STM data (first row) as a depression next to the molecule (circled in e, m) and as a brighter contrast above a phenyl ring as indicated by white arrows in e, m). In f), the solid white arrow highlights the phenyl that is lifted from the surface after the first pulse. The black solid arrows in row two and three mark protonated carbons and the white dotted arrows indicate missing hydrogens. The last row suggests models of the molecular structures. Scan parameters for STM data as well as setpoint for constant height imaging: $U = 30\,\mathrm{mV}$, $I = 6\,\mathrm{pA}$. Approach for AFM measurements b) $\Delta z = -1.4\,\text{Å}$; f, n) $\Delta z = -1.6\,\text{Å}$; j) $\Delta z = -2.0\,\text{Å}$.

10.2. Observation of partially flattened reaction intermediates

Since no degradation of the porphyrin backbone from a tetrapyrrole macrocycle to the pincer-like tripyrrin is observed on Ag(111), the Cu(111) surface obviously is responsible for the dissociation. Furthermore, it seems unlikely that the molecule is destroyed once it is planarized. All PPDs are either metalated or exhibit fused pyrroles. Both these modifications should stabilize the macrocycle. Therefore the initial substrate influences on the molecular geometry most likely determine the thermally activated reactions. In Sec-
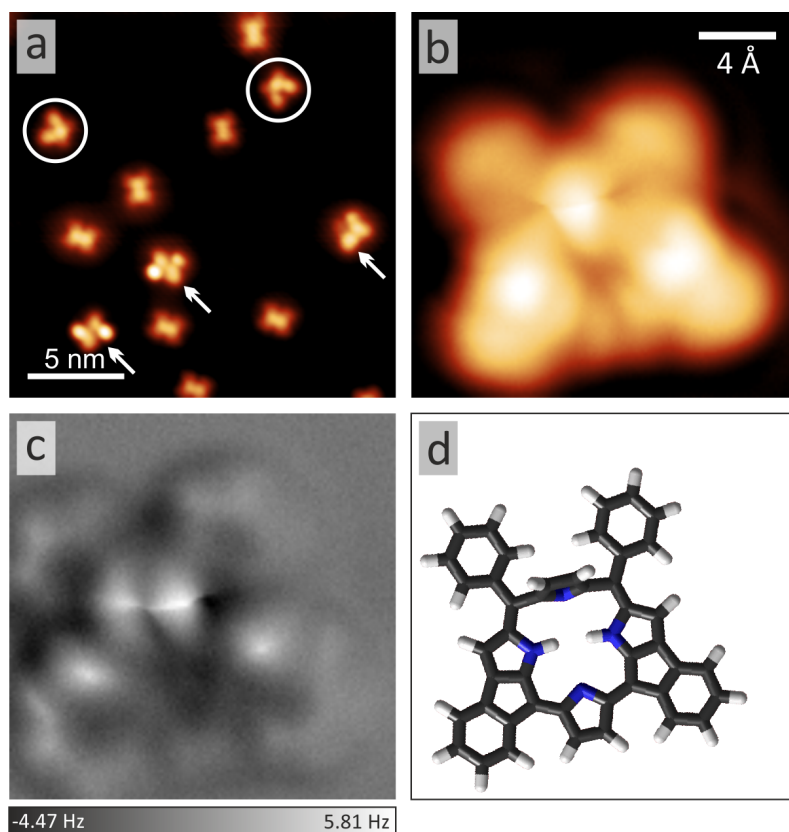
Figure 10.3. A partially flattened reaction intermediate. The first column shows STM data; the second column depicts the Δf channel during constant current measurements; the third column suggests models for the imaged molecule. Scan parameters: a) $U = 100\,\text{mV}$, $I = 6\,\text{pA}$; b, c) $U = 5\,\text{mV}$, $I = 65\,\text{pA}$.

tion 7 the adsorption geometries of 2H-TPPs on Ag(111) and Cu(111) were discussed. The molecular conformation on copper represents an extreme case for distortions of surface-confined tetrapyrrole species[11,319] and is distinctly different from the gas-phase geometry and from the comparatively weakly distorted saddle-shape on noble metal surfaces such as silver or gold[11,232,248,376]. In analogy to cyclodehydrogenation on Ag(111)[324], the reaction on copper also proceeds in multiple steps affording reaction intermediates. The intermediates represent partially planarized species with one, two or three flat legs. To get insight into the reaction pathway these intermediates were isolated by lighter annealing (395 K

for 20 min). The procedure yielded several modified species (see Figure 10.3), of which the one presented in Figure 10.3d–d can be identified as relevant reaction intermediate for the formation of PTP-TriPyr. Simultaneous STM and AFM measurements reveal a half-planarized TPP with one remaining upright pyrrole. In STM data one central protrusion is discernible (Figure 10.3b) that corresponds to a strongly repulsive feature at the position of the pyrrole in the Δf channel resembling the contrast of 2H-TPP/Cu(111) presented in Section 7. The suggested molecular structure is schematically shown in Figure 10.3d. Please note, that the intermediate is assumed to be free-base. A metalation reaction to Cu-TPP would flatten the macrocycle to a moderate saddle-shape that appears distinctly different in SPM data[33]. Furthermore the reaction intermediates would exhibit upright legs instead of flat phenyls in the periphery[324] as observed for other partially flattened species (cf. Figure 10.3a). The suggested tripyrrin reaction pathway implies that pyrrole loss precedes metalation. The metalation most likely helps to stabilize the final product.

10.3. Discussion of the porphyrin deconstruction

The disintegration of the macrocycle by separation of a complete pyrrole ring at the moderate temperatures around 500 K is very surprising. Note that the temperature at which pyrrole loss occurs is well below the temperature inside the evaporation cell during preparation (600 K). However without annealing the sample, only intact 2H-TPP was present. Furthermore on Ag, no decomposition could be observed and the porphyrin backbone—the porphine—represents a robust aromatic ring system that withstands temperatures as high as 900 K on Ag(111)[24]. At these high temperatures on-surface polymerization and complete dehydrogenation take place, the carbo-pyrrolic framework however remains intact. Similarly, other tetrapyrroles survive considerably higher annealing temperature[168,346]. These findings allow the conclusion that the weakening of the molecular frame on Cu(111) is not induced by temperature, but rather by surface–adsorbate interactions that are weaker or not active on Ag(111). Therefore it is reasonable to track the preconditions for porphyrin fracture to the initial molecular conformation. Carbon-based materials can reduce their ground state energy and gain considerable stability by sharing delocalized π-electrons in conjugated systems. In the case of cyclic systems—as the porphine macrocycle here—this is expressed in their aromaticity that underscores structural and chemical stability[377–379]. A prerequisite for the development of shared orbitals and aromaticity however is an adequate planar geometry that allows a better overlap of the p-orbitals[380]. Aromatic systems express structural flexibility and can be deformed to a certain extend without suffering the loss of stability[381,382]. Furthermore, conjugation and aromaticity can occur in polycyclic molecules with a non-planar geometry or with a non-coplanar arrangement of the fused rings such as e.g. in fullerenes[383]. However, the co-planarity of constituent atoms is considered a key restriction for aromaticity[379] and extreme out-of-plane distortions as described above will consequently result in the loss of aromaticity and structural stability. Therefore, the strong macrocycle deformation of 2H-TPP on Cu(111) is identified for the destabilization and breaking of the macrocycle. On the other hand, wet-chemical routes for porphyrin breaking, as well as processes in natural metabolism attack the macrocycle chemically by oxidation. A prominent example is the heme metabolism that de-metalates and cracks the macrocycle in a redox reaction

with the help of the enzyme heme oxygenase (HMOX). In the lab, the macrocycle can be attacked via dihydroxylation followed by subsequent ring-opening[384]. Our results however demonstrate an alternative strategy that does not involve catalyst and oxidant add-ons but solely relies on structural distortions.

Summary

FM-AFM with CO-functionalized tips was employed to identify the hitherto unreported porphyrin fragment copper-2,5-bis(6H-diindeno[2,1-b:1′,2′-d]pyrrol-5-yl)-1H-pyrrole, called Cu-PTP-TriPyr, and to characterize a decisive reaction intermediate. The degradation of a robust, conjugated porphyrin is unusual and was explained by the strong structural deformation of 2H-TPP on Cu(111). Surface interactions cause an almost perpendicular orientation of two pyrroles within the macrocycle, which most likely results in the loss of aromaticity and therefore structural stability to enable the removal of a complete pyrrolic ring from the porphine backbone. However, to fully understand the porphyrin destruction and to support the suggested reaction pathway, theoretical modeling would be desirable. Nevertheless, these findings open interesting routes for the disintegration of otherwise very robust molecular systems and widen the capabilities of heterogeneous catalysis.

11. Nanoscale phase engineering of niobium diselenide

With continuing miniaturization in semiconductor microelectronics, atomically thin materials are emerging as promising candidate materials for future ultra-scaled electronics. In particular, the layered transition metal dichalcogenides (TMDs) have attracted significant attention due to the variety of their electronic properties, depending on the type of transition metal and its coordination within the crystal. This section demonstrates STM-based structural and electronic phase-engineering of the group-V TMD niobium diselenide (NbSe$_2$). Voltage pulses with an STM tip can transform the material crystal phase locally from trigonal prismatic (2H) to octahedral (1T), as confirmed by the concomitant emergence of a characteristic $(\sqrt{13} \times \sqrt{13})$R13.9° charge density wave (CDW) order. At 77 K atomic-resolution STM images of the 2H/1T phase boundary confirm the successful phase-engineering of the material by resolving a slip of the top Se plane evidencing a difference in the Nb coordination. Different 1T-CDW intensities suggest interlayer interactions to be present in 1T-NbSe$_2$. Furthermore, a distinct voltage dependence suggests a complex CDW mechanism that does not just rely on a Star-of-David reconstruction as in the case of other 1T-TMDs. Additionally, bias pulses cause surface modifications inducing local lattice strain that favors a one-dimensional charge order (1D-CDW) over the intrinsic 3×3 CDW at 4.5 K for 2H-NbSe$_2$. A reversible switching between the two (quantum) states is possible using the STM tip.

Introduction

Recent advances in the fabrication of TMD nanodevices have impressively demonstrated their potential for future (opto-) electronics[170,385,386], catalysis, and energy storage[174,386]. Layered TMDs in particular, are quasi two-dimensional materials that consist of three atom thick van-der-Waals stacked layers of stoichiometry MX$_2$ (M: transition metal, X: chalcogen), where each layer consists of a sheet of transition metal atoms sandwiched between two chalcogen layers. Each transition metal atom is sixfold coordinated by chalcogens, assuming either trigonal prismatic (2H) or octahedral (1T) lattice structure. Indeed, it has been shown that these different polymorphs can coexist within the same sample, exhibiting atomically sharp boundaries.[169,387–389] Depending on the type of TMD, the two crystal phases can exhibit vastly different electronic properties, including metallic, insulating, semiconducting, or even superconducting. Substantial interest therefore exists to harness such atomically sharp homojunctions for the engineering of novel atomic-scale electronic devices.[169,386,390,391]

Phase-control in TMDs has been demonstrated using strain[390,392–394], chemical intercalation with alkali metals,[385,386] heat[389,391,395], in-plane electric fields[395–397], or injection of electronic charge[398–400]. Typically, one of the crystal phases is thermodynamically

more stable than the other, whereby the stability is determined by the type of transition metal.[174,386] The group-V TMD $NbSe_2$ is of particular interest as its 2H phase exhibits collective low-temperature ground states in the form of charge density waves (CDWs) ($T_{CDW} \approx 34$ K)[401,402] and superconductivity (SC) ($T_C \approx 7$ K)[403]. Owing to these properties, $NbSe_2$ has attracted significant attention over the years as a model system to study the origins of these low temperature ground states and their correlation.[401,402,404–422]

LT-STM is ideally suited for the engineering and investigation of the atomically sharp phase boundaries, owing to its unique ability to not only image materials' surfaces with atomic resolution, but also to manipulate matter at the atomic scale.[232,387,389,391,423–430] The creation of a 1T-phase in $NbSe_2$ appears particularly intriguing since it is has been believed to be thermodynamically unstable in bulk form[431]. More recently, however, is was reported that $1T-NbSe_2$ can be stabilized in nanometer scale regions of $NbSe_2$ monolayers[432] expressing Mott-insulating character.

11.1. Creation of atomically precise 2H–1T boundaries in NbSe$_2$

In bulk, $NbSe_2$ occurs as 2H-crystal, i.e. it consists of two layers per hexagonal unit cell with trigonal prismatic coordination of the Nb atoms. Due to weak van-der-Waals interlayer coupling, $NbSe_2$ cleaves between adjacent Se sheets, exposing a hexagonal chalcogen surface with a distance of $a = 3.44$ Å along the close packed $\langle 100 \rangle$ directions[433] and $a^* = a\sqrt{3}/2 = 2.98$ Å for the inter-row distance (see inset in Figure 11.1a). The atomic lattice corresponds to a "(1×1)-periodicity" wherefore its sharp spots in FFT images will be denoted by Q_1 (red circles, Figure 11.1b,d). $NbSe_2$ is a CDW material. It develops a coherent (3×3)-CDW state below the transition temperature of $T_{CDW} \approx 34$ K. At temperatures above T_{CDW} short-range (3×3)-CDW patches pinned to (sub-surface) impurities can be present[401] as highlighted by the green triangle in Figure 11.1a and evidenced by the diffuse Q_3 spots in Figure 11.1b. The patches develop into a coherent (3×3)-CDW state at 4.9 K[401,402] (cf. Figure 11.1c and sharp spots Q_3 at $q_3 = 1/3q_1$ in Figure 11.1d highlighted in green).

An atomic resolution STM image of an artificially created 1T/2H junction in $NbSe_2$ at 77 K is shown in Figure 11.2a. Here, the pristine 2H-surface has been locally modified by STM bias pulses with voltages of $U_{bias} > 4$ V resulting in pits as described in Reference [389]. Close to the pits regions—several hundred square nanometers in size—of a commensurate $(\sqrt{13} \times \sqrt{13})R13.9°$ CDW can be found (left hand side of Figure 11.2a). The superstructure is lattice matched across an atomically sharp and straight boundary to the pristine $NbSe_2$ (right hand side of Figure 11.2a).[389] As the data was recorded above the CDW transition temperature for $2H-NbSe_2$ the pristine surface does not exhibit charge modulations and the occurrence of the $(\sqrt{13} \times \sqrt{13})R13.9°$ CDW proofs a fundamental modification of the material. The alignment of the atomic lattices can be resolved across the boundary by applying a FFT filter to remove the CDW modulation as shown in Figure 11.2b. The image reveals a rectangular and continuous arrangement of atoms across the 2H/1T phase boundary, resulting from a shift of the top Se plane during the 2H-1T phase transformation as indicated by red arrows in Figure 11.2d.[387,389,434] The details of the matched lattices at the boundary are illustrated in the schematic of Figure 11.2d, showing the lattice structure of a single $NbSe_2$ layer after a shift of the top Se
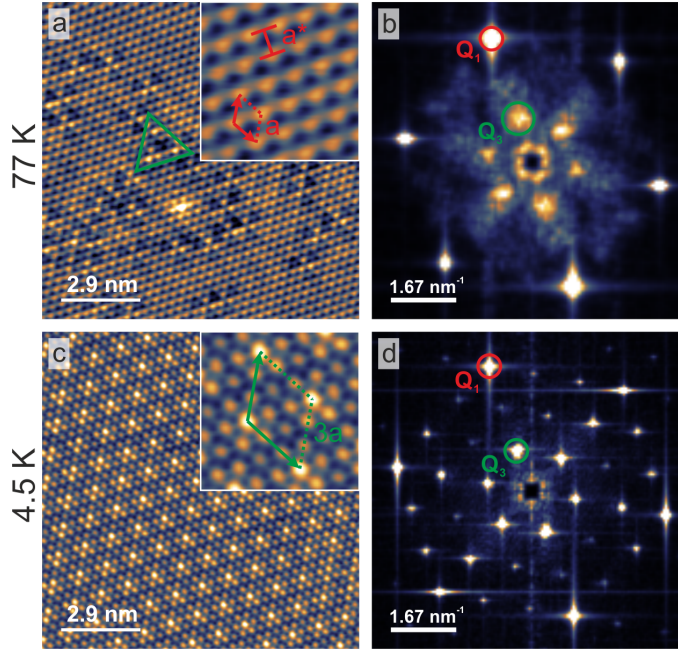
Figure 11.1. Atomically resolved STM data of the pristine NbSe$_2$ surface. a) The inset shows the hexagonally close packed Se top layer with lattice constant a and reciprocal lattice constant $1/a^*$. The red vectors along the close-packed directions depict the unit cell of the atomic lattice. At 77 K local, short-ranged (3×3)-CDW patches form as indicated by the green triangle. b) The FFT plot of a) exhibits sharp atomic spots (Q_1, red circle) and diffuse CDW spots (Q_3, green circle). (c) Fully established (3×3)-CDW pattern at 4.9 K. The inset focuses on the 3×3 unit cell with lattice constant $3a$. The green arrows depict the unit cell of the electronic modulation. d) The CDW results in sharp FFT spots and their linear combinations. Scan parameters: a) $U = -600$ mV, $I = 0.9$ nA; c) $U = 100$ mV, $I = 1.5$ nA.

layer in the left half of the image. In this schematic three distinctly different lattice sites can be discriminated, labeled A, B and C. A represents a Se atom (top site), B a void between Se top atoms (hollow site) and C a Nb atom within the first sub-surface sheet (hcp site). In the 2H-phase, two Se atoms from the top and bottom layers of a NbSe$_2$ monolayer are aligned on top of each other forming the trigonal prismatic coordination of the Nb center. However, in the 1T-phase, a hollow site is located above the Se atom of the sub-surface (lower) Se sheet. Following a shift of the top Se plane during phase transformation, the order of sites along the $\langle 210 \rangle$ crystal directions is now changed for the two phases (line-cuts of Figure 11.2c) and changes at the boundary.

These differences are reflected by the sub-lattice detail of the atomic resolution STM data, where the top Se atoms show as a bright protrusion, the hollow site as a shallow depression, and the Nb hcp site as a deep depression. Following the blue line in Figure 11.2b from left to right, the sequence for 2H is A–B–C while for 1T it changes to A–C–B. These differences are accentuated by profiles along a $\langle 210 \rangle$-direction for both phases in the FFT-filtered data. As shown in Figure 11.2c, the sequence of peak–shoulder–minimum switches to peak–minimum–shoulder at the phase border. Although a boundary between two 60° rotated 2H-crystals would have the same effect[435], it would fail to explain the
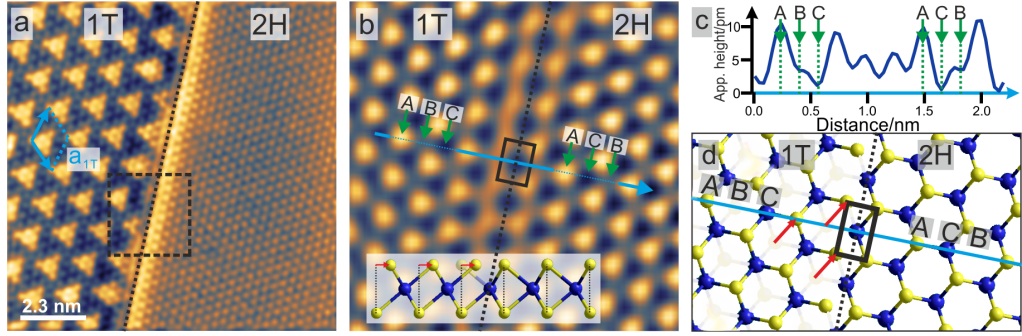
Figure 11.2. Atomically sharp phase boundary between 1T- and 2H-NbSe$_2$ at $T = 77\,$K (scan parameters: $U = -2\,$V, $I = 1.7\,$nA). a) The pristine surface on the right does not exhibit charge modulations while a clear CDW order indicates 1T-NbSe$_2$ on the left. The charge modulation of the 1T-phase (1T-CDW) manifests as commensurate $(\sqrt{13} \times \sqrt{13})$R13.9° superstructure (blue arrows) with lattice constant $a_{1T} = 12.4\,$Å. b) Close-up of the dashed square in a), showing an FFT filtered image to remove the electronic CDW modulation. Each bright dot corresponds to one selenium atom in the top Se layer. Across the boundary (black dotted line), a rectangular alignment can be clearly observed (black box). Distinct positions in the surface are highlighted by green arrows A, B and C (see text for a full description). Bottom inset: Side view of a model of one NbSe$_2$ layer. Red arrows indicate the shifted Se top plane after the 2H/1T transformation. c) Line profile along the blue line in b). Green arrows indicate lattice positions in b) correspondingly. d) A schematic of a single NbSe$_2$ layer at the phase boundary. Yellow balls represent the Se top plane that is imaged in STM, blue balls represent sub-surface Nb. Se in the bottom layer of 1T-NbSe$_2$ are shown in faded yellow. Red arrows indicate the top layer shift that leads to a rectangular Se atom arrangement at the boundary as highlighted in black. The lattice positions marked in b) and c) are labeled correspondingly.

observed electronic modulation in the form of CDW order above T_{CDW}. The correlated differences in atomic and electronic structure across the boundary thus gives strong evidence for a successful STM-induced 2H-1T phase transformation. It should be pointed out that a recent multimethod study identified single layer 1T-NbSe$_2$ on bilayer graphene as a Mott-insulator[432], suggesting here the engineering of an atomically defined Mott-insulator-to-metal junction. Such homojunctions could be exploited in functional devices as already shown in field effect transistors made from MoS$_2$[169] or MoTe$_2$[436].

The observation of regions of stable 1T-NbSe$_2$ phase is surprising as it has been believed that this phase is generally thermodynamically unstable[431]. There is no report of bulk 1T-NbSe$_2$ and only very recently, stable single-layer 1T-NbSe$_2$ nanoflakes were synthesized.[432] Following the arguments of Wang et al.[389] it can be speculated that regions of 1T-NbSe$_2$ are created by local heating via the injected STM tunneling current during the bias pulse, and then are rapidly quenched to $T = 77\,$K which, in combination with the energetics of the 2H/1T boundary and the confinement to single and few layers, may stabilize this phase. However, additional mechanisms such as local charge injection by the STM current may play an important role. Recently, charge driven switching of the metal coordination from trigonal prismatic (2H) to octahedral (1T) was reported for MoTe$_2$[393,400], MoS$_2$[393], TaSe$_2$[393], and W$_x$Mo$_{1-x}$Te$_2$[393,400]. No degradation of the 1T-

NbSe$_2$ CDW was observed over the course of the experiment (several hours), suggesting a CDW transition temperature in the 1T-phase above $T = 77$ K. Indeed, previous experiments on a $(\sqrt{13} \times \sqrt{13})$R13.9° CDW associated with a 1T-phase were carried out at room temperature (RT) indicating a 1T-CDW transition temperature above 290 K.[423]

The 1T-CDW can exist in both a disordered (top left of Figure 11.3a) and an ordered phase which feature the same CDW wave vector and amplitude[389]. Furthermore, the CDW phase can exhibit different amplitudes as clearly seen on the right hand side of Figure 11.3a that shows a (atomically) sharp boundary between two different CDW domains. A line profile across this boundary rules out a step edge as cause for the different contrast but instead reveals an abrupt change in CDW amplitude at the same wavelength and phase (Figure 11.3b). To further characterize both these CDW phases, the bias dependent contrast is depicted for the occupied states in Figure 11.3e–g (high amplitude) and Figure 11.3h–j (low amplitude), respectively. These data are close-ups from the same image (cf. white squares in Figure 11.3c) and hence were acquired with the same STM tip. Circles are centered at the location of the CDW maximum at −50 mV for reference. When decreasing the bias from −50 mV to −950 mV, the CDW maxima first continuously shift along one of the lattice vectors of the CDW and then perpendicular, resulting in a complete contrast inversion. Consequently, the maxima are located at different atoms of the NbSe$_2$ lattice for different voltages and assume different shapes. The CDW wavelength and orientation on the other hand remain constant over the whole voltage range. Interestingly, the CDW response to bias changes are very similar for both CDW amplitudes (Figure 11.3e–j), suggesting that they are closely related in their origin. Furthermore, the high to low amplitude boundary seems to be atomically smooth and does not exhibit distinct rectangular (or other) atomic arrangements (Figure 11.3d) suggesting the same phase (i.e. 1T-NbSe$_2$) on both sides. STM is only sensitive to the topmost TMD layer, however a 2H/1T phase transition is not limited to the top TMD sheet. It is likely to occur within several layers, creating stacks of 1T-NbSe$_2$ sheets of varying depth as well as (buried) 2H/1T interlayer boundaries. Since interlayer stacking is known to modify physical properties in TMDs[409,437,438], interlayer CDW stacking and/or lattice stacking may also be responsible for enhancements/attenuations of the CDW amplitude of an octahedrally coordinated first layer. Recently, STM studies of the TMD TaS$_2$ identified attenuated CDWs as buried second layer features and that changes in CDW stacking can lead to modified TMD properties.[391,439] However, on the length scale of an interlayer distance ($d \approx 6$ Å) the tunneling current drops approximately six orders of magnitude. It therefore seems more likely that STM reproduces the effects of interlayer interactions of buried 1T-2H boundaries.

As seen in Figure 11.3h–j, each CDW maximum always contains an identical arrangement of atoms at each bias voltage. Since wavelength and the orientation of the CDW with respect to the atomic lattice do not change, the CDW remains commensurate. 1T-TMDs such as 1T-TaS$_2$[172,391,439] and 1T-TaSe$_2$[387,440,441] have been reported to develop a Star-of-David reconstruction in the transition metal plane which is closely related to the material's electronic structure (Fermi surface nesting for 1T-TaS$_2$[172] and spatially localized sub-bands for TaSe$_2$[440,441]). Consequently, the CDW in these materials strictly locks to the reconstruction of the atomic lattice. As evident by the STM bias dependence, in 1T-NbSe$_2$ the CDW does not exhibit such a strict correlation with respect to the lattice. Therefore additional mechanisms are suggested besides periodic lattice distortions
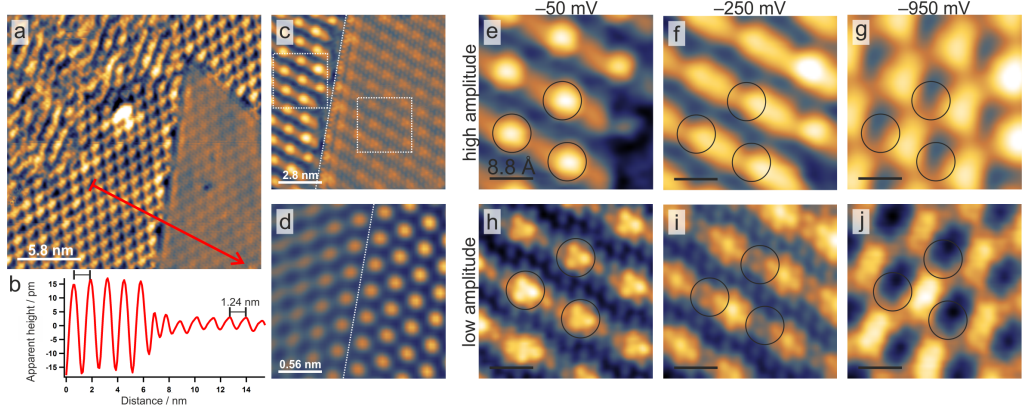
Figure 11.3. Characterization of the 1T-CDW at $T = 77\,$K. a) STM topography of the boundary between areas of different 1T-CDW amplitudes. The observed 1T-CDW can occur in a disordered (top left) or highly ordered state (rest of the image) and exhibits two different amplitudes as shown by a line profile (b) along the red line in a). The wavelength is the same for both amplitudes as highlighted by the black distance indicator. c) Overview image of the amplitude boundary. The white squares indicate the areas of magnification used to generate e–j). Within the high amplitude CDW, the electronic modulation largely conceals atomic corrugations. d) Fourier filtered and zoomed image of c) omitting the CDW periodicities. The atomic contrast does not give an indication for discontinuities across the boundary. The boundary is marked with the white dotted line. e–j) STM bias dependence for both amplitudes. The first row displays the large amplitude CDW and the second row the small amplitude CDW. The STM bias is indicated above each column. Black circles mark the same position in each image and are aligned with the maximum of the CDW for $-50\,$mV. Both rows are details from larger images across a phase boundary as indicated by white boxes in b. Please note that the contrast in the images was adapted for best visibility of CDW features. Scan parameters: a) $I = 2.0\,$nA, $U = -1.0\,$V; b) $I = 2.0\,$nA, $U = -50\,$mV; e–j) $I = 2.0\,$nA.

as a driver for the CDW formation in 1T-NbSe$_2$ such as strong (momentum-dependent) electron–phonon coupling. This is similar to the case of pristine 2H-NbSe$_2$ in which the underlying mechanism of CDW formation has been investigated for decades and still remains under intense debate. A consensus seems to exist that the driving force for CDW instabilities in 2H-NbSe$_2$ is a combined effect of lattice distortions[410–413,420] and its electronic structure leading to orbital dependent[405,407,417] and strong (momentum-dependent) electron–phonon coupling[404,405,407,411,412,417,438,442]. The main contributions arise from the Nb plane, concerning both, lattice distortions[410] and electronic contributions of the Nb d-orbitals.[407,410,417,442,443] Changes in CDW order are therefore likely related to changes in the electron–phonon coupling induced by structural variations within the Nb-plane for 2H-NbSe$_2$. In the case of 1T-NbSe$_2$, similarities in the voltage dependence to the (3×3)-CDW in terms of phase and amplitude (*cf.* Reference [401]) also suggests strong electron-phonon coupling as the driving mechanism for CDW formation and cannot be explained by Peierls instabilities of the lattice only. The CDW formation in 1T-NbSe$_2$ therefore turns out to be more complex than for other 1T-TMDs such as 1T-TaS$_2$[172,391,439] and 1T-TaSe$_2$[387,440,441].

11.2. The 1D stripe charge modulation

Finally, CDW instability at $T = 4.5\,\mathrm{K}$ are investigated. Here, the tridirectional (3×3)-CDW is expected pristine regions of 2H-NbSe$_2$ (Figure 11.1c) with $T_{CDW} = 34\,\mathrm{K}$. In the vicinity of the phase-engineered regions, however, one can observe large ($> 1000\,\mathrm{nm}$), atomically flat areas with a striped charge modulation (1D-CDW) with a smooth transition to the (3×3)-CDW as shown in Figure 11.4a,b. The CDW propagates perpendicular to the atomic lattice along a $\langle 210 \rangle$ direction (inset in Figure 11.4b) with a 1D-CDW wavelength of $a_{1D} = (\sqrt{3}a/2) = 3.5a^*$. This leads to a commensurate superstructure with doubled periodicity of $7a^*$ perpendicular to the close-packed rows of the surface. The inset in Figure 11.4b is a zoom-in of the underlying image to highlight the discussed periodicities. Interestingly, small regions of local (3×3)-order are discernible within the 1D-CDW pattern (green circle) as also reflected by diffuse spots Q_3 in the corresponding FFT (Figure 11.4c). It is likely that lattice defects are responsible for pinning the CDW, similar to what is observed in (3×3)-areas above T_{CDW}.[401] As the 1D stripe charge is suspected to be a strain-induced phenomenon (discussion below), this observation suggests that impurity engineering may be employed to render TMDs robust against deterioration by external influences like strain. Other spots within the FFT shown in Figure 11.4c correspond to the atomic lattice (Q_1, red), to the 1D-CDW ($Q_{3.5}$, blue) and to periodicities resulting from a superposition of the electronic modulation with the atomic lattice ($Q_{1+3.5}$, orange). Figure 11.4d presents an FFT-filtered image of Figure 11.4b that omits the (3×3)-patches and all contributions of the atomic corrugations that do not coincide with the CDW were filtered, i.e. only the spots Q_1, $Q_{1+3.5}$, and $Q_{3.5}$ were inversely Fourier transformed. This leaves only the 1D-CDW entangled with the atomic rows along the $\langle 210 \rangle$ direction. Interestingly, the filtered image bears remarkable similarity to the artificial image next to it. The model is a simple intensity plot of the amplitude of two superimposed $\cos^2(x)$-functions—one with periodicity a^* ($= 1/q_1$), the other with periodicity $3.5a^*$ ($= 1/q_{3.5}$). The model fit is further corroborated by line plots in the frequency space and in real space (Figure 11.4e and Figure 11.4f respectively). In frequency space, the peak positions and relative peak intensities agree well. In both real space cuts, one maximum of the CDW coincides with the atomic lattice resulting in a global maximum flanked by two shoulders, the next CDW peak however falls in between two atomic rows, creating two peaks. This picture also describes the observed apparent height of the atomic rows in the non-filtered images in Figure 11.4b very well. The good agreement strongly suggests a commensurate relationship of lattice and CDW.

Previously, the 1D-CDW has been observed to exist locally confined at buckled areas with an atomically smooth interface to the (3×3)-CDW of pristine NbSe$_2$[418]. Therefore, uniaxial strain in 2H-NbSe$_2$ was identified to cause an anisotropy in the electron–phonon coupling leading to transitions from tridirectional (2D) to unidirectional (1D) CDW order[407,418]. Intriguingly, a change in the interatomic distances of as little as $0.1\,\%$ (i.e. $\Delta a \approx 0.35\,\mathrm{pm}$) is sufficient to induce the transition. The magnitude of strain does not influence the CDW pattern, but always leads to the same 1D stripe structure.[407] Therefore it seems highly likely that the 1D-CDW observed in the vicinity of pulsed areas in this work is equivalent to the formerly reported "1Q"-pattern[418] at strongly buckled areas—despite the lack of evidence for strong structural distortions in our STM data.

Note that the external strain which favors the 1D-CDW likely acts uniformly on the
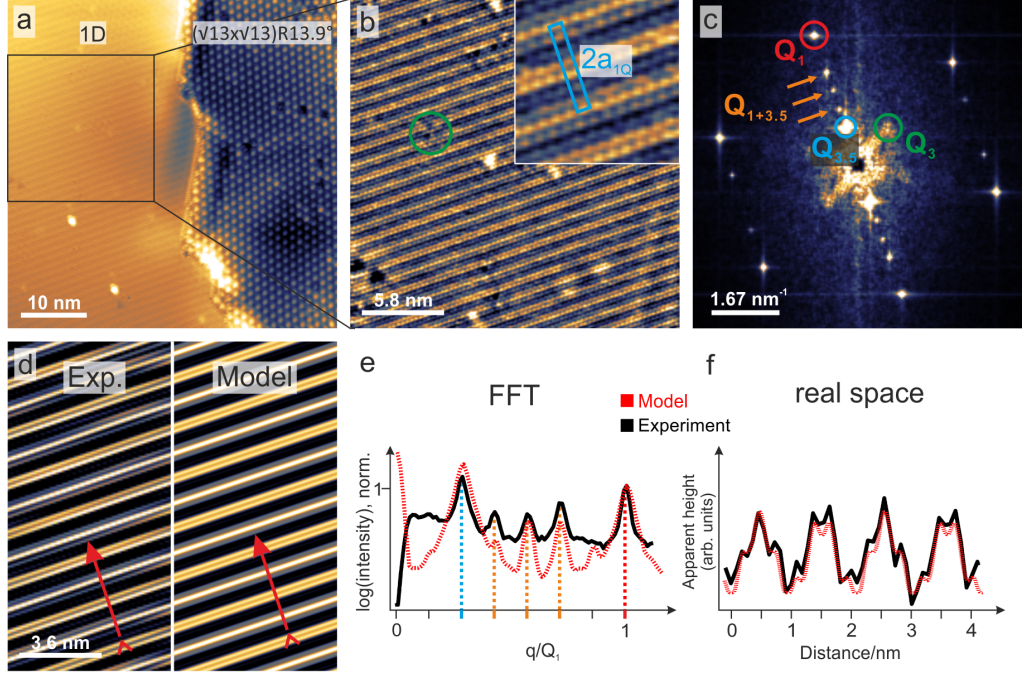
Figure 11.4. One dimensional CDW (1D-CDW) at the NbSe$_2$ surface at 4.5 K. a) In the vicinity of tip-induced surface modifications, a striped CDW was observed. b) STM image at $U = -200$ mV exhibiting local, short range (3×3)-CDW patches within the stripe pattern of the 1D-CDW as highlighted in green. The inset shows the CDW superstructure and its unit cell. c) The corresponding FFT image reflects the periodicities of the atomic lattice (Q_1, red), the 1D-CDW ($Q_{3.5}$, blue), the (3×3)-CDW (Q_3, green) as well as periodicities resulting from the superposition of the atomic lattice and the 1D-CDW ($Q_{1+3.5}$, orange). d) FFT-filtered image from b) that only includes information from $Q_{3.5}$ to Q_1 compared to a model (right image in d), for details of the model see text). e) Logarithmic plot of a line profile from the center of c) to Q_1 (normalized to the Bragg intensity) along with the corresponding intensity profile of the model FFT. f) Line profiles across both parts of d) along the same direction as indicated by the red arrows. The line profile accentuates the $7a^*$ periodicity of the 1D-CDW. Scan parameters: a, b) $U = -200$ mV, $I = 0.9$ nA.

lattice without introducing displacement periodicities related to the CDW wavelength. In contrast periodic lattice displacements associated with the Peierls instability create displacement patterns associated with distinct lattice positions. In the case of strain induced CDWs therefore, a strict relationship of the charge modulation to the lattice is not given a priori. Such a lock-in can however minimize the system's energy[418] and lead to a (locally) commensurate CDW from an intrinsically incommensurate CDW. The good agreement between STM data and the simple phenomenological model strongly suggests an alignment of lattice and electronic modulation. The lock-in will result in phase slips of the CDW or in simultaneous adaptations of the CDW maxima and the lattice to achieve a fit.[417] To determine whether a Peierls distortion is present, STM images of the occupied and unoccupied states were examined (*cf.* Figure 11.5). A purely Peierls driven CDW should exhibit contrast inversion (for example in one-dimensional charge order in MoSe$_2$[424]).
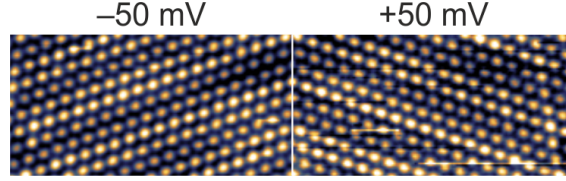
Figure 11.5. 1D-CDW stripe charge pattern imaged at $-50\,\mathrm{mV}$ (left) and $50\,\mathrm{mV}$ (right). The right image was vertically mirrored in order to arrange corresponding atomic rows from each image right next to one another. The data were atomically aligned in larger frames at distinct defects and the (3×3)-pattern before zooming on the region of interest shown here. At the mirror interface, bright (dim) atomic rows meet likewise bright (dim) ones: a contrast inversion as expected for CDW arising from Peierls instabilities accompanied by Fermi surface nesting cannot be observed.

However, the absence of a contrast inversion supports instead the phonon-driven scenario described for the stripe charge before.[407,417,418,444]

Reversible transitions from (3×3)- to 1D-CDW phases may be induced by the STM tip. This is illustrated by the findings presented in Figure 11.6 that shows the reversible transitions between both CDW phases (3×3 and 1D). For easier identification, the (3×3)-CDW regions are masked in green. Repeatedly scanning the STM-tip at comparatively high bias voltages of $U \approx 5\,\mathrm{V} - 6\,\mathrm{V}$ transforms parts of the (3×3)-CDW into the 1D-CDW (Figure 11.6b) and finally back to the initial (3×3)-CDW phase (Figure 11.6c). In addition, regions of the surface which were initially in 1D-CDW order (right hand side of Figure 11.6b) are also transformed. The observation of reversible phase transformations
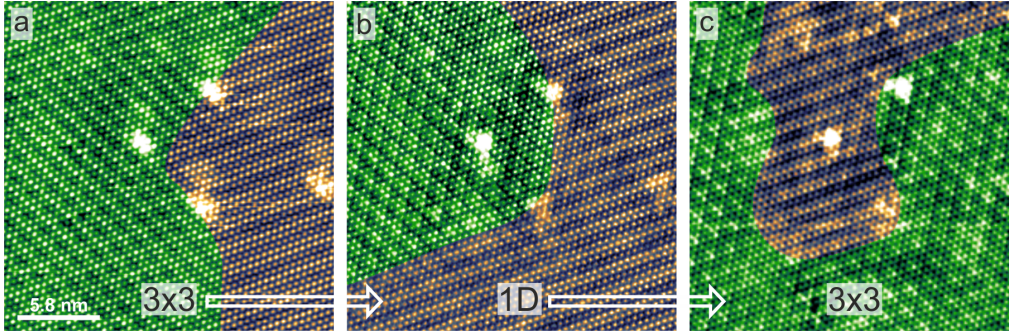
Figure 11.6. Tip-induced quantum phase transitions between 1D- and (3×3)-CDW. As a guide to the eye, the (3×3)-areas are masked in green. Scanning at high bias voltages ($U > 5\,\mathrm{V}$) can reversibly transform the CDW patterns. Scan parameters: a) $U = -50\,\mathrm{mV}$, $I = 2.0\,\mathrm{nA}$; b) $U = 50\,\mathrm{mV}$, $I = 2.5\,\mathrm{nA}$; c) $U = 70\,\mathrm{mV}$, $I = 2.5\,\mathrm{nA}$.

between 1D- and (3×3)-order underscores that (local) strain is a promising candidate to achieve phase engineering and manipulating TMD properties.[392,393,445,446] The switching mechanism however remains ambiguous. Since each imaged phase represents an energetic minimum of the system, the reversible switching between two minima suggests metastability of two states close in energy. Scanning the tip at high bias might be sufficient to locally heat the sample above T_{CDW} similar to STM assisted phase switching in 1T-

TaS_2[391]. Upon cooling the local pinning environment provided by the surrounding phases, defects, and local strain could favor one phase over the other. Besides a heating/cooling mechanism, charge driven phase transitions seem highly likely. For metastable ground states close in energy as observed here, the injection of charge was reported to cause switching for several TMDs[398–400]. Such phase transitions bare great promise for future applications as they can be electronically controlled via electrostatic gating[173,395–399].

Summary

In conclusion, low-temperature STM was used for structural and electronic phase engineering of the group-V TMD $NbSe_2$. By applying bias pulses with an STM tip, the coordination of the niobium atom switched from a trigonal prismatic (2H) to octahedral (1T) lattice, whereby the 1T-phase was identified by its characteristic $(\sqrt{13} \times \sqrt{13})R13.9°$ CDW order at temperatures down to $T = 4.5\,\text{K}$. Atomic-resolution STM images of the atomically sharp and lattice matched phase boundary corroborate the successful TMD phase-engineering, supported by the observation of concomitant changes in both atomic and associated electronic structure across the junction. Different 1T-CDW amplitudes were reported for the first time to hint the 2H-1T transition to be a few-layer phenomenon where interlayer interactions determine the CDW amplitude. The electronic properties of $2H\text{-}NbSe_2$ was furthermore reversibly modified between its intrinsic (3×3)- and a 1D-CDW by the STM tip. For the mechanisms of the phase transformation, different possible contributing factors were discussed, including temperature changes as well as charge injection by the STM tip. And whilst the precise mechanism of the phase changes is not known and warrants further investigation, the engineering of atomically sharp phase boundaries in transition metal dichalcogenides with substantially different electronic properties may promises their use for future atomically small electronic devices.

12. Summary and outlook

To conclude, this chapter summarizes the major results, provides ideas for future investigations and suggests potential experimental approaches for the investigation of low dimensional nano-architectures based on the LT-STM/AFM setup.

Summary

The summary follows the structure of the thesis and shortly reflects the key results.

Experimental setup. Prior to any experiments, a new experimental setup was installed, tested, and put into operation. The custom-designed UHV chamber houses a commercial LT-STM/AFM. Most importantly, small-amplitude non-contact AFM in the form of frequency modulation AFM was established at the chair for molecular nano-science (E20). The setup facilitates state-of-the-art, non-destructive investigations of surface confined nano-architectures in real-space with sub-molecular resolution and direct imaging of chemical bonds as well as force measurements, KPFM and other FM-AFM related techniques. Furthermore, crucial experimental routines like the epitaxial growth of sodium chloride and the controlled CO tip-functionalization were realized. The new setup delivered results for several high-impact publications in renowned peer-reviewed journals.

Metal-organic porphyrin networks on Ag(111). The formation of extended, porous, 2D, grid-like metal-organic networks was investigated by STM. The networks were comprised of deliberately functionalized porphyrin derivatives and copper adatoms. Steric constraints around the coordination center imposed by the molecules' functional groups were identified as driver for the network structures and their different formation pathways. The network formations were modeled by Monto Carlo simulations under consideration of the molecular characteristics only. Additionally, the intrinsic metal coordination properties turned out to be decisive for the emerging coordination motifs. So far, the metal's coordination qualities were mostly neglected when designing surface-based metal-organic coordination networks, but could be inferred to some extend from 3D metal-organic complexes. Consequently, this study introduced prospects for the programmed design and selection of molecular and monoatomic building blocks for surface-confined supramolecular networks and thus contributed to controlled engineering of metal-organic/organic architectures.

Adsorption geometries of 2H-TPP on coinage metal surfaces. A qualitative characterization of the adsorption geometries of individual, non-planar 2H-TPP molecules by means of FM-AFM confirmed a moderate saddle shape on Ag(111) but revealed an unexpected and unreported molecular conformation on Cu(111). The porphyrin exhibited an

extremely deformed macrocycle along with nearly flat phenyl legs. These findings refined the understanding of the molecular system and provided information neither accessible by STM imaging nor space-averaging experiments. FM-AFM—mostly applied to nearly flat species—can therefore also be employed as a powerful tool for the structural analysis of complex and flexible surface-anchored species and strongly deformed molecules with a pronounced 3D character without requiring costly particle-accelerator based experiments or sophisticated simulations for data analysis.

Synthesis of covalent nanostructures and single molecule chemistry.   This section presented a combined STM/nc-AFM study of porphyrin-based, surface-assisted C–C coupling reactions for single molecule chemistry and for the synthesis of covalent nanostructures on Ag(111) and Cu(111). The atomic-level structural analysis of the reaction products by nc-AFM with CO functionalized tips allowed their unambiguous characterization and helped to resolve contradicting conclusions of recently published studies—especially for the cyclodehydrogenative flattening of TPP molecules. In addition, changes in adsorption height of porphine molecules were detected by FM-AFM as a result of chemical modifications of the macrocycle indicating a changed substrate–adsorbate interaction. These findings highlight FM-AFM as powerful technique for the direct detection of relative adsorption height changes on the single molecule level, which is non-trivial to obtain by space-averaging methods or by theoretical modeling. Furthermore, the observation of a hitherto unreported tripyrrolic porphyrin fragment was observed on Cu(111). The unexpected degradation of the conjugated porphyrin macrocycle was related to its extreme structural deformations induced by the surface. These findings widened the capabilities of heterogeneous catalysis suggesting a novel route for destabilization and deconstruction of chemically and structurally robust molecular systems by conformational design.

Nanoscale phase engineering of niobium diselenide.   The structural and electronic properties of the group-V transition metal dichalcogenide $NbSe_2$ were engineered on the nanoscale by STM. The coordination geometry of the central niobium atom was switched from trigonal prismatic to octahedral resulting in a change of the crystal structure from $2H\text{-}NbSe_2$ to $1T\text{-}NbSe_2$ accompanied by modifications of electronic properties. Unprecedented high resolution data of the atomically sharp and lattice-matched phase boundary gave direct proof of a successful phase engineering for the first time. A detailed investigation of the resulting 1T-CDW suggested a complex formation mechanisms based on strong (momentum–dependent) electron–phonon coupling as well as interlayer interactions. Additionally, the first observation of extended 1D-CDW states in the 2H phase of $NbSe_2$ was reported and the electronic properties of $2H\text{-}NbSe_2$ were reversibly modified between its intrinsic 3x3- and the 1D-CDW. Therefore, this sections significantly advanced the understanding of charge density order and structural phase transitions in the transition metal dichalcogenide $NbSe_2$. The engineering of atomically sharp phase boundaries in transition metal dichalcogenides with substantially different electronic properties may be promising for future atomically small electronic devices.

Outlook

The presented experimental results were extensive and in many aspects also conclusive. However, some observations require additional research efforts to expedite a more comprehensive understanding; others inspire for pushing towards new, intriguing research fields. The following outlook is structured accordingly. First, possible follow up experiments are suggested that offer a straight forward approach for complementary investigations of previous observations. Then conceptional ideas are presented that might offer interesting routes for future experiments.

Complementary investigation of relative adsorption heights. Section 8 qualitatively revealed different adsorption heights for chemically in-equivalent porphine species and allowed a rough estimate of $\approx 0.3\,\text{Å}$ for the difference. FM-AFM however offers tools for determining relative heights precisely. This was first impressively demonstrated by Schuler et al. by determining adsorption heights and the adsorption geometries of single molecules[128] via extensive 3D Δf-spectroscopy maps. Furthermore, Albrecht et al. were able to determine height changes of only $0.5\,\text{Å}$ in the central copper ion of Cu-TPP by introducing vertical imaging, i.e. Δf-spectroscopy along a line[33]. And Schwarz et al. determined the geometric corrugation of a h-BN sheet on Cu(111) by calibrating the variation of the atomic contrast in Δf as a function of the tip height[447]. Such experimental procedures could be applied to porphines on metal surfaces to quantitatively determine adsorption height changes induced by chemical modifications of the macrocycle. This could advance the understanding of the absorbate–substrate interaction of this prototypical compound and help benchmarking theoretical simulations like density functional theory. Once the parameters are precisely determined for such a model system, it could be employed as a reference to determine the adsorption heights of unknown molecular systems without the need for space averaging methods like X-ray standing wave measurements or simulations.

Complementary characterization of 1T-NbSe$_2$. The nanoscale phase engineering of NbSe$_2$ presented in Section 11 offered STM techniques for the manipulation of TMDs. While it focused mostly on the engineering aspects, it would be desirable to clarify chemical and physical aspects like the phase change mechanisms (e.g. heat-/charge-/electric field-induced) as well as the electronic properties of 1T-NbSe$_2$ that was found to express Mott insulating properties as single layer[432]. The phase change mechanism could be elaborated by a detailed analysis of the material's response to bias pulses of different magnitude as a function of tip–sample separation, as e.g. done by Ma et al. (cf. Supplementary Figure 1 of the publication)[391]. A characterization of the electronic properties requires careful spectroscopic investigations that are however non-trivial to carry out. The tip often changes significantly upon the pulsing employed for phase engineering. Ideally, phase engineering would have to be followed by a sample exchange for tip-conditioning on a metal surface, after which the NbSe$_2$ sample would have to be re-transferred to recover the nano-meter scaled engineered regions. Alternatively, spectra on 2H-NbSe$_2$ could be established as reference with a conditioned tip. Or metal layers could be epitaxially grown on a TMD sample to circumvent multiple sample exchange procedures. The insights of the suggested experiments are crucial from a fundamental point of view for characterizing NbSe$_2$. Furthermore, this knowledge might upon intriguing aspects for the fabrication of

atomic-scale devices featuring atomically precise metal-to-insulator junctions[169] or electronically controllable phase transitions[173,395–399].

Towards chemical recognition in AFM. Section 6.3 and 9 exposed a lack of chemical contrast despite atomic resolution. This manifested in the inability to visualize metal atoms within metal-organic complexes as well as the non-distinction between elements within organic molecules (e.g. carbon vs. nitrogen). Considerable effort has been made to improve SPM capabilities by exploration of tip-terminations[120,197,199,448] (also see Section 5.3) and by the development of experimental techniques[10,33,35,37,447,449–452]. Some have achieved chemical sensitivity[449,453–455]. However, the chemical analysis of single molecules and the chemical identification of individual atoms is non-trivial and often requires extensive theory support. Chemical sensitivity can only be achieved in SPM by distinguishing tip–sample interactions of different elements with atomic resolution. Therefore it might be helpful to custom-tailor the tip termination for the desired tip–element interaction as demonstrated by an enhanced STM contrast above the metal ion of metal-porphyrins with modified STM tips[190,305]. The use of such "sensor molecules" was also suggested for AFM decades ago[456].

Generally, chemical recognition might also be achieved by employing reactive tips like metal tips[457]. Contrary, a CO tip is ideal to easily achieve high lateral resolution but is chemically inert. Here, it is important to emphasize that a reactive tip does not necessarily goes in hand with the loss of atomic resolution as demonstrated in several studies[35,198,450,457]. However, adsorbates might easily be manipulated at close tip–sample distances necessary for structure determination by AFM. Therefore, it seems important to immobilizing molecules by anchoring on reactive surfaces, through strong surface-adsorbate interactions via functional groups, in covalent networks or metal-organic structures. Additionally, probing at close distances using the multipass technique[35,450,458] might be beneficial over constant height imaging. Employing reactive tips might also enable the characterization of chemically active sites[459,460] for catalysis research. On a final note, the most promising approach seems to be joining complementary information gathered with a combined STM/AFM setup, i.e. a structural analysis by AFM with CO-terminated tips, completed by investigations with reactive tips and force spectroscopy, STS, STM, KPFM, IETS, and others, supported by theory.

The search for novel materials. For the biggest part, this work presented molecular nanoscience based on organic materials and finished with a glimpse into the vivid field of transition metal dichalcogenides. However, the two research fields also exhibit some overlap opening intriguing possibilities for creating hybrid systems that have yet to be explored. The combination of TMDs with organic molecules for catalysis, TMD functionalization and manipulation is still in its infancy.[461–467] Recent reviews highlight successes of this burgeoning research field[174,468].

Furthermore, a general research interest in atomically thin and 2D materials was triggered by the discovery of graphene and has led to a considerable interest in single layer TMDs. As demonstrated in Section 11 and recent high-impact publications[391,419,424,439], SPM techniques are ideal for exploring and characterizing TMD samples. The enormous interest in TMD research is reflected by the high citation counts that these publications

have gathered in only a year or two. It therefore seems highly promising to pursue SPM based TMD research. A starting point—and possibly relatively easy to realize—could be the exploration of molecular adsorption onto TMD surfaces of bulk or single layer samples[26,27]. This might offer structural and phase control of TMDs[467] and could e.g. be exploited for gas sensors[469]. Furthermore, the characterization of single layer TMDs that have not yet been investigated by SPM techniques might offer interesting physics[398]. Additionally, the investigation of TMD samples suggests implementing new experimental techniques. The manipulator and scanning stage presented in Section 4 offer six electrical contacts and it is feasible to carry out (in-plane) transport measurements and apply in-plane electric fields[397,400].

References

1. Lyshevski, S. E. *Nano and Molecular Electronics Handbook.* Boca Raton: CRC Press, 2016. 931 pp. (cited on p. 1).

2. Waser, R. *Nanoelectronics and Information Technology.* Weinheim: Wiley-VCH, 2012. 1041 pp. (cited on p. 1).

3. Zäch, M., Hägglund, C., Chakarov, D., and Kasemo, B. Nanoscience and Nanotechnology for Advanced Energy Systems. *Curr. Opin. Solid State Mater. Sci.* **10**, 132–143 (2006). DOI: 10.1016/j.cossms.2007.04.004 (cited on p. 1).

4. Aricò, A. S., Bruce, P., Scrosati, B., Tarascon, J.-M., and van Schalkwijk, W. Nanostructured Materials for Advanced Energy Conversion and Storage Devices. *Nat Mater* **4**, 366–377 (2005). DOI: 10.1038/nmat1368 (cited on p. 1).

5. Rothenberg, G. *Catalysis: Concepts and Green Applications.* Weinheim: Wiley-VCH, 2017. 319 pp. (cited on p. 1).

6. The Royal Swedish Academy of Sciences. Chemical Processes on Solid Surfaces - Scientific Background on the Nobel Prize in Chemitrsy 2007. 2007. https://www.nobelprize.org/nobel_prizes/chemistry/laureates/2007/advanced-chemistryprize2007.pdf (cited on p. 1).

7. The Royal Swedish Academy of Sciences. Graphene - Scientific Background on the Nobel Prize in Physics 2010. 2010. https://www.nobelprize.org/nobel_prizes/physics/laureates/2010/advanced-physicsprize2010.pdf (cited on p. 1).

8. The Royal Swedish Academy of Sciences. Molecular Machines - Scientific Background on the Nobel Prize in Chemistry 2016. 2016. https://www.nobelprize.org/nobel_prizes/chemistry/laureates/2016/advanced-chemistryprize2016.pdf (cited on p. 1).

9. Gross, L., Mohn, F., Moll, N., Liljeroth, P., and Meyer, G. The Chemical Structure of a Molecule Resolved by Atomic Force Microscopy. *Science* **325**, 1110–1114 (2009). DOI: 10.1126/science.1176210 (cited on pp. 1, 23, 29 sq., 36, 64, 67, 85 sq., 89–92).

10. Morita, S., Giessibl, F. J., Meyer, E., and Wiesendanger, R., eds. *Noncontact Atomic Force Microscopy Vol. 3.* Cham: Springer International Publishing, 2015. 539 pp. DOI: 10.1007/978-3-319-15588-3 (cited on pp. 1, 38, 136).

11. Auwärter, W., Écija, D., Klappenberger, F., and Barth, J. V. Porphyrins at Interfaces. *Nat. Chem.* **7**, 105–120 (2015). DOI: 10.1038/nchem.2159 (cited on pp. 1, 63, 74, 89 sq., 92 sq., 95, 115, 119).

12. Gottfried, J. M. Surface Chemistry of Porphyrins and Phthalocyanines. *Surf. Sci. Rep.* **70**, 259–379 (2015). DOI: 10.1016/j.surfrep.2015.04.001 (cited on pp. 1, 63, 74, 89 sq., 95, 115).

13. Milgrom, L. R. *The Colours of Life: An Introduction to the Chemistry of Porphyrins and Related Compounds.* Oxford: Oxford University Press, 1997. 258 pp. (cited on p. 1).

14. Ishikawa, N., Sugita, M., Ishikawa, T., Koshihara, S.-y., and Kaizu, Y. Mononuclear Lanthanide Complexes with a Long Magnetization Relaxation Time at High Temperatures: A New Category of Magnets at the Single-Molecular Level. *J. Phys. Chem. B* **108**, 11265–11271 (2004). DOI: 10.1021/jp0376065 (cited on p. 1).

References

15. Wäckerlin, C., Donati, F., Singha, A., Baltic, R., Rusponi, S., Diller, K., Patthey, F., Pivetta, M., Lan, Y., Klyatskaya, S., Ruben, M., Brune, H., and Dreiser, J. Giant Hysteresis of Single-Molecule Magnets Adsorbed on a Nonmagnetic Insulator. *Adv. Mater.* **28**, 5195–5199 (2016). DOI: 10.1002/adma.201506305 (cited on p. 1).

16. Barona-Castaño, J. C., Carmona-Vargas, C. C., Brocksom, T. J., and de Oliveira, K. T. Porphyrins as Catalysts in Scalable Organic Reactions. *Molecules* **21**, 310 (2016). DOI: 10.3390/molecules21030310 (cited on p. 1).

17. Qiao, J., Liu, Y., Hong, F., and Zhang, J. A Review of Catalysts for the Electroreduction of Carbon Dioxide to Produce Low-Carbon Fuels. *Chem. Soc. Rev.* **43**, 631–675 (2013). DOI: 10.1039/C3CS60323G (cited on pp. 1, 62).

18. Kesters, J., Verstappen, P., Kelchtermans, M., Lutsen, L., Vanderzande, D., and Maes, W. Porphyrin-Based Bulk Heterojunction Organic Photovoltaics: The Rise of the Colors of Life. *Adv. Energy Mater.* **5** (2015). DOI: 10.1002/aenm.201500218 (cited on pp. 1, 62).

19. Li, L.-L. and Wei-Guang Diau, E. Porphyrin-Sensitized Solar Cells. *Chem. Soc. Rev.* **42**, 291–304 (2013). DOI: 10.1039/C2CS35257E (cited on p. 1).

20. Barth, J. V., Costantini, G., and Kern, K. Engineering Atomic and Molecular Nanostructures at Surfaces. *Nature* **437**, 671–679 (2005). DOI: 10.1038/nature04166 (cited on pp. 1, 73 sq., 95).

21. Boyd, P. D. W. and Reed, C. A. Fullerene-Porphyrin Constructs. *Acc. Chem. Res.* **38**, 235–242 (2005). DOI: 10.1021/ar040168f (cited on p. 1).

22. Vijayaraghavan, S., Écija, D., Auwärter, W., Joshi, S., Seufert, K., Seitsonen, A. P., Tashiro, K., and Barth, J. V. Selective Supramolecular Fullerene–Porphyrin Interactions and Switching in Surface-Confined C_{60}–Ce(TPP)$_2$ Dyads. *Nano Lett.* **12**, 4077–4083 (2012). DOI: 10.1021/nl301534p (cited on p. 1).

23. Bottari, G., Herranz, M. Á., Wibmer, L., Volland, M., Rodríguez-Pérez, L., Guldi, D. M., Hirsch, A., Martín, N., D'Souza, F., and Torres, T. Chemical Functionalization and Characterization of Graphene-Based Materials. *Chem. Soc. Rev.* **46**, 4464–4500 (2017). DOI: 10.1039/C7CS00229G (cited on p. 1).

24. He, Y., Garnica, M., Bischoff, F., Ducke, J., Bocquet, M.-L., Batzill, M., Auwärter, W., and Barth, J. V. Fusing Tetrapyrroles to Graphene Edges by Surface-Assisted Covalent Coupling. *Nat. Chem.* **9**, 33–38 (2017). DOI: 10.1038/nchem.2600 (cited on pp. 1 sq., 63, 71, 85, 87, 95, 102 sq., 111, 120, 175).

25. Takagi, S., Eguchi, M., Tryk, D. A., and Inoue, H. Porphyrin Photochemistry in Inorganic/Organic Hybrid Materials: Clays, Layered Semiconductors, Nanotubes, and Mesoporous Materials. *J. Photochem. Photobiol. C* **7**, 104–126 (2006). DOI: 10.1016/j.jphotochemrev.2006.04.002 (cited on p. 1).

26. Zhang, H., Ji, J., Gonzalez, A. A., and Choi, J. H. Tailoring Photoelectrochemical Properties of Semiconducting Transition Metal Dichalcogenide Nanolayers with Porphyrin Functionalization. *J. Mater. Chem. C* (2017). DOI: 10.1039/C7TC02861J (cited on pp. 1, 137).

27. Rückerl, F., Klaproth, T., Schuster, R., Büchner, B., and Knupfer, M. Surface Functionalization of WSe$_2$ by F$_{16}$CoPc. *Phys. Status Solidi (b)* **254** (2017). DOI: 10.1002/pssb.201600656 (cited on pp. 1, 137).

28. Rao, C. N. R., Gopalakrishnan, K., and Maitra, U. Comparative Study of Potential Applications of Graphene, MoS$_2$, and Other Two-Dimensional Materials in Energy Devices, Sensors, and Related Areas. *ACS Appl. Mater. Interfaces* **7**, 7809–7832 (2015). DOI: 10.1021/am509096x (cited on p. 2).

29. Novoselov, K. S., Fal'ko, V. I., Colombo, L., Gellert, P. R., Schwab, M. G., and Kim, K. A Roadmap for Graphene. *Nature* **490**, 192–200 (2012). DOI: 10.1038/nature11458 (cited on p. 2).

30. Jariwala, D., Sangwan, V. K., Lauhon, L. J., Marks, T. J., and Hersam, M. C. Emerging Device Applications for Semiconducting Two-Dimensional Transition Metal Dichalcogenides. *ACS Nano* **8**, 1102–1120 (2014). DOI: 10.1021/nn500064s (cited on pp. 2, 58).

31. Jarvis, S. P., Taylor, S., Baran, J. D., Champness, N. R., Larsson, J. A., and Moriarty, P. Measuring the Mechanical Properties of Molecular Conformers. *Nat. Commun.* **6**, 8338 (2015). DOI: 10.1038/ncomms9338 (cited on pp. 2, 89 sq., 94).

32. Jarvis, S. P., Taylor, S., Baran, J. D., Thompson, D., Saywell, A., Mangham, B., Champness, N. R., Larsson, J. A., and Moriarty, P. Physisorption Controls the Conformation and Density of States of an Adsorbed Porphyrin. *J. Phys. Chem. C* **119**, 27982–27994 (2015). DOI: 10.1021/acs.jpcc.5b08350 (cited on pp. 2, 89 sq., 94).

33. Albrecht, F., Bischoff, F., Auwärter, W., Barth, J. V., and Repp, J. Direct Identification and Determination of Conformational Response in Adsorbed Individual Nonplanar Molecular Species Using Noncontact Atomic Force Microscopy. *Nano Lett.* **16**, 7703–7709 (2016). DOI: 10.1021/acs.nanolett.6b03769 (cited on pp. 2, 66, 71, 84 sq., 89–92, 94, 102, 120, 135 sq., 170, 175).

34. Chen, X., Lei, S., Lotze, C., Czekelius, C., Paulus, B., and Franke, K. J. Conformational Adaptation and Manipulation of Manganese Tetra(4-Pyridyl)Porphyrin Molecules on Cu(111). *J. Chem. Phys.* **146**, 092316 (2017). DOI: 10.1063/1.4974313 (cited on pp. 2, 89 sq., 94).

35. Moreno, C., Stetsovych, O., Shimizu, T. K., and Custance, O. Imaging Three-Dimensional Surface Objects with Submolecular Resolution by Atomic Force Microscopy. *Nano Lett.* **15**, 2257–2262 (2015). DOI: 10.1021/nl504182w (cited on pp. 2, 37, 90, 136).

36. Gross, L., Mohn, F., Moll, N., Schuler, B., Criado, A., Guitián, E., Peña, D., Gourdon, A., and Meyer, G. Bond-Order Discrimination by Atomic Force Microscopy. *Science* **337**, 1326–1329 (2012). DOI: 10.1126/science.1225621 (cited on pp. 2, 66, 85 sq., 89 sqq., 102, 117).

37. Albrecht, F., Pavliček, N., Herranz-Lancho, C., Ruben, M., and Repp, J. Characterization of a Surface Reaction by Means of Atomic Force Microscopy. *J. Am. Chem. Soc.* **137**, 7424–7428 (2015). DOI: 10.1021/jacs.5b03114 (cited on pp. 2, 85, 89–92, 94, 102, 136).

38. Amato, I. Candid Cameras for the Nanoworld. *Science* **276**, 1982–1985 (1997). DOI: 10.1126/science.276.5321.1982 (cited on p. 7).

39. Binnig, G. and Rohrer, H. Scanning Tunneling Microscopy. *IBM J. Res. Dev.* **30**, 355–369 (1986) (cited on p. 7).

40. Binnig, G. and Rohrer, H. Scanning Tunneling Microscopy—from Birth to Adolescence. *Rev. Mod. Phys.* **59**, 615–625 (1987). DOI: 10.1103/RevModPhys.59.615 (cited on p. 7).

41. Binnig, G., Rohrer, H., Gerber, C., and Weibel, E. 7 x 7 Reconstruction on Si(111) Resolved in Real Space. *Phys. Rev. Lett.* **50**, 120–123 (1983). DOI: 10.1103/PhysRevLett.50.120 (cited on p. 7).

42. Binnig, G., Quate, C. F., and Gerber, C. Atomic Force Microscope. *Phys. Rev. Lett.* **56**, 930–933 (1986). DOI: 10.1103/PhysRevLett.56.930 (cited on p. 7).

43. Hansma, P. K., Elings, V. B., Marti, O., and Bracker, C. E. Scanning Tunneling Microscopy and Atomic Force Microscopy: Application to Biology and Technology. *Science* **242**, 209–216 (1988). DOI: 10.1126/science.3051380 (cited on p. 7).

44. Drake, B., Prater, C. B., Weisenhorn, A. L., Gould, S. A., Albrecht, T. R., Quate, C. F., Cannell, D. S., Hansma, H. G., and Hansma, P. K. Imaging Crystals, Polymers, and Processes in Water with the Atomic Force Microscope. *Science* **243**, 1586–1589 (1989). DOI: 10.1126/science.2928794 (cited on p. 7).

45. Giessibl, F. J. High-Speed Force Sensor for Force Microscopy and Profilometry Utilizing a Quartz Tuning Fork. *Appl. Phys. Lett.* **73**, 3956–3958 (1998). DOI: 10.1063/1.122948 (cited on pp. 7, 23, 34).

46. Giessibl, F. J. Atomic Resolution on Si(111)-(7 x 7) by Noncontact Atomic Force Microscopy with a Force Sensor Based on a Quartz Tuning Fork. *Appl. Phys. Lett.* **76**, 1470–1472 (2000). DOI: 10.1063/1.126067 (cited on p. 7).

References

47. Majzik, Z., Setvín, M., Bettac, A., Feltz, A., Cháb, V., and Jelínek, P. Simultaneous Current, Force and Dissipation Measurements on the Si(111) 7 x 7 Surface with an Optimized qPlus AFM/STM Technique. *Beilstein J. Nanotechnol.* **3**, 249–259 (2012). DOI: 10.3762/bjnano.3.28 (cited on pp. 7, 34).

48. Torbrügge, S., Schaff, O., and Rychen, J. Application of the KolibriSensor® to Combined Atomic-Resolution Scanning Tunneling Microscopy and Noncontact Atomic-Force Microscopy Imaging. *J. Vac. Sci. Technol.* **28**, C4E12–C4E20 (2010). DOI: 10.1116/1.3430544 (cited on pp. 7, 23).

49. Giessibl, F. J., Pielmeier, F., Eguchi, T., An, T., and Hasegawa, Y. Comparison of Force Sensors for Atomic Force Microscopy Based on Quartz Tuning Forks and Length-Extensional Resonators. *Phys. Rev. B* **84**, 125409 (2011). DOI: 10.1103/PhysRevB.84.125409 (cited on p. 7).

50. Albers, B. J., Liebmann, M., Schwendemann, T. C., Baykara, M. Z., Heyde, M., Salmeron, M., Altman, E. I., and Schwarz, U. D. Combined Low-Temperature Scanning Tunneling/Atomic Force Microscope for Atomic Resolution Imaging and Site-Specific Force Spectroscopy. *Rev. Sci. Instrum.* **79**, 033704 (2008). DOI: 10.1063/1.2842631 (cited on pp. 7, 34).

51. IEEE-SA Style Manual. 2014. https://development.standards.ieee.org/myproject/Public/mytools/draft/styleman.pdf (cited on pp. 10, 16).

52. Stroscio, J. A. and Kaiser, W. J. *Scanning Tunneling Microscopy.* San Diego, London: Academic Press, 1993 (cited on p. 10).

53. Bai, C. *Scanning tunneling microscopy and its applications.* Springer-Verlag Berlin Heidelberg, 2000 (cited on p. 10).

54. Chen, C. J. *Introduction to scanning tunneling microscopy.* Oxford: Oxford University Press, 2008 (cited on p. 10).

55. Oura, K., Lifshits, V., Saranin, A., Zotov, A., and Katayama, M. *Surface Science.* Springer-Verlag Berlin Heidelberg, 2003 (cited on pp. 10, 44, 62).

56. Binnig, G., Rohrer, H., Gerber, C., and Weibel, E. Tunneling through a Controllable Vacuum Gap. *Appl. Phys. Lett.* **40**, 178–180 (1982). DOI: 10.1063/1.92999 (cited on p. 12).

57. Bardeen, J. Tunnelling from a Many-Particle Point of View. *Phys. Rev. Lett.* **6**, 57–59 (1961). DOI: 10.1103/PhysRevLett.6.57 (cited on p. 12).

58. Tersoff, J. and Hamann, D. R. Theory of the Scanning Tunneling Microscope. *Phys. Rev. B* **31**, 805–813 (1985). DOI: 10.1103/PhysRevB.31.805 (cited on p. 12).

59. Tersoff, J. and Hamann, D. R. Theory and Application for the Scanning Tunneling Microscope. *Phys. Rev. Lett.* **50**, 1998–2001 (1983). DOI: 10.1103/PhysRevLett.50.1998 (cited on p. 13).

60. Hamers, R. J. Atomic-Resolution Surface Spectroscopy with the Scanning Tunneling Microscope. *Annu. Rev. Phys. Chem.* **40**, 531–559 (1989). DOI: 10.1146/annurev.pc.40.100189.002531 (cited on p. 16).

61. Wahl, P., Diekhöner, L., Schneider, M. A., and Kern, K. Background Removal in Scanning Tunneling Spectroscopy of Single Atoms and Molecules on Metal Surfaces. *Rev. Sci. Instrum.* **79**, 043104 (2008). DOI: 10.1063/1.2907533 (cited on p. 17).

62. Passoni, M., Donati, F., Li Bassi, A., Casari, C. S., and Bottani, C. E. Recovery of Local Density of States Using Scanning Tunneling Spectroscopy. *Phys. Rev. B* **79**, 045404 (2009). DOI: 10.1103/PhysRevB.79.045404 (cited on p. 17).

63. Wagner, C., Franke, R., and Fritz, T. Evaluation of $I(V)$ Curves in Scanning Tunneling Spectroscopy of Organic Nanolayers. *Phys. Rev. B* **75**, 235432 (2007). DOI: 10.1103/PhysRevB.75.235432 (cited on p. 17).

64. Koslowski, B., Dietrich, C., Tschetschetkin, A., and Ziemann, P. Evaluation of Scanning Tunneling Spectroscopy Data: Approaching a Quantitative Determination of the Electronic Density of States. *Phys. Rev. B* **75**, 035421 (2007). DOI: 10.1103/PhysRevB.75.035421 (cited on p. 17).

65. Hipps, K. W. and Mazur, U. Inelastic Electron Tunneling: An Alternative Molecular Spectroscopy. *J. Phys. Chem.* **97**, 7803–7814 (1993). DOI: 10.1021/j100132a004 (cited on p. 17).

66. Hipps, K. and Mazur, U. Inelastic Electron Tunneling Spectroscopy. In: *Handbook of Vibrational Spectroscopy.* John Wiley & Sons, Ltd, 2006 (cited on p. 17).

67. Reed, M. A. Inelastic Electron Tunneling Spectroscopy. *Mater. Today* **11**, 46–50 (2008). DOI: 10.1016/S1369-7021(08)70238-4 (cited on p. 17).

68. Binnig, G., Frank, K. H., Fuchs, H., Garcia, N., Reihl, B., Rohrer, H., Salvan, F., and Williams, A. R. Tunneling Spectroscopy and Inverse Photoemission: Image and Field States. *Phys. Rev. Lett.* **55**, 991–994 (1985). DOI: 10.1103/PhysRevLett.55.991 (cited on p. 18).

69. Becker, R. S., Golovchenko, J. A., Hamann, D. R., and Swartzentruber, B. S. Real-Space Observation of Surface States on Si(111) 7 × 7 with the Tunneling Microscope. *Phys. Rev. Lett.* **55**, 2032–2034 (1985). DOI: 10.1103/PhysRevLett.55.2032 (cited on p. 18).

70. Feenstra, R. M. Scanning Tunneling Spectroscopy. *Surf. Sci.* **299**, 965–979 (1994). DOI: 10.1016/0039-6028(94)90710-2 (cited on p. 18).

71. Eigler, D. M. and Schweizer, E. K. Positioning Single Atoms with a Scanning Tunnelling Microscope. *Nature* **344**, 524–526 (1990). DOI: 10.1038/344524a0 (cited on p. 18).

72. Stroscio, J. A. and Eigler, D. M. Atomic and Molecular Manipulation with the Scanning Tunneling Microscope. *Science* **254**, 1319–1326 (1991). DOI: 10.1126/science.254.5036.1319 (cited on p. 18).

73. Crommie, M. F., Lutz, C. P., and Eigler, D. M. Imaging Standing Waves in a Two-Dimensional Electron Gas. *Nature* **363**, 524–527 (1993). DOI: 10.1038/363524a0 (cited on p. 18).

74. Hasegawa, Y. and Avouris, P. Direct Observation of Standing Wave Formation at Surface Steps Using Scanning Tunneling Spectroscopy. *Phys. Rev. Lett.* **71**, 1071–1074 (1993). DOI: 10.1103/PhysRevLett.71.1071 (cited on p. 18).

75. Avouris, P., Lyo, I.-W., Walkup, R. E., and Hasegawa, Y. Real Space Imaging of Electron Scattering Phenomena at Metal Surfaces. *J. Vac. Sci. Technol. B* **12**, 1447–1455 (1994). DOI: 10.1116/1.587314 (cited on p. 18).

76. Crommie, M. F., Lutz, C. P., and Eigler, D. M. Confinement of Electrons to Quantum Corrals on a Metal Surface. *Science* **262**, 218–220 (1993). DOI: 10.1126/science.262.5131.218 (cited on pp. 18, 21).

77. Avouris, P. and Lyo, I.-W. Probing the Chemistry and Manipulating Surfaces at the Atomic Scale with the STM. *Appl. Surf. Sci.* **60**, 426–436 (1992). DOI: 10.1016/0169-4332(92)90455-7 (cited on p. 18).

78. van der Lit, J. Non-contact AFM and STM studies of molecular systems on weakly interacting surfaces—Can't touch this! Dissertation. Utrecht University, 2016 (cited on p. 20).

79. Avouris, P. Manipulation of Matter at the Atomic and Molecular Levels. *Acc. Chem. Res.* **28**, 95–102 (1995). DOI: 10.1021/ar00051a002 (cited on p. 21).

80. Lorente, N., Rurali, R., and Tang, H. Single-Molecule Manipulation and Chemistry with the STM. *J. Phys.: Condens. Matter* **17**, S1049 (2005). DOI: 10.1088/0953-8984/17/13/003 (cited on p. 21).

81. Poon, C. Y. and Bhushan, B. Comparison of Surface Roughness Measurements by Stylus Profiler, AFM and Non-Contact Optical Profiler. *Wear* **190**, 76–88 (1995). DOI: 10.1016/0043-1648(95)06697-7 (cited on p. 23).

82. Rugar, D. and Hansma, P. Atomic Force Microscopy. *Phys. Today* **43**, 23–30 (1990) (cited on pp. 23, 25).

83. Binnig, G., Gerber, C., Stoll, E., Albrecht, T. R., and Quate, C. F. Atomic Resolution with Atomic Force Microscope. *EPL* **3**, 1281 (1987). DOI: 10.1209/0295-5075/3/12/006 (cited on p. 23).

84. Albrecht, T. R., Grütter, P., Horne, D., and Rugar, D. Frequency Modulation Detection Using High-Q Cantilevers for Enhanced Force Microscope Sensitivity. *J. Appl. Phys.* **69**, 668–673 (1991). DOI: 10.1063/1.347347 (cited on p. 23).

References

85. Bhushan, B. and Marti, O. Scanning Probe Microscopy – Principle of Operation, Instrumentation, and Probes. In: *Springer Handbook of Nanotechnology.* Springer-Verlag Berlin Heidelberg, 2010, 573–617 (cited on p. 23).

86. Martin, Y., Williams, C. C., and Wickramasinghe, H. K. Atomic Force Microscope–force Mapping and Profiling on a Sub 100-A Scale. *J. Appl. Phys.* **61**, 4723–4729 (1987). DOI: 10.1063/1.338807 (cited on p. 23).

87. Sader, J. E. and Jarvis, S. P. Accurate Formulas for Interaction Force and Energy in Frequency Modulation Force Spectroscopy. *Appl. Phys. Lett.* **84**, 1801–1803 (2004). DOI: 10.1063/1.1667267 (cited on pp. 25, 39).

88. Baykara, M. Z. and Schwarz, U. D. 3D Force Field Spectroscopy. In: *Noncontact Atomic Force Microscopy.* Ed. by S. Morita, F. J. Giessibl, E. Meyer, and R. Wiesendanger. Springer International Publishing, 2015, 9–28. DOI: 10.1007/978-3-319-15588-3_2 (cited on pp. 25, 39).

89. Pawlak, R., Kawai, S., Glatzel, T., and Meyer, E. Single Molecule Force Spectroscopy. In: *Noncontact Atomic Force Microscopy.* Ed. by S. Morita, F. J. Giessibl, E. Meyer, and R. Wiesendanger. Springer International Publishing, 2015, 195–222. DOI: 10.1007/978-3-319-15588-3_11 (cited on pp. 25 sq.).

90. Giessibl, F. J. Forces and Frequency Shifts in Atomic-Resolution Dynamic-Force Microscopy. *Phys. Rev. B* **56**, 16010–16015 (1997). DOI: 10.1103/PhysRevB.56.16010 (cited on pp. 25, 27 sq.).

91. Giessibl, F. J. Advances in Atomic Force Microscopy. *Rev. Mod. Phys.* **75**, 949–983 (2003). DOI: 10.1103/RevModPhys.75.949 (cited on pp. 25, 27, 33 sq., 38).

92. Ternes, M., Lutz, C. P., Hirjibehedin, C. F., Giessibl, F. J., and Heinrich, A. J. The Force Needed to Move an Atom on a Surface. *Science* **319**, 1066–1069 (2008). DOI: 10.1126/science.1150288 (cited on p. 25).

93. Weymouth, A. J., Hofmann, T., and Giessibl, F. J. Quantifying Molecular Stiffness and Interaction with Lateral Force Microscopy. *Science* **343**, 1120–1122 (2014). DOI: 10.1126/science.1249502 (cited on pp. 25, 29).

94. Kisiel, M., Samadashvili, M., Gysin, U., and Meyer, E. Non-Contact Friction. In: *Noncontact Atomic Force Microscopy.* Ed. by S. Morita, F. J. Giessibl, E. Meyer, and R. Wiesendanger. Springer International Publishing, 2015, 93–110. DOI: 10.1007/978-3-319-15588-3_6 (cited on p. 25).

95. Giessibl, F. J., Herz, M., and Mannhart, J. Friction Traced to the Single Atom. *PNAS* **99**, 12006–12010 (2002). DOI: 10.1073/pnas.182160599 (cited on p. 25).

96. Pfeiffer, O., Bennewitz, R., Baratoff, A., Meyer, E., and Grütter, P. Lateral-Force Measurements in Dynamic Force Microscopy. *Phys. Rev. B* **65**, 161403 (2002). DOI: 10.1103/PhysRevB.65.161403 (cited on p. 25).

97. Ott, W., Jobst, M. A., Schoeler, C., Gaub, H. E., and Nash, M. A. Single-Molecule Force Spectroscopy on Polyproteins and Receptor–ligand Complexes: The Current Toolbox. *J. Struct. Biol.* **197**, 3–12 (2017). DOI: 10.1016/j.jsb.2016.02.011 (cited on p. 25).

98. Kobayashi, K. and Yamada, H. Recent Progress in Frequency Modulation Atomic Force Microscopy in Liquids. In: *Noncontact Atomic Force Microscopy.* Ed. by S. Morita, F. J. Giessibl, E. Meyer, and R. Wiesendanger. Springer International Publishing, 2015, 411–433. DOI: 10.1007/978-3-319-15588-3_19 (cited on p. 25).

99. Schwarz, A. and Wiesendanger, R. Magnetic Sensitive Force Microscopy. *Nano Today* **3**, 28–39 (2008). DOI: 10.1016/S1748-0132(08)70013-6 (cited on p. 26).

100. Koblischka, M. R. and Hartmann, U. Recent Advances in Magnetic Force Microscopy. *Ultramicroscopy* **97**, 103–112 (2003). DOI: 10.1016/S0304-3991(03)00034-2 (cited on p. 26).

101. Grütter, P., Mamin, H. J., and Rugar, D. Magnetic Force Microscopy (MFM). In: *Scanning Tunneling Microscopy II.* Ed. by D. R. Wiesendanger and P. D. H.-J. Güntherodt. Springer-Verlag Berlin Heidelberg, 1995, 151–207. DOI: 10.1007/978-3-642-79366-0_5 (cited on p. 26).

102. Schwarz, A. and Heinze, S. Magnetic Exchange Force Spectroscopy. In: *Noncontact Atomic Force Microscopy*. Ed. by S. Morita, F. J. Giessibl, E. Meyer, and R. Wiesendanger. Springer International Publishing, 2015, 111–125. DOI: 10.1007/978-3-319-15588-3_7 (cited on p. 26).

103. Mohn, F., Gross, L., Moll, N., and Meyer, G. Imaging the Charge Distribution within a Single Molecule. *Nat. Nanotechnol.* **7**, 227–231 (2012). DOI: 10.1038/nnano.2012.20 (cited on pp. 26, 56).

104. Hamaker, H. C. The London-van Der Waals Attraction between Spherical Particles. *Physica* **4**, 1058–1072 (1937). DOI: 10.1016/S0031-8914(37)80203-7 (cited on p. 26).

105. Israelachvili, J. N. Van Der Waals Forces. In: *Intermolecular and Surface Forces (Third Edition)*. San Diego: Academic Press, 2011, 107–132. DOI: 10.1016/B978-0-12-375182-9.10006-5 (cited on pp. 26 sq.).

106. Israelachvili, J. N. Repulsive Steric Forces, Total Intermolecular Pair Potentials, and Liquid Structure. In: *Intermolecular and Surface Forces (Third Edition)*. San Diego: Academic Press, 2011, 133–149. DOI: 10.1016/B978-0-12-375182-9.10007-7 (cited on pp. 26 sq., 29).

107. Ibe, J. P., Bey Jr., P., Brandow, S. L., Brizzolara, R. A., Burnham, N. A., DiLella, D. P., Lee, K. P., Marrian, C. R. K., and Colton, R. J. On the Electrochemical Etching of Tips for Scanning Tunneling Microscopy. *J. Vac. Sci. Technol. A* **8**, 3570–3575 (1990). DOI: 10.1116/1.576509 (cited on pp. 27, 63).

108. Israelachvili, J. N. Thermodynamic and Statistical Aspects of Intermolecular Forces. In: *Intermolecular and Surface Forces (Third Edition)*. San Diego: Academic Press, 2011, 23–51. DOI: 10.1016/B978-0-12-375182-9.10002-8 (cited on p. 27).

109. Morse, P. M. Diatomic Molecules According to the Wave Mechanics. II. Vibrational Levels. *Phys. Rev.* **34**, 57–64 (1929). DOI: 10.1103/PhysRev.34.57 (cited on p. 29).

110. Gildemeister, A. E., Ihn, T., Barengo, C., Studerus, P., and Ensslin, K. Construction of a Dilution Refrigerator Cooled Scanning Force Microscope. *Rev. Sci. Instrum.* **78**, 013704 (2007). DOI: 10.1063/1.2431793 (cited on pp. 32 sq.).

111. Dürig, U., Steinauer, H. R., and Blanc, N. Dynamic Force Microscopy by Means of the Phase-Controlled Oscillator Method. *J. Appl. Phys.* **82**, 3641–3651 (1997). DOI: 10.1063/1.365726 (cited on p. 32).

112. Giessibl, F. J. Vorrichtung zum berührungslosen Abtasten von Oberflächen und Verfahren dafür. German patent, DE 19633546. 1998 (cited on p. 34).

113. Giessibl, F. J. Atomic Resolution of the Silicon (111)-(7x7) Surface by Atomic Force Microscopy. *Science* **267**, 68–71 (1995). DOI: 10.1126/science.267.5194.68 (cited on p. 34).

114. Giessibl, F. J. Principle of NC-AFM. In: *Noncontact Atomic Force Microscopy*. Ed. by P. S. Morita, P. R. Wiesendanger, and P. E. Meyer. Springer-Verlag Berlin Heidelberg, 2002, 11–46. DOI: 10.1007/978-3-642-56019-4_2 (cited on p. 34).

115. Falter, J., Stiefermann, M., Langewisch, G., Schurig, P., Hölscher, H., Fuchs, H., and Schirmeisen, A. Calibration of Quartz Tuning Fork Spring Constants for Non-Contact Atomic Force Microscopy: Direct Mechanical Measurements and Simulations. *Beilstein J. Nanotechnol.* **5**, 507–516 (2014). DOI: 10.3762/bjnano.5.59 (cited on p. 34).

116. Giessibl, F. J. Sensor und Verfahren zum berührungslosen Abtasten einer Oberfläche. German patent, DE102010052037 B4. 2013 (cited on p. 35).

117. Pielmeier, F. Atomic Force Microscopy in the Picometer Regime - Resolving Spins and Non-Trivial Surface Terminations. Dissertation. 2014 (cited on p. 35).

118. Welker, J., Weymouth, A. J., and Giessibl, F. J. The Influence of Chemical Bonding Configuration on Atomic Identification by Force Spectroscopy. *ACS Nano* **7**, 7377–7382 (2013). DOI: 10.1021/nn403106v (cited on p. 36).

119. Sang, H., Jarvis, S. P., Zhou, Z., Sharp, P., Moriarty, P., Wang, J., Wang, Y., and Kantorovich, L. Identifying Tips for Intramolecular NC-AFM Imaging via in Situ Fingerprinting. *Sci. Rep.* **4**, 6678 (2014). DOI: 10.1038/srep06678 (cited on p. 36).

120. Gross, L., Schuler, B., Mohn, F., Moll, N., Repp, J., and Meyer, G. Atomic Resolution on Molecules with Functionalized Tips. In: *Noncontact Atomic Force Microscopy.* Ed. by S. Morita, F. J. Giessibl, E. Meyer, and R. Wiesendanger. Springer International Publishing, 2015, 223–246. DOI: 10.1007/978-3-319-15588-3_12 (cited on pp. 36, 136).

121. Moll, N., Gross, L., Mohn, F., Curioni, A., and Meyer, G. The Mechanisms Underlying the Enhanced Resolution of Atomic Force Microscopy with Functionalized Tips. *New J. Phys.* **12**, 125020 (2010). DOI: 10.1088/1367-2630/12/12/125020 (cited on pp. 36 sq., 91).

122. Boneschanscher, M. P., van der Lit, J., Sun, Z., Swart, I., Liljeroth, P., and Vanmaekelbergh, D. Quantitative Atomic Resolution Force Imaging on Epitaxial Graphene with Reactive and Nonreactive AFM Probes. *ACS Nano* **6**, 10216–10221 (2012). DOI: 10.1021/nn3040155 (cited on p. 37).

123. Pawlak, R., Kawai, S., Fremy, S., Glatzel, T., and Meyer, E. Atomic-Scale Mechanical Properties of Orientated C_{60} Molecules Revealed by Noncontact Atomic Force Microscopy. *ACS Nano* **5**, 6349–6354 (2011). DOI: 10.1021/nn201462g (cited on p. 37).

124. Schulz, F., Hämäläinen, S., and Liljeroth, P. Atomic-Scale Contrast Formation in AFM Images on Molecular Systems. In: *Noncontact Atomic Force Microscopy.* Ed. by S. Morita, F. J. Giessibl, E. Meyer, and R. Wiesendanger. Springer International Publishing, 2015, 173–194. DOI: 10.1007/978-3-319-15588-3_10 (cited on p. 37).

125. Hämäläinen, S. K., van der Heijden, N., van der Lit, J., den Hartog, S., Liljeroth, P., and Swart, I. Intermolecular Contrast in Atomic Force Microscopy Images without Intermolecular Bonds. *Phys. Rev. Lett.* **113**, 186102 (2014). DOI: 10.1103/PhysRevLett.113.186102 (cited on pp. 37, 87, 108).

126. Morita, S., Wiesendanger, R., and Meyer, E. *Noncontact Atomic Force Microscopy Vol. 1.* Springer, 2002 (cited on p. 38).

127. Morita, S., Giessibl, F. J., and Wiesendanger, R. *Noncontact Atomic Force Microscopy Vol. 2.* 2009 (cited on p. 38).

128. Schuler, B., Liu, W., Tkatchenko, A., Moll, N., Meyer, G., Mistry, A., Fox, D., and Gross, L. Adsorption Geometry Determination of Single Molecules by Atomic Force Microscopy. *Phys. Rev. Lett.* **111**, 106103 (2013). DOI: 10.1103/PhysRevLett.111.106103 (cited on pp. 39, 85, 89–92, 94, 102, 135).

129. Albrecht, F. Combined STM/AFM with Functionalized Tips Applied to Individual Molecules: Chemical Reactions, Geometric Structure and Charge Distribution. Dissertation. 2017 (cited on pp. 43, 170).

130. Pavliček, N. Scanning Probe Methods Applied to Molecular Electronics. Dissertation. University of Regensburg, 2013 (cited on p. 43).

131. Mohn, F. Probing electronic and structural properties of single molecules on the atomic scale. Dissertation. University of Regensburg, 2012 (cited on pp. 43, 49).

132. He, Y. Installation of a Low-temperature Scanning Probe Microscope and Investigations of Low-dimensional Metal-organic Networks. M.Sc. thesis. Technische Universität München, 2013 (cited on p. 44).

133. Createc Fischer & Co. GmbH, Industriestr. 9, 74391 Erligheim, Germany. http://createc.de (cited on pp. 44, 47, 50).

134. VAb Vakuum-Anlagenbau GmbH, Marie-Curie-Straße 11, 25337 Elmshorn, Germany. http://www.vab-vakuum.com (cited on pp. 43, 48).

135. Newport Corporation, 1791 Deere Avenue, Irvine, California 92606, USA. https://www.newport.com (cited on p. 43).

136. Redhead, P., Hobson, J., and Kornelsen, E. *The Physical Basis of Ultrahigh Vacuum.* London: Chapman and Hall, 1968 (cited on p. 44).

137. Leybold GmbH, Bonner Str. 498, 50968 Köln, Germany. https://www.leybold.com (cited on p. 45).

138. Pfeiffer Vacuum GmbH, Berliner Strasse 43, 35614 Asslar, Germany. https://www.pfeiffer-vacuum.com (cited on p. 45).

139. Gamma Vacuum, 2915 133rd Street West, Shakopee, MN 55379, USA. http://www.gammavacuum.com (cited on p. 45).

140. H. Seider, Createc Fischer & Co. GmbH. *KryostatNW250CF.* Manual. 2012 (cited on p. 46).

141. Createc Fischer & Co. GmbH. *How to install the LT-STM head.* Manual. 2013 (cited on pp. 46, 49).

142. CryoVac GmbH & Co. KG, Heuserweg 14, 53842 Troisdorf, Germany. http://www.cryovac.de (cited on p. 47).

143. SPECS GmbH, Voltastrasse 5, 13355 Berlin, Germany. http://www.specs.de (cited on p. 47).

144. Stanford Research Systems, Inc., 1290-D Reamwood Avenue, Sunnyvale, CA 94089, USA. http://www.thinksrs.com (cited on p. 48).

145. Zöphel, S. Der Aufbau eines Tieftemperatur-Rastertunnelmikroskops und Strukturuntersuchungen auf vicinalen Kupferoberflächen. Dissertation. Freie Universität Berlin, 2000 (cited on pp. 48 sq.).

146. Createc Fischer & Co. GmbH. *How to Assemble a Metal Sample Holder.* Manual. 2002 (cited on pp. 48 sq.).

147. Scienta Omicron GmbH, Limburger Strasse 75, 65232 Taunusstein, Germany. http://www.scientaomicron.com (cited on pp. 48 sq.).

148. HeatWave Labs, Inc., 195 Aviation Way, Suite 100, Watsonville, CA 95076-2069, USA. http://www.cathode.com/h_uhv.htm (cited on p. 48).

149. Frohn, J., Wolf, J. F., Besocke, K., and Teske, M. Coarse Tip Distance Adjustment and Positioner for a Scanning Tunneling Microscope. *Rev. Sci. Instrum.* **60**, 1200–1201 (1989). DOI: 10.1063/1.1140287 (cited on p. 49).

150. Pan, S. H., Hudson, E. W., and Davis, J. C. 3He Refrigerator Based Very Low Temperature Scanning Tunneling Microscope. *Rev. Sci. Instrum.* **70**, 1459–1463 (1999). DOI: 10.1063/1.1149605 (cited on pp. 50 sq.).

151. Chen, L., Kim, S. H., Lee, A. K. H., and Lozanne, A. de. Simple Electronics for Inertial and Pan-Type Piezoelectric Positioners Used in Scanning Probe Microscopes. *Rev. Sci. Instrum.* **83**, 013708 (2012). DOI: 10.1063/1.3680082 (cited on p. 51).

152. PiezoDrive Pty Ltd. Piezoelectric Tube Scanners. https://www.piezodrive.com/actuators/piezoelectric-tube-scanners/ (cited on p. 52).

153. SPECS Zurich GmbH, Technoparkstrasse 1, 8005 Zurich, Switzerland. http://www.specs-zurich.com (cited on p. 52).

154. National Instruments, 11500 N Mopac Expy, Austin, TX 78759, USA. http://www.ni.com (cited on p. 52).

155. Repp, J., Meyer, G., Stojković, S. M., Gourdon, A., and Joachim, C. Molecules on Insulating Films: Scanning-Tunneling Microscopy Imaging of Individual Molecular Orbitals. *Phys. Rev. Lett.* **94**, 026803 (2005). DOI: 10.1103/PhysRevLett.94.026803 (cited on pp. 56, 64).

156. Gross, L., Moll, N., Mohn, F., Curioni, A., Meyer, G., Hanke, F., and Persson, M. High-Resolution Molecular Orbital Imaging Using a *p*-Wave STM Tip. *Phys. Rev. Lett.* **107**, 086101 (2011). DOI: 10.1103/PhysRevLett.107.086101 (cited on pp. 56, 64).

157. Repp, J. and Meyer, G. Scanning Tunneling Spectroscopy of Molecules on Insulating Films. *CHIMIA* **64**, 370–375 (2010). DOI: 10.2533/chimia.2010.370 (cited on p. 56).

158. Repp, J., Meyer, G., Olsson, F. E., and Persson, M. Controlling the Charge State of Individual Gold Adatoms. *Science* **305**, 493–495 (2004). DOI: 10.1126/science.1099557 (cited on p. 56).

159. Olsson, F. E., Paavilainen, S., Persson, M., Repp, J., and Meyer, G. Multiple Charge States of Ag Atoms on Ultrathin NaCl Films. *Phys. Rev. Lett.* **98**, 176803 (2007). DOI: 10.1103/PhysRevLett.98.176803 (cited on p. 56).

160. Wiesendanger, R. *Scanning Probe Microscopy and Spectroscopy: Methods and Applications.* Cambridge: Cambridge University Press, 1994. 664 pp. DOI: 10.1017/CBO9780511524356 (cited on p. 56).

161. Repp, J., Meyer, G., Paavilainen, S., Olsson, F. E., and Persson, M. Scanning Tunneling Spectroscopy of Cl Vacancies in NaCl Films: Strong Electron-Phonon Coupling in Double-Barrier Tunneling Junctions. *Phys. Rev. Lett.* **95**, 225503 (2005). DOI: 10.1103/PhysRevLett.95.225503 (cited on p. 56).

162. Baron, T., Gentile, P., Magnea, N., and Mur, P. Single-Electron Charging Effect in Individual Si Nanocrystals. *Appl. Phys. Lett.* **79**, 1175–1177 (2001). DOI: 10.1063/1.1392302 (cited on p. 56).

163. Nazin, G. V., Wu, S. W., and Ho, W. Tunneling Rates in Electron Transport through Double-Barrier Molecular Junctions in a Scanning Tunneling Microscope. *PNAS* **102**, 8832–8837 (2005). DOI: 10.1073/pnas.0501171102 (cited on p. 56).

164. Sigma-Aldrich Chemie GmbH, Eschenstraße 5, 82024 Taufkirchen, Germany. http://www.sigmaaldrich.com (cited on p. 57).

165. Bennewitz, R., Barwich, V., Bammerlin, M., Loppacher, C., Guggisberg, M., Baratoff, A., Meyer, E., and Güntherodt, H. Ultrathin Films of NaCl on Cu(111): A LEED and Dynamic Force Microscopy Study. *Surf. Sci.* **438**, 289–296 (1999). DOI: 10.1016/S0039-6028(99)00586-5 (cited on p. 57).

166. Repp, J., Meyer, G., and Rieder, K.-H. Snell's Law for Surface Electrons: Refraction of an Electron Gas Imaged in Real Space. *Phys. Rev. Lett.* **92**, 036803 (2004). DOI: 10.1103/PhysRevLett.92.036803 (cited on pp. 57 sq.).

167. Bischoff, F., Seufert, K., Auwärter, W., Joshi, S., Vijayaraghavan, S., Écija, D., Diller, K., Papageorgiou, A. C., Fischer, S., Allegretti, F., Duncan, D. A., Klappenberger, F., Blobner, F., Han, R., and Barth, J. V. How Surface Bonding and Repulsive Interactions Cause Phase Transformations: Ordering of a Prototype Macrocyclic Compound on Ag(111). *ACS Nano* **7**, 3139–3149 (2013). DOI: 10.1021/nn305487c (cited on pp. 58, 97 sq., 176).

168. Snezhkova, O., Bischoff, F., He, Y., Wiengarten, A., Chaudhary, S., Johansson, N., Schulte, K., Knudsen, J., Barth, J. V., Seufert, K., Auwärter, W., and Schnadt, J. Iron Phthalocyanine on Cu(111): Coverage-Dependent Assembly and Symmetry Breaking, Temperature-Induced Homocoupling, and Modification of the Adsorbate-Surface Interaction by Annealing. *J. Chem. Phys* **144**, 094702 (2016). DOI: 10.1063/1.4942121 (cited on pp. 58, 71, 120, 175).

169. Kappera, R., Voiry, D., Yalcin, S. E., Branch, B., Gupta, G., Mohite, A. D., and Chhowalla, M. Phase-Engineered Low-Resistance Contacts for Ultrathin MoS_2 Transistors. *Nat. Mater.* **13**, 1128–1134 (2014). DOI: 10.1038/nmat4080 (cited on pp. 58, 123, 126, 136).

170. Wang, Q. H., Kalantar-Zadeh, K., Kis, A., Coleman, J. N., and Strano, M. S. Electronics and Optoelectronics of Two-Dimensional Transition Metal Dichalcogenides. *Nat. Nanotechnol.* **7**, 699–712 (2012). DOI: 10.1038/nnano.2012.193 (cited on pp. 58 sq., 123).

171. Bissett, M. A., Worrall, S. D., Kinloch, I. A., and Dryfe, R. A. W. Comparison of Two-Dimensional Transition Metal Dichalcogenides for Electrochemical Supercapacitors. *Electrochimica Acta* **201**, 30–37 (2016). DOI: 10.1016/j.electacta.2016.03.190 (cited on p. 58).

172. Rossnagel, K. On the Origin of Charge-Density Waves in Select Layered Transition-Metal Dichalcogenides. *J. Phys.: Condens. Matter* **23**, 213001 (2011). DOI: 10.1088/0953-8984/23/21/213001 (cited on pp. 58, 127 sq.).

173. Hollander, M. J., Liu, Y., Lu, W.-J., Li, L.-J., Sun, Y.-P., Robinson, J. A., and Datta, S. Electrically Driven Reversible Insulator–Metal Phase Transition in 1T-TaS_2. *Nano Lett.* **15**, 1861–1866 (2015). DOI: 10.1021/nl504662b (cited on pp. 58, 132, 136).

174. Chhowalla, M., Shin, H. S., Eda, G., Li, L.-J., Loh, K. P., and Zhang, H. The Chemistry of Two-Dimensional Layered Transition Metal Dichalcogenide Nanosheets. *Nat. Chem.* **5**, 263–275 (2013). DOI: 10.1038/nchem.1589 (cited on pp. 59, 123 sq., 136).

175. Yamamura, Y. and Tawara, H. Energy Dependence of Ion-Induced Sputtering Yields from Monatomic Solids at Normal Incidence. *At. Data Nucl. Data Tables* **62**, 149–253 (1996). DOI: 10.1006/adnd.1996.0005 (cited on pp. 60 sq.).

176. SPECS GmbH. Useful Information and Facts about the Practice of Sputtering. http://www.specs.de/cms/upload/PDFs/IQE11-35/sputter-info.pdf (cited on p. 60).

177. Schmid, M. A Simple Sputter Yield Calculator [IAP/TU Wien]. 2006. https://www.iap.tuwien.ac.at/www/surface/sputteryield (cited on p. 61).

178. Garnica, M., Schwarz, M., Ducke, J., He, Y., Bischoff, F., Barth, J. V., Auwärter, W., and Stradi, D. Comparative Study of the Interfaces of Graphene and Hexagonal Boron Nitride with Silver. *Phys. Rev. B* **94**, 155431 (2016). DOI: 10.1103/PhysRevB.94.155431 (cited on pp. 61, 71, 175).

179. Seufert, K., Bocquet, M.-L., Auwärter, W., Weber-Bargioni, A., Reichert, J., Lorente, N., and Barth, J. V. Cis-Dicarbonyl Binding at Cobalt and Iron Porphyrins with Saddle-Shape Conformation. *Nat. Chem.* **3**, 114–119 (2011). DOI: 10.1038/nchem.956 (cited on pp. 61, 65, 89).

180. Tao, S., Li, G., and Zhu, H. Metalloporphyrins as Sensing Elements for the Rapid Detection of Trace TNT Vapor. *J. Mater. Chem.* **16**, 4521–4528 (2006). DOI: 10.1039/B606061G (cited on p. 62).

181. Costley, D., Ewan, C. M., Fowley, C., McHale, A. P., Atchison, J., Nomikou, N., and Callan, J. F. Treating Cancer with Sonodynamic Therapy: A Review. *Int. J. Hyperthermia* **31**, 107–117 (2015). DOI: 10.3109/02656736.2014.992484 (cited on p. 62).

182. Mori, H., Tanaka, T., and Osuka, A. Fused Porphyrinoids as Promising Near-Infrared Absorbing Dyes. *J. Mater. Chem. C* **1**, 2500–2519 (2013). DOI: 10.1039/C3TC00932G (cited on p. 63).

183. Tanaka, T. and Osuka, A. Conjugated Porphyrin Arrays: Synthesis, Properties and Applications for Functional Materials. **44**, 943–969 (2015). DOI: 10.1039/C3CS60443H (cited on p. 63).

184. Wiengarten, A., Seufert, K., Auwärter, W., Ecija, D., Diller, K., Allegretti, F., Bischoff, F., Fischer, S., Duncan, D. A., Papageorgiou, A. C., Klappenberger, F., Acres, R. G., Ngo, T. H., and Barth, J. V. Surface-Assisted Dehydrogenative Homocoupling of Porphine Molecules. *J. Am. Chem. Soc.* **136**, 9346–9354 (2014). DOI: 10.1021/ja501680n (cited on pp. 63, 95, 97, 99, 101 sq., 108, 111, 176).

185. Gottfried, M. and Marbach, H. Surface-Confined Coordination Chemistry with Porphyrins and Phthalocyanines: Aspects of Formation, Electronic Structure, and Reactivity. *Z. Phys. Chem.* **223**, 53–74 (2009). DOI: 10.1524/zpch.2009.6024 (cited on pp. 63, 95).

186. Lucier, A.-S. Preparation and Characterization of Tungsten Tips Suitable for Molecular Electronics Studies. M.Sc. thesis. McGill University, 2004 (cited on p. 63).

187. Garnaes, J., Kragh, F., Mo/rch, K. A., and Thölén, A. R. Transmission Electron Microscopy of Scanning Tunneling Tips. *J. Vac. Sci. Technol. A* **8**, 441–444 (1990). DOI: 10.1116/1.576417 (cited on p. 63).

188. Ernst, S. Optimisation of the Preparation Process for Tips Used in Scanning Tunneling Microscopy. Diplomarbeit. Technische Universität Dresden, 2006 (cited on p. 63).

189. Bartels, L., Meyer, G., and Rieder, K.-H. Controlled Vertical Manipulation of Single CO Molecules with the Scanning Tunneling Microscope: A Route to Chemical Contrast. *Appl. Phys. Lett.* **71**, 213–215 (1997). DOI: 10.1063/1.119503 (cited on pp. 64 sq., 67).

190. Nishino, T., Ohshiro, T., and Umezawa, Y. Molecular Tips for "Intermolecular Tunneling Microscopy". *Jpn. J. Appl. Phys.* **46**, 5519 (2007). DOI: 10.1143/JJAP.46.5519 (cited on pp. 64, 88, 136).

191. Temirov, R., Soubatch, S., Neucheva, O., Lassise, A. C., and Tautz, F. S. A Novel Method Achieving Ultra-High Geometrical Resolution in Scanning Tunnelling Microscopy. *New J. Phys.* **10**, 053012 (2008). DOI: 10.1088/1367-2630/10/5/053012 (cited on p. 64).

192. Weiss, C., Wagner, C., Kleimann, C., Rohlfing, M., Tautz, F. S., and Temirov, R. Imaging Pauli Repulsion in Scanning Tunneling Microscopy. *Phys. Rev. Lett.* **105**, 086103 (2010). DOI: 10.1103/PhysRevLett.105.086103 (cited on p. 64).

193. Kichin, G., Weiss, C., Wagner, C., Tautz, F. S., and Temirov, R. Single Molecule and Single Atom Sensors for Atomic Resolution Imaging of Chemically Complex Surfaces. *J. Am. Chem. Soc.* **133**, 16847–16851 (2011). DOI: 10.1021/ja204624g (cited on p. 64).

194. Hapala, P., Kichin, G., Wagner, C., Tautz, F. S., Temirov, R., and Jelínek, P. Mechanism of High-Resolution STM/AFM Imaging with Functionalized Tips. *Phys. Rev. B* **90**, 085421 (2014). DOI: 10.1103/PhysRevB.90.085421 (cited on pp. 64, 87, 108).

195. Jarvis, S. P., Rashid, M. A., Sweetman, A., Leaf, J., Taylor, S., Moriarty, P., and Dunn, J. Intermolecular Artifacts in Probe Microscope Images of C_{60} Assemblies. *Phys. Rev. B* **92**, 241405 (2015). DOI: 10.1103/PhysRevB.92.241405 (cited on pp. 64, 87, 108).

196. Wagner, C., Green, M. F. B., Leinen, P., Deilmann, T., Krüger, P., Rohlfing, M., Temirov, R., and Tautz, F. S. Scanning Quantum Dot Microscopy. *Phys. Rev. Lett.* **115**, 026101 (2015). DOI: 10.1103/PhysRevLett.115.026101 (cited on p. 64).

197. Mohn, F., Schuler, B., Gross, L., and Meyer, G. Different Tips for High-Resolution Atomic Force Microscopy and Scanning Tunneling Microscopy of Single Molecules. *Appl. Phys. Lett.* **102**, 073109 (2013). DOI: 10.1063/1.4793200 (cited on pp. 64, 136).

198. Mönig, H., Hermoso, D. R., Díaz Arado, O., Todorović, M., Timmer, A., Schüer, S., Langewisch, G., Pérez, R., and Fuchs, H. Submolecular Imaging by Noncontact Atomic Force Microscopy with an Oxygen Atom Rigidly Connected to a Metallic Probe. *ACS Nano* **10**, 1201–1209 (2016). DOI: 10.1021/acsnano.5b06513 (cited on pp. 64, 136).

199. Xin, X., Gan, L.-Y., Van Hove, M. A., Ren, X., Wang, H., Guo, C.-S., and Zhao, Y. Exploring Molecules beyond CO as Tip Functionalizations in High-Resolution Noncontact Atomic Force Microscopy: A First Principles Approach. *ACS Omega* **1**, 1004–1009 (2016). DOI: 10.1021/acsomega.6b00168 (cited on pp. 64, 136).

200. Bartels, L., Meyer, G., Rieder, K.-H., Velic, D., Knoesel, E., Hotzel, A., Wolf, M., and Ertl, G. Dynamics of Electron-Induced Manipulation of Individual CO Molecules on Cu(111). *Phys. Rev. Lett.* **80**, 2004–2007 (1998). DOI: 10.1103/PhysRevLett.80.2004 (cited on pp. 65, 67).

201. Gajdoš, M., Eichler, A., and Hafner, J. CO Adsorption on Close-Packed Transition and Noble Metal Surfaces: Trends from Ab Initio Calculations. *J. Phys.: Condens. Matter* **16**, 1141 (2004). DOI: 10.1088/0953-8984/16/8/001 (cited on p. 65).

202. Snezhkova, O., Lüder, J., Wiengarten, A., Burema, S. R., Bischoff, F., He, Y., Rusz, J., Knudsen, J., Bocquet, M.-L., Seufert, K., Barth, J. V., Auwärter, W., Brena, B., and Schnadt, J. Nature of the Bias-Dependent Symmetry Reduction of Iron Phthalocyanine on Cu(111). *Phys. Rev. B* **92**, 075428 (2015). DOI: 10.1103/PhysRevB.92.075428 (cited on pp. 65, 71, 175).

203. Lee, H. J. and Ho, W. Single-Bond Formation and Characterization with a Scanning Tunneling Microscope. *Science* **286**, 1719–1722 (1999). DOI: 10.1126/science.286.5445.1719 (cited on pp. 65 sq.).

204. Bischoff, F., He, Y., Seufert, K., Stassen, D., Bonifazi, D., Barth, J. V., and Auwärter, W. Tailoring Large Pores of Porphyrin Networks on Ag(111) by Metal-Organic Coordination. *Chem. Eur. J.* **22**, 15298–15306 (2016). DOI: 10.1002/chem.201602154 (cited on pp. 71, 81, 170, 175).

205. Bischoff, F., Auwärter, W., Barth, J. V., Schiffrin, A., Fuhrer, M., and Weber, B. Nanoscale Phase Engineering of Niobium Diselenide. *Chem. Mater.* (2017). DOI: 10.1021/acs.chemmater.7b03061 (cited on pp. 71, 175).

206. Bischoff, F., Michelitsch, G., Riss, A., Reuter, K., Barth, J. V., and Auwärter, W. Surface-catalyzed ring-opening reaction and porphyrin deconstruction via conformational design. In preparation (cited on pp. 71, 175).

207. Craig, G. A. and Murrie, M. 3d Single-Ion Magnets. *Chem. Soc. Rev.* **44**, 2135–2147 (2015). DOI: 10.1039/C4CS00439F (cited on p. 73).

208. Gao, S., ed. *Molecular Nanomagnets and Related Phenomena.* **164**. Berlin, Heidelberg: Springer, 2015. DOI: 10.1007/978-3-662-45723-8 (cited on p. 73).

209. Lux, L., Williams, K., and Ma, S. Heat-Treatment of Metal–organic Frameworks for Green Energy Applications. *CrystEngComm* **17**, 10–22 (2014). DOI: 10.1039/C4CE01499E (cited on p. 73).

210. Ke, F.-S., Wu, Y.-S., and Deng, H. Metal-Organic Frameworks for Lithium Ion Batteries and Supercapacitors. *J. Solid State Chem.* **223**, 109–121 (2015). DOI: 10.1016/j.jssc.2014.07.008 (cited on p. 73).

211. Leus, K., Liu, Y.-Y., and Voort, P. V. D. Metal-Organic Frameworks as Selective or Chiral Oxidation Catalysts. *Catal. Rev. Sci. Eng.* **56**, 1–56 (2014). DOI: 10.1080/01614940.2014.864145 (cited on p. 73).

212. Ruben, M., Rojo, J., Romero-Salguero, F. J., Uppadine, L. H., and Lehn, J.-M. Grid-Type Metal Ion Architectures: Functional Metallosupramolecular Arrays. *Angew. Chem. Int. Ed.* **43**, 3644–3662 (2004). DOI: 10.1002/anie.200300636 (cited on p. 73).

213. Bartels, L. Tailoring Molecular Layers at Metal Surfaces. *Nat. Chem.* **2**, 87–95 (2010). DOI: 10.1038/nchem.517 (cited on pp. 73 sq.).

214. Lin, N., Stepanow, S., Ruben, M., and Barth, J. V. Surface-Confined Supramolecular Coordination Chemistry. In: *Templates in Chemistry III.* Ed. by P. Broekmann, K.-H. Dötz, and C. A. Schalley. Springer-Verlag Berlin Heidelberg, 2008, 1–44. DOI: 10.1007/128_2008_150 (cited on pp. 73 sq.).

215. Gutzler, R., Stepanow, S., Grumelli, D., Lingenfelder, M., and Kern, K. Mimicking Enzymatic Active Sites on Surfaces for Energy Conversion Chemistry. *Acc. Chem. Res.* **48**, 2132–2139 (2015). DOI: 10.1021/acs.accounts.5b00172 (cited on pp. 73 sq.).

216. Grumelli, D., Wurster, B., Stepanow, S., and Kern, K. Bio-Inspired Nanocatalysts for the Oxygen Reduction Reaction. *Nat. Commun.* **4**, 2904 (2013). DOI: 10.1038/ncomms3904 (cited on pp. 73 sq.).

217. Schlickum, U., Decker, R., Klappenberger, F., Zoppellaro, G., Klyatskaya, S., Ruben, M., Silanes, I., Arnau, A., Kern, K., Brune, H., and Barth, J. V. Metal-Organic Honeycomb Nanomeshes with Tunable Cavity Size. *Nano Lett.* **7**, 3813–3817 (2007). DOI: 10.1021/nl072466m (cited on pp. 74, 83).

218. Decker, R., Schlickum, U., Klappenberger, F., Zoppellaro, G., Klyatskaya, S., Ruben, M., Barth, J. V., and Brune, H. Using Metal-Organic Templates to Steer the Growth of Fe and Co Nanoclusters. *Appl. Phys. Lett.* **93**, 243102 (2008). DOI: 10.1063/1.3040328 (cited on p. 74).

219. Kühne, D., Klappenberger, F., Krenner, W., Klyatskaya, S., Ruben, M., and Barth, J. V. Rotational and Constitutional Dynamics of Caged Supramolecules. *Proc. Natl. Acad. Sci. USA* **107**, 21332–21336 (2010). DOI: 10.1073/pnas.1008991107 (cited on p. 74).

220. Nowakowska, S., Wäckerlin, A., Kawai, S., Ivas, T., Nowakowski, J., Fatayer, S., Wäckerlin, C., Nijs, T., Meyer, E., Björk, J., Stöhr, M., Gade, L. H., and Jung, T. A. Interplay of Weak Interactions in the Atom-by-Atom Condensation of Xenon within Quantum Boxes. *Nat. Commun.* **6**, 6071 (2015). DOI: 10.1038/ncomms7071 (cited on p. 74).

221. Zhang, R., Lyu, G., Chen, C., Lin, T., Liu, J., Liu, P. N., and Lin, N. Two-Dimensional Superlattices of Bi Nanoclusters Formed on a Au(111) Surface Using Porous Supramolecular Templates. *ACS Nano* **9**, 8547–8553 (2015). DOI: 10.1021/acsnano.5b03676 (cited on p. 74).

222. Abdurakhmanova, N., Tseng, T.-C., Langner, A., Kley, C. S., Sessi, V., Stepanow, S., and Kern, K. Superexchange-Mediated Ferromagnetic Coupling in Two-Dimensional Ni-TCNQ Networks on Metal Surfaces. *Phys. Rev. Lett.* **110**, 027202 (2013). DOI: 10.1103/PhysRevLett.110.027202 (cited on p. 74).

223. Pacchioni, G. E., Pivetta, M., and Brune, H. Competing Interactions in the Self-Assembly of NC-Ph₃-CN Molecules on Cu(111). *J. Phys. Chem. C* **119**, 25442–25448 (2015). DOI: 10.1021/acs.jpcc.5b08644 (cited on p. 74).

References

224. Li, Y., Xiao, J., Shubina, T. E., Chen, M., Shi, Z., Schmid, M., Steinrück, H.-P., Gottfried, J. M., and Lin, N. Coordination and Metalation Bifunctionality of Cu with 5,10,15,20-Tetra(4-Pyridyl)Porphyrin: Toward a Mixed-Valence Two-Dimensional Coordination Network. *J. Am. Chem. Soc.* **134**, 6401–6408 (2012). DOI: 10.1021/ja300593w (cited on pp. 74, 79, 82 sq.).

225. Stepanow, S., Lingenfelder, M., Dmitriev, A., Spillmann, H., Delvigne, E., Lin, N., Deng, X., Cai, C., Barth, J. V., and Kern, K. Steering Molecular Organization and Host–guest Interactions Using Two-Dimensional Nanoporous Coordination Systems. *Nat. Mater.* **3**, 229–233 (2004). DOI: 10.1038/nmat1088 (cited on p. 74).

226. Urgel, J. I., Schwarz, M., Garnica, M., Stassen, D., Bonifazi, D., Ecija, D., Barth, J. V., and Auwärter, W. Controlling Coordination Reactions and Assembly on a Cu(111) Supported Boron Nitride Monolayer. *J. Am. Chem. Soc.* **137**, 2420–2423 (2015). DOI: 10.1021/ja511611r (cited on pp. 74, 82).

227. Mohnani, S. and Bonifazi, D. Supramolecular Architectures of Porphyrins on Surfaces: The Structural Evolution from 1D to 2D to 3D to Devices. *Coord. Chem. Rev.* **254**, 2342–2362 (2010). DOI: 10.1016/j.ccr.2010.05.006 (cited on p. 74).

228. Fendt, L.-A., Stöhr, M., Wintjes, N., Enache, M., Jung, T. A., and Diederich, F. Modification of Supramolecular Binding Motifs Induced By Substrate Registry: Formation of Self-Assembled Macrocycles and Chain-Like Patterns. *Chem. Eur. J.* **15**, 11139–11150 (2009). DOI: 10.1002/chem.200901502 (cited on p. 74).

229. Wintjes, N., Lobo-Checa, J., Hornung, J., Samuely, T., Diederich, F., and Jung, T. A. Two-Dimensional Phase Behavior of a Bimolecular Porphyrin System at the Solid-Vacuum Interface. *J. Am. Chem. Soc.* **132**, 7306–7311 (2010). DOI: 10.1021/ja909674e (cited on p. 74).

230. Iacovita, C., Fesser, P., Vijayaraghavan, S., Enache, M., Stöhr, M., Diederich, F., and Jung, T. A. Controlling the Dimensionality and Structure of Supramolecular Porphyrin Assemblies by Their Functional Substituents: Dimers, Chains, and Close-Packed 2D Assemblies. *Chem. Eur. J.* **18**, 14610–14613 (2012). DOI: 10.1002/chem.201201037 (cited on p. 74).

231. Sedona, F., Di Marino, M., Sambi, M., Carofiglio, T., Lubian, E., Casarin, M., and Tondello, E. Fullerene/Porphyrin Multicomponent Nanostructures on Ag(110): From Supramolecular Self-Assembly to Extended Copolymers. *ACS Nano* **4**, 5147–5154 (2010). DOI: 10.1021/nn101161a (cited on pp. 74, 83).

232. Auwärter, W., Seufert, K., Bischoff, F., Ecija, D., Vijayaraghavan, S., Joshi, S., Klappenberger, F., Samudrala, N., and Barth, J. V. A Surface-Anchored Molecular Four-Level Conductance Switch Based on Single Proton Transfer. *Nat. Nanotechnol.* **7**, 41–46 (2012). DOI: 10.1038/nnano.2011.211 (cited on pp. 74 sqq., 90, 92, 119, 124, 176).

233. Marbach, H. Surface-Mediated in Situ Metalation of Porphyrins at the Solid–Vacuum Interface. *Acc. Chem. Res.* **48**, 2649–2658 (2015). DOI: 10.1021/acs.accounts.5b00243 (cited on pp. 74, 95, 115).

234. Urgel, J. I., Ecija, D., Auwärter, W., Stassen, D., Bonifazi, D., and Barth, J. V. Orthogonal Insertion of Lanthanide and Transition-Metal Atoms in Metal–Organic Networks on Surfaces. *Angew. Chem. Int. Ed.* **54**, 6163–6167 (2015). DOI: 10.1002/anie.201410802 (cited on pp. 74, 79, 82 sq., 88).

235. Diller, K., C. Papageorgiou, A., Klappenberger, F., Allegretti, F., V. Barth, J., and Auwärter, W. In Vacuo Interfacial Tetrapyrrole Metallation. *Chem. Soc. Rev.* **45**, 1629–1656 (2016). DOI: 10.1039/C5CS00207A (cited on pp. 74, 90, 95, 111, 115).

236. Hulsken, B., Van Hameren, R., Gerritsen, J. W., Khoury, T., Thordarson, P., Crossley, M. J., Rowan, A. E., Nolte, R. J. M., Elemans, J. A. A. W., and Speller, S. Real-Time Single-Molecule Imaging of Oxidation Catalysis at a Liquid–solid Interface. *Nat. Nanotechnol.* **2**, 285–289 (2007). DOI: 10.1038/nnano.2007.106 (cited on p. 74).

152

237. Wäckerlin, C., Tarafder, K., Girovsky, J., Nowakowski, J., Hählen, T., Shchyrba, A., Siewert, D., Kleibert, A., Nolting, F., Oppeneer, P. M., Jung, T. A., and Ballav, N. Ammonia Coordination Introducing a Magnetic Moment in an On-Surface Low-Spin Porphyrin. *Angew. Chem. Int. Ed.* **52**, 4568–4571 (2013). DOI: 10.1002/anie.201208028 (cited on p. 74).

238. Lin, T., Shang, X. S., Adisoejoso, J., Liu, P. N., and Lin, N. Steering On-Surface Polymerization with Metal-Directed Template. *J. Am. Chem. Soc.* **135**, 3576–3582 (2013). DOI: 10.1021/ja311890n (cited on pp. 74, 80).

239. Auwärter, W., Weber-Bargioni, A., Riemann, A., Schiffrin, A., Gröning, O., Fasel, R., and Barth, J. V. Self-Assembly and Conformation of Tetrapyridyl-Porphyrin Molecules on Ag(111). *J. Chem. Phys.* **124**, 194708 (2006). DOI: 10.1063/1.2194541 (cited on pp. 74, 89).

240. Avouris, P. and Demuth, J. E. Electronic Excitations of Benzene, Pyridine, and Pyrazine Adsorbed on Ag(111). *J. Chem. Phys.* **75**, 4783–4794 (1981). DOI: 10.1063/1.441914 (cited on p. 75).

241. Gottardi, S., Müller, K., Moreno-López, J. C., Yildirim, H., Meinhardt, U., Kivala, M., Kara, A., and Stöhr, M. Cyano-Functionalized Triarylamines on Au(111): Competing Intermolecular versus Molecule/Substrate Interactions. *Adv. Mater. Interfaces* **1**, 1300025 (2014). DOI: 10.1002/admi.201300025 (cited on p. 76).

242. Marschall, M., Reichert, J., Seufert, K., Auwärter, W., Klappenberger, F., Weber-Bargioni, A., Klyatskaya, S., Zoppellaro, G., Nefedov, A., Strunskus, T., Wöll, C., Ruben, M., and Barth, J. V. Supramolecular Organization and Chiral Resolution of P-Terphenyl-m-Dicarbonitrile on the Ag(111) Surface. *ChemPhysChem* **11**, 1446–1451 (2010). DOI: 10.1002/cphc.200900938 (cited on p. 76).

243. Marschall, M., Reichert, J., Weber-Bargioni, A., Seufert, K., Auwärter, W., Klyatskaya, S., Zoppellaro, G., Ruben, M., and Barth, J. V. Random Two-Dimensional String Networks Based on Divergent Coordination Assembly. *Nat. Chem.* **2**, 131–137 (2010). DOI: 10.1038/nchem.503 (cited on pp. 76, 82).

244. Heim, D., Écija, D., Seufert, K., Auwärter, W., Aurisicchio, C., Fabbro, C., Bonifazi, D., and Barth, J. V. Self-Assembly of Flexible One-Dimensional Coordination Polymers on Metal Surfaces. *J. Am. Chem. Soc.* **132**, 6783–6790 (2010). DOI: 10.1021/ja1010527 (cited on pp. 76, 79 sq., 82 sq.).

245. Heim, D., Seufert, K., Auwärter, W., Aurisicchio, C., Fabbro, C., Bonifazi, D., and Barth, J. V. Surface-Assisted Assembly of Discrete Porphyrin-Based Cyclic Supramolecules. *Nano Lett.* **10**, 122–128 (2010). DOI: 10.1021/nl9029994 (cited on p. 76).

246. Ecija, D., Marschall, M., Reichert, J., Kasperski, A., Nieckarz, D., Szabelski, P., Auwärter, W., and Barth, J. V. Dynamics and Thermal Stability of Surface-Confined Metal–organic Chains. *Surf. Sci.* **643**, 91–97 (2016). DOI: 10.1016/j.susc.2015.08.013 (cited on p. 76).

247. Kaposi, T., Joshi, S., Hoh, T., Wiengarten, A., Seufert, K., Paszkiewicz, M., Klappenberger, F., Ecija, D., Đorđević, L., Marangoni, T., Bonifazi, D., Barth, J. V., and Auwärter, W. Supramolecular Spangling, Crocheting, and Knitting of Functionalized Pyrene Molecules on a Silver Surface. *ACS Nano* **10**, 7665–7674 (2016). DOI: 10.1021/acsnano.6b02989 (cited on p. 76).

248. Auwärter, W., Seufert, K., Klappenberger, F., Reichert, J., Weber-Bargioni, A., Verdini, A., Cvetko, D., Dell'Angela, M., Floreano, L., Cossaro, A., Bavdek, G., Morgante, A., Seitsonen, A. P., and Barth, J. V. Site-Specific Electronic and Geometric Interface Structure of Co-Tetraphenyl-Porphyrin Layers on Ag(111). *Phys. Rev. B* **81**, 245403 (2010). DOI: 10.1103/PhysRevB.81.245403 (cited on pp. 76, 89 sq., 107, 119).

249. Pivetta, M., Pacchioni, G. E., Fernandes, E., and Brune, H. Temperature-Dependent Self-Assembly of NC–Ph$_5$–CN Molecules on Cu(111). *J. Chem. Phys.* **142**, 101928 (2015). DOI: 10.1063/1.4909518 (cited on pp. 78 sqq., 82 sq.).

250. Mińkowski, M. and Załuska-Kotur, M. A. Diffusion of Cu Adatoms and Dimers on Cu(111) and Ag(111) Surfaces. *Surf. Sci.* **642**, 22–32 (2015). DOI: 10.1016/j.susc.2015.07.026 (cited on p. 79).

251. Hayat, S. S., Alcántara Ortigoza, M., Choudhry, M. A., and Rahman, T. S. Diffusion of the Cu Monomer and Dimer on Ag(111): Molecular Dynamics Simulations and Density Functional Theory Calculations. *Phys. Rev. B* **82**, 085405 (2010). DOI: 10.1103/PhysRevB.82.085405 (cited on p. 79).

252. Tait, S. L., Langner, A., Lin, N., Stepanow, S., Rajadurai, C., Ruben, M., and Kern, K. One-Dimensional Self-Assembled Molecular Chains on Cu(100): Interplay between Surface-Assisted Coordination Chemistry and Substrate Commensurability. *J. Phys. Chem. C* **111**, 10982–10987 (2007). DOI: 10.1021/jp071100v (cited on pp. 79, 82 sqq.).

253. Henningsen, N., Rurali, R., Limbach, C., Drost, R., Pascual, J. I., and Franke, K. J. Site-Dependent Coordination Bonding in Self-Assembled Metal-Organic Networks. *J. Phys. Chem. Lett.* **2**, 55–61 (2011). DOI: 10.1021/jz1015907 (cited on pp. 79, 84).

254. Vijayaraghavan, S., Ecija, D., Auwärter, W., Joshi, S., Seufert, K., Drach, M., Nieckarz, D., Szabelski, P., Aurisicchio, C., Bonifazi, D., and Barth, J. V. Supramolecular Assembly of Interfacial Nanoporous Networks with Simultaneous Expression of Metal–Organic and Organic-Bonding Motifs. *Chem. Eur. J.* **19**, 14143–14150 (2013). DOI: 10.1002/chem.201301852 (cited on pp. 79 sq.).

255. Umbach, T. R., Bernien, M., Hermanns, C. F., Sun, L. L., Mohrmann, H., Hermann, K. E., Krüger, A., Krane, N., Yang, Z., Nickel, F., Chang, Y.-M., Franke, K. J., Pascual, J. I., and Kuch, W. Site-Specific Bonding of Copper Adatoms to Pyridine End Groups Mediating the Formation of Two-Dimensional Coordination Networks on Metal Surfaces. *Phys. Rev. B* **89**, 235409 (2014). DOI: 10.1103/PhysRevB.89.235409 (cited on p. 79).

256. Ecija, D., Vijayaraghavan, S., Auwärter, W., Joshi, S., Seufert, K., Aurisicchio, C., Bonifazi, D., and Barth, J. V. Two-Dimensional Short-Range Disordered Crystalline Networks from Flexible Molecular Modules. *ACS Nano* **6**, 4258–4265 (2012). DOI: 10.1021/nn3007948 (cited on p. 80).

257. Spillmann, H., Kiebele, A., Stöhr, M., Jung, T. A., Bonifazi, D., Cheng, F., and Diederich, F. A Two-Dimensional Porphyrin-Based Porous Network Featuring Communicating Cavities for the Templated Complexation of Fullerenes. *Adv. Mater.* **18**, 275–279 (2006). DOI: 10.1002/adma.200501734 (cited on p. 80).

258. Palma, C.-A., Björk, J., Klappenberger, F., Arras, E., Kühne, D., Stafström, S., and Barth, J. V. Visualization and Thermodynamic Encoding of Single-Molecule Partition Function Projections. *Nat. Commun.* **6**, 6210 (2015). DOI: 10.1038/ncomms7210 (cited on p. 80).

259. Horike, S., Shimomura, S., and Kitagawa, S. Soft Porous Crystals. *Nat. Chem.* **1**, 695–704 (2009). DOI: 10.1038/nchem.444 (cited on p. 80).

260. Sirtl, T., Schlögl, S., Rastgoo-Lahrood, A., Jelic, J., Neogi, S., Schmittel, M., Heckl, W. M., Reuter, K., and Lackinger, M. Control of Intermolecular Bonds by Deposition Rates at Room Temperature: Hydrogen Bonds versus Metal Coordination in Trinitrile Monolayers. *J. Am. Chem. Soc.* **135**, 691–695 (2013). DOI: 10.1021/ja306834a (cited on p. 80).

261. Lin, T., Wu, Q., Liu, J., Shi, Z., Liu, P. N., and Lin, N. Thermodynamic versus Kinetic Control in Self-Assembly of Zero-, One-, Quasi-Two-, and Two-Dimensional Metal-Organic Coordination Structures. *J. Chem. Phys.* **142**, 101909 (2015). DOI: 10.1063/1.4906174 (cited on p. 80).

262. Lin, T., Shang, X. S., Liu, P. N., and Lin, N. Multicomponent Assembly of Supramolecular Coordination Polygons on a Au(111) Surface. *J. Phys. Chem. C* **117**, 23027–23033 (2013). DOI: 10.1021/jp408504b (cited on p. 80).

263. Kasperski, A. and Szabelski, P. Two-Dimensional Molecular Sieves: Structure Design by Computer Simulations. *Adsorption* **19**, 283–289 (2013). DOI: 10.1007/s10450-012-9451-x (cited on p. 80).

264. Lin, T., Kuang, G., Wang, W., and Lin, N. Two-Dimensional Lattice of Out-of-Plane Dinuclear Iron Centers Exhibiting Kondo Resonance. *ACS Nano* **8**, 8310–8316 (2014). DOI: 10.1021/nn502765g (cited on pp. 82 sqq.).

265. Garah, M. E., Ciesielski, A., Marets, N., Bulach, V., Hosseini, M. W., and Samorì, P. Molecular Tectonics Based Nanopatterning of Interfaces with 2D Metal–organic Frameworks (MOFs). **50**, 12250–12253 (2014). DOI: 10.1039/C4CC03622K (cited on p. 82).

266. Wurster, B., Grumelli, D., Hötger, D., Gutzler, R., and Kern, K. Driving the Oxygen Evolution Reaction by Nonlinear Cooperativity in Bimetallic Coordination Catalysts. *J. Am. Chem. Soc.* **138**, 3623–3626 (2016). DOI: 10.1021/jacs.5b10484 (cited on pp. 82, 84).

267. Long, G. J. and Clarke, P. J. Crystal and Molecular Structures of Trans-Tetrakis(Pyridine)Dichloroiron(II), -Nickel(II), and -Cobalt(II) and Trans-Tetrakis(Pyridine)Dichloroiron(II) Monohydrate. *Inorg. Chem.* **17**, 1394–1401 (1978). DOI: 10.1021/ic50184a002 (cited on p. 82).

268. Agnus, Y., Labarelle, M., Louis, R., and Metz, B. Absolute-Configuration of Di(Perchlorato-*O*)Tetra(Pyridine-*N*)Copper(II), [Cu(Clo$_4$)$_2$(py)$_4$]. *Acta Crystallogr. Sect. A* **50**, 536–538 (1994). DOI: 10.1107/S0108270193009813 (cited on p. 82).

269. Hamm, D. J., Bordner, J., and Schreiner, A. F. The Crystal and Molecular Structure of Diiodotetrakis(Pyridine)Nickel(II) [Nipy$_4$I$_2$]. *Inorg. Chim. Acta* **7**, 637–641 (1973). DOI: 10.1016/S0020-1693(00)94900-4 (cited on p. 82).

270. Dmitriev, A., Spillmann, H., Lin, N., Barth, J. V., and Kern, K. Modular Assembly of Two-Dimensional Metal–Organic Coordination Networks at a Metal Surface. *Angew. Chem.* **115**, 2774–2777 (2003). DOI: 10.1002/ange.200250610 (cited on p. 82).

271. Tseng, T.-C., Lin, C., Shi, X., Tait, S. L., Liu, X., Starke, U., Lin, N., Zhang, R., Minot, C., Van Hove, M. A., Cerdá, J. I., and Kern, K. Two-Dimensional Metal-Organic Coordination Networks of Mn-7,7,8,8-Tetracyanoquinodimethane Assembled on Cu(100): Structural, Electronic, and Magnetic Properties. *Phys. Rev. B* **80**, 155458 (2009). DOI: 10.1103/PhysRevB.80.155458 (cited on p. 82).

272. Abdurakhmanova, N., Floris, A., Tseng, T.-C., Comisso, A., Stepanow, S., Vita, A. D., and Kern, K. Stereoselectivity and Electrostatics in Charge-Transfer Mn- and Cs-TCNQ$_4$ Networks on Ag(100). *Nat. Commun.* **3**, 940 (2012). DOI: 10.1038/ncomms1942 (cited on p. 82).

273. Lyu, G., Zhang, Q., Urgel, J. I., Kuang, G., Auwärter, W., Ecija, D., Barth, J. V., and Lin, N. Tunable Lanthanide-Directed Metallosupramolecular Networks by Exploiting Coordinative Flexibility through Ligand Stoichiometry. *Chem. Commun.* **52**, 1618–1621 (2016). DOI: 10.1039/C5CC08526H (cited on p. 82).

274. Breitruck, A., Hoster, H. E., Meier, C., Ziener, U., and Behm, R. J. Interaction of Cu Atoms with Ordered 2D Oligopyridine Networks. *Surf. Sci.* **601**, 4200–4205 (2007). DOI: 10.1016/j.susc.2007.04.173 (cited on p. 83).

275. Lin, N., Dmitriev, A., Weckesser, J., Barth, J. V., and Kern, K. Real-Time Single-Molecule Imaging of the Formation and Dynamics of Coordination Compounds. *Angew. Chem. Int. Ed.* **41**, 4779–4783 (2002). DOI: 10.1002/anie.200290046 (cited on p. 83).

276. Langner, A., Tait, S. L., Lin, N., Chandrasekar, R., Ruben, M., and Kern, K. Ordering and Stabilization of Metal–Organic Coordination Chains by Hierarchical Assembly through Hydrogen Bonding at a Surface. *Angew. Chem. Int. Ed.* **47**, 8835–8838 (2008). DOI: 10.1002/anie.200803124 (cited on p. 83).

277. Tait, S. L., Langner, A., Lin, N., Chandrasekar, R., Fuhr, O., Ruben, M., and Kern, K. Assembling Isostructural Metal-Organic Coordination Architectures on Cu(100), Ag(100) and Ag(111) Substrates. *ChemPhysChem* **9**, 2495–2499 (2008). DOI: 10.1002/cphc.200800575 (cited on p. 83).

278. Venkataraman, D., Du, Y., Wilson, S. R., Hirsch, K. A., Zhang, P., and Moore, J. S. A Coordination Geometry Table of the D-Block Elements and Their Ions. *J. Chem. Educ.* **74**, 915 (1997). DOI: 10.1021/ed074p915 (cited on p. 83).

279. Pawin, G., Wong, K. L., Kim, D., Sun, D., Bartels, L., Hong, S., Rahman, T. S., Carp, R., and Marsella, M. A Surface Coordination Network Based on Substrate-Derived Metal Adatoms with Local Charge Excess. *Angew. Chem.* **120**, 8570–8573 (2008). DOI: 10.1002/ange.200802543 (cited on p. 83).

280. Flechtner, K., Kretschmann, A., Steinrück, H.-P., and Gottfried, J. M. NO-Induced Reversible Switching of the Electronic Interaction between a Porphyrin-Coordinated Cobalt Ion and a Silver Surface. *J. Am. Chem. Soc.* **129**, 12110–12111 (2007). DOI: 10.1021/ja0756725 (cited on p. 83).

281. Hieringer, W., Flechtner, K., Kretschmann, A., Seufert, K., Auwärter, W., Barth, J. V., Görling, A., Steinrück, H.-P., and Gottfried, J. M. The Surface Trans Effect: Influence of Axial Ligands on the Surface Chemical Bonds of Adsorbed Metalloporphyrins. *J. Am. Chem. Soc.* **133**, 6206–6222 (2011). DOI: 10.1021/ja1093502 (cited on p. 83).

282. Classen, T., Fratesi, G., Costantini, G., Fabris, S., Stadler, F. L., Kim, C., de Gironcoli, S., Baroni, S., and Kern, K. Templated Growth of Metal–Organic Coordination Chains at Surfaces. *Angew. Chem.* **117**, 6298–6301 (2005). DOI: 10.1002/ange.200502007 (cited on p. 84).

283. Walch, H., Dienstmaier, J., Eder, G., Gutzler, R., Schlögl, S., Sirtl, T., Das, K., Schmittel, M., and Lackinger, M. Extended Two-Dimensional Metal–Organic Frameworks Based on Thiolate–Copper Coordination Bonds. *J. Am. Chem. Soc.* **133**, 7909–7915 (2011). DOI: 10.1021/ja200661s (cited on p. 84).

284. Capsoni, M. C. On-Surface Self-Assembly and Characterization of a Macromolecular Charge Transfer Complex by Scanning Tunneling Microscopy and Spectroscopy. University of British Columbia, 2016 (cited on p. 84).

285. Gambardella, P., Stepanow, S., Dmitriev, A., Honolka, J., de Groot, F. M. F., Magalí Lingenfelder, Gupta, S. S., Sarma, D. D., Bencok, P., Stanescu, S., Clair, S., Pons, S., Lin, N., Seitsonen, A. P., Brune, H., Barth, J. V., and Kern, K. Supramolecular Control of the Magnetic Anisotropy in Two-Dimensional High-Spin Fe Arrays at a Metal Interface. *Nat. Mater.* **8**, 189–193 (2009). DOI: 10.1038/nmat2376 (cited on p. 84).

286. Tyo, E. C. and Vajda, S. Catalysis by Clusters with Precise Numbers of Atoms. *Nat. Nanotechnol.* **10**, 577–588 (2015). DOI: 10.1038/nnano.2015.140 (cited on p. 84).

287. Kawai, S., Sadeghi, A., Okamoto, T., Mitsui, C., Pawlak, R., Meier, T., Takeya, J., Goedecker, S., and Meyer, E. Organometallic Bonding in an Ullmann-Type On-Surface Chemical Reaction Studied by High-Resolution Atomic Force Microscopy. *Small* **12**, 5303–5311 (2016). DOI: 10.1002/smll.201601216 (cited on pp. 85, 90, 102).

288. Albrecht, F., Neu, M., Quest, C., Swart, I., and Repp, J. Formation and Characterization of a Molecule–Metal–Molecule Bridge in Real Space. *J. Am. Chem. Soc.* **135**, 9200–9203 (2013). DOI: 10.1021/ja404084p (cited on pp. 85, 87–90).

289. Pavliček, N., Schuler, B., Collazos, S., Moll, N., Pérez, D., Guitián, E., Meyer, G., Peña, D., and Gross, L. On-Surface Generation and Imaging of Arynes by Atomic Force Microscopy. *Nat. Chem.* **7**, 623–628 (2015). DOI: 10.1038/nchem.2300 (cited on pp. 85, 87, 95, 115, 117).

290. Schuler, B., Fatayer, S., Mohn, F., Moll, N., Pavliček, N., Meyer, G., Peña, D., and Gross, L. Reversible Bergman Cyclization by Atomic Manipulation. *Nat. Chem.* **8**, 220–224 (2016). DOI: 10.1038/nchem.2438 (cited on pp. 85, 89, 95, 115).

291. De Oteyza, D. G., Gorman, P., Chen, Y.-C., Wickenburg, S., Riss, A., Mowbray, D. J., Etkin, G., Pedramrazi, Z., Tsai, H.-Z., Rubio, A., Crommie, M. F., and Fischer, F. R. Direct Imaging of Covalent Bond Structure in Single-Molecule Chemical Reactions. *Science* **340**, 1434–1437 (2013). DOI: 10.1126/science.1238187 (cited on pp. 85, 89 sq., 92).

292. Pawlak, R., Kisiel, M., Klinovaja, J., Meier, T., Kawai, S., Glatzel, T., Loss, D., and Meyer, E. Probing Atomic Structure and Majorana Wavefunctions in Mono-Atomic Fe-Chains on Superconducting Pb-Surface (2015) (cited on p. 85).

293. Emmrich, M., Huber, F., Pielmeier, F., Welker, J., Hofmann, T., Schneiderbauer, M., Meuer, D., Polesya, S., Mankovsky, S., Ködderitzsch, D., Ebert, H., and Giessibl, F. J. Subatomic Resolution Force Microscopy Reveals Internal Structure and Adsorption Sites of Small Iron Clusters. *Science* **348**, 308–311 (2015). DOI: 10.1126/science.aaa5329 (cited on pp. 85, 87).

294. Kocić, N., Liu, X., Chen, S., Decurtins, S., Krejčí, O., Jelínek, P., Repp, J., and Liu, S.-X. Control of Reactivity and Regioselectivity for On-Surface Dehydrogenative Aryl–Aryl Bond Formation. *J. Am. Chem. Soc.* **138**, 5585–5593 (2016). DOI: 10.1021/jacs.5b13461 (cited on p. 85).

295. Pavliček, N., Herranz-Lancho, C., Fleury, B., Neu, M., Niedenführ, J., Ruben, M., and Repp, J. High-Resolution Scanning Tunneling and Atomic Force Microscopy of Stereochemically Resolved Dibenzo[a,h]Thianthrene Molecules. *Phys. Status Solidi B* **250**, 2424–2430 (2013). DOI: 10.1002/pssb.201349229 (cited on pp. 85, 90 sq.).

296. Moll, N., Schuler, B., Kawai, S., Xu, F., Peng, L., Orita, A., Otera, J., Curioni, A., Neu, M., Repp, J., Meyer, G., and Gross, L. Image Distortions of a Partially Fluorinated Hydrocarbon Molecule in Atomic Force Microscopy with Carbon Monoxide Terminated Tips. *Nano Lett.* **14**, 6127–6131 (2014). DOI: 10.1021/nl502113z (cited on pp. 87, 108).

297. Guo, C.-S., Xin, X., Van Hove, M. A., Ren, X., and Zhao, Y. Origin of the Contrast Interpreted as Intermolecular and Intramolecular Bonds in Atomic Force Microscopy Images. *J. Phys. Chem. C* **119**, 14195–14200 (2015). DOI: 10.1021/acs.jpcc.5b02649 (cited on pp. 87, 108).

298. Riss, A., Paz, A. P., Wickenburg, S., Tsai, H.-Z., De Oteyza, D. G., Bradley, A. J., Ugeda, M. M., Gorman, P., Jung, H. S., Crommie, M. F., Rubio, A., and Fischer, F. R. Imaging Single-Molecule Reaction Intermediates Stabilized by Surface Dissipation and Entropy. *Nat. Chem.* **8**, 678–683 (2016). DOI: 10.1038/nchem.2506 (cited on p. 87).

299. Riss, A., Wickenburg, S., Gorman, P., Tan, L. Z., Tsai, H.-Z., de Oteyza, D. G., Chen, Y.-C., Bradley, A. J., Ugeda, M. M., Etkin, G., Louie, S. G., Fischer, F. R., and Crommie, M. F. Local Electronic and Chemical Structure of Oligo-Acetylene Derivatives Formed Through Radical Cyclizations at a Surface. *Nano Lett.* **14**, 2251–2255 (2014). DOI: 10.1021/nl403791q (cited on pp. 87, 89 sq., 92).

300. Van der Lit, J., Boneschanscher, M. P., Vanmaekelbergh, D., Ijäs, M., Uppstu, A., Ervasti, M., Harju, A., Liljeroth, P., and Swart, I. Suppression of Electron–vibron Coupling in Graphene Nanoribbons Contacted via a Single Atom. *Nat. Commun.* **4**, 2023 (2013). DOI: 10.1038/ncomms3023 (cited on pp. 87, 89 sq., 117).

301. Van der van der Lit, J., Jacobse, P. H., Vanmaekelbergh, D., and Swart, I. Bending and Buckling of Narrow Armchair Graphene Nanoribbons via STM Manipulation. *New J. Phys.* **17**, 053013 (2015). DOI: 10.1088/1367-2630/17/5/053013 (cited on pp. 87, 117).

302. Urgel, J. I., Ecija, D., Auwärter, W., and Barth, J. V. Controlled Manipulation of Gadolinium-Coordinated Supramolecules by Low-Temperature Scanning Tunneling Microscopy. *Nano Lett.* **14**, 1369–1373 (2014). DOI: 10.1021/nl4044339 (cited on p. 88).

303. Écija, D., Urgel, J. I., Papageorgiou, A. C., Joshi, S., Auwärter, W., Seitsonen, A. P., Klyatskaya, S., Ruben, M., Fischer, S., Vijayaraghavan, S., Reichert, J., and Barth, J. V. Five-Vertex Archimedean Surface Tessellation by Lanthanide-Directed Molecular Self-Assembly. *PNAS* **110**, 6678–6681 (2013). DOI: 10.1073/pnas.1222713110 (cited on p. 88).

304. Urgel, J. I., Écija, D., Lyu, G., Zhang, R., Palma, C.-A., Auwärter, W., Lin, N., and Barth, J. V. Quasicrystallinity Expressed in Two-Dimensional Coordination Networks. *Nat. Chem.* **8**, 657–662 (2016). DOI: 10.1038/nchem.2507 (cited on p. 88).

305. Ohshiro, T., Ito, T., Bühlmann, P., and Umezawa, Y. Scanning Tunneling Microscopy with Chemically Modified Tips: Discrimination of Porphyrin Centers Based on Metal Coordination and Hydrogen Bond Interactions. *Anal. Chem.* **73**, 878–883 (2001). DOI: 10.1021/ac001056e (cited on pp. 88, 136).

306. Buchner, F., Zillner, E., Röckert, M., Gläßel, S., Steinrück, H.-P., and Marbach, H. Substrate-Mediated Phase Separation of Two Porphyrin Derivatives on Cu(111). *Chem. Eur. J.* **17**, 10226–10229 (2011). DOI: 10.1002/chem.201100462 (cited on pp. 89 sq.).

307. Auwärter, W., Klappenberger, F., Weber-Bargioni, A., Schiffrin, A., Strunskus, T., Wöll, C., Pennec, Y., Riemann, A., and Barth, J. V. Conformational Adaptation and Selective Adatom Capturing of Tetrapyridyl-Porphyrin Molecules on a Copper (111) Surface. *J. Am. Chem. Soc.* **129**, 11279–11285 (2007). DOI: 10.1021/ja071572n (cited on pp. 89 sq.).

308. Weber-Bargioni, A., Auwärter, W., Klappenberger, F., Reichert, J., Lefrançois, S., Strunskus, T., Wöll, C., Schiffrin, A., Pennec, Y., and Barth, J. V. Visualizing the Frontier Orbitals of a Conformationally Adapted Metalloporphyrin. *ChemPhysChem* **9**, 89–94 (2008). DOI: 10.1002/cphc.200700600 (cited on pp. 89 sq.).

309. Xiao, J., Ditze, S., Chen, M., Buchner, F., Stark, M., Drost, M., Steinrück, H.-P., Gottfried, J. M., and Marbach, H. Temperature-Dependent Chemical and Structural Transformations from 2H-Tetraphenylporphyrin to Copper(II)-Tetraphenylporphyrin on Cu(111). *J. Phys. Chem. C* **116**, 12275–12282 (2012). DOI: 10.1021/jp301757h (cited on pp. 89 sq.).

310. Stark, M., Ditze, S., Drost, M., Buchner, F., Steinrück, H.-P., and Marbach, H. Coverage Dependent Disorder–Order Transition of 2H-Tetraphenylporphyrin on Cu(111). *Langmuir* **29**, 4104–4110 (2013). DOI: 10.1021/la3046753 (cited on pp. 89 sq.).

311. Röckert, M., Ditze, S., Stark, M., Xiao, J., Steinrück, H.-P., Marbach, H., and Lytken, O. Abrupt Coverage-Induced Enhancement of the Self-Metalation of Tetraphenylporphyrin with Cu(111). *J. Phys. Chem. C* **118**, 1661–1667 (2014). DOI: 10.1021/jp412121b (cited on pp. 89 sq.).

312. Diller, K., Klappenberger, F., Marschall, M., Hermann, K., Nefedov, A., Wöll, C., and Barth, J. V. Self-Metalation of 2H-Tetraphenylporphyrin on Cu(111): An x-Ray Spectroscopy Study. *J. Chem. Phys* **136**, 014705 (2012). DOI: 10.1063/1.3674165 (cited on pp. 89 sq., 93 sq.).

313. Klappenberger, F. Two-Dimensional Functional Molecular Nanoarchitectures – Complementary Investigations with Scanning Tunneling Microscopy and X-Ray Spectroscopy. *Progr. Surf. Sci.* **89**, 1–55 (2014). DOI: 10.1016/j.progsurf.2013.10.002 (cited on p. 89).

314. Houwaart, T., Le Bahers, T., Sautet, P., Auwärter, W., Seufert, K., Barth, J. V., and Bocquet, M.-L. Scrutinizing Individual CoTPP Molecule Adsorbed on Coinage Metal Surfaces from the Interplay of STM Experiment and Theory. *Surf. Sci.* **635**, 108–114 (2015). DOI: 10.1016/j.susc.2014.12.011 (cited on p. 89).

315. Hanssen, K. Ø., Schuler, B., Williams, A. J., Demissie, T. B., Hansen, E., Andersen, J. H., Svenson, J., Blinov, K., Repisky, M., Mohn, F., Meyer, G., Svendsen, J.-S., Ruud, K., Elyashberg, M., Gross, L., Jaspars, M., and Isaksson, J. A Combined Atomic Force Microscopy and Computational Approach for the Structural Elucidation of Breitfussin A and B: Highly Modified Halogenated Dipeptides from Thuiaria Breitfussi. *Angew. Chem. Int. Ed.* **51**, 12238–12241 (2012). DOI: 10.1002/anie.201203960 (cited on pp. 89 sq., 115).

316. Pavliček, N., Fleury, B., Neu, M., Niedenführ, J., Herranz-Lancho, C., Ruben, M., and Repp, J. Atomic Force Microscopy Reveals Bistable Configurations of Dibenzo[a,h]Thianthrene and Their Interconversion Pathway. *Phys. Rev. Lett.* **108**, 086101 (2012). DOI: 10.1103/PhysRevLett.108.086101 (cited on pp. 89–92).

317. Wölfle, T., Görling, A., and Hieringer, W. Conformational Flexibility of Metalloporphyrins Studied by Density-Functional Calculations. *Phys. Chem. Chem. Phys.* **10**, 5739–5742 (2008). DOI: 10.1039/B800566B (cited on p. 90).

318. Gross, L., Mohn, F., Moll, N., Meyer, G., Ebel, R., Abdel-Mageed, W. M., and Jaspars, M. Organic Structure Determination Using Atomic-Resolution Scanning Probe Microscopy. *Nat. Chem.* **2**, 821–825 (2010). DOI: 10.1038/nchem.765 (cited on p. 92).

319. Donovan, P., Robin, A., Dyer, M. S., Persson, M., and Raval, R. Unexpected Deformations Induced by Surface Interaction and Chiral Self-Assembly of Co^{II}-Tetraphenylporphyrin (Co-TPP) Adsorbed on Cu(110): A Combined STM and Periodic DFT Study. *Chem. Eur. J.* **16**, 11641–11652 (2010). DOI: 10.1002/chem.201001776 (cited on pp. 93, 119).

320. Rojas, G., Simpson, S., Chen, X., Kunkel, D. A., Nitz, J., Xiao, J., Dowben, P. A., Zurek, E., and Enders, A. Surface State Engineering of Molecule–molecule Interactions. *Phys. Chem. Chem. Phys.* **14**, 4971 (2012). DOI: 10.1039/c2cp40254h (cited on p. 94).

321. Iancu, V., Deshpande, A., and Hla, S.-W. Manipulating Kondo Temperature via Single Molecule Switching. *Nano Lett.* **6**, 820–823 (2006). DOI: 10.1021/nl0601886 (cited on p. 94).

322. Barth, J. V. Molecular Architectonic on Metal Surfaces. *Annu. Rev. Phys. Chem.* **58**, 375–407 (2007). DOI: 10.1146/annurev.physchem.56.092503.141259 (cited on p. 95).

323. Otero, R., Gallego, J. M., de Parga, A. L. V., Martín, N., and Miranda, R. Molecular Self-Assembly at Solid Surfaces. *Adv. Mater.* **23**, 5148–5176 (2011). DOI: 10.1002/adma.201102022 (cited on p. 95).

324. Wiengarten, A., Lloyd, J. A., Seufert, K., Reichert, J., Auwärter, W., Han, R., Duncan, D. A., Allegretti, F., Fischer, S., Oh, S. C., Sağlam, Ö., Jiang, L., Vijayaraghavan, S., Écija, D., Papageorgiou, A. C., and Barth, J. V. Surface-Assisted Cyclodehydrogenation; Break the Symmetry, Enhance the Selectivity. *Chem. Eur. J.* **21**, 12285–12290 (2015). DOI: 10.1002/chem.201502001 (cited on pp. 95, 105, 107 sq., 110–113, 119 sq.).

325. Zhang, Y.-Q., Kepčija, N., Kleinschrodt, M., Diller, K., Fischer, S., Papageorgiou, A. C., Allegretti, F., Björk, J., Klyatskaya, S., Klappenberger, F., Ruben, M., and Barth, J. V. Homo-Coupling of Terminal Alkynes on a Noble Metal Surface. *Nat. Commun.* **3**, 1286 (2012) (cited on p. 95).

326. Cirera, B., Zhang, Y.-Q., Björk, J., Klyatskaya, S., Chen, Z., Ruben, M., Barth, J. V., and Klappenberger, F. Synthesis of Extended Graphdiyne Wires by Vicinal Surface Templating. *Nano Lett.* **14**, 1891–1897 (2014). DOI: 10.1021/nl4046747 (cited on p. 95).

327. Haq, S., Hanke, F., Sharp, J., Persson, M., Amabilino, D. B., and Raval, R. Versatile Bottom-Up Construction of Diverse Macromolecules on a Surface Observed by Scanning Tunneling Microscopy. *ACS Nano* **8**, 8856–8870 (2014). DOI: 10.1021/nn502388u (cited on p. 95).

328. Coraux, J., N'Diaye, A. T., Engler, M., Busse, C., Wall, D., Buckanie, N., Heringdorf, F.-J. M. zu, Gastel, R. van, Poelsema, B., and Michely, T. Growth of Graphene on Ir(111). *New J. Phys.* **11**, 023006 (2009). DOI: 10.1088/1367-2630/11/2/023006 (cited on p. 95).

329. Auwärter, W., Weber-Bargioni, A., Brink, S., Riemann, A., Schiffrin, A., Ruben, M., and Barth, J. V. Controlled Metalation of Self-Assembled Porphyrin Nanoarrays in Two Dimensions. *ChemPhysChem* **8**, 250–254 (2007). DOI: 10.1002/cphc.200600675 (cited on pp. 95, 115).

330. Shubina, T. E. Computational Studies on Properties, Formation, and Complexation of M(II)-Porphyrins. In: *Advances in Inorganic Chemistry*. Ed. by R. van Eldik and J. Harvey. **62**. Academic Press, 2010, 261–299. DOI: 10.1016/S0898-8838(10)62007-7 (cited on p. 97).

331. Dyer, M. S., Robin, A., Haq, S., Raval, R., Persson, M., and Klimeš, J. Understanding the Interaction of the Porphyrin Macrocycle to Reactive Metal Substrates: Structure, Bonding, and Adatom Capture. *ACS Nano* **5**, 1831–1838 (2011). DOI: 10.1021/nn102610k (cited on p. 97).

332. Diller, K., Klappenberger, F., Allegretti, F., Papageorgiou, A. C., Fischer, S., Wiengarten, A., Joshi, S., Seufert, K., Écija, D., Auwärter, W., and Barth, J. V. Investigating the Molecule-Substrate Interaction of Prototypic Tetrapyrrole Compounds: Adsorption and Self-Metalation of Porphine on Cu(111). *J. Chem. Phys.* **138**, 154710 (2013). DOI: 10.1063/1.4800771 (cited on pp. 97, 108).

333. Hanke, F., Haq, S., Raval, R., and Persson, M. Heat-to-Connect: Surface Commensurability Directs Organometallic One-Dimensional Self-Assembly. *ACS Nano* **5**, 9093–9103 (2011). DOI: 10.1021/nn203337v (cited on p. 97).

334. Haq, S., Hanke, F., Dyer, M. S., Persson, M., Iavicoli, P., Amabilino, D. B., and Raval, R. Clean Coupling of Unfunctionalized Porphyrins at Surfaces To Give Highly Oriented Organometallic Oligomers. *J. Am. Chem. Soc.* **133**, 12031–12039 (2011). DOI: 10.1021/ja201389u (cited on p. 97).

335. Lin, V. S., DiMagno, S. G., and Therien, M. J. Highly Conjugated, Acetylenyl Bridged Porphyrins: New Models for Light-Harvesting Antenna Systems. *Science* **264**, 1105–1111 (1994). DOI: 10.1126/science.8178169 (cited on p. 97).

336. Tsuda, A. and Osuka, A. Fully Conjugated Porphyrin Tapes with Electronic Absorption Bands That Reach into Infrared. *Science* **293**, 79–82 (2001). DOI: 10.1126/science.1059552 (cited on p. 97).

337. Cho, H. S., Jeong, D. H., Cho, S., Kim, D., Matsuzaki, Y., Tanaka, K., Tsuda, A., and Osuka, A. Photophysical Properties of Porphyrin Tapes. *J. Am. Chem. Soc.* **124**, 14642–14654 (2002). DOI: 10.1021/ja020826w (cited on p. 97).

338. Kim, D. Y., Ahn, T. K., Kwon, J. H., Kim, D., Ikeue, T., Aratani, N., Osuka, A., Shigeiwa, M., and Maeda, S. Large Two-Photon Absorption (TPA) Cross-Section of Directly Linked Fused Diporphyrins. *J. Phys. Chem. A* **109**, 2996–2999 (2005). DOI: 10.1021/jp050747h (cited on p. 97).

339. Biggs, J. D., Zhang, Y., Healion, D., and Mukamel, S. Watching Energy Transfer in Metalloporphyrin Heterodimers Using Stimulated X-Ray Raman Spectroscopy. *PNAS* **110**, 15597–15601 (2013). DOI: 10.1073/pnas.1308604110 (cited on p. 97).

340. Ryan, A. A. and Senge, M. O. Synthesis and Functionalization of Triply Fused Porphyrin Dimers. *Eur. J. Org. Chem.* **2013**, 3700–3711 (2013). DOI: 10.1002/ejoc.201201622 (cited on pp. 97, 99).

References

341. Li, E. Y. and Marzari, N. Conductance Switching and Many-Valued Logic in Porphyrin Assemblies. *J. Phys. Chem. Lett.* **4**, 3039–3044 (2013). DOI: 10.1021/jz401649a (cited on p. 97).

342. Osuka, A. and Shimidzu, H. Meso, Meso-Linked Porphyrin Arrays. *Angew. Chem. Int. Ed. Engl.* **36**, 135–137 (1997). DOI: 10.1002/anie.199701351 (cited on pp. 97, 99).

343. Lafferentz, L., Eberhardt, V., Dri, C., Africh, C., Comelli, G., Esch, F., Hecht, S., and Grill, L. Controlling On-Surface Polymerization by Hierarchical and Substrate-Directed Growth. *Nat. Chem.* **4**, 215–220 (2012). DOI: 10.1038/nchem.1242 (cited on p. 98).

344. Takagi, A., Yanagawa, Y., Tsuda, A., Aratani, N., Matsumoto, T., Osuka, A., and Kawai, T. STM Images of Individual Porphyrin Hexamers; Meso–meso Singly Linked Orthogonal Hexamer and Meso–meso, β–β, β–β Triply-Linked Planar Hexamer on Cu(100) Surface, 2986–2987 (2003). DOI: 10.1039/B309656D (cited on p. 99).

345. Treier, M., Pignedoli, C. A., Laino, T., Rieger, R., Müllen, K., Passerone, D., and Fasel, R. Surface-Assisted Cyclodehydrogenation Provides a Synthetic Route towards Easily Processable and Chemically Tailored Nanographenes. *Nat. Chem.* **3**, 61–67 (2011). DOI: 10.1038/nchem.891 (cited on pp. 100, 105, 110).

346. Ruggieri, C., Rangan, S., Bartynski, R. A., and Galoppini, E. Zinc(II) Tetraphenylporphyrin on Ag(100) and Ag(111): Multilayer Desorption and Dehydrogenation. *J. Phys. Chem. C* **120**, 7575–7585 (2016). DOI: 10.1021/acs.jpcc.6b00159 (cited on pp. 105, 108, 120).

347. Di Santo, G., Blankenburg, S., Castellarin-Cudia, C., Fanetti, M., Borghetti, P., Sangaletti, L., Floreano, L., Verdini, A., Magnano, E., Bondino, F., Pignedoli, C. A., Nguyen, M.-T., Gaspari, R., Passerone, D., and Goldoni, A. Supramolecular Engineering through Temperature-Induced Chemical Modification of 2H-Tetraphenylporphyrin on Ag(111): Flat Phenyl Conformation and Possible Dehydrogenation Reactions. *Chem. Eur. J.* **17**, 14354–14359 (2011). DOI: 10.1002/chem.201102268 (cited on pp. 105, 108).

348. Röckert, M., Franke, M., Tariq, Q., Ditze, S., Stark, M., Uffinger, P., Wechsler, D., Singh, U., Xiao, J., Marbach, H., Steinrück, H.-P., and Lytken, O. Coverage- and Temperature-Dependent Metalation and Dehydrogenation of Tetraphenylporphyrin on Cu(111). *Chem. Eur. J.* **20**, 8948–8953 (2014). DOI: 10.1002/chem.201402420 (cited on pp. 105, 107 sq., 111 sq.).

349. Williams, C. G., Wang, M., Skomski, D., Tempas, C. D., Kesmodel, L. L., and Tait, S. L. Dehydrocyclization of Peripheral Alkyl Groups in Porphyrins at Cu(100) and Ag(111) Surfaces. *Surf. Sci.* **653**, 130–137 (2016). DOI: 10.1016/j.susc.2016.06.013 (cited on pp. 105, 108).

350. Chong, M. C., Reecht, G., Bulou, H., Boeglin, A., Scheurer, F., Mathevet, F., and Schull, G. Narrow-Line Single-Molecule Transducer between Electronic Circuits and Surface Plasmons. *Phys. Rev. Lett.* **116**, 036802 (2016). DOI: 10.1103/PhysRevLett.116.036802 (cited on pp. 105, 108).

351. Papageorgiou, A. C., Fischer, S., Oh, S. C., Sağlam, Ö., Reichert, J., Wiengarten, A., Seufert, K., Vijayaraghavan, S., Écija, D., Auwärter, W., Allegretti, F., Acres, R. G., Prince, K. C., Diller, K., Klappenberger, F., and Barth, J. V. Self-Terminating Protocol for an Interfacial Complexation Reaction in Vacuo by Metal–Organic Chemical Vapor Deposition. *ACS Nano* **7**, 4520–4526 (2013). DOI: 10.1021/nn401171z (cited on pp. 105, 108).

352. Pinardi, A. L., Otero-Irurueta, G., Palacio, I., Martinez, J. I., Sanchez-Sanchez, C., Tello, M., Rogero, C., Cossaro, A., Preobrajenski, A., Gómez-Lor, B., Jancarik, A., Stará, I. G., Starý, I., Lopez, M. F., Méndez, J., and Martin-Gago, J. A. Tailored Formation of N-Doped Nanoarchitectures by Diffusion-Controlled on-Surface (Cyclo)Dehydrogenation of Heteroaromatics. *ACS Nano* **7**, 3676–3684 (2013). DOI: 10.1021/nn400690e (cited on p. 105).

353. Walch, H., Gutzler, R., Sirtl, T., Eder, G., and Lackinger, M. Material- and Orientation-Dependent Reactivity for Heterogeneously Catalyzed Carbon-Bromine Bond Homolysis. *J. Phys. Chem. C* **114**, 12604–12609 (2010). DOI: 10.1021/jp102704q (cited on p. 105).

354. Violi, A. Cyclodehydrogenation Reactions to Cyclopentafused Polycyclic Aromatic Hydrocarbons. *J. Phys. Chem. A* **109**, 7781–7787 (2005). DOI: 10.1021/jp052384r (cited on pp. 105, 110).

355. Cai, J., Ruffieux, P., Jaafar, R., Bieri, M., Braun, T., Blankenburg, S., Muoth, M., Seitsonen, A. P., Saleh, M., Feng, X., Müllen, K., and Fasel, R. Atomically Precise Bottom-up Fabrication of Graphene Nanoribbons. *Nature* **466**, 470–473 (2010). DOI: 10.1038/nature09211 (cited on pp. 105, 110).

356. Grill, L., Dyer, M., Lafferentz, L., Persson, M., Peters, M. V., and Hecht, S. Nano-Architectures by Covalent Assembly of Molecular Building Blocks. *Nat. Nanotechnol.* **2**, 687–691 (2007). DOI: 10.1038/nnano.2007.346 (cited on pp. 105, 110).

357. Buchner, F., Flechtner, K., Bai, Y., Zillner, E., Kellner, I., Steinrück, H.-P., Marbach, H., and Gottfried, J. M. Coordination of Iron Atoms by Tetraphenylporphyrin Monolayers and Multilayers on Ag(111) and Formation of Iron-Tetraphenylporphyrin. *J. Phys. Chem. C* **112**, 15458–15465 (2008). DOI: 10.1021/jp8052955 (cited on p. 107).

358. Buchner, F., Kellner, I., Hieringer, W., Görling, A., Steinrück, H.-P., and Marbach, H. Ordering Aspects and Intramolecular Conformation of Tetraphenylporphyrins on Ag(111). *Phys. Chem. Chem. Phys.* **12**, 13082–13090 (2010). DOI: 10.1039/C004551A (cited on p. 107).

359. Wiengarten, A. C. Scanning tunneling microscopy investigation of structure and electronic properties of surface-confined tetrapyrrolic species. Dissertation. München: Technische Universität München, 2015 (cited on pp. 108, 110 sq.).

360. Smykalla, L., Shukrynau, P., Zahn, D. R. T., and Hietschold, M. Self-Metalation of Phthalocyanine Molecules with Silver Surface Atoms by Adsorption on Ag(110). *J. Phys. Chem. C* **119**, 17228–17234 (2015). DOI: 10.1021/acs.jpcc.5b04977 (cited on p. 111).

361. Zhou, Z. and Shen, Z. The Development of Artificial Porphyrinoids Embedded with Functional Building Blocks. *J. Mater. Chem. C* **3**, 3239–3251 (2015). DOI: 10.1039/C5TC00115C (cited on p. 115).

362. Sessler, J. L. and Weghorn, S. J., eds. *Expanded, Contracted & Isomeric Porphyrins*. Elsevier, 1997. 531 pp. (cited on p. 115).

363. Baudron, S. A. Luminescent Dipyrrin Based Metal Complexes. *Dalton Trans.* **42**, 7498–7509 (2013). DOI: 10.1039/C3DT50493J (cited on p. 115).

364. Maeda, H., Hasegawa, M., Hashimoto, T., Kakimoto, T., Nishio, S., and Nakanishi, T. Nanoscale Spherical Architectures Fabricated by Metal Coordination of Multiple Dipyrrin Moieties. *J. Am. Chem. Soc.* **128**, 10024–10025 (2006). DOI: 10.1021/ja0637301 (cited on p. 115).

365. Bahnmüller, S., Plotzitzka, J., Baabe, D., Cordes, B., Menzel, D., Schartz, K., Schweyen, P., Wicht, R., and Bröring, M. Hexaethyltripyrrindione (H_3Et_6tpd): A Non-Innocent Ligand Forming Stable Radical Complexes with Divalent Transition-Metal Ions. *Eur. J. Inorg. Chem.* 4761–4768 (2016). DOI: 10.1002/ejic.201600934 (cited on p. 115).

366. Ding, Y., Xie, Y., Li, X., Hill, J. P., Zhang, W., and Zhu, W. Selective and Sensitive "Turn-on" Fluorescent Zn^{2+} Sensors Based on Di- and Tripyrrins with Readily Modulated Emission Wavelengths. *Chem. Commun.* **47**, 5431–5433 (2011). DOI: 10.1039/C1CC11493J (cited on p. 115).

367. Wang, Q., Xie, Y., Ding, Y., Li, X., and Zhu, W. Colorimetric Fluoride Sensors Based on Deprotonation of Pyrrole–hemiquinone Compounds. *Chem. Commun.* **46**, 3669–3671 (2010). DOI: 10.1039/C001509A (cited on p. 115).

368. Yamaguchi, T., Shioji, I., Sugimoto, A., Komoda, Y., and Nakajima, H. Chemical Structure of a New Family of Bile Pigments from Human Urine. *J. Biochem.* **116**, 298–303 (1994). DOI: 10.1093/oxfordjournals.jbchem.a124523 (cited on p. 115).

369. Chang, S.-H., Scarfato, A., Kleeberg, C., Bröring, M., Hoffmann, G., and Wiesendanger, R. Adsorption Behavior of Asymmetric Pd Pincer Complexes on a Cu(111) Surface. *Langmuir* **26**, 10868–10871 (2010). DOI: 10.1021/la100746a (cited on p. 115).

370. Haq, S., Wit, B., Sang, H., Floris, A., Wang, Y., Wang, J., Pérez-García, L., Kantorovitch, L., Amabilino, D. B., and Raval, R. A Small Molecule Walks Along a Surface Between Porphyrin Fences That Are Assembled In Situ. *Angew. Chem. Int. Ed.* **54**, 7101–7105 (2015). DOI: 10.1002/anie.201502153 (cited on p. 115).

371. Bröring, M. and Brandt, C. D. Tripyrrin—the Missing Link in the Series of Oligopyrrolic Ligands. *Chem. Commun.* 499–500 (2001). DOI: 10.1039/B009847G (cited on p. 117).

372. Zhao, A., Li, Q., Chen, L., Xiang, H., Wang, W., Pan, S., Wang, B., Xiao, X., Yang, J., Hou, J. G., and Zhu, Q. Controlling the Kondo Effect of an Adsorbed Magnetic Ion Through Its Chemical Bonding. *Science* **309**, 1542–1544 (2005). DOI: 10.1126/science.1113449 (cited on p. 117).

373. Komeda, T., Kim, Y., Fujita, Y., Sainoo, Y., and Kawai, M. Local Chemical Reaction of Benzene on Cu(110) via STM-Induced Excitation. *J. Chem. Phys* **120**, 5347–5352 (2004). DOI: 10.1063/1.1647044 (cited on p. 117).

374. Lauhon, L. J. and Ho, W. Single-Molecule Chemistry and Vibrational Spectroscopy: Pyridine and Benzene on Cu(001). *J. Phys. Chem. A* **104**, 2463–2467 (2000). DOI: 10.1021/jp991768c (cited on p. 117).

375. Majzik, Z., Cuenca, A. B., Pavliček, N., Miralles, N., Meyer, G., Gross, L., and Fernández, E. Synthesis of a Naphthodiazaborinine and Its Verification by Planarization with Atomic Force Microscopy. *ACS Nano* **10**, 5340–5345 (2016). DOI: 10.1021/acsnano.6b01484 (cited on p. 117).

376. Yokoyama, T., Yokoyama, S., Kamikado, T., and Mashiko, S. Nonplanar Adsorption and Orientational Ordering of Porphyrin Molecules on Au(111). *J. Chem. Phys* **115**, 3814–3818 (2001). DOI: 10.1063/1.1389276 (cited on p. 119).

377. Cyrañski, M. K., Krygowski, T. M., Wisiorowski, M., van Eikema Hommes, N. J. R., and Schleyer, P. v. R. Global and Local Aromaticity in Porphyrins: An Analysis Based on Molecular Geometries and Nucleus-Independent Chemical Shifts. *Angew. Chem. Int. Ed.* **37**, 177–180 (1998). DOI: 10.1002/(SICI)1521-3773(19980202)37:1/2<177::AID-ANIE177>3.0.CO;2-H (cited on p. 120).

378. Krygowski, T. M. and Cyrański, M. K. Structural Aspects of Aromaticity. *Chem. Rev.* **101**, 1385–1420 (2001). DOI: 10.1021/cr990326u (cited on p. 120).

379. Balaban, A. T., Oniciu, D. C., and Katritzky, A. R. Aromaticity as a Cornerstone of Heterocyclic Chemistry. *Chem. Rev.* **104**, 2777–2812 (2004). DOI: 10.1021/cr0306790 (cited on p. 120).

380. Glukhovtsev, M. Aromaticity Today: Energetic and Structural Criteria. *J. Chem. Educ.* **74**, 132 (1997). DOI: 10.1021/ed074p132 (cited on p. 120).

381. Shishkin, O. V., Pichugin, K. Y., Gorb, L., and Leszczynski, J. Structural Non-Rigidity of Six-Membered Aromatic Rings. *J. Mol. Struct.* **616**, 159–166 (2002). DOI: 10.1016/S0022-2860(02)00328-9 (cited on p. 120).

382. Zhigalko, M. V., Shishkin, O. V., Gorb, L., and Leszczynski, J. Out-of-Plane Deformability of Aromatic Systems in Naphthalene, Anthracene and Phenanthrene. *J. Mol. Struct.* **693**, 153–159 (2004). DOI: 10.1016/j.molstruc.2004.02.027 (cited on p. 120).

383. Haddon, R. C., Brus, L. E., and Raghavachari, K. Electronic Structure and Bonding in Icosahedral C_{60}. *Chem. Phys. Lett.* **125**, 459–464 (1986). DOI: 10.1016/0009-2614(86)87079-8 (cited on p. 120).

384. Brückner, C. The Breaking and Mending of Meso-Tetraarylporphyrins: Transmuting the Pyrrolic Building Blocks. *Acc. Chem. Res.* **49**, 1080–1092 (2016). DOI: 10.1021/acs.accounts.6b00043 (cited on p. 121).

385. Wang, H., Yuan, H., Hong, S. S., Li, Y., and Cui, Y. Physical and Chemical Tuning of Two-Dimensional Transition Metal Dichalcogenides. *Chem. Soc. Rev.* **44**, 2664–2680 (2015). DOI: 10.1039/C4CS00287C (cited on p. 123).

386. Voiry, D., Mohite, A., and Chhowalla, M. Phase Engineering of Transition Metal Dichalcogenides. *Chem. Soc. Rev.* **44**, 2702–2712 (2015). DOI: 10.1039/C5CS00151J (cited on pp. 123 sq.).

387. Zhang, J., Liu, J., Huang, J. L., Kim, P., and Lieber, C. M. Creation of Nanocrystals Through a Solid-Solid Phase Transition Induced by an STM Tip. *Science* **274**, 757–760 (1996). DOI: 10.1126/science.274.5288.757 (cited on pp. 123 sq., 127 sq.).

388. Komori, F., Iwaki, T., Hattori, K., Shiino, O., and Hasegawa, T. New Superstructure on the Surface of 2H-NbSe 2 and Tunneling Spectra at 4.2 K. *J. Phys. Soc. Jpn.* **66**, 298–301 (1997). DOI: 10.1143/JPSJ.66.298 (cited on p. 123).

389. Wang, H., Lee, J., Dreyer, M., and Barker, B. I. A Scanning Tunneling Microscopy Study of a New Superstructure around Defects Created by Tip–sample Interaction on 2H-NbSe$_2$. *J. Phys.: Condens. Matter* **21**, 265005 (2009). DOI: 10.1088/0953-8984/21/26/265005 (cited on pp. 123 sq., 126 sq.).

390. Lin, Y.-C., Dumcenco, D. O., Huang, Y.-S., and Suenaga, K. Atomic Mechanism of the Semiconducting-to-Metallic Phase Transition in Single-Layered MoS$_2$. *Nat. Nanotechnol.* **9**, 391–396 (2014). DOI: 10.1038/nnano.2014.64 (cited on p. 123).

391. Ma, L., Ye, C., Yu, Y., Lu, X. F., Niu, X., Kim, S., Feng, D., Tománek, D., Son, Y.-W., Chen, X. H., and Zhang, Y. A Metallic Mosaic Phase and the Origin of Mott-Insulating State in 1T-TaS$_2$. *Nat. Commun.* **7**, 10956 (2016). DOI: 10.1038/ncomms10956 (cited on pp. 123 sq., 127 sq., 132, 135 sq.).

392. Johari, P. and Shenoy, V. B. Tuning the Electronic Properties of Semiconducting Transition Metal Dichalcogenides by Applying Mechanical Strains. *ACS Nano* **6**, 5449–5456 (2012). DOI: 10.1021/nn301320r (cited on pp. 123, 131).

393. Duerloo, K.-A. N., Li, Y., and Reed, E. J. Structural Phase Transitions in Two-Dimensional Mo- and W-Dichalcogenide Monolayers. *Nat. Commun.* **5**, 4214 (2014). DOI: 10.1038/ncomms5214 (cited on pp. 123, 126, 131).

394. Bhattacharyya, S. and Singh, A. K. Semiconductor-Metal Transition in Semiconducting Bilayer Sheets of Transition-Metal Dichalcogenides. *Phys. Rev. B* **86**, 075454 (2012). DOI: 10.1103/PhysRevB.86.075454 (cited on p. 123).

395. Yoshida, M., Suzuki, R., Zhang, Y., Nakano, M., and Iwasa, Y. Memristive Phase Switching in Two-Dimensional 1T-TaS$_2$ Crystals. *Sci. Adv.* **1**, e1500606 (2015). DOI: 10.1126/sciadv.1500606 (cited on pp. 123, 132, 136).

396. Yoshida, M., Zhang, Y., Ye, J., Suzuki, R., Imai, Y., Kimura, S., Fujiwara, A., and Iwasa, Y. Controlling Charge-Density-Wave States in Nano-Thick Crystals of 1T-TaS$_2$. *Sci. Rep.* **4**, 7302 (2014). DOI: 10.1038/srep07302 (cited on pp. 123, 132, 136).

397. Tsen, A. W., Hovden, R., Wang, D., Kim, Y. D., Okamoto, J., Spoth, K. A., Liu, Y., Lu, W., Sun, Y., Hone, J. C., Kourkoutis, L. F., Kim, P., and Pasupathy, A. N. Structure and Control of Charge Density Waves in Two-Dimensional 1T-TaS$_2$. *PNAS* **112**, 15054–15059 (2015). DOI: 10.1073/pnas.1512092112 (cited on pp. 123, 132, 136 sq.).

398. Li, Y., Duerloo, K.-A. N., Wauson, K., and Reed, E. J. Structural Semiconductor-to-Semimetal Phase Transition in Two-Dimensional Materials Induced by Electrostatic Gating. *Nat. Commun.* **7**, 10671 (2016). DOI: 10.1038/ncomms10671 (cited on pp. 123, 132, 136 sq.).

399. Vaskivskyi, I., Mihailovic, I. A., Brazovskii, S., Gospodaric, J., Mertelj, T., Svetin, D., Sutar, P., and Mihailovic, D. Fast Non-Thermal Switching between Macroscopic Charge-Ordered Quantum States Induced by Charge Injection. *Nat. Commun.* **7**, 11442 (2016). DOI: 10.1038/NCOMMS11442 (cited on pp. 123, 132, 136).

400. Zhang, C., KC, S., Nie, Y., Liang, C., Vandenberghe, W. G., Longo, R. C., Zheng, Y., Kong, F., Hong, S., Wallace, R. M., and Cho, K. Charge Mediated Reversible Metal–Insulator Transition in Monolayer MoTe$_2$ and W$_x$Mo$_{1-x}$Te$_2$ Alloy. *ACS Nano* **10**, 7370–7375 (2016). DOI: 10.1021/acsnano.6b00148 (cited on pp. 123, 126, 132, 137).

401. Arguello, C. J., Chockalingam, S. P., Rosenthal, E. P., Zhao, L., Gutiérrez, C., Kang, J. H., Chung, W. C., Fernandes, R. M., Jia, S., Millis, A. J., Cava, R. J., and Pasupathy, A. N. Visualizing the Charge Density Wave Transition in 2H-NbSe$_2$ in Real Space. *Phys. Rev. B* **89**, 235115 (2014). DOI: 10.1103/PhysRevB.89.235115 (cited on pp. 124, 128 sq.).

References

402. Chatterjee, U., Zhao, J., Iavarone, M., Di Capua, R., Castellan, J. P., Karapetrov, G., Malliakas, C. D., Kanatzidis, M. G., Claus, H., Ruff, J. P. C., Weber, F., van Wezel, J., Campuzano, J. C., Osborn, R., Randeria, M., Trivedi, N., Norman, M. R., and Rosenkranz, S. Emergence of Coherence in the Charge-Density Wave State of 2H-NbSe$_2$. *Nat. Commun.* **6**, 6313 (2015). DOI: 10.1038/ncomms7313 (cited on p. 124).

403. Revolinsky, E., Spiering, G. A., and Beerntsen, D. J. Superconductivity in the Niobium-Selenium System. *J. Phys. Chem. Solids* **26**, 1029–1034 (1965). DOI: 10.1016/0022-3697(65)90190-3 (cited on p. 124).

404. Weber, F., Hott, R., Heid, R., Bohnen, K.-P., Rosenkranz, S., Castellan, J.-P., Osborn, R., Said, A. H., Leu, B. M., and Reznik, D. Optical Phonons and the Soft Mode in 2H-NbSe$_2$. *Phys. Rev. B* **87**, 245111 (2013). DOI: 10.1103/PhysRevB.87.245111 (cited on pp. 124, 128).

405. Weber, F., Rosenkranz, S., Castellan, J.-P., Osborn, R., Hott, R., Heid, R., Bohnen, K.-P., Egami, T., Said, A. H., and Reznik, D. Extended Phonon Collapse and the Origin of the Charge-Density Wave in 2H-NbSe$_2$. *Phys. Rev. Lett.* **107**, 107403 (2011). DOI: 10.1103/PhysRevLett.107.107403 (cited on pp. 124, 128).

406. Koley, S., Mohanta, N., and Taraphder, A. The Unusual Normal State and Charge-Density-Wave Order in 2H-NbSe$_2$. *J. Phys.: Condens. Matter* **27**, 185601 (2015). DOI: 10.1088/0953-8984/27/18/185601 (cited on p. 124).

407. Flicker, F. and van Wezel, J. Charge Order from Orbital-Dependent Coupling Evidenced by NbSe$_2$. *Nat. Commun.* **6**, 7034 (2015). DOI: 10.1038/ncomms8034 (cited on pp. 124, 128 sq., 131).

408. Zhu, X., Cao, Y., Zhang, J., Plummer, E. W., and Guo, J. Classification of Charge Density Waves Based on Their Nature. *PNAS* **112**, 2367–2371 (2015). DOI: 10.1073/pnas.1424791112 (cited on p. 124).

409. Xi, X., Wang, Z., Zhao, W., Park, J.-H., Law, K. T., Berger, H., Forró, L., Shan, J., and Mak, K. F. Ising Pairing in Superconducting NbSe$_2$ Atomic Layers. *Nat. Phys.* **12**, 139–143 (2016). DOI: 10.1038/nphys3538 (cited on pp. 124, 127).

410. Malliakas, C. D. and Kanatzidis, M. G. Nb–Nb Interactions Define the Charge Density Wave Structure of 2H-NbSe$_2$. *J. Am. Chem. Soc.* **135**, 1719–1722 (2013). DOI: 10.1021/ja3120554 (cited on pp. 124, 128).

411. Johannes, M. D. and Mazin, I. I. Fermi Surface Nesting and the Origin of Charge Density Waves in Metals. *Phys. Rev. B* **77**, 165135 (2008). DOI: 10.1103/PhysRevB.77.165135 (cited on pp. 124, 128).

412. Johannes, M. D., Mazin, I. I., and Howells, C. A. Fermi-Surface Nesting and the Origin of the Charge-Density Wave in NbSe$_2$. *Phys. Rev. B* **73**, 205102 (2006). DOI: 10.1103/PhysRevB.73.205102 (cited on pp. 124, 128).

413. Silva-Guillén, J. Á., Ordejón, P., Guinea, F., and Canadell, E. Electronic Structure of 2H-NbSe$_2$ Single-Layers in the CDW State. *2D Mater.* **3**, 035028 (2016). DOI: 10.1088/2053-1583/3/3/035028 (cited on pp. 124, 128).

414. Shen, D. W., Zhang, Y., Yang, L. X., Wei, J., Ou, H. W., Dong, J. K., Xie, B. P., He, C., Zhao, J. F., Zhou, B., Arita, M., Shimada, K., Namatame, H., Taniguchi, M., Shi, J., and Feng, D. L. Primary Role of the Barely Occupied States in the Charge Density Wave Formation of NbSe$_2$. *Phys. Rev. Lett.* **101**, 226406 (2008). DOI: 10.1103/PhysRevLett.101.226406 (cited on p. 124).

415. Borisenko, S. V., Kordyuk, A. A., Zabolotnyy, V. B., Inosov, D. S., Evtushinsky, D., Büchner, B., Yaresko, A. N., Varykhalov, A., Follath, R., Eberhardt, W., Patthey, L., and Berger, H. Two Energy Gaps and Fermi-Surface "Arcs" in NbSe$_2$. *Phys. Rev. Lett.* **102**, 166402 (2009). DOI: 10.1103/PhysRevLett.102.166402 (cited on p. 124).

416. Feng, Y., Wang, J., Jaramillo, R., Wezel, J. van, Haravifard, S., Srajer, G., Liu, Y., Xu, Z.-A., Littlewood, P. B., and Rosenbaum, T. F. Order Parameter Fluctuations at a Buried Quantum Critical Point. *PNAS* **109**, 7224–7229 (2012). DOI: 10.1073/pnas.1202434109 (cited on p. 124).

417. Flicker, F. and van Wezel, J. Charge Ordering Geometries in Uniaxially Strained NbSe$_2$. *Phys. Rev. B* **92**, 201103 (2015). DOI: 10.1103/PhysRevB.92.201103 (cited on pp. 124, 128, 130 sq.).

418. Soumyanarayanan, A., Yee, M. M., He, Y., Wezel, J. van, Rahn, D. J., Rossnagel, K., Hudson, E. W., Norman, M. R., and Hoffman, J. E. Quantum Phase Transition from Triangular to Stripe Charge Order in NbSe$_2$. *PNAS* **110**, 1623–1627 (2013). DOI: 10.1073/pnas.1211387110 (cited on pp. 124, 129 sqq.).

419. Ugeda, M. M., Bradley, A. J., Zhang, Y., Onishi, S., Chen, Y., Ruan, W., Ojeda-Aristizabal, C., Ryu, H., Edmonds, M. T., Tsai, H.-Z., Riss, A., Mo, S.-K., Lee, D., Zettl, A., Hussain, Z., Shen, Z.-X., and Crommie, M. F. Characterization of Collective Ground States in Single-Layer NbSe$_2$. *Nat. Phys.* **12**, 92–97 (2016). DOI: 10.1038/nphys3527 (cited on pp. 124, 136).

420. Dai, J., Calleja, E., Alldredge, J., Zhu, X., Li, L., Lu, W., Sun, Y., Wolf, T., Berger, H., and McElroy, K. Microscopic Evidence for Strong Periodic Lattice Distortion in Two-Dimensional Charge-Density Wave Systems. *Phys. Rev. B* **89**, 165140 (2014). DOI: 10.1103/PhysRevB.89.165140 (cited on pp. 124, 128).

421. Arguello, C. J., Rosenthal, E. P., Andrade, E. F., Jin, W., Yeh, P. C., Zaki, N., Jia, S., Cava, R. J., Fernandes, R. M., Millis, A. J., Valla, T., Osgood, R. M., and Pasupathy, A. N. Quasiparticle Interference, Quasiparticle Interactions, and the Origin of the Charge Density Wave in 2H-NbSe$_2$. *Phys. Rev. Lett.* **114**, 037001 (2015). DOI: 10.1103/PhysRevLett.114.037001 (cited on p. 124).

422. Noat, Y., Silva-Guillén, J. A., Cren, T., Cherkez, V., Brun, C., Pons, S., Debontridder, F., Roditchev, D., Sacks, W., Cario, L., Ordejón, P., García, A., and Canadell, E. Quasiparticle Spectra of 2H-NbSe$_2$: Two-Band Superconductivity and the Role of Tunneling Selectivity. *Phys. Rev. B* **92**, 134510 (2015). DOI: 10.1103/PhysRevB.92.134510 (cited on p. 124).

423. Ramsak, N., van Midden, H. J. P., Prodan, A., Marinkovic, V., Boswell, F. W., and Bennett, J. C. Defect-Induced Room-Temperature Modulation in NbSe$_2$. *Phys. Rev. B* **60**, 4513–4516 (1999). DOI: 10.1103/PhysRevB.60.4513 (cited on pp. 124, 127).

424. Barja, S., Wickenburg, S., Liu, Z.-F., Zhang, Y., Ryu, H., Ugeda, M. M., Hussain, Z., Shen, Z.-X., Mo, S.-K., Wong, E., Salmeron, M. B., Wang, F., Crommie, M. F., Ogletree, D. F., Neaton, J. B., and Weber-Bargioni, A. Charge Density Wave Order in 1D Mirror Twin Boundaries of Single-Layer MoSe$_2$. *Nat. Phys.* **12**, 751–756 (2016). DOI: 10.1038/nphys3730 (cited on pp. 124, 130, 136).

425. Weber, B., Tan, Y. H. M., Mahapatra, S., Watson, T. F., Ryu, H., Rahman, R., Hollenberg, L. C. L., Klimeck, G., and Simmons, M. Y. Spin Blockade and Exchange in Coulomb-Confined Silicon Double Quantum Dots. *Nat. Nanotechnol.* **9**, 430–435 (2014). DOI: 10.1038/nnano.2014.63 (cited on p. 124).

426. Weber, B., Mahapatra, S., Ryu, H., Lee, S., Fuhrer, A., Reusch, T. C. G., Thompson, D. L., Lee, W. C. T., Klimeck, G., Hollenberg, L. C. L., and Simmons, M. Y. Ohm's Law Survives to the Atomic Scale. *Science* **335**, 64–67 (2012). DOI: 10.1126/science.1214319 (cited on p. 124).

427. Kalff, F. E., Rebergen, M. P., Fahrenfort, E., Girovsky, J., Toskovic, R., Lado, J. L., Fernández-Rossier, J., and Otte, A. F. A Kilobyte Rewritable Atomic Memory. *Nat. Nanotechnol.* **11**, 926–929 (2016). DOI: 10.1038/nnano.2016.131 (cited on p. 124).

428. Tapasztó, L., Dobrik, G., Lambin, P., and Biró, L. P. Tailoring the Atomic Structure of Graphene Nanoribbons by Scanning Tunnelling Microscope Lithography. *Nat. Nanotechnol.* **3**, 397–401 (2008). DOI: 10.1038/nnano.2008.149 (cited on p. 124).

429. Seufert, K., Auwärter, W., García de Abajo, F. J., Ecija, D., Vijayaraghavan, S., Joshi, S., and Barth, J. V. Controlled Interaction of Surface Quantum-Well Electronic States. *Nano Lett.* **13**, 6130–6135 (2013). DOI: 10.1021/nl403459m (cited on p. 124).

430. Dubost, V., Cren, T., Vaju, C., Cario, L., Corraze, B., Janod, E., Debontridder, F., and Roditchev, D. Resistive Switching at the Nanoscale in the Mott Insulator Compound GaTa$_4$Se$_8$. *Nano Lett.* **13**, 3648–3653 (2013). DOI: 10.1021/nl401510p (cited on p. 124).

431. Kadijk, F. and Jellinek, F. On the Polymorphism of Niobium Diselenide. *J. Less-Common Met.* **23**, 437–441 (1971). DOI: 10.1016/0022-5088(71)90053-1 (cited on pp. 124, 126).

References

432. Nakata, Y., Sugawara, K., Shimizu, R., Okada, Y., Han, P., Hitosugi, T., Ueno, K., Sato, T., and Takahashi, T. Monolayer 1T-NbSe$_2$ as a Mott Insulator. *NPG Asia Mater* **8**, e321 (2016). DOI: 10.1038/am.2016.157 (cited on pp. 124, 126, 135).

433. Marezio, M., Dernier, P. D., Menth, A., and Hull, G. W. The Crystal Structure of NbSe$_2$ at 15K. *J. Solid State Chem.* **4**, 425–429 (1972). DOI: 10.1016/0022-4596(72)90158-2 (cited on p. 124).

434. Kim, J.-J., Park, C., Yamaguchi, W., Shiino, O., Kitazawa, K., and Hasegawa, T. Observation of a Phase Transition from the T Phase to the H Phase Induced by a STM Tip in 1T–TaS$_2$. *Phys. Rev. B* **56**, R15573–R15576 (1997). DOI: 10.1103/PhysRevB.56.R15573 (cited on p. 124).

435. Zhou, W., Zou, X., Najmaei, S., Liu, Z., Shi, Y., Kong, J., Lou, J., Ajayan, P. M., Yakobson, B. I., and Idrobo, J.-C. Intrinsic Structural Defects in Monolayer Molybdenum Disulfide. *Nano Lett.* **13**, 2615–2622 (2013). DOI: 10.1021/nl4007479 (cited on p. 125).

436. Cho, S., Kim, S., Kim, J. H., Zhao, J., Seok, J., Keum, D. H., Baik, J., Choe, D.-H., Chang, K. J., Suenaga, K., Kim, S. W., Lee, Y. H., and Yang, H. Phase Patterning for Ohmic Homojunction Contact in MoTe$_2$. *Science* **349**, 625–628 (2015). DOI: 10.1126/science.aab3175 (cited on p. 126).

437. He, R., Baren, J. van, Yan, J.-A., Xi, X., Ye, Z., Ye, G., Lu, I.-H., Leong, S. M., and Lui, C. H. Interlayer Breathing and Shear Modes in NbSe$_2$ Atomic Layers. *2D Mater.* **3**, 031008 (2016). DOI: 10.1088/2053-1583/3/3/031008 (cited on p. 127).

438. Calandra, M., Mazin, I. I., and Mauri, F. Effect of Dimensionality on the Charge-Density Wave in Few-Layer 2H-NbSe$_2$. *Phys. Rev. B* **80**, 241108 (2009). DOI: 10.1103/PhysRevB.80.241108 (cited on pp. 127 sq.).

439. Cho, D., Cheon, S., Kim, K.-S., Lee, S.-H., Cho, Y.-H., Cheong, S.-W., and Yeom, H. W. Nanoscale Manipulation of the Mott Insulating State Coupled to Charge Order in 1T-TaS$_2$. *Nat. Commun.* **7**, 10453 (2016). DOI: 10.1038/ncomms10453 (cited on pp. 127 sq., 136).

440. Stoltz, D., Bielmann, M., Bovet, M., Schlapbach, L., and Berger, H. Tunneling Evidence for Spatial Location of the Charge-Density-Wave Induced Band Splitting in 1T-TaSe$_2$. *Phys. Rev. B* **76**, 073410 (2007). DOI: 10.1103/PhysRevB.76.073410 (cited on pp. 127 sq.).

441. Stoltz, D., Bielmann, M., Schlapbach, L., Bovet, M., Berger, H., Göthelid, M., Stoltz, S. E., and Starnberg, H. I. Atomic Origin of the Scanning Tunneling Microscopy Images of Charge-Density-Waves on 1T-TaSe$_2$. *Physica B: Condensed Matter* **403**, 2207–2210 (2008). DOI: 10.1016/j.physb.2007.11.026 (cited on pp. 127 sq.).

442. Valla, T., Fedorov, A. V., Johnson, P. D., Glans, P.-A., McGuinness, C., Smith, K. E., Andrei, E. Y., and Berger, H. Quasiparticle Spectra, Charge-Density Waves, Superconductivity, and Electron-Phonon Coupling in 2H-NbSe$_2$. *Phys. Rev. Lett.* **92**, 086401 (2004). DOI: 10.1103/PhysRevLett.92.086401 (cited on p. 128).

443. Rossnagel, K., Seifarth, O., Kipp, L., Skibowski, M., Voß, D., Krüger, P., Mazur, A., and Pollmann, J. Fermi Surface of 2H-NbSe$_2$ and Its Implications on the Charge-Density-Wave Mechanism. *Phys. Rev. B* **64**, 235119 (2001). DOI: 10.1103/PhysRevB.64.235119 (cited on p. 128).

444. Flicker, F. and van Wezel, J. One-Dimensional Quasicrystals from Incommensurate Charge Order. *Phys. Rev. Lett.* **115**, 236401 (2015). DOI: 10.1103/PhysRevLett.115.236401 (cited on p. 131).

445. Bissett, M. A., Tsuji, M., and Ago, H. Strain Engineering the Properties of Graphene and Other Two-Dimensional Crystals. *Phys. Chem. Chem. Phys.* **16**, 11124–11138 (2014). DOI: 10.1039/C3CP55443K (cited on p. 131).

446. Roldán, R., Castellanos-Gomez, A., Cappelluti, E., and Guinea, F. Strain Engineering in Semiconducting Two-Dimensional Crystals. *J. Phys.: Condens. Matter* **27**, 313201 (2015). DOI: 10.1088/0953-8984/27/31/313201 (cited on p. 131).

447. Schwarz, M., Riss, A., Garnica, M., Ducke, J., Deimel, P. S., Duncan, D. A., Thakur, P. K., Lee, T.-L., Seitsonen, A. P., Barth, J. V., Allegretti, F., and Auwärter, W. Corrugation in the Weakly Interacting Hexagonal-BN/Cu(111) System: Structure Determination by Combining Noncontact Atomic Force Microscopy and X-Ray Standing Waves. *ACS Nano* **11**, 9151–9161 (2017). DOI: 10.1021/acsnano.7b04022 (cited on pp. 135 sq.).

448. Jelínek, P. High Resolution SPM Imaging of Organic Molecules with Functionalized Tips. *J. Phys.: Condens. Matter* **29**, 343002 (2017). DOI: 10.1088/1361-648X/aa76c7 (cited on p. 136).

449. Van der Heijden, N. J., Hapala, P., Rombouts, J. A., van der Lit, J., Smith, D., Mutombo, P., Švec, M., Jelinek, P., and Swart, I. Characteristic Contrast in Δf_{min} Maps of Organic Molecules Using Atomic Force Microscopy. *ACS Nano* **10**, 8517–8525 (2016). DOI: 10.1021/acsnano.6b03644 (cited on p. 136).

450. Iwata, K., Yamazaki, S., Mutombo, P., Hapala, P., Ondráček, M., Jelínek, P., and Sugimoto, Y. Chemical Structure Imaging of a Single Molecule by Atomic Force Microscopy at Room Temperature. *Nat. Commun.* **6**, 7766 (2015). DOI: 10.1038/ncomms8766 (cited on p. 136).

451. Ebeling, D., Zhong, Q., Ahles, S., Chi, L., Wegner, H. A., and Schirmeisen, A. Chemical Bond Imaging Using Higher Eigenmodes of Tuning Fork Sensors in Atomic Force Microscopy. *Appl. Phys. Lett.* **110**, 183102 (2017). DOI: 10.1063/1.4982801 (cited on p. 136).

452. Chiang, C.-l., Xu, C., Han, Z., and Ho, W. Real-Space Imaging of Molecular Structure and Chemical Bonding by Single-Molecule Inelastic Tunneling Probe. *Science* **344**, 885–888 (2014). DOI: 10.1126/science.1253405 (cited on p. 136).

453. Sugimoto, Y., Pou, P., Abe, M., Jelinek, P., Pérez, R., Morita, S., and Custance, Ó. Chemical Identification of Individual Surface Atoms by Atomic Force Microscopy. *Nature* **446**, 64–67 (2007). DOI: 10.1038/nature05530 (cited on p. 136).

454. Setvín, M., Mutombo, P., Ondráček, M., Majzik, Z., Švec, M., Cháb, V., Ošt'ádal, I., Sobotík, P., and Jelínek, P. Chemical Identification of Single Atoms in Heterogeneous III–IV Chains on Si(100) Surface by Means of Nc-AFM and DFT Calculations. *ACS Nano* **6**, 6969–6976 (2012). DOI: 10.1021/nn301996k (cited on p. 136).

455. Stetsovych, O., Todorović, M., Shimizu, T. K., Moreno, C., Ryan, J. W., León, C. P., Sagisaka, K., Palomares, E., Matolín, V., Fujita, D., Perez, R., and Custance, O. Atomic Species Identification at the (101) Anatase Surface by Simultaneous Scanning Tunnelling and Atomic Force Microscopy. *Nat. Commun.* **6**, 7265 (2015). DOI: 10.1038/ncomms8265 (cited on p. 136).

456. Nakagawa, T., Ogawa, K., Kurumizawa, T., and Ozaki, S. Discriminating Molecular Length of Chemically Adsorbed Molecules Using an Atomic Force Microscope Having a Tip Covered with Sensor Molecules (An Atomic Force Microscope Having Chemical Sensing Function). *Jpn. J. Appl. Phys.* **32**, L294 (1993). DOI: 10.1143/JJAP.32.L294 (cited on p. 136).

457. Hauptmann, N., Robles, R., Abufager, P., Lorente, N., and Berndt, R. AFM Imaging of Mercaptobenzoic Acid on Au(110): Submolecular Contrast with Metal Tips. *J. Phys. Chem. Lett.* **7**, 1984–1990 (2016). DOI: 10.1021/acs.jpclett.6b00684 (cited on p. 136).

458. Yurtsever, A., Sugimoto, Y., Fukumoto, M., Abe, M., and Morita, S. Effect of Tip Polarity on Kelvin Probe Force Microscopy Images of Thin Insulator CaF$_2$ Films on Si(111). *Appl. Phys. Lett.* **101**, 083119 (2012). DOI: 10.1063/1.4748291 (cited on p. 136).

459. Sweetman, A., Stirling, J., Jarvis, S. P., Rahe, P., and Moriarty, P. Measuring the Reactivity of a Silicon-Terminated Probe. *Phys. Rev. B* **94**, 115440 (2016). DOI: 10.1103/PhysRevB.94.115440 (cited on p. 136).

460. Dagdeviren, O. E., Götzen, J., Altman, E. I., and Schwarz, U. D. Exploring Site-Specific Chemical Interactions at Surfaces: A Case Study on Highly Ordered Pyrolytic Graphite. *Nanotechnology* **27**, 485708 (2016). DOI: 10.1088/0957-4484/27/48/485708 (cited on p. 136).

461. Tuxen, A., Kibsgaard, J., Gøbel, H., Lægsgaard, E., Topsøe, H., Lauritsen, J. V., and Besenbacher, F. Size Threshold in the Dibenzothiophene Adsorption on MoS$_2$ Nanoclusters. *ACS Nano* **4**, 4677–4682 (2010). DOI: 10.1021/nn1011013 (cited on p. 136).

462. Tuxen, A. K., Füchtbauer, H. G., Temel, B., Hinnemann, B., Topsøe, H., Knudsen, K. G., Besenbacher, F., and Lauritsen, J. V. Atomic-Scale Insight into Adsorption of Sterically Hindered Dibenzothiophenes on MoS$_2$ and Co–Mo–S Hydrotreating Catalysts. *J. Catal.* **295**, 146–154 (2012). DOI: 10.1016/j.jcat.2012.08.004 (cited on p. 136).

463. Topsøe, N.-Y., Tuxen, A., Hinnemann, B., Lauritsen, J. V., Knudsen, K. G., Besenbacher, F., and Topsøe, H. Spectroscopy, Microscopy and Theoretical Study of NO Adsorption on MoS$_2$ and Co–Mo–S Hydrotreating Catalysts. *J. Catal.* **279**, 337–351 (2011). DOI: 10.1016/j.jcat.2011.02.002 (cited on p. 136).

464. Sørensen, S. G., Füchtbauer, H. G., Tuxen, A. K., Walton, A. S., and Lauritsen, J. V. Structure and Electronic Properties of In Situ Synthesized Single-Layer MoS$_2$ on a Gold Surface. *ACS Nano* **8**, 6788–6796 (2014). DOI: 10.1021/nn502812n (cited on p. 136).

465. Lauritsen, J. V., Kibsgaard, J., Helveg, S., Topsøe, H., Clausen, B. S., Lægsgaard, E., and Besenbacher, F. Size-Dependent Structure of MoS$_2$ Nanocrystals. *Nat. Nanotechnol.* **2**, 53–58 (2007). DOI: 10.1038/nnano.2006.171 (cited on p. 136).

466. Zhu, X., Guo, Y., Cheng, H., Dai, J., An, X., Zhao, J., Tian, K., Wei, S., Zeng, X. C., Wu, C., and Xie, Y. Signature of Coexistence of Superconductivity and Ferromagnetism in Two-Dimensional NbSe$_2$ Triggered by Surface Molecular Adsorption. *Nat. Commun.* **7**, ncomms11210 (2016). DOI: 10.1038/ncomms11210 (cited on p. 136).

467. Zhou, Y. and Reed, E. J. Structural Phase Stability Control of Monolayer MoTe$_2$ with Adsorbed Atoms and Molecules. *J. Phys. Chem. C* **119**, 21674–21680 (2015). DOI: 10.1021/acs.jpcc.5b05770 (cited on pp. 136 sq.).

468. Chen, X. and McDonald, A. R. Functionalization of Two-Dimensional Transition-Metal Dichalcogenides. *Adv. Mater.* **28**, 5738–5746 (2016). DOI: 10.1002/adma.201505345 (cited on p. 136).

469. Feng, Z., Xie, Y., Chen, J., Yu, Y., Zheng, S., Zhang, R., Li, Q., Xuejiao Chen, Sun, C., Zhang, H., Pang, W., Liu, J., and Zhang, D. Highly Sensitive MoTe$_2$ Chemical Sensor with Fast Recovery Rate through Gate Biasing. *2D Mater.* **4**, 025018 (2017). DOI: 10.1088/2053-1583/aa57fe (cited on p. 137).

470. Mohn, F., Gross, L., and Meyer, G. Measuring the Short-Range Force Field above a Single Molecule with Atomic Resolution. *Applied Physics Letters* **99**, 053106 (2011). DOI: 10.1063/1.3619829 (cited on p. 170).

471. Nečas, D. and Klapetek, P. Gwyddion: An Open-Source Software for SPM Data Analysis. *Open Physics* **10**, 181–188 (2011). DOI: 10.2478/s11534-011-0096-2 (cited on p. 173).

472. Bischoff, F., Seufert, K., Auwärter, W., Heim, D., and Barth, J. V. Direct Observation and Stimulation of 2H-TPP Metalation by Cerium on Ag(111). *submitted to J. Phys. Chem.* (2017) (cited on p. 175).

473. Joshi, S., Bischoff, F., Koitz, R., Ecija, D., Seufert, K., Seitsonen, A. P., Hutter, J., Diller, K., Urgel, J. I., Sachdev, H., Barth, J. V., and Auwärter, W. Control of Molecular Organization and Energy Level Alignment by an Electronically Nanopatterned Boron Nitride Template. *ACS Nano* **8**, 430–442 (2014). DOI: 10.1021/nn406024m (cited on p. 176).

474. Joshi, S., Ecija, D., Koitz, R., Iannuzzi, M., Seitsonen, A. P., Hutter, J., Sachdev, H., Vijayaraghavan, S., Bischoff, F., Seufert, K., Barth, J. V., and Auwärter, W. Boron Nitride on Cu(111): An Electronically Corrugated Monolayer. *Nano Lett.* **12**, 5821–5828 (2012). DOI: 10.1021/nl303170m (cited on p. 176).

475. Écija, D., Auwärter, W., Vijayaraghavan, S., Seufert, K., Bischoff, F., Tashiro, K., and Barth, J. V. Assembly and Manipulation of Rotatable Cerium Porphyrinato Sandwich Complexes on a Surface. *Angew. Chem. Int. Ed.* **50**, 3872–3877 (2011). DOI: 10.1002/anie.201007370 (cited on p. 176).

Experimental details

If not mentioned otherwise, all experiments were performed in the Munich setup (see 4) operated at $5\,K$. The base pressure during the experiments was below $3 \cdot 10^{-10}\,mbar$. Repeated cycles of Ar^+ sputtering and annealing to $725\,K$ were used to prepare the Ag(111) and Cu(111) single crystals. In the figure captions voltage U refers to the bias voltage applied to the sample.

All AFM data were recorded with a qPlus sensor in the frequency modulation mode using a CO functionalized tip. The tungsten tip at the sensor was prepared by focused-ion-beam processing and in situ tip forming. To facilitate the CO pickup on Cu(111), a small amount of bilayer NaCl islands were grown. Therefor NaCl powder (Sigma Aldrich, purity $99.999\,\%$) was thoroughly degassed in a quartz crucible and deposited at $910\,K$ onto the sample held at $280\,K$ for $2\,min$ (also see Section 5.1). A CO transfer from NaCl/Cu(111) and Ag(111) to the tip can be achieved by approaching the tip at a CO several hundred pm from the STM set point (also see Section 5.3). All data were recorded away from NaCl islands on the metal sample. The change in tip height Δz for constant height AFM images refers to the stabilization of the tip in STM constant current mode above the bare metal substrate. Generally the SP corresponds to the scan parameters of the STM image presented together with the AFM data. If not mentioned otherwise, AFM images were recorded in constant-height mode at $U = 0\,V$ bias with an oscillation amplitude of $50\,pm$–$100\,pm$.

Prior to all AFM experiments, the cantilever oscillation amplitude was calibrated, the qPlus sensor was characterized by frequency sweeps, and PLL parameters were optimized. Additionally, piezo offsets were determined to account for tilting of the sample and to guarantee a parallel movement of the cantilever with respect to the surface plane. When recording constant height Δf-maps, the tip was stabilized above bare metal before switching off the STM feedback. To ensure the same reference point for all constant height measurements, the STM feedback parameters were set to a very slow regulation. This avoids sudden tip movements caused by fluctuations and noise in the tunneling junction and stabilizes the sensor at an "average height". Furthermore, a constant current image was recorded before and after every AFM measurement in order to compensate for drifts in z-direction. The area for AFM investigations was usually scanned for several hours in constant current more before disabling the STM feedback to account for piezo creep.

Metal-organic porphyrin networks on Ag(111)

2H-TPyPP and 2H-TPCN molecules were dosed from a thoroughly degassed quartz crucible held at $760\,K$. During deposition the sample was kept at room temperature. Cu was evaporated from a home-built, water-cooled cell by resistively heating a W filament supporting a Cu wire of high purity ($99.9999\,\%$). All STM images were recorded in constant

current mode using an electrochemically etched tungsten tip prepared by sputtering and controlled dipping into the Ag(111) substrate.

2H-TPyPP and 2H-TPCN molecules were synthesized and provided by Daphne Stassen (Department of Chemistry and Namur Research College, University of Namur, Belgium) and Prof. D. Bonifazi (Department of Chemistry and Namur Research College, University of Namur, Belgium; School of Chemistry, Cardiff University Main Building, Park Place, Cardiff CF10 3AT, United Kingdom). For details on the synthesis, please see Supporting Information of Reference [204].

FM-AFM investigation of cyano–copper coordination nodes

Experiments were performed in Regensburg using a home-built combined STM/AFM operated in ultrahigh vacuum ($p \approx 5 \cdot 10^{-11}$ mbar) at low temperature (≈ 5 K)[129]. The microscope is equipped with a qPlus sensor and operated in the frequency modulation mode. The oscillation amplitude was fixed to 0.5 Å to increase the lateral resolution, and bias voltages refer to the sample with respect to the tip. 2H-TPCN and copper were consecutively sublimed onto the cold Ag(111) surface with the sample being located inside the scanner, subsequently transferred to the preparation chamber for annealing to room temperature and re-transferred to the scanner.

Adsorption geometry of 2H-TPP on coinage metal surfaces

2H-TPP molecules (Sigma Aldrich, purity > 99 %) were dosed from a thoroughly degassed quartz crucible held at 600 K onto a sample held at ≈ 80 K for single molecule investigations on Ag(111) and onto a room temperature sample for Cu(111). The experiments were carried out with a qPlus sensor with fixed oscillation amplitude at 0.8 Å.

Figure 7.2e was recorded in Regensburg[33,129] using a home-built combined STM/AFM operated in ultrahigh vacuum ($p \approx 5 \cdot 10^{-11}$ mbar) at low temperature (≈ 5 K). Individual 2H-TPP molecules (Sigma-Aldrich) were sublimed onto the cold Cu(111) surface with the sample being located inside the scanner. The oscillation amplitude was fixed to 0.5 Å. The $\Delta f(z)$-grid on 2H-TPP contains 50×50 pixels and was recorded with disabled z-feedback. To correct for lateral drift and creep during the 15 h of data acquisition, a constant-height image was recorded after each line of spectra. In the data analysis, a cross correlation procedure of these images allowed to correct for lateral mismatch by shifting the grid pixels accordingly. In order to record all $\Delta f(z)$-spectra for the grid in a sufficiently close but safe distance regime, a threshold criterion was implemented as introduced by Mohn et al.[470]

Dehydrogenative homocoupling of porphine molecules

2H-P (purity > 95 %, Frontier Scientific) were deposited using organic molecular beam epitaxy from a thoroughly degassed quartz container held at 570 K. During deposition the Ag(111) substrate was kept at room temperature. To trigger the coupling reaction, the sample was subsequently heated to 570 K for 20 min. For the AFM imaging, the tip

was typically approached by a distance Δz of 60 pm to 70 pm with respect to the STM set point on Ag(111).

Cyclodehydrogenative flattening of porphyrins and surface-catalyzed porphyrin deconstruction

2H-TPP (Sigma Aldrich, purity $> 99\,\%$) was deposited using organic molecular beam epitaxy from a thoroughly degassed quartz container held at 600 K. During deposition the sample temperature was kept at room temperature and subsequently heated to 510 K for 5 min to induce complete chemical reactions on Cu(111). Annealing to 390 K for 20 min led to reaction intermediates. For AFM imaging, the tip was approached by a distance Δz of 1 Å–2 Å with respect to a typical STM setpoint of $U = 30\,\text{mV}$, $I = 10\,\text{pA}$.

Nanoscale phase engineering of niobium diselenide

All experiments were performed at Monash University Melbourne in a commercial ultra-high vacuum chamber housing a slider-type STM by CreaTec. The STM was operated at 77 K and 4.5 K. The base pressure during the experiments was below $p \approx 3 \cdot 10^{-10}\,\text{mbar}$. The NbSe$_2$ sample was either prepared by ex-situ tape exfoliation or by in-situ cleaving. When exfoliated in ambient conditions, the sample was transferred within seconds into a UHV load-lock and immediately pumped. All STM images were recorded in constant current mode. The tip was prepared by field emission and controlled dipping into an Au(111) substrate as well as by voltage pulsing on NbSe$_2$. The phase transformation from 2H- to 1T-NbSe$_2$ was realized by pulsing the bias voltage from the scan setpoint to values exceeding 4 V for 100 ms. The tip feedback was switched off during the pulse, i.e. the tip was stabilized at the scan parameters. For the reversible switching of charge order from 3×3- to 1D-CDW, the STM feedback was kept on and the bias was increased to 5 V–6 V during scanning. The area of interest was scanned for several scan frames at elevated bias before resuming to the initial scan parameters. In the figure captions voltage U refers to the bias voltage applied to the sample.

Data post-processing

For data post-processing of SPM raw data, the Gwyddion software package[471] (http://gwyddion.net/) and the WsXM program (www.nanotec.es) were used. For STM data, only standard procedures were employed like Gaussian blurring to remove noise, plane subtractions and contrast adaptations for optimized visibility of relevant features. For AFM, to accentuate the chemical structure within the displayed constant height Δf-maps, the data was first low-pass filtered to remove (high frequency) noise (indicated by "lowpass" at the image) and then edges—i.e. sharp transitions from dark to bright—were detected by displaying the second derivative of the image (Laplace filter). When applied it is indicated by "Laplace" at the image. A noise-minimum filter can further sharpen the edges by setting all pixel values to the lowest (i.e. darkest) value within a pre-defined radius. In doing so, only the central bright pixels survive that do not adjoin dark pixels and chemical bonds appear sharpened. When this filter was used, it is indicated by the label "NoiseMin". All filtering procedures can cause image artifacts and were employed with care.

List of publications

1. Bischoff, F., Michelitsch, G., Riss, A., Reuter, K., Barth, J. V., and Auwärter, W. Surface-catalyzed ring-opening reaction and porphyrin deconstruction via conformational design. In preparation.

2. Bischoff, F., Seufert, K., Auwärter, W., Heim, D., and Barth, J. V. Direct Observation and Stimulation of 2H-TPP Metalation by Cerium on Ag(111). *submitted to J. Phys. Chem.* (2017).

3. Bischoff, F., Auwärter, W., Barth, J. V., Schiffrin, A., Fuhrer, M., and Weber, B. Nanoscale Phase Engineering of Niobium Diselenide. *Chem. Mater.* (2017). DOI: 10.1021/acs.chemmater.7b03061.

4. Garnica, M., Schwarz, M., Ducke, J., He, Y., Bischoff, F., Barth, J. V., Auwärter, W., and Stradi, D. Comparative Study of the Interfaces of Graphene and Hexagonal Boron Nitride with Silver. *Phys. Rev. B* **94**.15, 155431 (2016). DOI: 10.1103/PhysRevB.94.155431.

5. Albrecht, F., Bischoff, F., Auwärter, W., Barth, J. V., and Repp, J. Direct Identification and Determination of Conformational Response in Adsorbed Individual Nonplanar Molecular Species Using Noncontact Atomic Force Microscopy. *Nano Lett.* **16**.12, 7703–7709 (2016). DOI: 10.1021/acs.nanolett.6b03769.

6. Bischoff, F., He, Y., Seufert, K., Stassen, D., Bonifazi, D., Barth, J. V., and Auwärter, W. Tailoring Large Pores of Porphyrin Networks on Ag(111) by Metal-Organic Coordination. *Chem. Eur. J.* **22**.43, 15298–15306 (2016). DOI: 10.1002/chem.201602154.

7. He, Y., Garnica, M., Bischoff, F., Ducke, J., Bocquet, M.-L., Batzill, M., Auwärter, W., and Barth, J. V. Fusing Tetrapyrroles to Graphene Edges by Surface-Assisted Covalent Coupling. *Nat. Chem.* **9**.1, 33–38 (2017). DOI: 10.1038/nchem.2600.

8. Snezhkova, O., Bischoff, F., He, Y., Wiengarten, A., Chaudhary, S., Johansson, N., Schulte, K., Knudsen, J., Barth, J. V., Seufert, K., Auwärter, W., and Schnadt, J. Iron Phthalocyanine on Cu(111): Coverage-Dependent Assembly and Symmetry Breaking, Temperature-Induced Homocoupling, and Modification of the Adsorbate-Surface Interaction by Annealing. *J. Chem. Phys* **144**.9, 094702 (2016). DOI: 10.1063/1.4942121.

9. Snezhkova, O., Lüder, J., Wiengarten, A., Burema, S. R., Bischoff, F., He, Y., Rusz, J., Knudsen, J., Bocquet, M.-L., Seufert, K., Barth, J. V., Auwärter, W., Brena, B., and Schnadt, J. Nature of the Bias-Dependent Symmetry Reduction of Iron Phthalocyanine on Cu(111). *Phys. Rev. B* **92**.7, 075428 (2015). DOI: 10.1103/PhysRevB.92.075428.

10. Wiengarten, A., Seufert, K., Auwärter, W., Ecija, D., Diller, K., Allegretti, F., Bischoff, F., Fischer, S., Duncan, D. A., Papageorgiou, A. C., Klappenberger, F., Acres, R. G., Ngo, T. H., and Barth, J. V. Surface-Assisted Dehydrogenative Homocoupling of Porphine Molecules. *J. Am. Chem. Soc.* **136**.26, 9346–9354 (2014). DOI: 10.1021/ja501680n.

11. Joshi, S., Bischoff, F., Koitz, R., Ecija, D., Seufert, K., Seitsonen, A. P., Hutter, J., Diller, K., Urgel, J. I., Sachdev, H., Barth, J. V., and Auwärter, W. Control of Molecular Organization and Energy Level Alignment by an Electronically Nanopatterned Boron Nitride Template. *ACS Nano* **8**.1, 430–442 (2014). DOI: 10.1021/nn406024m.

12. Bischoff, F., Seufert, K., Auwärter, W., Joshi, S., Vijayaraghavan, S., Écija, D., Diller, K., Papageorgiou, A. C., Fischer, S., Allegretti, F., Duncan, D. A., Klappenberger, F., Blobner, F., Han, R., and Barth, J. V. How Surface Bonding and Repulsive Interactions Cause Phase Transformations: Ordering of a Prototype Macrocyclic Compound on Ag(111). *ACS Nano* **7**.4, 3139–3149 (2013). DOI: 10.1021/nn305487c.

13. Joshi, S., Ecija, D., Koitz, R., Iannuzzi, M., Seitsonen, A. P., Hutter, J., Sachdev, H., Vijayaraghavan, S., Bischoff, F., Seufert, K., Barth, J. V., and Auwärter, W. Boron Nitride on Cu(111): An Electronically Corrugated Monolayer. *Nano Lett.* **12**.11, 5821–5828 (2012). DOI: 10.1021/nl303170m.

14. Auwärter, W., Seufert, K., Bischoff, F., Ecija, D., Vijayaraghavan, S., Joshi, S., Klappenberger, F., Samudrala, N., and Barth, J. V. A Surface-Anchored Molecular Four-Level Conductance Switch Based on Single Proton Transfer. *Nat. Nanotechnol.* **7**.1, 41–46 (2012). DOI: 10.1038/nnano.2011.211.

15. Écija, D., Auwärter, W., Vijayaraghavan, S., Seufert, K., Bischoff, F., Tashiro, K., and Barth, J. V. Assembly and Manipulation of Rotatable Cerium Porphyrinato Sandwich Complexes on a Surface. *Angew. Chem. Int. Ed.* **50**.17, 3872–3877 (2011). DOI: 10.1002/anie.201007370.